Turbulent Vortex Shedding from a Blunt Trailing Edge Hydrofoil

THÈSE N^{O} 4475 (2009)

PRÉSENTÉE LE 11 SEPTEMBRE 2009
À LA FACULTE SCIENCES ET TECHNIQUES DE L'INGÉNIEUR
LABORATOIRE DE MACHINES HYDRAULIQUES
PROGRAMME DOCTORAL EN MÉCANIQUE

ÉCOLE POLYTECHNIQUE FÉDÉRALE DE LAUSANNE

POUR L'OBTENTION DU GRADE DE DOCTEUR ÈS SCIENCES

PAR

Philippe AUSONI

acceptée sur proposition du jury:

Prof. Ph. Wieser, président du jury
Prof. F. Avellan, Dr M. Farhat, directeurs de thèse
Prof. C. Ancey, rapporteur
Prof. E. Egusquiza, rapporteur
Dr H. Keck, rapporteur

ÉCOLE POLYTECHNIQUE
FÉDÉRALE DE LAUSANNE

Suisse
2009

A Jean-Claude

Theories come and go,
the experiment is here forever

Hannes Alfvén,
Physicist, Nobel Prize winner

Remerciements

En préambule de ce document, il m'importe d'exprimer ma gratitude à toutes celles et ceux qui ont contribué à la réalisation et au succès de cette thèse.

J'exprime mes sincères remerciements à mes directeurs de thèse, le Professeur François Avellan et le Dr. Mohamed Farhat, pour m'avoir accordé leur confiance tout au long de ce travail. Je les remercie pour m'avoir confié le dispositif expérimental nécessaire. Le lecteur ne peut être qu'impressionné par les moyens techniques mis en oeuvre. Merci au premier pour avoir toujours exigé le meilleur de moi-même. Le Professeur Avellan a également su diriger ma recherche dans les moments clés et opportuns. Je remercie le Dr. Farhat pour son encadrement. Il s'est passionné pour les phénomènes étudiés et n'a manqué aucun de mes avancements. Ces conseils ont sensiblement contribué à la réussite de ce projet. Je le remercie également pour les interminables discussions de cafétéria et pour sa sincérité sur des sujets plus personnels. Je remercie également mes directeurs de thèse pour m'avoir donné la chance de présenter ma recherche lors de différents congrès. De Houston à Barcelone, de Wageningen à San Diego en passant par Timisoara, j'ai eu l'opportunité de me confronter à des scientifiques émérites.

Ce travail de recherche n'aurait pas été possible sans l'appui scientifique et financier de l'Hydrodyna Eureka Research Project dont les partenaires industriels sont Alstom Hydro, Andritz Hydro, EDF, GE Hydro, UPC-CDIF et Voith Hydro. Je remercie spécialement M. Deniau, Dr. Sick et M. Keller, M. Vu et M. Nennemann, Prof. Egusquiza et Dr. Escaler, Dr. Aschenbrenner, Dr. Hübner et M. Seidel pour leur intérêt et leurs encouragements. Je garderai un excellent souvenir des présentations et brainstormings lors des comités techniques semestriels. Le projet est également financièrement supporté par l'agence pour la promotion de l'innovation et le fond national suisse.

Je remercie les membres du jury, les Professeurs Wieser, Ancey et Egusquiza ainsi que le Dr. Keck, pour les discussions constructives lors de la défense de thèse privée.

Je remercie également mes collègues doctorants pour leur soutien. Je remercie Faiçal, Silvia, Youcef, Lluis et Ali pour m'avoir mis le pied à l'étrier. Faiçal et Silvia m'ont transmis leur savoir-faire d'expérimentateur. Youcef, Lluis et Ali celui de calculateur, enfin...seulement ce que je voulais bien entendre. Ils m'ont communiqué tous les trucs et astuces suffisants et nécessaires pour accomplir ma recherche. Ils m'appelaient affectueusement *gamin*. Je remercie ensuite le clan des Silverbacks, Alexandre et Christophe. Alexandre m'a conseillé sur les techniques de visualisations rapides. Je ne pouvais aussi que m'inspirer de sa rigueur. Je remercie Christophe pour ses conseils permanents. Rares, je pense, sont les doctorants à posséder autant de connaissances pluridisciplinaires. Mes remerciements se tournent ensuite vers le groupe Hydroacoustique... ou plutôt celui des surfeurs. Merci à Nicolas pour son soutien et sa disponibilité. Il m'a secouru, plus d'une

fois, en sortant une routine de derrière les fagots. Sa facilité et son calme m'ont toujours impressionné. Merci à Sébastien pour les bonnes parties de rigolades. Il faut du temps pour changer un parisien, mais j'en suis sûr... il ne jurera un jour que par les fromages et vins suisses ! Merci au clan germanique: Stephan pour les discussions toujours approfondies et Olivier pour les bons souvenirs de conférences. Ensuite, mes remerciements vont à Cécile, calculatrice hors pair. Malgré son implication dans d'innombrables projets, nous sommes parvenus à collaborer. Un article est le fruit de ce travail. En outre, je la remercie pour ses conseils toujours pertinents. Je remercie Steven pour sa bonne humeur et son état d'esprit. Il dynamisera certainement le laboratoire entier. A peine lancés dans l'aventure d'une thèse, je souhaite bonne route à Amir, Vlad, Martin et Marc. Mes sincères encouragements vont à Amir qui a la lourde tâche de perpétuer les tourbillons de von Kármán au laboratoire. Finalement, je remercie Etienne et Francisco pour leur éternelle joie de vivre et Pierre pour sa camaraderie.

Je tiens également à remercier tous les étudiants et stagiaires qui ont contribués à une ambiance de travail amicale et festive. Un Oscar revient à Richard, Raphael et Adrien. La Palme d'Or à Martino et Olivier.

Je remercie Shadije, véritable soutien psychologique au laboratoire. Merci à Isabelle pour son efficacité dans les travaux administratifs.

Un grand merci à toute l'équipe des mécaniciens emmenée par le chef d'atelier Louis. Leur savoir-faire est mondialement reconnu. Merci à Christian, Jérôme, Jean-Daniel, Maxime et Raymond pour avoir toujours su transformer mes souhaits en mécanismes fiables et précis. Je les remercie également pour leur sens de l'humour et leur sympathie.

Je remercie les membres du bureau d'étude, Pierre Barmaverain, Philippe Faucherre, Alain Renaud et Vincent Berruex, pour leurs travaux de conception. Je remercie aussi Philippe Cerrutti qui garantit le fonctionnement des moyens informatiques.

Je remercie mon ami d'enfance Cédric, compagnon d'infortune dans ma formation pré-et universitaire.

Je remercie naturellement ma famille. Ma mère, Maria, et mes frères, Marc et Frédéric, pour m'avoir encouragé tout au long de ces années. Leur fierté à mon égard, démesurée à mon sens, a été une motivation supplémentaire à l'accomplissement de la tâche. Je remercie ma tante, Maria, et mon oncle, Paolo, pour leur accueil chaleureux à Zürich.

Je remercie également Cyril pour m'avoir incité à faire une thèse de doctorat. Son assiduité, sa formation et son parcours professionnel en font un exemple.

Du fond de mon coeur, je remercie Magali pour la patience, la compréhension, le soutien et l'amour dont elle a fait preuve durant ce travail. Un doctorat est un accomplissement personnel mais nous y sommes parvenus ensemble. Présente à mes côtés à chaque instant, elle mérite toute ma reconnaissance.

Finalement, je dédie ce travail à mon père. Il a su, je pense, m'inculquer sa droiture et m'a dirigé vers les études. Il nous a soudainement quittés avant l'aboutissement de ma formation. J'espère qu'il est fier de moi.

Philippe Ausoni

Résumé

Pour des valeurs supérieures au nombre de Reynolds critique, le sillage d'une structure mécanique est soumis à une instabilité hydrodynamique qui est à l'origine d'un détachement périodique de tourbillons alternés constituant l'allée tourbillonnaire de von Kármán. De par la configuration asymétrique de l'allée tourbillonnaire, la structure est soumise à une excitation périodique à une fréquence qui, selon sa proximité avec l'une des fréquences propres de la structure, peut donner lieu à un couplage hydro-élastique. Selon l'amplitude de vibration induite, un accrochage des fréquences de détachement tourbillonnaire sur une gamme de vitesse de référence peut être observé, phénomène de lock-in. Pour de telles conditions de résonance et de par des vibrations intenses, des fissures dans la structure mécanique apparaissent et se propagent, pouvant donner lieu à une rupture par fatigue de l'élément. Malgré de nombreuses études approfondies sur le sujet, le caractère destructif de l'allée tourbillonnaire est encore observé. Le sillage d'une structure profilée est le cas test adéquat pour de nombreuses applications industrielles telles la production hydro-électrique et la propulsion de navires. Malgré cela, l'intérêt de la recherche à ce jour se porte principalement sur le sillage de cylindres ou de corps épais hydrauliquement lisses et soumis à un écoulement de faible vitesse.

De ce fait, la présente étude considère un profil hydrodynamique symétrique dont le bord de fuite est tronqué droit et soumis à un écoulement uniforme à haute vitesse à un angle d'incidence nul. Le profil fait l'objet de mesures dans la veine d'essais du tunnel de cavitation à grande vitesse de l'EPFL-Laboratoire de Machines Hydrauliques. Les moyens expérimentaux comprennent un vibromètre laser, des vélocimètres par laser Doppler et par images de particules et une caméra digitale à haute vitesse. Une analyse de l'influence de la cavitation sur le mécanisme de génération de l'allée tourbillonnaire est proposée. De plus, les effets d'un déclenchement de couche limite turbulente sur les caractéristiques du sillage sont étudiés et comparés au cas d'une transition de couche limite naturelle.

En régime sub-cavitant et en accord avec la loi de Strouhal, la fréquence de détachement tourbillonnaire varie quasi linéairement avec la vitesse de l'écoulement moyen à condition qu'une fréquence propre du profil ne soit pas excitée, condition de lock-off. Pour de telles conditions, les tourbillons advectés révèlent une forte instabilité et des dislocations le long de l'envergure du profil. Une relation directe entre l'organisation spatiale des lâchers tourbillonnaires et l'amplitude des vibrations induites est montrée. Dans le cas de résonance du profil, la cohérence du détachement tourbillonnaire est fortement augmentée. Les modes propres de la structure sont identifiés et l'accrochage de fréquences de détachement tourbillonnaire sur une gamme de vitesse de référence apparait pour le premier mode de torsion.

Dans un écoulement liquide, quand la valeur de pression est inférieure à celle de la pression de vapeur saturante, la cavitation se forme dans le coeur des tourbillons. Le paramètre de cavitation naissante est montré linéairement dépendant de la racine carrée du nombre de Reynolds et est en accord avec des études antérieures. En revanche et pour des conditions de résonance, lock-in, les valeurs du paramètre de cavitation naissante sont fortement augmentées par rapport à des conditions de lock-off. Cette augmentation montre l'amplification de l'enroulement tourbillonnaire par la vibration transversale du bord de fuite. Pour le paramètre de cavitation naissante, et tenant compte de la vitesse de déplacement du bord de fuite, une nouvelle relation est proposée et validée pour des conditions de lock-off et de lock-in. De plus, il est montré que la vitesse de déplacement transverse du bord de fuite augmente linéairement l'intensité des tourbillons. La vitesse de déplacement du bord de fuite augmente donc les forces fluctuantes sur le profil et cet effet est additionnel à l'augmentation de l'organisation des tourbillons le long de l'envergure telle qu'observée pour des conditions de lock-in.

Il est montré que la cavitation se développant au coeur des tourbillons ne peut être considérée comme un moyen passif de visualisation, le sillage réagissant dès son apparition. Pour de faibles développements de cavitation, les vibrations induites par détachement tourbillonnaire et les fluctuations de vitesses de l'écoulement sont augmentées de manières significatives. Pour une cavitation développée, la fréquence de détachement tourbillonnaire est augmentée de 15% et est accompagnée par une augmentation de la vitesse d'advection des tourbillons et une réduction des distances inter-tourbillons. Ces effets sont analysés et attribués à une augmentation de la vorticité par la cavitation. Par ailleurs, il est montré que la cavitation ne modifie pas l'organisation des tourbillons le long de l'envergure. De plus, les conditions de couplages hydro-élastiques peuvent être activées/désactivées en permettant un développement suffisant de la cavitation de sillage.

Les effets d'un déclenchement de couche limite turbulente sur les caractéristiques du sillage sont étudiés et comparés au cas d'une transition de couche limite naturelle. Le profil est hydrauliquement lisse et le déclenchement de la transition au bord d'attaque est réalisé à l'aide d'une rugosité distribuée.

Pour les deux cas de transitions, la couche limite est caractérisée. Le procédé de détachement tourbillonnaire est montré fortement dépendant du développement de la couche limite. Une transition déclenchée promeut un rétablissement de détachements tourbillonnaires organisés. De plus, les résultats révèlent des augmentations significatives de vibrations induites, de fluctuations de vitesses dans le sillage, d'énergie du sillage et d'intensité des tourbillons pour une transition déclenchée. L'intermittence du détachement tourbillonnaire est diminuée et la cohérence est augmentée. Bien que la fréquence de détachement des tourbillons soit diminuée pour une transition déclenchée, un nombre de Strouhal modifié et basé sur l'épaisseur du sillage est constant sur la gamme de vitesses expérimentée. Ce résultat révèle la similitude des sillages et permet une estimation efficace de la fréquence de détachement tourbillonnaire.

Mots-clés: Allée tourbillonnaire de von Kármán, cavitation, couche limite, détachement tourbillonnaire, lock-in, lock-off, résonance, sillage, transition de couche limite, vibration

Abstract

Placed in a fluid stream, solid bodies can exhibit a separated flow that extends to their wake. The detachment of the boundary layer on both upper and lower surfaces forms two shear layers which generate above a critical value of Reynolds number a periodic array of discrete vortices termed von Kármán street. The body experiences a fluctuating lift force transverse to the flow caused by the asymmetric formation of vortices. The structural vibration amplitude is significantly amplified when the vortex shedding frequency lies close to a resonance frequency of the combined fluid-structure system. For resonance condition, fatigue cracks are likely to occur and lead to the premature failure of the mechanical system. Despite numerous and extensive studies on the topic, the periodic vortex shedding is considered to be a primary damage mechanism. The wake produced by a streamlined body, such as a hydrofoil, is an important issue for a variety of applications, including hydropower generation and marine vessel propulsion. However, the current state of the laboratory art focuses mainly in the wakes produced by hydraulically smooth bluff bodies at low Reynolds numbers.

The present work considers a blunt trailing edge symmetric hydrofoil operating at zero angle of attack in a uniform high speed flow, $Re_h = 16.1 \cdot 10^3 - 96.6 \cdot 10^3$ where the reference length h is the trailing edge thickness. Experiments are performed in the test section of the EPFL-LMH high speed cavitation tunnel. With the help of various measurement devices including laser Doppler vibrometer, particle image velocimetry, laser Doppler velocimetry and high speed digital camera, the effects of cavitation on the generation mechanism of the vortex street are investigated. Furthermore, the effects of a tripped turbulent boundary layer on the wake characteristics are analyzed and compared with the condition of a natural turbulent transition.

In cavitation free regime and according to the Strouhal law, the vortex shedding frequency is found to vary quasi-linearly with the free-stream velocity provided that no hydrofoil resonance frequency is excited, the so-called lock-off condition. For such regime, the shed vortices exhibit strong span-wise instabilities and dislocations. A direct relation between vortex span-wise organization and vortex-induced vibration amplitude is found. In the case of resonance, the coherence of the vortex shedding process is significantly enhanced. The eigen modes are identified so that the lock-in of the vortex shedding frequency on a free-stream velocity range occurs for the first torsional mode.

In the case of liquid flows, when the pressure falls below the vapor pressure, cavitation occurs in the vortex core. For lock-off condition, the cavitation inception index is linearly dependent on the square root of the Reynolds number which is in accordance with former models. For lock-in, it is significantly increased and makes clear that the vortex roll-up is amplified by the phase locked vibrations of the trailing edge. For the cavitation inception index and considering the trailing edge displacement velocity, a new correlation relationship that encompasses the lock-off and the lock-in conditions is proposed and validated. In addition, it is found that the transverse velocity of the trailing edge increases the vortex strength linearly. Therefore, the displacement velocity of the hydrofoil trailing edge increases the fluctuating forces on the body and this effect is additional to any increase of vortex span-wise organization, as observed for the lock-in condition.

Cavitation developing in the vortex street cannot be considered as a passive agent for the visualization of the turbulent wake flow. The cavitation reacts on the wake as soon as it appears. At early stage of cavitation development, the vortex-induced vibration and flow velocity fluctuations are significantly increased. For fully developed cavitation, the vortex shedding frequency increases up to 15%, which is accompanied by the increase of the vortex advection velocity and reduction of the stream-wise and cross-stream inter-vortex spacings. These effects are addressed and thought to be a result of the increase of the vorticity by cavitation. Besides, it is shown that the cavitation does not obviously modify the vortex span-wise organization. Moreover, hydro-elastic couplings are found to be enabled/disabled by permitting a sufficient vortex cavitation development.

The effects on the wake characteristics of a tripped turbulent boundary layer, as opposed to the natural turbulent transition, are investigated. The foil surface is hydraulically smooth and a fully effective boundary-layer tripping at the leading edge is achieved with the help of a distributed roughness.

The vortex shedding process is found to be strongly influenced by the boundary-layer development. The tripped turbulent transition promotes the re-establishment of organized vortex shedding. In the context of the tripped transition and in comparison with the natural one, significant increases in the vortex span-wise organization, the induced hydrofoil vibration, the wake velocity fluctuations, the wake energies and the vortex strength are revealed. The vortex shedding process intermittency is decreased and the coherence is increased. Although the vortex shedding frequency is decreased, a modified Strouhal number based on the wake width at the end of the vortex formation region is constant and evidences the similarity of the wakes. This result leads to an effective estimation of the vortex shedding frequency.

Keywords: Boundary layer, boundary-layer tripping, cavitation, lock-in, lock-off, resonance, vortex-induced vibration, vortex shedding, von Kármán street, wake

Contents

I Introduction 1

1 Problem overview 3
- 1.1 Thesis document organization 4

2 Vortex shedding 5
- 2.1 Historical aspects 5
- 2.2 Benchmark case study: Flow past a cylinder 6
  - 2.2.1 Overview of regimes 6
- 2.3 Strouhal number 8
  - 2.3.1 Dimensional analysis 8
- 2.4 Vortex-induced vibration 10
  - 2.4.1 Definitions 10
  - 2.4.2 Lock-in 11
  - 2.4.3 Hydraulic machinery failure 12
  - 2.4.4 Wake flow control 14

3 Boundary layer 15
- 3.1 Fundamentals of boundary layer 15
  - 3.1.1 Turbulent boundary-layer transition 16
  - 3.1.2 Boundary layer on a flat plate 17
- 3.2 Turbulent boundary-layer structure 17
- 3.3 Boundary-layer tripping 19

4 Cavitation 21
- 4.1 Fundamentals of cavitation 21
  - 4.1.1 Cavitation types 22
- 4.2 Vortex cavitation 23
  - 4.2.1 Cavitation and rotational flows 23
  - 4.2.2 Vortex model in viscous fluids 23

5 Literature review 25
- 5.1 Normalized vortex shedding frequency 25
  - 5.1.1 Strouhal number 25
  - 5.1.2 Griffin number 25
  - 5.1.3 Roshko number 26
- 5.2 Three-dimensional vortex shedding 27
- 5.3 Free-stream turbulence and surface roughness 27

5.4 Vortex-induced vibration 28
5.5 Flow stability property 28
5.6 Vortex cavitation 29

II Experimental setup and techniques 31

6 Test facility and hydrofoil setup 33
6.1 Test facility overview 33
6.1.1 Test section flow quality 34
6.2 Hydrofoil setup 36
6.2.1 Hydrofoil geometry 36
6.2.2 Surface roughness and boundary-layer tripping 36
6.2.3 Hydro-elastic coupling: Similarity law 38

7 Measuring apparatus 41
7.1 Vortex-induced vibration 41
7.1.1 Accelerometer 41
7.1.2 Laser Doppler vibrometer 41
7.1.3 Data acquisition system 45
7.2 Flow measurement 45
7.2.1 Laser Doppler velocimetry 45
7.2.2 Particle image velocimetry 47
7.2.3 Double laser optical probe 48
7.3 Flow visualization 50
7.3.1 Image acquisition and lighting system 50

III Vortex cavitation 51

8 Cavitation free 53
8.1 Vortex-induced vibration 53
8.1.1 Vortex shedding frequency and Strouhal number 53
8.1.2 Vibration amplitude 54
8.1.3 Time-frequency analysis 56
8.1.4 Hydrofoil eigen modes 60
8.2 PIV velocity fields 62
8.2.1 Lock-off condition 62
8.2.2 Lock-in condition 63
8.3 LDV velocity profiles 65
8.3.1 Time-averaged velocity profiles 65

9 Cavitation inception 69
9.1 Detection 69
9.2 Vortex strength 70

10 Developed cavitation **73**
10.1 Lock-off condition 73
10.1.1 Wake structure 73
10.1.2 Vortex shedding frequency and induced vibration 74
10.1.3 Flow velocity fluctuations 76
10.1.4 Vortex advection velocity and inter-vortex spacings 76
10.1.5 Discussion 80
10.2 Lock-in condition 82
10.2.1 Wake structure 82
10.2.2 Vortex shedding frequency and induced vibration 85

IV Boundary layer and vortex shedding **87**

11 Boundary-layer flow **89**
11.1 Reynolds effects 89
11.1.1 Time-averaged velocity profiles 89
11.1.2 Boundary-layer thickness and form factor 89
11.1.3 Turbulent boundary-layer transition 90
11.1.4 Boundary-layer structure 91
11.2 Development along the hydrofoil chord 93
11.2.1 Time-averaged velocity profiles 93
11.2.2 Boundary-layer thickness and form factor 94
11.2.3 Boundary-layer structure 94

12 Vortex-induced hydrofoil vibration **97**
12.1 Vortex shedding frequency and Strouhal number 97
12.2 Vibration amplitude 98

13 Wake structure **101**
13.1 Simultaneous wake high-speed visualization and vortex-induced vibration 101
13.1.1 Lock-in condition 101
13.1.2 Lock-off condition 101
13.2 Vortex shedding process coherence 102
13.3 Vortex shedding process intermittency 103
13.4 Time-frequency analysis 104
13.5 Discussion 104

14 Wake flow **109**
14.1 LDV velocity profiles: Near field 109
14.1.1 Vortex formation region 109
14.1.2 Time-averaged velocity profiles 109
14.1.3 Vortex strength 110
14.2 LDV velocity profiles: Far field 114
14.2.1 Time-averaged velocity profiles 114
14.2.2 Wake energies and velocity fluctuations 114
14.2.3 Inter-vortex spacings 117

15 Normalized vortex shedding frequency 119
15.1 Modified Strouhal number 119
15.2 Roshko number 120
15.3 Griffin number 121

16 Wake flow stability property 123
16.1 Family of wake profiles and instability characteristic 124

V Conclusions and Perspectives 127

17 Conclusions 129

18 Perspectives 131

Appendix 135

A Other results of interest 135
A.1 Polyoxymethylene hydrofoil 135
A.2 LDV phase-averaged velocity profiles 135
A.3 Computational fluid dynamics validation 137

B Hydro-elastic coupling: Similarity law 143

C Body oscillator 149

References 155

Index 165

Curriculum Vitae 166

Notations

Latin

a_s	Stream-wise inter-vortex spacing	[m]
b_s	Cross-stream inter-vortex spacing	[m]
f_s	Vortex shedding frequency	[Hz]
f_n	Hydrofoil natural frequency	[Hz]
l_f	Vortex formation region length	[m]
h	Hydrofoil trailing edge thickness	[m]
p_{ref}	Static pressure at the test section inlet	[Pa]
p_v	Saturation vapor pressure	[Pa]
t	Time	[s]
y_f	Wake width	[m]
A	Hydrofoil vertical displacement velocity	[m/s]
B	Hydrofoil span	[m]
L	Hydrofoil chord	[m]
C_{ref}	Velocity at the test section inlet, free-stream velocity	[m/s]
$C_{x_{mean}}$	Mean stream-wise velocity	[m/s]
$C_{y_{mean}}$	Mean transverse velocity	[m/s]
$C_{x_{stdv}}$	Fluctuating stream-wise velocity	[m/s]
$C_{y_{stdv}}$	Fluctuating transverse velocity	[m/s]
E_x	Stream-wise wake energy	[-]
E_y	Transverse wake energy	[-]
E	Wake energy	[-]
K_s	Height of the roughness element	[m]
$R_{z_{DIN}}$	Average surface roughness	[m]

Greek

α	Hydrofoil angle of attack	[$^\circ$]
δ	Boundary-layer thickness	[m]
δ_1	Boundary-layer displacement thickness	[m]

δ_2	Boundary-layer momentum thickness	[m]
γ^2	Coherence factor	[-]
η_i	Transit time weighting factor	[-]
λ	Intermittency factor	[-]
Γ	Vortex strength	[m^2/s]

Subscripts

Cl	Centerline quantity
$crit$	Turbulent boundary-layer transition location quantity
e	Boundary-layer edge quantity
f	Vortex formation region quantity
max	Maximum quantity
min	Minimum quantity
$mean$	Mean quantity
n	Eigen quantity
ref	Free-stream quantity
rms	Root mean square quantity
$stdv$	Standard deviation quantity
s	Vortex shedding quantity
x, y, z	Referred to cartesian directions
M	Referred to reduced-scale model
P	Referred to full-scale prototype

Dimensionless Numbers

Re_h	Reynolds number	$Re_h = \frac{C_{ref} h}{\nu}$	[-]
St	Strouhal number	$St = \frac{f_s h}{C_{ref}}$	[-]
St_{y_f}	Griffin number	$St_{y_f} = \frac{f_s y_f}{C_{ref}}$	[-]
$F_{(h+2\delta_1)}$	Roshko number	$F_{(h+2\delta_1)} = \frac{f_s (h+2\delta_1)^2}{\nu}$	[-]
H_{12}	Boundary-layer form factor	$H_{12} = \frac{\delta_1}{\delta_2}$	[-]
σ	Cavitation number	$\sigma = \frac{p_{ref} - p_v}{\frac{1}{2}\rho C_{ref}^2}$	[-]

Acronyms

EPFL	Ecole Polytechnique Fédérale de Lausanne
LMH	Laboratoire de Machines Hydrauliques
CFD	Computational Fluid Dynamics
FFT	Fast Fourier Transform
STFT	Short-Time Fourier Transform
LDV	Laser Doppler Velocimetry
PIV	Particle Image Velocimetry
VIV	Vortex-Induced Vibration

Part I

Introduction

Chapter 1

Problem overview

Placed in a fluid stream, solid bodies can exhibit a separated flow that extends to their wake. The detachment of the boundary layer on both upper and lower surfaces forms two shear layers which generate above a critical value of Reynolds number a periodic array of discrete vortices termed von Kármán street. Caused by the asymmetric formation of vortices, the body experiences a fluctuating lift force transverse to the flow. The structural vibration amplitude is significantly amplified when the vortex shedding frequency lies close to a resonance frequency of the combined fluid-structure system. Should the amplitude be large enough, the body motion can take control of the instability mechanism that leads to vortex shedding and synchronize the vortex shedding frequency with the body motion frequency on a wide range of free-stream velocity, *i.e.* lock-in phenomenon. For resonance condition, fatigue cracks are likely to occur and lead to the premature failure of the mechanical system.

Despite numerous and extensive studies on the topic, the periodic vortex shedding is still considered to be a primary damage mechanism. The ultimate objective is the understanding, the prediction and prevention of vortex-induced vibration. The wake produced by a streamlined body, such as a hydrofoil, is an important issue for a variety of applications, including hydropower generation and marine vessel propulsion. However, the current state of the laboratory art focuses mainly in the wakes produced by hydraulically smooth bluff bodies at low Reynolds numbers. There exist very few reports regarding the influence of the boundary layer on a streamlined body wake flow at high Reynolds numbers. To the author's knowledge, no studies have been reported in the literature that assess the effects of a tripped turbulent boundary layer on vortex shedding frequency and its normalization, on vortex-induced vibration, on wake-velocity fluctuations and energies, on vortex strength and on vortex shedding process coherence and intermittency. The results are compared with the condition of a natural turbulent boundary-layer transition. Besides, when the pressure falls below the vapor pressure, cavitation occurs in the vortex core. However, except for several early studies, the phenomenon of cavitation developing in the shed vortices has been ignored for a long time. Again, the studies were focused on bluff body wakes. The goal of the present work is to investigate the effect of cavitation on the development of the vortex street in the wake of a streamlined body at high Reynolds numbers. Moreover, the influence of wake cavitation on vortex-induced vibration is studied. The role of the hydrofoil vibration in the cavitation inception and vortex strength is pointed out.

Therefore, the present work considers a blunt trailing edge symmetric hydrofoil operating at zero angle of attack in a uniform high speed flow, $Re_h = 16.1 \cdot 10^3 - 96.6 \cdot 10^3$ where the reference length h is the trailing edge thickness. The measurements devices involved within the study include a laser Doppler vibrometer, a particle image velocimetry (PIV), a laser Doppler velocimetry (LDV) and a high speed digital camera.

1.1 Thesis document organization

The thesis document is organized in five main parts:

Part I is the introduction of the present work. The problem overview is first described and is followed by fundamentals aspects of vortex shedding, boundary layer and cavitation phenomena, chapters 1 to 3. Chapter 5 is devoted to the literature review.

Part II details the experimental setup and techniques. Both test facility and hydrofoil are described as well as the measuring apparatus. The results and analysis are provided in Parts III and IV.

Part III concerns the cavitation effects on the vortex shedding process. Chapter 8 concerns the cavitation free regime. The vortex shedding process is depicted by vortex-induced vibration, velocity fields and velocity profiles analysis. The wake cavitation inception is treated in chapter 9. The analysis provides a direct insight into the role of the trailing edge vibration on the cavitation occurrence. Chapter 10 is devoted to the developed wake cavitation. The wake structures, the vortex shedding frequency and induced hydrofoil vibration as well as the vortex advection velocity and inter-vortex spacings are analyzed for different cavitation developments.

Part IV is devoted to the tripped turbulent boundary layer effects on the vortex shedding process. The results are compared with the condition of a natural boundary-layer transition. In chapter 11, the boundary-layer flow is characterized. In chapters 12 and 13, the vortex-induced hydrofoil vibration and the wake structure are respectively analyzed. In chapter 14, the wake flow is described with the help of LDV data. Normalized vortex shedding frequency are proposed in chapter 15 and the wake flow stability properties in chapter 16.

Finally, a general conclusion is drawn in Part V. Suggestions for future work are provided.

Chapter 2

Vortex shedding

2.1 Historical aspects

The formation of vortices in body wakes takes its name from Theodore von Kármán (1881-1963). Although Leonardo da Vinci [46] had already drawn some rather accurate sketches of the vortex formation in the flow behind bluff bodies, the first experimental observations are due to Strouhal [107] in 1878. These observations were concerned with the relation between vibration frequency and wind velocity. The first modern pictures showing the alternating arrangement of vortices in the wake were published by Ahlborn [2] in 1902, Mallock [75] in 1907 and Bénard [24] in 1908. In particular, Bénard observed the vortices in different viscous fluids. Von Kármán highly contributed to the knowledge of the topic since he found that the symmetric arrangement of vortices is unstable. The only asymmetric arrangement is stable and only for a certain ratio of stream-wise and cross-stream inter-vortex spacings, [115] and [116]. He became interested in the problem of vortex shedding in 1911 when he was a graduate assistant in Göttingen [117]. At that time, Prandtl's main interest was in the theory of the boundary layer. His experimental investigations on a cylinder geometry were perturbed due to the flow oscillation in the test section. Von Kármán believed that the phenomenon must have a natural and intrinsic reason and calculated the stability of the vortex street. His famous theory stimulated series of investigations on the subject. Bénard claimed several times priority for earlier observation of the phenomenon but the vortex system remained connected to von Kármán.

The vortex shedding phenomenon has many physical applications and causes severe damage. When certain struts, used on underwater vehicles, sang a high tune, Gongwer [56] in 1952 showed that the vibration was caused by the periodical shedding of vortices. This also explains the singing of marine propellers, as was previously found by Gutsche [64] in 1937. Resonances of submarine periscopes have also been reported as well as resonance of radio towers in natural wind. The galloping motion of power lines has some connections with the shedding of vortices. The collapse of the bridge over the Tacoma Narrows in 1940 was caused by aero-elastic flutter which involves periodic vortex shedding. The bridge started torsional oscillations, which developed amplitudes up to 40° before it broke. In tall building engineering, vortex shedding phenomenon is carefully taken into account. For example, the Burj Dubai Tower, the world′s highest building, is purposely shaped to reduce the vortex-induced forces on the tower [11].

2.2 Benchmark case study: Flow past a cylinder

Uniform flow past a cylinder is the benchmark configuration for investigating vortex shedding and is well documented experimentally particularly at low Reynolds number. This section presents the fundamental mechanisms involved in the vortex formation and shedding process in the cylinder wake. Irrespective of body geometry, these general concepts are useful in the comprehension of the wake flows.

Above a certain value of free-stream velocity, the boundary layers separate from each side of the cylinder surface and form two shear layers. Since the innermost portion of the shear layers, which is in contact with the cylinder, moves much more slowly than the outermost portion, which is in contact with the free flow, the shear layers roll into the near wake, where they fold on each other and coalesce into discrete vortices [85]. Gerrard [51] gives a physical description of the mechanism of the vortex-formation region. A key factor in the formation of a vortex street is the mutual interaction between the two separating shear layers. It is postulated that a vortex continues to grow, fed by circulation from its connected shear layer, until it is strong enough to draw the opposing shear layer across the wake. The approach of oppositely signed vorticity in sufficient concentration cuts off further supply of circulation to the growing vortex, which is then shed and moves off downstream. The vortex-formation model showing entrainment flows is illustrated in Figure 2.1. Therefore, body wakes are complex since they involve the interactions of three shear layers in the same problem; namely a boundary layer, a separating free shear layer and a wake [124].

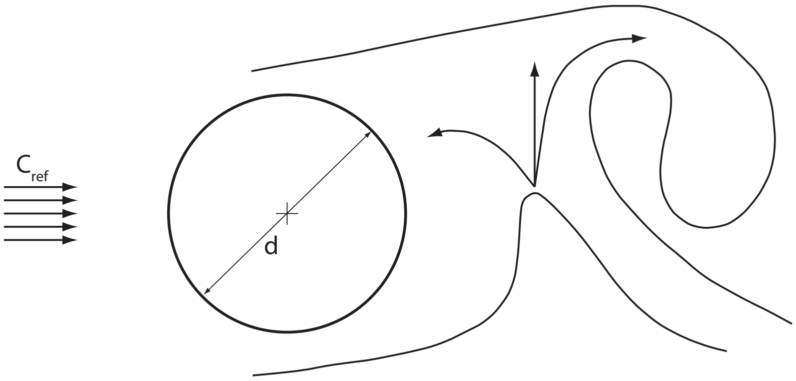

Figure 2.1: Vortex-formation model showing entrainment flows [51]

2.2.1 Overview of regimes

To characterize the uniform flow of a fluid past a cylinder, the Reynolds number Re_d is introduced,

$$Re_d = \frac{C_{ref} d}{\nu} \tag{2.1}$$

where C_{ref} is the free-stream velocity, d the cylinder diameter and ν the kinematic viscosity. A guide to flow regimes in the cylinder wake as a function of the Reynolds number is given in Williamson [124]. The discussion is here limited to a brief overview of the principle flow regimes. The first definitions of flow regimes based on measurements of velocity fluctuation are given by Roshko [92]. A *stable* periodic laminar vortex shedding regime is found for $Re_d = 40$–150, a *transition* regime in the range $Re_d = 150$–300, and an *irregular* regime for $Re_d = 300$–10000, where velocity time trace is not harmonic but shows distinct weak shedding cycles. Similar regimes were confirmed by Bloor [23]. A surge of recent work has shed further light on phenomena occurring in these regimes and their precise Reynolds number range. The surface roughness, the turbulence levels, the cylinder aspect and blockage ratios and the end conditions are known to affect the transitions from one regime to another.

Laminar steady regime: $Re_d < 49$

For Reynolds numbers less than 5, the flow past a cylinder is steady and without recirculation. For higher Re_d but below around 49, the wake comprises a steady recirculation region of two symmetrically placed vortices on each side of the wake, whose length grows as the Reynolds number increases [110].

Laminar vortex shedding: $49 < Re_d < 194$

Vortices are generated alternately on either sides of the cylinder and are advected downstream. Roshko [92] observed a critical Reynolds number for the onset of vortex shedding and a continuous relationship between the Reynolds number and the non-dimensional vortex shedding frequency given by the Strouhal number $St_d = f_s d / C_{ref}$ where f_s is the shedding frequency, d is the cylinder diameter and C_{ref} is the free-stream velocity up to $Re_d = 150$. The wake oscillations are purely periodic over this complete regime if care is taken to manipulate the end boundary conditions such that the vortex shedding is parallel to the cylinder axis [121].

Wake transition regime: $194 < Re_d < 260$

The regime is manifested by the variation in Strouhal number as the Reynolds number is increased and by the change in base suction [122]. Vortex loops and the formation of stream-wise vortex pairs appear in the wake and are due to the deformation of primary vortices as they are shed. The intermittent wake velocity fluctuations are shown to be due to the presence of large-scale vortex dislocations, which are caused by local shedding-phase difference along the span [123].

Three-dimensional vortex shedding: $260 < Re_d < 1 \cdot 10^3$

As the Reynolds number is increased, the three dimensionality becomes increasingly disordered. The base suction is reduced and the length of the vortex formation region is increased [114].

Shear-layer transition regime: $1 \cdot 10^3 < Re_d < 200 \cdot 10^3$

In the transition regime, the base suction increases again, the Strouhal number gradually decreases and the formation length decreases [81], [82]. Three dimensional structures develop. It is shown that the flow around mid-span is decoupled from the end effects at some finite aspect ratio L/d where L and d are respectively the cylinder length and its diameter. The required ratio is $L/d > 25$ for $10 \cdot 10^3 < Re_d < 40 \cdot 10^3$. Moreover, the region which is directly affected by the end condition remain smaller than 5 diameters and decreases with increasing Reynolds number [106].

Critical transition: $200 \cdot 10^3 < Re_d < 500 \cdot 10^3$
The base suction and the drag decrease drastically [14].

Supercritical regime: $500 \cdot 10^3 < Re_d < 1 \cdot 10^6$
Fluctuations are detected in the wake at large Strouhal number value, $St_d \cong 0.4$, which is consistent with the relatively thin wake in the regime [14]. One expects that the vortex shedding frequency scales inversely with the wake width.

Post-critical regime: $Re_d > 1 \cdot 10^6$
The increase in Reynolds numbers, through the various regimes, to this point is associated with a sequence of fundamental shear flow instabilities, namely wake transition, shear layer transition and boundary-layer transition. The effect of an increase in Re_d up to this particular regime is to move the turbulent transition point further upstream, until at high Re_d value, the boundary layer on the surface of the cylinder becomes turbulent. The vortex shedding phenomenon however continues to be recognizable and remains at Re_d up to $8 \cdot 10^6$ [101].

2.3 Strouhal number

The vortex shedding frequency is commonly expressed in a non-dimensional form called the Strouhal number St_h. The vortex shedding frequency f_s is multiplied by the inertial time h/C_{ref} where h is the body height and C_{ref} the free-stream velocity,

$$St_h = \frac{f_s h}{C_{ref}} \tag{2.2}$$

2.3.1 Dimensional analysis

Most phenomena in fluid mechanics depend in a complex way on geometric and flow parameters. Buckingham proved that for any given physical problem, the number m of dimensionless grouping of parameters is the total number of dimensional parameter n less the rank of the dimensional matrix r. The fundamental independent dimensions are the mass, the length, the time and the temperature. This general result regarding of the number of dimensionless groupings is known as the Buckingham Π Theorem [120];

$$m = n - r \tag{2.3}$$

The objective is to correlate the vortex shedding frequency in terms of dimensionless parameters. Assuming that the body is not heated or cooled and that any external forces are of no consequence, the vortex shedding frequency f_s is likely dependent of the body height h, the density of the fluid ρ, the viscosity μ and the velocity C_{ref}. Found in the literature, the vortex shedding frequency also depends on the body surface roughness height k_s [22]. Moreover and in the context of liquid flows, cavitation occurs in the wake when the vortex core pressure falls below the vapor pressure, chapter 4. For wake cavitation regime, the vortex shedding frequency f_s is dependent on the pressure difference $\Delta p = p_{ref} - p_v$ where p_{ref} and p_v are respectively the reference and the vapor pressure [128]. Consequently, there are a total of seven dimensional parameter in the problem $n = 7$, Table 2.1, and there are three fundamental dimensions $r = 3$, namely the mass

Table 2.1: Dimensional parameters involved in the flow past a body

Dimensional quantity	Symbol	Dimension
Vortex shedding frequency	f_s	T^{-1}
Body height	h	L
Density of the fluid	ρ	ML^{-3}
Viscosity of the fluid	μ	$ML^{-1}T^{-1}$
Velocity of the fluid	C_{ref}	LT^{-1}
Body surface roughness height	k_s	L
Pressure difference in the fluid	Δp	MLT^{-2}

M, the length L and the time T. Therefore and considering the Buckingham Π theorem, equation (2.3), there are four dimensionless groupings $m = 4$.

The dimensional equation relating the dimensions of the vortex shedding frequency to the other four dimensional quantities is,

$$[f_s] = [h]^{a_1}[\rho]^{a_2}[\mu]^{a_3}[C_{ref}]^{a_4}[k_s]^{a_5}[\Delta p]^{a_6} \tag{2.4}$$

where a_1, a_2, a_3, a_4, a_5 and a_6 are unknown exponents. The vortex shedding frequency is written as the product of factors as follows,

$$[f_s] = [f_0]\prod_{i=1}^{m-1}[P_i]^{b_i} \tag{2.5}$$

where $m = 4$ is the number of dimensionless groupings. The term f_0 has dimension of frequency and the exponents b_i are functions of the a_i exponents. The quantities P_i, known as pi factors, are dimensionless. In the present case, there is three dimensionless groupings on the right hand side of equation (2.5), namely P_1, P_2 and P_3. The fourth dimensionless grouping predicted by the Buckingham Π theorem, P_0, is the ratio of f_s to f_0.

The dimensional quantities are identified and written in terms of fundamental dimensions, Table 2.1. The substitution of these expressions into equation (2.4) and regrouping terms yields an equation relating the primary dimensions M, L and T,

$$T^{-1} = L^{a_1-3a_2-a_3+a_4+a_5-a_6}M^{a_2+a_3+a_6}T^{-a_3-a_4-2a_6} \tag{2.6}$$

Since, from algebraic point of view, M, L and T are independent variables, the only way the equation (2.6) is satisfied is to have identical exponents on both sides of the equation. This statement thus lead to the indicial equations,

$$\begin{cases} -a_3 - a_4 - 2a_6 = -1 \\ a_1 - 3a_2 - a_3 + a_4 + a_5 - a_6 = 0 \\ a_2 + a_3 + a_6 = 0 \end{cases} \tag{2.7}$$

Solving the coupled set of equations, considering the equation (2.4) and regrouping the terms lead to,

$$[f_s] = \left[\frac{\rho h C_{ref}}{\mu}\right]^{a_1+1}\left[\frac{C_{ref}}{h}\right]\left[\frac{\rho C_{ref} k_s}{\mu}\right]^{a_5}\left[\frac{\Delta p}{\rho C_{ref}^2}\right]^{a_6} \tag{2.8}$$

Therefore, the dimensionless groupings are,

$$P_1 = \frac{\rho h C_{ref}}{\mu}\ , \qquad P_2 = \frac{\rho k_s C_{ref}}{\mu}\ , \qquad P_3 = \frac{\Delta p}{\rho C_{ref}^2}\ , \qquad \frac{f_s}{f_0} = \frac{f_s h}{C_{ref}} \tag{2.9}$$

Finally, recalling equation (2.5), we obtain

$$\frac{f_s h}{C_{ref}} = F(\frac{\rho h C_{ref}}{\mu},\ \frac{\rho k_s C_{ref}}{\mu},\ \frac{\Delta p}{\rho C_{ref}^2}) \tag{2.10}$$

With the definition of non-dimensional numbers, namely the Strouhal number St_h, the Reynolds number Re_h, the dimensionless roughness height k_s^+ and the cavitation number σ,

$$St_h = \frac{f_s h}{C_{ref}}\ , \qquad Re_h = \frac{\rho h C_{ref}}{\mu}\ , \qquad k_s^+ = \frac{\rho k_s C_{ref}}{\mu}\ , \qquad \sigma = \frac{P_{ref} - P_v}{\frac{1}{2}\rho C_{ref}^2} \tag{2.11}$$

we obtain

$$\underline{\mathbf{St_h} = \mathbf{F}(\mathbf{Re_h},\ \mathbf{k_s^+},\ \sigma)} \tag{2.12}$$

The variation of the Strouhal number in function of the Reynolds number is found experimentally and reported by number of studies. The Strouhal number of a circular cylinder is shown in Figure 2.2. The influence of the body surface roughness is evidenced, [22]. The cavitation effect on the vortex shedding frequency is presented in [128] among others.

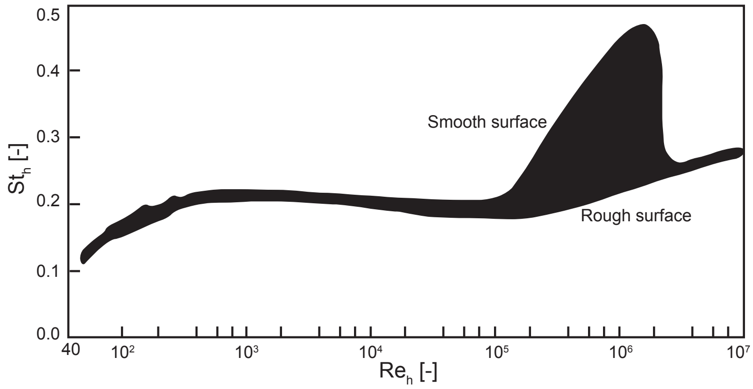

Figure 2.2: Strouhal number-Reynolds number relationship for circular cylinder [22]

2.4 Vortex-induced vibration

2.4.1 Definitions

Flow-induced vibrations phenomena have been treated by a variety of engineering disciplines, each having its particular terminology. In an attempt to provide a unified overview, Naudasher and Rockwell [80] propose the following definitions of basic elements of flow-induced vibrations:

- **Body oscillators** consists of a rigid structure that is elastically supported so that it can perform linear/angular movement or a structure that is elastic in itself so that it can be deformed.
- **Fluid oscillators** consists of a fluid mass that can undergo oscillations usually governed either by fluid compressibility or by gravity.
- **Sources of excitation** for either body and fluid oscillators are numerous. In the following, one distinguishes three types:
    1. **Extraneously induced excitation** is caused by fluctuations in flow velocities or pressure that are independent of any flow instability originating from the structure considered and independent of structural movements. Examples: Body excited by turbulence of the upcoming flow.
    2. **Instability-induced excitation** is brought about by a flow instability. This instability is intrinsic to the flow system and is therefore inherent to the flow created by the structure considered. Examples: Alternate vortex shedding in the body wake. The exciting force is produced through the flow instability that takes the form of local flow oscillations even in the cases where body or fluid oscillators are absent. The excitation mechanism is described in terms of a self-excited *flow oscillator.*
    3. **Movement-induced excitation** is due to fluctuating forces that arises from movements of the vibrating body. Example: Foil flutter when the foil is given an appropriate disturbance in both the bending and torsional mode, the flow induce a pressure field that tends to increase that disturbance.

An important role regarding instability-induced vibrations of body is played by the type and strength of the control exerted on the flow instability. The nature of control can be fluid-dynamic, fluid-elastic or fluid-resonant. In the fluid-dynamic case, the exciting force is function of the flow conditions only. In the fluid-elastic and fluid-resonant cases, this force depends on the dynamics of both the flow and the resonator in the system: A resonating body oscillator in the former case and a resonating fluid oscillator in the latter. The main feature of fluid-elastic and fluid-resonant control is an amplification of the exciting force and a *lock-in* of its frequency to that of the resonator within a certain range of flow velocities.

Finally and in our case study, the hydrofoil, which is the body oscillator, experiences mainly an instability-induced excitation, which is the alternate vortex shedding. The control of the instability is fluid-elastic, because dependent of the flow conditions and resonating body. For such resonance condition, one speaks of *hydro-elastic coupling.*

2.4.2 Lock-in

Reviews on vortex-induced vibration are provided by Williamson and Govardhan [126] and Sarpkaya [97] among others. Placed in a flow, bodies experience a fluctuating lift force transverse to the flow caused by the asymmetric formation of vortices. The fluctuating lift can cause the structure to vibrate. One of the fundamental features of vortex-induced vibration is the ability of the structure oscillating at its natural frequency to synchronize the vortex shedding frequency on a free-stream velocity range. This range, over which the lock-in of frequencies occurs, increases as the oscillation amplitude increases [127]. Description of the lock-in is given by Koopmann [71]. When the flow velocity approaches the boundaries of the resonance region, the shedding frequencies are close enough to the natural frequency of the system to cause the system to respond in short bursts of periodic motion in the plane perpendicular to the direction of the flow. If the motion during one of these bursts is large enough to correlate the vortex wake along the span, the body jumps to a higher displacement amplitude and a steady-state oscillation follows. The body motion controls the wake frequency, and the resulting oscillation takes place at the natural frequency of the system. Therefore, when the body is oscillating, the vortex shedding can be dramatically modified: The oscillations provide a means to couple the flow along the span of the body so that the vortex span-wise organization is significantly increased, Bearman [15]. The body oscillations increase the vortex strength when the amplitude in the transverse direction exceeds a threshold value, Davies [33].

Therefore, the major fluctuating force on the body acts normal to the free-stream direction with a frequency equal to the shedding frequency from one side of the body. However, minor force fluctuations are also induced at twice this frequency since each vortex produced a drop in base pressure during its formation. Therefore, stream-wise vibrations are also possible. Besides, the structural resonance ordinarily occurs at the vortex shedding frequency but structures are also excited at harmonics of the shedding frequency [22].

2.4.3 Hydraulic machinery failure

The vortex-induced vibration is of practical importance because of its potentially destructive effects. In particular, the blades and the stay vanes of hydraulic machines face the potential dynamic problem of vortex shedding. For hydraulic efficiency purposes the structures tend to be relatively slender in the direction normal to the flow, thus being flexible in this direction, [21]. Moreover, when the excitation frequency coincides with one of the structural natural frequencies, resonance occurs, causing significant increase of the vibration amplitude and potentially initiating fatigue cracks.

Damage of any part of hydraulic machinery is difficult and expensive to repair. Repairs also imply an expensive loss of power generation hours, so that vortex shedding in hydraulic machines is a subject for concern. The typical arrangement of spiral case, stay vane and guide vane for a Francis turbine is shown in Figure 2.3. The spiral case distributes uniformly the flow into the stay vanes. The stay vanes are fixed blades having the structural role to close the force loop of the pressurized spiral case and the guide vanes are mobile blades allowing controlling the flow rate through the runner.

Gummer and Hensmann [63] review the stay vane cracking in hydraulic turbines. One of the first reported incidence was described by Goldwag and Berry [55] in their 1968 paper on Ontario Hydro *Little Long* units, which deliver 500 MW of power. When the two units were being operated under load, abnormal level of noise and vibration were observed. About six months after commissioning, the units were unwatered and a detailed inspection revealed that the stay vanes contained numerous and serious fatigue cracks. The damage were found to result from a structural resonance due to vortex shedding. The geometry of the trailing edge has a direct influence on the amplitude of the wake flow oscillations and thus on the vortex-induced vibration level, Donaldson [35] and Heskestad and Olberts

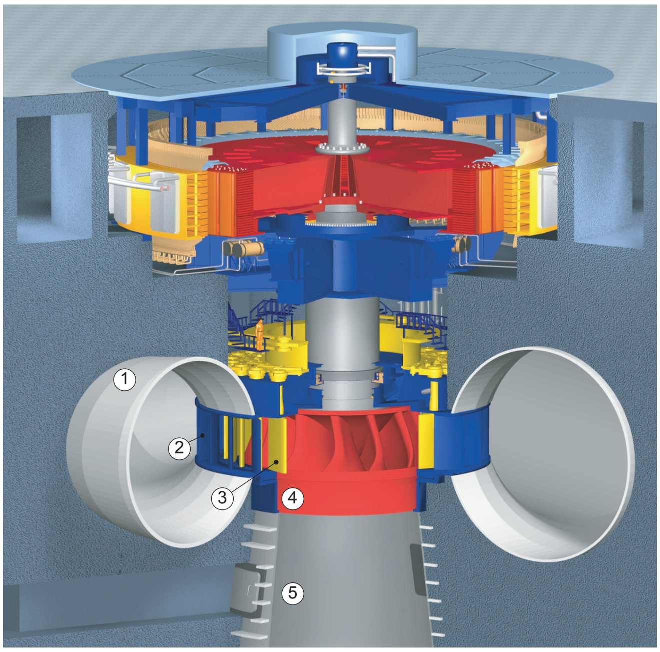

Figure 2.3: Components of a Francis turbine: Three Gorges, Sanxia, 26 × 700 MW, Courtesy of Voith-Siemens Hydro. 1. Spiral case, 2. Stay vanes, 3. Guide vanes, 4. Runner and 5. Diffuser

[66]. Moreover, with trailing edge geometry modification, the vortex shedding frequency is shifted so that no resonance is likely to occur at the same flow operating conditions. Therefore, the trailing edges of the stay vanes were machined to a V-style design. With this measure it was nevertheless not possible to achieve a sustained success and regular repairs had to be done over the following decades, Lockey *et al.* [73].

Since the damage in the *Little Long* units, many cases of premature fatigue cracks have been reported and the stay vanes are not the only component in hydraulic machines to suffer the vortex shedding. For instance, Shi [100] reports on the abnormal noise and runner cracks in *Dachaoshan* hydroelectic project, China. The project is equipped with six Francis turbines of 6105 mm inlet diameter producing up to 225 MW each. During the commissioning, abnormal noises occurred from mid through high power output. After only 72 hours of operation, an inspection was made and a large number of cracks were found on all runner blade outflow edges ! After repairing all cracks, three consecutive reshaping of blade trailing edges were necessary to eliminate the abnormal noise which was caused by the resonance of the blade due to vortex shedding.

The *Xiao Lang Di* project, China, is another case of hydroelastic coupling causing runner cracks, Fisher *et al.* [45]. The projects involves six Francis turbine designed to produce up to 330 MW. After about 1000 hours of operation, cracks of about 300 mm long were found on all of the 13 runner blades. The cracks were located on the blade discharge edge adjacent to the runner crown. The blades discharge edges were reinforced and beveled.

For stay vane hydro-elastic coupling, the two basic principles known to restore the machines are therefore the following ones, Grein and Staehle [58]: Modification of the trailing edge to reduce the vibration excitation and to shift the vortex shedding frequency and alteration of the natural frequency of the stay vanes. The latter can be done either by slotting the vane longitudinally, replacing the vanes by stiffer ones, or by dividing the stay vane channels in two by installing damping plates of the spiral casing. The plates de-tune the structure, especially of the vibration in the torsional mode, so that no further resonance occurs.

In order to avoid such premature fatigue cracks, the manufacturers of hydraulic machinery are nowadays carrying both flow and structural analysis to identify the best design. In addition Alstom Hydro, Ge Hydro, Andritz Hydro, Voith Hydro and EDF have joined forces in the *HydroDyna* project, a research project at the EPFL-Laboratory for Hydraulic Machines, to harness the issues related to vortex shedding. The present work is part of the deliveries.

2.4.4 Wake flow control

Because vortex-induced vibration can cause tremendous damage to all kind of engineering structures, there has been a number of studies attempting to control the wake behind structures with the practical goal of reducing the pressure drag on the body and the wake flow fluctuations, see Fransson [49] for a deep review on wake flow control. The different methods include thin splitter plate aligned in the stream-wise direction on the center line of the near wake, [93], forced rotary oscillations [112], acoustic waves [94], magnetic field [103], blowing and suction [84], [76], [54], [29] and beveling the body trailing edge [35], [66], [57].

Transverse body motion, *i.e.* motion perpendicular to the free-stream, with frequency at or near the vortex shedding frequency has large effects on wakes structure. The body vibration increases the vortex strength, Davies [33], increase the spanwise correlation of the wake, Toebes [111], and synchronize the vortex shedding frequency and the body motion frequency on a wide range of free-stream velocity, *i.e.* lock-in. Therefore, instead of suppressing the vortex shedding in the wake of structures, *VIVACE*, Vortex Induced Vibration Aquatic Clean Energy, is a concept in the generation of clean and renewable energy from fluid flow, *i.e.* ocean or river current. In its simplest form, a module of the Vivace consists of a rigid circular cylinder mounted on elastic springs placed in a fluid flow. The body undergoes vortex-induced vibration and transmits the mechanical energy to a generator for conversion to electricity. The design of the system is optimized in order to a have the synchronization of the vortex shedding frequency and the natural frequency of the structure on a wide range of flow velocity. The system is scalable and estimation of power, efficiency, costs and other design data are reported in [18].

Chapter 3

Boundary layer

Body wakes are complex since they involve the interactions of three shear layers in the same problem; namely a boundary layer, a separating free shear layer and a wake [124]. The boundary layer concept is defined though this chapter.

3.1 Fundamentals of boundary layer

Directly at the body wall there is a thin layer where the velocity is considerably lower than at some distance from the wall. The thickness of this layer increases along the body from leading to trailing edges. The concept of boundary-layer thickness δ is artificially introduced. The transition from boundary-layer flow to the outer flow takes places continuously, so that a precise boundary cannot be given. Conventionally, the boundary-layer thickness is defined as being the distance from the body surface, measured along the perpendicular to the surface, where the flow reaches 99% of the external velocity C_e,

$$\delta = y|_{C_x=0.99C_e} \tag{3.1}$$

A correct and fluid mechanically interpretable measure of the thickness of the boundary layer is the displacement thickness δ_1 defined by,

$$\delta_1 = \int_0^\delta \left(1 - \frac{C_x}{C_e}\right) dy \tag{3.2}$$

The displacement thickness shows how far the inviscid outer flow is displaced outwards by the drop in velocity in the boundary layer. The boundary-layer momentum thickness δ_2 is given by,

$$\delta_2 = \int_0^\delta \left(1 - \frac{C_x}{C_e}\right) \frac{C_x}{C_e}\, dy \tag{3.3}$$

The form factor H_{12}, defined as the ratio of the boundary-layer displacement thickness δ_1 and its momentum thickness δ_2, reveals accordingly to theoretical velocity profiles the type of boundary-layer flow, *i.e.* laminar, transitional or turbulent.

$$H_{12} = \frac{\delta_1}{\delta_2} \tag{3.4}$$

Tangential forces occur both between layers in the fluid and between the fluid and the walls. These tangential forces or friction forces are connected to the viscosity of the fluid. The wall shear stress is defined by

$$\tau_w(x) = \mu \left(\frac{\partial C_x}{\partial y} \right)_w \tag{3.5}$$

The reference velocity being noted C_{ref}, the skin friction coefficient is

$$c_f(x) = \frac{\tau_w(x)}{\frac{1}{2}\rho C_{ref}^2} \tag{3.6}$$

3.1.1 Turbulent boundary-layer transition

After a certain distance from the leading edge, $x = x_{crit}$, transition occurs and the boundary layer becomes turbulent. The critical Reynolds number formed with the distance to the transition point x_{crit} is,

$$Re_{crit} = \frac{C_{ref} x_{crit}}{\nu} \tag{3.7}$$

The numerical value of Re_{crit} is dependent on the flow turbulence intensity, the surface roughness and the pressure distribution of the outer flow, which is imposed by the body geometry.

The surface roughness is defined by following equations and Figure 3.1,

$$R_{a_{DIN}} = \frac{1}{L_m} \int_0^{L_m} |y| dx \ , \qquad R_{z_{DIN}} = \frac{1}{5}(z_1 + z_2 + z_3 + z_4 + z_5) \tag{3.8}$$

The surface is considered to be hydraulically smooth, *i.e.* no difference compared to the ideal smooth surface, if the roughness meets the following criterion [99],

$$\frac{C_{ref} R_{z_{DIN}}}{\nu} < 100 \tag{3.9}$$

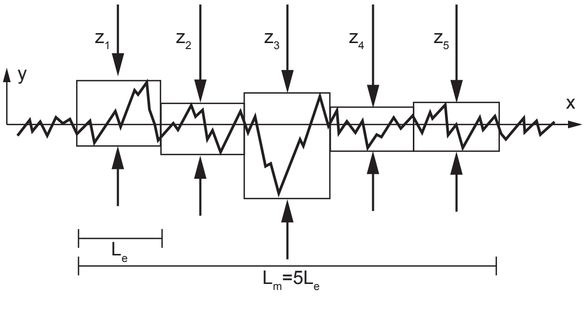

Figure 3.1: Definition of the surface roughness parameters

On a hydraulically smooth surface, a natural turbulent transition can occur beyond a certain distance from the leading edge. The transition to turbulent boundary layer is not sudden but occurs via subsequent formation of three-dimensional structures. As one moves downstream from leading edge, the transition consists in the following processes, which are sketched on Figure 3.2. Therefore, span-wise non uniformities in the boundary-layer transition process occur even if the free-stream velocity is uniform.

a. Stable laminar flow
b. Unstable two-dimensional Tollmien-Schlichting waves
c. Development of three-dimensional unstable waves
d. Formation of turbulent spots
e. Coalescence of spots into fully turbulent flow

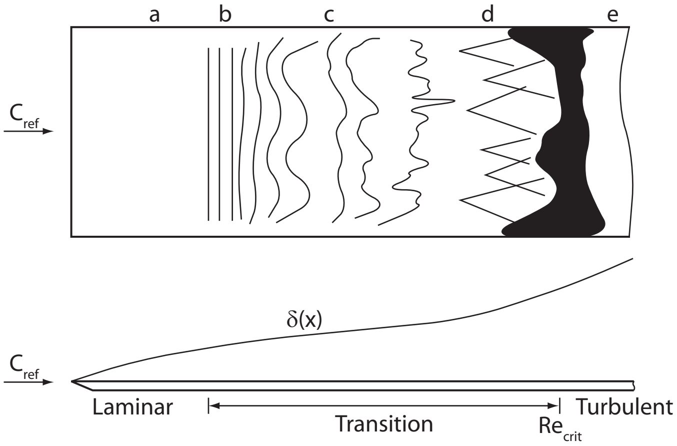

Figure 3.2: Sketch of boundary layer laminar-turbulent transition [119]

3.1.2 Boundary layer on a flat plate

The flat plate at zero incidence is the benchmark configuration for studying the boundary layer. With both theoretical arguments and experiments, characteristics of the boundary layer are reported in Table 3.1, [99]. Whereas a form factor H value of 2.6 is reached for a laminar boundary layer, the boundary layer is commonly considered as turbulent for a form factor value below 1.5. Between 2.6 and 1.5, the boundary layer is transitional.

Table 3.1: Integral parameter for laminar and turbulent flat-plate boundary layers [99]

	Symbol	Laminar flow	Turbulent flow
Boundary-layer thickness	$\delta(x)$	$5.0\ x\ Re_x^{-1/2}$	$0.37\ x\ Re_x^{-1/5}$
Boundary-layer displacement thickness	$\delta_1(x)$	$0.344\ \delta(x)$	$0.125\ \delta(x)$
Boundary-layer momentum thickness	$\delta_2(x)$	$0.133\ \delta(x)$	$0.097\ \delta(x)$
Form factor	H	2.59	1.29
Skin friction coefficient	c_f	$0.664\ Re_x^{-1/2}$	$0.0576\ Re_x^{-1/5}$

3.2 Turbulent boundary-layer structure

The structure of the turbulent boundary layer is described with the help of inner variables, which are thereafter defined. By denoting the shear stress at the surface by τ_w, equation (3.5), the friction velocity is given by

$$C_{x\,\tau} = \sqrt{\frac{\tau_w}{\rho}} \tag{3.10}$$

The dimensionless velocity u^+ and distance y^+ are function of the friction velocity,

$$C_x^+ = \frac{C_x}{C_{x\,\tau}}\ , \qquad y^+ = \frac{C_{x\,\tau}\, y}{\nu} \tag{3.11}$$

Figure 3.3 shows a typical velocity profile for a turbulent boundary layer. Three distinct regions are evidenced, namely the viscous sublayer, the log layer and the defect layer.

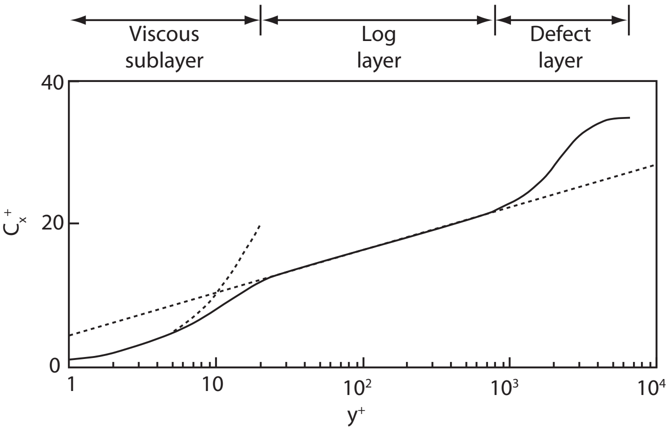

Figure 3.3: Sketch of a typical velocity profile for a turbulent boundary layer [119]

Viscous sublayer

The viscous sublayer is the region between the body surface and the log layer. Consequence of the no-slip condition at the wall, the horizontal velocity C_x varies linearly with y close to the surface. For higher distances, it gradually asymptotes to the log law. In terms of dimensionless quantity, we have for typically $y^+ < 7$,

$$C_x^+ = y^+ \tag{3.12}$$

Log layer

The log layer typically lies between $y^+ = 30$ and $y = 0.1\delta$. The velocity varies logarithmicaly with y^+ as,

$$C_x^+ = \frac{1}{K} \ln\, y^+ + c \tag{3.13}$$

where K is the Kármán constant and c a constant depending on surface roughness. The equation (3.13) is known as the log law. Measurements indicate the value $K = 0.40$ to 0.42 and, for a ideally smooth surface, $c = 5.0$ to 5.2. As the roughness height increases, the value of c decreases,

$$c = 8.0 - \frac{1}{K} \ln\, k_s^+ \tag{3.14}$$

Defect layer

The defect layer lies between the log layer and the edge of the boundary layer. The velocity makes a noticeable departure from the log law approaching the free-stream. Coles [32] introduces a wake function

$$W\left(\frac{y}{\delta}\right) = 2\ \sin^2\left(\frac{\pi}{2}\frac{y}{\delta}\right) \tag{3.15}$$

so that the log law is modified as

$$C_x^+ = \frac{1}{K}\ \ln\ y^+ + c + \frac{2\Pi}{K}\ \sin^2\left(\frac{\pi}{2}\frac{y}{\delta}\right) \tag{3.16}$$

The Π parameter is the Coles' wake strength and varies with pressure gradient. For a constant pressure, the wake strength is $\Pi = 0.6$. The equation (3.15) is known as the law of the wake profile.

3.3 Boundary-layer tripping

The introduction of roughness at the wall cause earlier transition because of the additional disturbances fed in the boundary layer. Let us consider a distributed roughness, which height is k_s, placed on a plate at position x_{k_s}. If k_s is much smaller than $\delta_1(x_{k_s})$, the roughness has little effect and transition occurs at a position x_{crit} as if the wall were ideally smooth. As k_s increases until $k_s/\delta_1(x_{k_s})$ exceeds 0.3, the transition point x_{crit} moves closer to the roughness position x_{k_s}. The condition for which the transition first occurs at the element $x_{crit} = x_{k_s}$, *i.e.* fully effective tripping to turbulent flow, is given by [38],

$$\frac{C_{ref}k_s}{\nu} \geq 900 \tag{3.17}$$

Chapter 4

Cavitation

Cavitation is the formation of vapor phase within a liquid due to pressure drop. The term cavitation can therefore imply anything from the initial formation of bubbles, *i.e.* cavitation inception, to large-scale cavities. The formation of individual bubbles and subsequent development is directly related to the reduction in local fluid pressure below some critical value.

Cavitation development may be the origin of several negative effects, such as noise, vibrations, performance alterations, erosion and structural damage. These effects make a cavitation regime a situation to be most of the time avoided. Nevertheless, it sometimes serves useful properties. For instance, applications include surface cleaning and liquids degassing.

4.1 Fundamentals of cavitation

Cavitation in liquid flows is a two-phase flow with phase transition driven by pressure change without any heating. It can be interpreted as the rupture of the liquid continuum due to excessive stresses [47]. In a phase diagram, Figure (4.1), the liquid to vapor transition is obtained whether by heating the liquid at constant pressure, which is boiling, or by decreasing the pressure in the liquid at constant temperature, which is the cavitation process. It is commonly admitted that cavitation occurs at a given location and given temperature T whenever the pressure p in the liquid reaches the saturated vapor pressure $p_v(T)$,

$$p_M(T) \leq p_v(T) \tag{4.1}$$

Under particular conditions, liquids may withstand significant tension without vaporizing. Briggs [27] and Zheng [130] have shown that cavitation can occur at negative pressure, *i.e.* that is tension. A maximum tension of 280 and 1400 bar were reached respectively. In a case study much closer to industrial applications, Guennoun [62] measures a tension of 1 bar in flow around hydrofoil experiments. Nevertheless the cavitation inception criterion, equation (4.1), remains valid for industrial liquids due to the existence of weak sites made of gas and vapor micro bubbles in the liquid, usually called cavitation nuclei.

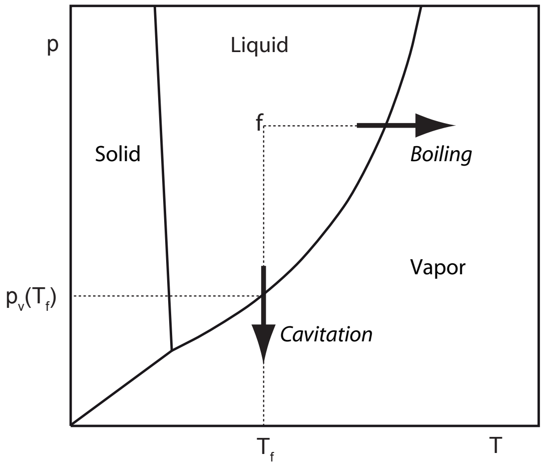

Figure 4.1: State phase diagram and phase change curves [47]

4.1.1 Cavitation types

Different types of cavitation are observed depending on the flow conditions, Figure 4.2. Knapp *et al.* [69] proposed two classification families; the attached cavitation, where the cavity interface is partly attached to the solid surface, and the advected cavitation where the entire interface is moving with the flow:

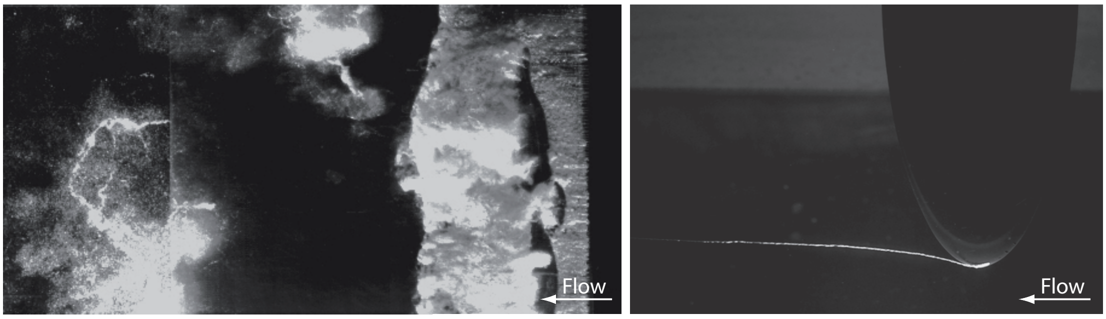
Attached cavitation:

(a) Leading edge cavitation
(Naca0009, α=4.5°, C_{ref}=14 m/s, σ=1.2)

(b) Tip vortex cavitation
(Naca16020, α=10°, C_{ref}=14 m/s, σ=1.7)

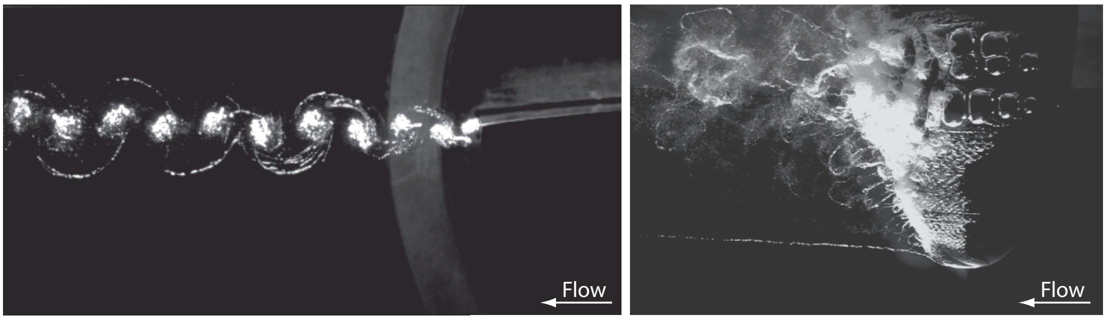
Advected cavitation:

(c) Vortex street cavitation
(Naca0009, α=0°, C_{ref}=12 m/s, σ=0.8)

(d) Bubble cavitation
(Naca16020, α=6°, C_{ref}=14 m/s, σ=0.4)

Figure 4.2: Cavitation types

- Attached cavitation
  - Figure 4.2 (a): The attached cavitation occurs on the blade surface. When the cavity is thin and quasi-steady, it is called sheet cavitation. It is named cloud cavitation when significant transient cavities are generated. The attached cavitation can be partial or super-cavitation when respectively the cavity length is shorter or longer than the chord length.
  - Figure 4.2 (b): The tip vortex cavitation occurs at blade extremities. Cavitation is formed in the center of the vortex core, which is characterized by a local minimum pressure.
- Advected cavitation
  - Figure 4.2 (c): The cavitation occurs in the core of the advected vortices. The cavitation vortex street is example of the advected cavitation.
  - Figure 4.2 (d): The bubble cavitation are individual transient bubbles that expand and collapse as they are convected by the liquid.

4.2 Vortex cavitation

The rotational structures generate low pressure regions inside the liquid. Such pressure drops can be very intense, so that cavitation often starts for high value of cavitation number in comparison with other types of cavitation.

4.2.1 Cavitation and rotational flows

The characteristics of a vortex are changed due to the inception of cavitation. To generate a cylindrical vapor core of diameter d_v, conservation of mass shows that the corresponding cylindrical volume of liquid, before phase change, has a diameter d_l such that their ratio is

$$\frac{d_l}{d_v} = \sqrt{\frac{\rho_v}{\rho_l}} \tag{4.2}$$

For water at room temperature, the ratio of liquid to vapor densities is about 58000 [48]. For a vapor core of about 1 mm, the diameter d_l is of the order of 4 μm. In other words, liquid particles situated initially at 2 μm from the axis are ejected at 0.5 mm because of cavitation. Therefore, the flow in the close neighborhood of the vortex axis is strongly modified.

4.2.2 Vortex model in viscous fluids

A vortex is characterized by two zones: Its core where the vorticity is constant and the viscous effects are dominant and an outer region where the motion is irrotational and the fluid considered as inviscid. The Rankine model assumes that the vortex core $r \leq a$ is in solid body rotation so that the tangential velocity v_θ at a distance r from the vortex axis is given by,

$$r \leq a\ ; \qquad v_\theta(r) = \frac{\Gamma}{2\pi a^2} r \tag{4.3}$$

The rotation rate is $\omega = \Gamma/2\pi a^2$. In the outer region $r > a$, the tangential velocity is

$$r > a \; ; \qquad v_\theta(r) = \frac{\Gamma}{2\pi r} \tag{4.4}$$

By definition, Γ is the vortex strength. The core radius a is the distance to the vortex axis where the tangential velocity is maximum.

The radial equilibrium equation

$$\frac{\partial p}{\partial r} = \rho \frac{v_\theta^2}{r} \tag{4.5}$$

allows the computation of the radial pressure distribution. Especially, the minimum pressure p_{min}, which is located at the vortex center, is given by

$$p_{min} = p_{ref} - \rho \left(\frac{\Gamma}{2\pi a} \right)^2 \tag{4.6}$$

where p_{ref} is the reference pressure. Cavitation occurs on the vortex axis when the minimum pressure falls below the vapor pressure p_v. The pressure coefficient at the vortex center is written as,

$$c_{p_{min}} = \frac{p_{min} - p_{ref}}{\frac{1}{2}\rho C_{ref}^2} = -2 \left(\frac{\Gamma}{2\pi a C_{ref}} \right)^2 \tag{4.7}$$

Moreover, the cavitation number is defined by

$$\sigma = \frac{p_{ref} - p_v}{\frac{1}{2}\rho C_{ref}^2} \tag{4.8}$$

Vortex cavitation inception

At cavitation inception, the vortex core pressure reaches the vapor pressure. The pressure in the vortex core is the sum of the static pressure at the separation point c_{p_s} and the additional pressure drop due to the vortex rotation, so that the cavitation inception index is given by,

$$\sigma_i = -c_{p_s} + 2 \left(\frac{\Gamma}{2\pi a C_{ref}} \right)^2 \tag{4.9}$$

The pressure coefficient c_{p_s} is known by pressure measurements. With the introduction of the external velocity of the boundary layer C_e at the detachment point, one finds from the Bernoulli equation between a point in the free-stream (C_{ref}, p_{ref}) and the separation point,

$$c_{p_s} = 1 - \left(\frac{C_e}{C_{ref}} \right)^2 \tag{4.10}$$

Considering equation (4.9), Arndt [5] and Belahadji *et al.* [16] proposed a model for the cavitation inception in the wake of fixed bluff bodies. Both development lead to linear law between the cavitation inception index and the root square of the Reynolds number,

$$\sigma_i = -c_{p_b} + cte \sqrt{Re} \tag{4.11}$$

Although remarkably successful in describing the wake cavitation inception for fixed bluff bodies, none of these studies provides a direct insight into the role of the trailing edge vibration, lock-in condition, on the cavitation occurrence.

Chapter 5

Literature review

5.1 Normalized vortex shedding frequency

5.1.1 Strouhal number

Uniform flow past a cylinder is the benchmark configuration for investigating vortex shedding and has been extensively studied experimentally at low Reynolds numbers. The understanding of wake vortex dynamics is reviewed by Williamson [124]. The dependency of the Strouhal number, $St_h = f_s h / C_{ref}$ where f_s is the shedding frequency, h the body height and C_{ref} the free-stream velocity, versus the Reynolds number and the wall surface roughness is introduced in section 2.3. Some discontinuity exists in the Strouhal-Reynolds number relationship. However, if parallel vortex shedding can be induced, whereby the vortices in the wake are shed parallel to the body axis, then the relation between Strouhal and Reynolds numbers is continuous [121]. The question has also arisen as to how the relation between the Strouhal number and the Reynolds number can be represented, and what physical basis one can attribute to these representations. Williamson and Brown [125] shows that the St–Re relation may be expressed as an expansion in powers of $1/\sqrt{Re}$, the constant term being due to the size of the body while the terms in $1/\sqrt{Re}$ are associated with the shear layer thickness. Besides, Bauer [12] normalized the vortex shedding frequency using a characteristic length scale equal to twice the boundary-layer displacement thickness plus the plate thickness. Nevertheless, Eisenlohr and Eckelmann [41] showed some dispersion of this normalized shedding frequency. The influence of the boundary layer state on the Strouhal number was clearly shown by Sieverding and Heinemann [102]. Tripping the boundary layer on a flat plate drastically reduces by 30% the Strouhal number even if the boundary-layer displacement thickness is taken into account.

5.1.2 Griffin number

In an attempt to generalize the results in the literature, several authors introduced universal wake numbers to correlate the frequency of vortex shedding from bluff bodies of different cross-sections. Most of these numbers are essentially examples of a modified Strouhal number. The characteristic scales of wake formation are used instead of body dimensions and free-stream velocity. The mean velocity at the edge of the boundary layer at the separation point is taken as the reference velocity. Various reference lengths have been proposed by several authors, but this parameter may still essentially be considered a measure of the wake width. In particular, Griffin [59] [60] has proposed a universal Strouhal number based on the measured wake width at the end of the vortex-formation region. The combination of this width, the shedding frequency and the mean velocity at the edge of the separated boundary layer collapses these characteristic parameters for bluff bodies onto a single curve for wake Reynolds numbers between 100 and 10^7.

Vortex formation region and wake width

The width of the wake is defined as the cross-stream distance between the maxima of the stream-wise velocity fluctuations in the context of a traverse measurement across the wake, Figure 5.1. Moreover, Griffin [61] reviewed the definitions of the end of the vortex-formation region. The one commonly used refers to the position of the maximum stream-wise velocity fluctuations off/on the wake centerline. Bearman's [13] measurements revealed that the velocity fluctuation peak appears sharper off the wake centerline and positioned at the same locations downstream of the body as for measurements on the wake centerline. Moreover, the determination of the end of the vortex formation region is not dependent on band-pass filtering the velocity signals around the shedding frequency. Regarding transverse measurement across the wake, Schaeffer [98] concluded that the two stream-wise velocity fluctuation maxima do not occur along the path of vortex centers but at the core edges farthest from the centerline. Bearman [13] confirmed this statement with the help of hot-wire measurements. Blake [20] defined a vortex root-mean-square circulation and stated that the wake width is four times the vortex viscous core radius.

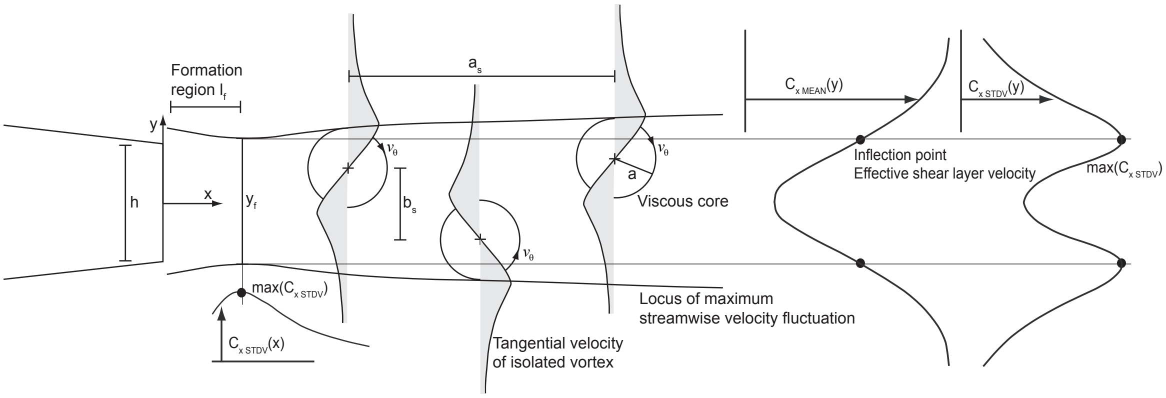

Figure 5.1: Idealization and definitions of scaling parameters for the vortex structure in the wake of a hydrofoil

5.1.3 Roshko number

Instead of the Strouhal number, where the shedding frequency is multiplied by the inertial time scale, h/C_{ref}, Roshko [92] expressed the non-dimensional form with the help of the viscous diffusion time, h^2/ν, where ν is the kinematic viscosity. Sometimes referred to as the Roshko number, the F number is $F = f_s h^2/\nu$.

5.2 Three-dimensional vortex shedding

Also evidenced for low Reynolds numbers, many authors have observed that the wake structure may exhibit three-dimensional characteristics, even if the body cross-section is constant along the span and the upcoming flow uniform. Gerrard [52] and Williamson [124] give reviews of the three-dimensional structures of shed vortices. Tritton [113] and Slaouti and Gerrard [104] report that vortices may be shed at a swept angle from the cylinder axis, which is called oblique shedding. Vortex dislocations or vortex splitting also occur and are generated between span-wise cells of different frequency when the vortices in each cell move out of phase with each other. These dislocations grow rapidly in the span-wise direction into large scale structures as they travel downstream, as reported by Williamson [123]. Three-dimensional vortex organization is responsible for characteristic envelop shapes of wake flow velocity and induced-vibration time traces. Prasad and Williamson [86] and Williamson [121] find that the spanwise end conditions control the primary vortex shedding and significantly affect the stability of the separating shear layer. Slight disturbances, induced by test section walls, endplates or span-wise flow instabilities, can significantly influence the vortex shedding process, as described by Gerich and Heckelmann [50] and by Hammache and Gharib [65]. Eisenlohr and Eckelmann [42] show how the vortices interact with the horseshoe vortex generated by the boundary layer of the endplate. The vortex splitting is constantly taking place at this position. The test body is therefore decoupled from any end effects and parallel vortex shedding takes place. In many applications, however, the flow fields in which bodies are immersed are turbulent and the three-dimensional aspects of the wake arise not only from the end conditions but also from the turbulence of the shear layers and the wake, as concluded by Szepessy [108]. This intrinsically developed turbulence and secondary vortical structures of the shear layers interact in a complex manner with the stability of the vortex street.

5.3 Free-stream turbulence and surface roughness

It is known that the introduction of turbulence to the flow field promotes the vortex shedding critical transition at lower Reynolds numbers than for laminar flows. Achenbach and Heinecke [1] report that increasing the surface roughness of the body has a similar effect. Wind-tunnel studies show that the introduction of free-stream turbulence increases the cylinder lift coefficients such that they exceed those associated with laminar flow, as recorded by Cheung and Melbourne [30]. Blackburn and Melbourne [19] examined the effects of grid-generated turbulence on the lift forces of a circular cylinder. According to the correlation length analysis, it appears that the increase of the turbulence intensity of the mean flow promotes the re-establishment of organized vortex shedding. With increased surface roughness or free-stream turbulence, Zhang *et al.* [129] believed to a certain reduction in vortex strength, which is caused by a greater diffusion of vorticity in the wake. El-Gammal and Hangan [43] noticed that the velocity fluctuations across the near wake tend to increase with the free-stream turbulence. In the far wake, the dissipation rate is faster.

5.4 Vortex-induced vibration

Vortex-induced vibration phenomena have been subjected to much research, which Rockwell [91], Sarpkaya [97] and Williamson and Govardhan [126] have reviewed among others. It is known that the bodies that shed span-wise vortices may be excited into oscillation by the fluctuating pressure forces resulting from the asymmetric formation of vorticies. The resonance occurs when the vortex shedding frequency coincides with one of the eigenfrequencies of the combined fluid-structure system. Amplified due to resonance condition, the response amplitude becomes sufficiently large so that the structural displacement controls the fluid excitation leading to the so-called lock-in phenomenon. The vortex shedding frequency is therefore locked onto the structural eigenfrequency over a rather extended range of free-stream velocity. The velocity range over which synchronization occurs increases with oscillation amplitude [127]. The vortex span-wise non-uniformities is replaced by parallel vortex shedding mode. The vortex strength is significantly increased in the case of an oscillating cylinder and in comparison with the wake of the stationary body, Davies [33]. For lock-in, vibration amplitude hysteresis is observed when reduced velocity is increased over a certain range and then is decreased back over the same range, Feng [44]. This hysteresis is still to be fully explained. The vortex formation region length is found to decrease for lock-in condition, Kim *et al.* [68]. Gilbert and Sigurdson [53] investigated the influence of the structural vibration on the vortex street span-wise organization. They visualized hydrogen bubble flow of a self-oscillating cylinder vortex street *void*. Interestingly, vortex dislocations did not originate at nodes in the cylinder vibration. Besides, it is commonly said that the vortex formed on one side of the cylinder is shed when the cylinder is near the maximum displacement on the same side. Nevertheless, different modes of vortex shedding occur in the lock-in range depending on the location in the said range, Sarpkaya [97]. 180° phase shift between the vortex shedding and the body displacement can occur from one end of the lock-in range to the other. For a stationary cylinder, it is shown that the vortices is shed nearly at the zero lift force, Sarpkaya [96].

5.5 Flow stability property

When the flow is disturbed, the disturbance may either die away, persist as a disturbance of similar magnitude or grow. Respectively, the disturbance is called stable, neutrally stable or unstable. In the review on wakes behind blunt bodies, Oertel [83] discusses the existence of the absolute unstable regions in the near wake. Monkewitz and Nguyen [79] describe the terms absolute and convective nature of instability as the behavior of the impulse response of an unstable medium. If an impulsively generated small amplitude transient grows exponentially in place, the flow is termed absolutely unstable. If, on the other hand, the transient is convected away from the source and leaves the flow ultimately undisturbed, one speaks of convective instability. The existence of absolutely unstable region offers the possibility of effective wake control [83]. Monkewitz [78] determines the absolute or convective nature of the instability as a function of mean velocity profile parameters and Reynolds number. A two-parameter family of symmetric wake profiles is considered and allows for the variation of the wake depth as well as for a variable ratio of wake width to mixing layer thickness.

The concept of absolute instability in wakes is quite new and has been a subject of controversy in the scientific community. The reason for this is that no experiment on wake flows has yet directly proven the existence of an absolutely unstable region in the wake. Its existence has been demonstrate numerically by simulating the impulse response. The absolutely unstable region is defined on the basis of a quasi-steady Navier-Stokes solution, which is the object of a numerical impulse-response simulations, as well as for the Orr-Sommerfeld stability analysis [36].

5.6 Vortex cavitation

There is a vast quantity of cavitation literature and two reviews are provided by Arndt [6] and [7]. In the case of liquid flows, when the pressure falls below the vapor pressure, cavitation occurs in the vortices formed in the body wake. Typically, a nucleus is present within or captured by the vortex. If the pressure in the vortex core falls below the liquid vapor pressure, the critical tension of the nucleus is reached, resulting in a growing vapor bubble. The bubble expands to a fraction of the vortex core size in the radial direction and grows along the vortex axis, [31].

Effects of cavitation on periodic wakes are investigated by Young and Holl [128]. They observe that the cavitation development in the wake of wedges increases the vortex shedding frequency by up to 25%. The stream-wise and cross-stream inter-vortex vortex spacings are also modified, leading to a narrowing of the vortex street. Few studies on wakes behind wedges confirm these effects, Ramamurthy and Balachandar [87] and Belahadji *et al.* [16]. In the wake of a symmetrical hydrofoil, the increase of the vortex shedding frequency with the decrease of the cavitation index value is measured by Roao and Petrikat [88] and Dupont *et al.* [39], [40]. It is therefore concluded that cavitation is not a passive agent of wake flow visualization. For moderate cavitation development, it is believed that the vortex span-wise organization is not affected. Nevertheless, the above mentioned cavitation effects on vortex street dynamic have not been entirely elucidated until now.

Models for cavitation inception in the wake of bluff bodies are presented by Arndt [5] and Belahadji *et al.* [16]. The models lead to a linear $\sigma_i \sim \sqrt{Re_h}$ law that correctly predicts the correlation between the cavitation inception index and the Reynolds number for the considered range of free-stream velocities. Although remarkably successful in describing the wake cavitation inception for fixed bluff bodies, none of these studies provides a direct insight into the role of the trailing edge vibration on the cavitation occurrence.

Sridhar and Katz [105] investigate the effect of entrained bubbles on the structure of vortex rings. It is shown that few microscopic bubbles are able to fragment the core of the vortex into regions with peak vorticities that were 20% higher than the original maximum vorticity. Considering a Rankine vortex, Arndt and Keller [8] established that the maximum velocity in the cavitation vortex is $\sqrt{2}$ higher than in the non-cavitation vortex. Finally, Choi and Ceccio [31] investigate the growth and collapse of a cavitation bubble forming within the core of a line vortex. They conclude that the traditional scaling variables of vortex, *i.e.* vortex strength, core radius and core pressure, may be used to scale inception of vortex cavitation, but are insufficient to scale the developed vortex cavitation.

Part II

Experimental setup and techniques

Chapter 6

Test facility and hydrofoil setup

6.1 Test facility overview

The experiments are performed in the EPFL-LMH high-speed cavitation tunnel, described by Avellan *et al.* [10] and sketched in Figure 6.1. The test facility is a closed loop built on three levels. Upstream of the test section, a honeycomb, a screen and a contraction nozzle are installed to avoid macroscopic flow rotation and to reduce the turbulence intensity. The nozzle area reduction from 46 to 1 results in a uniform velocity distribution in the test section inlet. The rectangular test section has inner dimensions of 150 x 150 x 750 mm. The tested hydrofoil spans the test section and is mounted 4 mm above the test section center axis. The blockage ratio based on the hydrofoil maximum thickness, 9.9 mm, is 6.6%.

The double suction pump provides a total head of 36.5 m for 1.125 m^3/s at 885 rpm. The maximum free-stream velocity at the test section inlet is 50 m/s. The pump is driven by a 500 kW power DC-electric motor. The transit time resulting from a complete tunnel loop of one fluid particle is 98 s at the maximum flow rate.

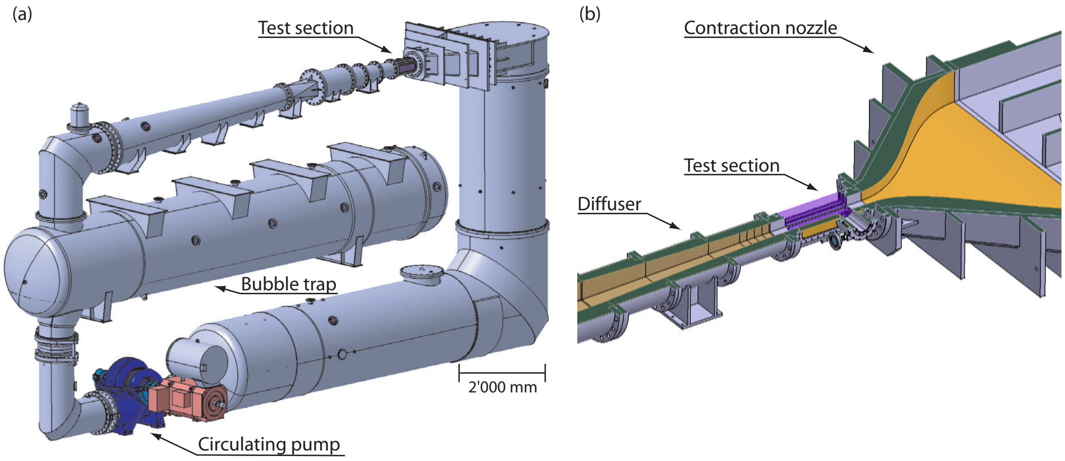

Figure 6.1: EPFL-LMH high speed cavitation tunnel: (a) Hydraulic circuit and (b) details of the contraction nozzle, the test section and the diffuser

The operating flow parameters that are controlled are the free-stream velocity at the test section inlet C_{ref} and the cavitation index $\sigma = 2(p_{ref} - p_v)/\rho C_{ref}^2$, where p_{ref} and p_v are the reference pressure at the test section inlet and the vapor pressure respectively. The mean flow velocity is derived from absolute pressure measurements at both ends of the contraction nozzle. The vapor pressure and the density of the fluid are function of the temperature, which is measured upstream of the contraction nozzle. The pressure is set by controlling the air pressure over the free surface in the pressure vessel. Due to the highest available nominal pressure of the pipe-industry standards, the maximum static pressure is limited to 16 bar. The automatic control of flow conditions is ensured by an *Allen Bradley* programable automation. The user interface, *NI-Labview* programming, is described by Guennoun [62]. For cavitation-free experiments, the test section pressure is held constant and sufficiently high to suppress any cavitation development. For experiments with wake cavitation development, the cavitation index is set high enough to allow cavitation to occur in the wake, but not on the hydrofoil wall. For all reported results, the hydrofoil is mounted and fixed at an angle of attack of $\alpha = 0°$, measured within an estimated uncertainty of 0.02°.

6.1.1 Test section flow quality

Single-point two-component Laser Doppler Velocimetry, section 7.2.1, is used to measure the free-stream velocity profiles at the inlet of the test section, $x/L = -0.5$. During the measurements, the hydrofoil is mounted, section 6.2.1. Stream-wise and transverse mean velocity profiles are shown in Figure 6.2 for $C_{ref} = 20$ m/s free-stream velocity, $Re_h = 64.4 \cdot 10^3$, $Re_L = 2.0 \cdot 10^6$ where h and L are respectively the hydrofoil trailing edge thickness and chord length. Figures 6.2 (a) and (b) presents traverse measurements following the vertical axis and Figures 6.2 (c) and (d) span-wise traverse measurements.

Across the test section, Figure 6.2 (a), the mean stream-wise velocity is constant to within 2% and slightly affected by the presence of the foil. The fluctuations are constant to within 0.4%. The mean normalized stream-wise velocity fluctuations is $I_x = 0.96\%$, equation (6.1). In Figure 6.2 (b), there is a mean transverse velocity, less than $0.01C_{ref}$, across the test section due to the presence of the hydrofoil. The mean normalized transverse velocity fluctuations is $I_y = 1.37\%$, equation (6.1).

$$I_x = \frac{1}{N}\sum_{i=1}^{N}\frac{C_{x\ stdv\ i}}{C_{ref}}\ , \qquad I_y = \frac{1}{N}\sum_{i=1}^{N}\frac{C_{y\ stdv\ i}}{C_{ref}} \tag{6.1}$$

Span-wise variation of mean stream-wise and transverse velocities are shown in Figures 6.2 (c) and (d). Both mean velocities are constant to within 0.8% and their fluctuations respectively to within 0.2% and 0.4%. The mean normalized velocity fluctuations are $I_x = 0.99\%$ and $I_y = 1.34\%$. Additional measurements are carried out for $C_{ref} = 5$ m/s free-stream velocity. No significant Reynolds effects has been noted: The above mentioned normalized quantities are of the same order of magnitude as for $C_{ref} = 20$ m/s free-stream velocity.

The boundary-layer thickness δ, upstream of the foil at $x/L = -0.5$, is found from velocity measurements close to the test sections walls, Figure 6.3. The boundary-layer thickness δ is estimated to be 3 mm and the boundary-layer displacement thickness $\delta_1 = 0.4$ mm, which is less than 0.3% of the hydrofoil span.

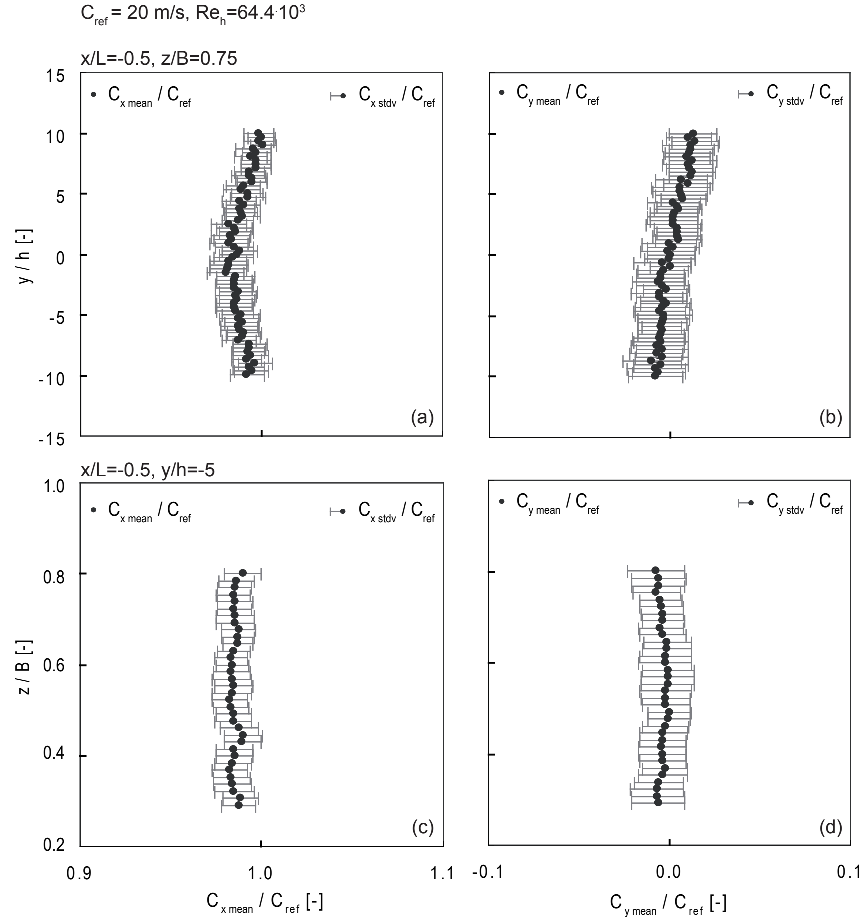

Figure 6.2: (a) Stream-wise and (b) transverse mean velocity profiles and fluctuations at $x/L = -0.5$ and $z/b = 0.75$. (c) Stream-wise and (d) transverse mean velocity profiles and fluctuations at $x/L = -0.5$, $y/h = -5$. Hydrofoil mounted in the test section, $C_{ref} = 20$ m/s, $Re_h = 64.4 \cdot 10^3$, $Re_L = 2.0 \cdot 10^6$

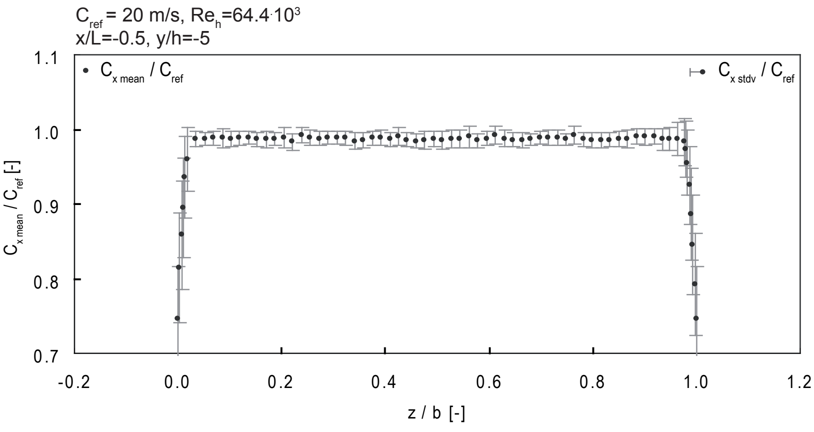

Figure 6.3: Stream-wise mean velocity profile and fluctuation at $x/L = -0.5$, $y/h = -5$. Hydrofoil mounted in the test section, $C_{ref} = 20$ m/s, $Re_h = 64.4 \cdot 10^3$, $Re_L = 2.0 \cdot 10^6$

6.2 Hydrofoil setup

6.2.1 Hydrofoil geometry

The hydrofoil, sketched in Figure 6.4, features a blunt trailing edge *NACA 0009* geometry. The first two digits describe respectively the maximum camber and the distance of maximum camber from the foil leading edge. The selected geometry is therefore symmetric. The last two digits describe the maximum thickness of the foil as percentage of the chord. The complete geometry designation is *NACA 0009 - 7.8 45/1.93* where the first extension helps to describe the leading edge radius, the second one the position of the maximum thickness and the last one the slope at the trailing edge, [62]. The foil chord length is originally 110 mm. It is blunt truncated at $L = 100$ mm and the resulted trailing edge thickness h is 3.22 mm. The foil thickness distribution is written as

$$\begin{aligned} &0 \leq \tfrac{y}{L_0} \leq 0.5 && \tfrac{y}{L_0} = a_0\left(\tfrac{x}{L_0}\right)^{1/2} + a_1\left(\tfrac{x}{L_0}\right) + a_2\left(\tfrac{x}{L_0}\right)^2 + a_3\left(\tfrac{x}{L_0}\right)^3 \\ &0.5 < \tfrac{y}{L_0} \leq 1.0 && \tfrac{y}{L_0} = b_0 + b_1\left(1-\tfrac{x}{L_0}\right) + b_2\left(1-\tfrac{x}{L_0}\right) + b_3\left(1-\tfrac{x}{L_0}\right)^3 \end{aligned} \tag{6.2}$$

with L_0 being the original chord length and :

$$\begin{cases} a_0 = +0.1737 \\ a_1 = -0.2422 \\ a_2 = +0.3046 \\ a_3 = -0.2657 \end{cases} \begin{cases} b_0 = +0.0004 \\ b_1 = +0.1737 \\ b_2 = -0.1898 \\ b_3 = +0.0387 \end{cases} \tag{6.3}$$

The hydrofoil is made of stainless steel. After machining, the hydrofoil geometry is verified by reverse engineering method. The discrepancies remains in the tolerance. Because of the blunt geometry, the flow separation point is fixed at the trailing edge, with the vortices rolling-up at the rear face of the foil. Therefore, the trailing edge thickness is used as the reference length for non-dimensional parameters, including the Reynolds $Re_h = C_{ref}h/\nu$ and Strouhal $St_h = f_s h/C_{ref}$ numbers. The hydrofoil span B is 150 mm. The hydrofoil mounting in the test section can be assumed to embody a perfect embedding on one side and a pivot embedding on the other.

The results are presented in the $x,\ y,\ z$ coordinate frame, Figure 6.4. Its origin is fixed on the hydrofoil symmetry plane at the leading edge. The *x–axis* is directed downstream (defined stream-wise), the *y–axis* is normal (defined transverse) to the hydrofoil symmetry plane, and the *z–axis* lies along the span of the foil (defined span-wise). The boundary-layer flow is shown in a rotated surfaced-aligned coordinated frame, where the x_1*–axis* is defined by the local surface tangent and the y_1*–axis* is perpendicular to the x_1*–axis.*

Figure 6.5 presents the pressure coefficient distribution along the hydrofoil at 0° angle of attack. It is computed by the inviscid formulation of the X-foil program [37]. The computational methodology is described by Ait Bouziad [3].

6.2.2 Surface roughness and boundary-layer tripping

The hydrofoil is milled from stainless steel and polished to mean surface roughnesses, $R_{a_{DIN}}$ and $R_{z_{DIN}}$, equation (3.8), of 0.15 μm and 1.5 μm, respectively. A *Hommel tester*

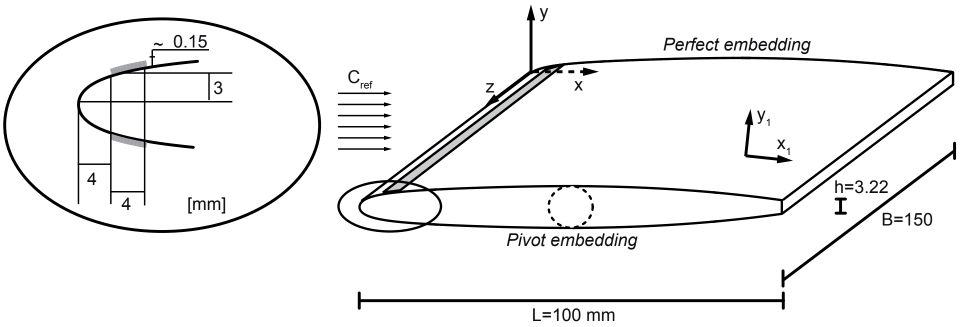

Figure 6.4: Blunt trailing edge *NACA 0009* hydrofoil and distributed roughness at the leading edge

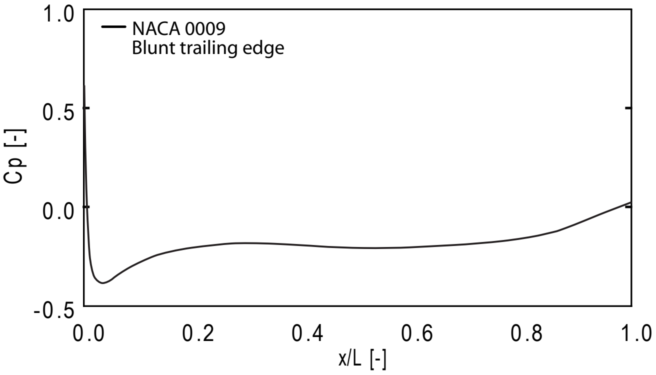

Figure 6.5: Pressure coefficient distribution along the blunt trailing edge *NACA 0009* hydrofoil, Ait Bouziad [3]

T1000 roughness meter is used for the measurements. According to the following criterion, $C_{ref}R_{z_{DIN}}/\nu < 100$, equation (3.9), the hydrofoil surface is considered to be hydraulically smooth over the entire experimented free-stream velocity range. A natural turbulent transition can occur beyond a certain distance from the leading edge.

Dryden [38] reviews published data on the roughness effect on the transition from laminar to turbulent flow on flat plates. The transition occurs when $C_{ref}k_s/\nu \geq 900$ where k_s is the height of the surface roughness pattern. A distributed roughness made of glue and 125 μm diameter sand is placed on both sides of the hydrofoil, 4 mm downstream from the stagnation line and 4 mm wide, Figure 6.4. The glue and sand combination create a 150 μm high, two-dimensional flow obstacle while the sand strip itself provides multiple three-dimensional protuberances. Assuming that the above mentioned relationship holds true in our case study, the boundary-layer transition is tripped at the roughness position from a local tangential velocity of 6 m/s. Laser Doppler Velocimetry (LDV) measurements at the leading edge revealed that this specific velocity is reached above 5 m/s free-stream velocity. Henceforth, this configuration is designated as the tripped transition. In contrast, the case without rough strips is designated as the natural transition.

The measurements reported in the part III are performed without any rough strips so that a natural turbulent boundary-layer transition can occur. The effects of a tripped turbulent boundary layer on vortex shedding are studied in part IV.

6.2.3 Hydro-elastic coupling: Similarity law

As the flow velocity is changed so that the vortex shedding frequency approaches one of the natural frequency of the foil, resonance takes place. The question arises as to how the free-stream velocity implying hydro-elastic coupling during model testing is modified for the prototype assuming geometrical similarity. The torsion and bending of a uniform straight bar with rectangular cross-section are investigated. The main results are summarized below. The complete formulations are detailed in appendix B.

Torsion and bending of a straight bar

In Figure 6.6, a bar of rectangular section under pure (a) torsion and (b) bending is considered. In the case of a hydrofoil, the length l is the chord length, h the thickness and b the span.

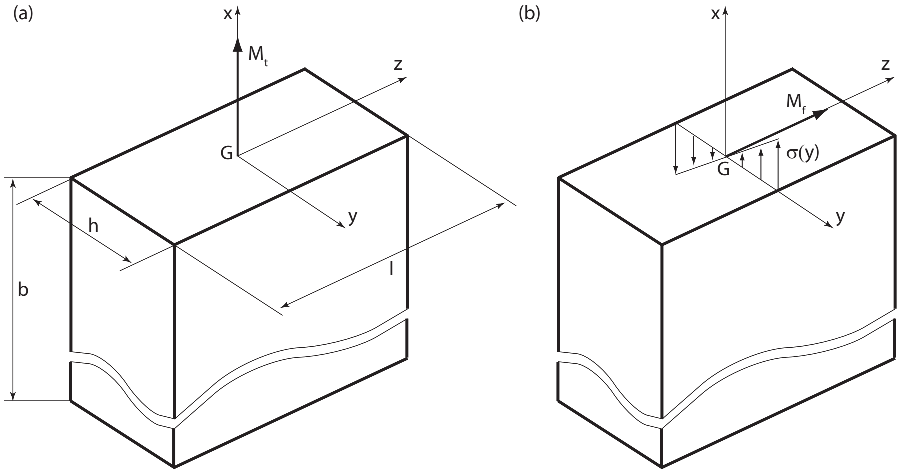

Figure 6.6: Bar of rectangular section under pure (a) torsion and (b) bending

The natural frequencies of a uniform bar, whose mass is uniformly distributed along the *x–axis*, in pure torsion or bending with one end fixed and the other free are

$$f_{Torsion} = \frac{N_n}{2\pi}\sqrt{12\frac{G\beta}{\rho}\frac{h^2}{b^2(l^2+h^2)}}\,, \qquad f_{Bending} = \frac{N_n}{2\pi}\frac{h}{b^2}\sqrt{\frac{E}{12\rho}} \tag{6.4}$$

where E is the Young modulus of the material, $G = E/2(1+\mu)$ the modulus of elasticity in shear, μ the Poisson ratio, ρ the density and β a factor dependent of the ratio l/h. A factor N_n is introduced according to the mode of vibration and the boundary conditions, Table 6.1 [90].

Besides, the Strouhal number St_h, whose reference length is the bar thickness h, is

$$St_h = \frac{f_s h}{C_{ref}} \tag{6.5}$$

Matching the vortex shedding frequency and the natural frequency of the system $f_s = f_{Torsion}$ and $f_s = f_{Bending}$ means,

$$\frac{St_h\, C_{ref_{Torsion}}}{h} = \frac{N_n}{2\pi}\sqrt{12\frac{G\beta}{\rho}\frac{h^2}{b^2(l^2+h^2)}}\,, \quad \frac{St_h\, C_{ref_{Bending}}}{h} = \frac{N_n}{2\pi}\frac{h}{b^2}\sqrt{\frac{E}{12\rho}} \tag{6.6}$$

Table 6.1: Constants referring to the mode of vibration for a uniform bar under pure torsion or bending, one end fixed the other free [90]

Eigen mode	Torsional mode: N_n value	Bending mode: N_n value
1^{st}	1.57	3.5
2^{nd}	4.71	22.0
3^{rd}	7.85	61.7

Therefore, the resonances occur for free-stream velocities given by,

$$C_{ref_{Torsion}} = \frac{N_n}{2\pi\ St_h}\sqrt{12\frac{G\beta}{\rho}\ \frac{h^4}{b^2(l^2+h^2)}}\ , \quad C_{ref_{Bending}} = \frac{N_n}{2\pi\ St_h}\left(\frac{h}{b}\right)^2\sqrt{\frac{E}{12\rho}} \tag{6.7}$$

The geometrical similarity between the model $()_M$ and the prototype $()_P$ leads to

$$\left(\frac{h^4}{b^2(l^2+h^2)}\right)_M = \left(\frac{h^4}{b^2(l^2+h^2)}\right)_P\ , \qquad \left(\frac{h}{b}\right)^2_M = \left(\frac{h}{b}\right)^2_P \tag{6.8}$$

β is function of the ratio l/h, so that

$$(\beta)_M = (\beta)_P \tag{6.9}$$

Finally, G, E and ρ are properties of the material, so that

$$\left(\frac{G}{\rho}\right)_M = \left(\frac{G}{\rho}\right)_P\ , \qquad \left(\frac{E}{\rho}\right)_M = \left(\frac{E}{\rho}\right)_M \tag{6.10}$$

The Strouhal number St_h being constant on specific free-stream velocity range and considering equations (6.8) to (6.10), the equation (6.7) leads to,

$$\underline{\left(\mathbf{C_{ref_{Torsion}}}\right)_\mathbf{M} = \left(\mathbf{C_{ref_{Torsion}}}\right)_\mathbf{P}}\ , \qquad \underline{\left(\mathbf{C_{ref_{Bending}}}\right)_\mathbf{M} = \left(\mathbf{C_{ref_{Bending}}}\right)_\mathbf{P}} \tag{6.11}$$

Therefore and assuming the geometrical similarity, if the torsional or bending resonance occurs during model testing, it is expected to excite the torsional or bending mode in the prototype at the same free-stream velocity.

Added mass effects

Whenever acceleration is imposed on a fluid flow either by acceleration of a body or by acceleration externally imposed on the fluid, non-negligible additional fluid forces act on the surfaces in contact with the fluid, Brennen [26]. For the torsion of the straight bar and based on potential flow analysis, the hydrodynamic inertia per unit length of a rectangular section of length l rotating about its central axis is

$$J_{fluid} = \frac{1}{8}\rho\pi\left(\frac{l}{2}\right)^4 \tag{6.12}$$

Therefore, the total inertia to be taken into account is

$$J_{total} = J_{structure} + J_{fluid} = \frac{\rho_{structure} bhl(l^2 + h^2)}{12} + \frac{1}{8}\rho_{fluid}\pi \left(\frac{l}{2}\right)^4 b \tag{6.13}$$

The bending of the bar is assimilated to a vertical displacement of a rectangular section of length l. The hydrodynamic mass per unit length is

$$m_{fluid} = \frac{\pi}{4}\rho l^2 \tag{6.14}$$

Therefore, the total mass per unit length to be taken into account is

$$m_{total} = m_{structure} + m_{fluid} = \rho_{structure} hl + \frac{\pi}{4}\rho_{fluid} l^2 \tag{6.15}$$

Considering the added mass effects does not change the main conclusion of the previous section: The free-stream velocity leading to structural resonance, torsional or bending ones, is the same for the model as for the prototype.

Numerical applications

Applying dimensions and material properties of our case study, the eigen frequencies of the first torsional and bending modes are below calculated. The hydrofoil is considered to be fixed on one side and free on the other. The density of the stainless steel $\rho_{structure}$ is 7900 kg/m^3, the modulus of elasticity E is 200 GPa, and the poisson ratio μ is 0.30. The maximum hydrofoil thickness h is 9.9 mm and the chord length L and span B are 100 mm and 150 mm, respectively.

Taking into account the hydrodynamic inertia and mass, equations (6.12) and (6.14), in equation (6.4) and applying dimensions and material properties of our case study, the eigen frequency of the first torsional and bending modes are calculated, equations (6.16) and (6.17). The effect of the added mass is significant. The first torsional and bending eigen frequencies are respectively decreased of about 15% and 30%,

$$f_{Torsion\ (water)} = 846\ Hz\ ,\ \ \Delta f_{Torsion} = \frac{f_{Torsion\ (air)} - f_{Torsion\ (water)}}{f_{Torsion\ (air)}} = 14.6\% \tag{6.16}$$

$$f_{Bending\ (water)} = 253\ Hz\ ,\ \Delta f_{Bending} = \frac{f_{Bending\ (air)} - f_{Bending\ (water)}}{f_{Bending\ (air)}} = 29.4\% \tag{6.17}$$

Considering a Strouhal number of 0.2 and a trailing edge thickness h of 3.22 mm, chapter 6, the corresponding free-stream velocities for the first torsional and bending modes are

$$C_{ref\ Torsion} = \frac{f_{Torsion} h}{St_h} = 13.6\ m/s\ ,\ \ \ C_{ref\ Bending} = \frac{f_{Bending} h}{St_h} = 4.1\ m/s \tag{6.18}$$

The eigen frequencies are highly dependent on the boundary conditions, *i.e.* the way the structure is fixed. This dependency is depicted through the N_n parameters. Nevertheless, the terms of the eigen frequency, equations (6.4), are not changed and the above dimensional analysis is true for all kind of boundary conditions. Roark and Young [90] give the numerical values for N_n for several cases of loadings and boundary conditions.

Chapter 7

Measuring apparatus

7.1 Vortex-induced vibration

Vortex-induced vibration is a convenient measure of the energy associated with the shedding mode, since it reliably integrates the pressure fluctuations along the entire span. With vibration measurements, the vortex shedding frequency is detected, the vortex shedding process intermittency characterized and the hydrofoil eigen modes identified.

7.1.1 Accelerometer

The vortex-induced vibrations are measured with the help of a piezoelectric accelerometer, *Kistler K-shear 8702B25*. The unit is a low impedance accelerometer, which utilizes quartz shear sensing element and incorporates a miniaturized built-in charge-to-voltage converter. It is sketched on Figure 7.1. Low impedance accelerometer types require an external power supply coupler, *Kistler Power Supply/Coupler 5134A*, to energize the electronics. The main technical data are summarized in Table 7.1. The accelerometer is fitted on the hydrofoil support.

Table 7.1: Main technical data of the *Kistler K-shear 8702B25* accelerometer

Specification	
Acceleration range	±25 g
Sensitivity	200 mv/g
Resonant frequency	54 kHz
Frequency response	10 kHz
Transverse sensitivity	1.5%

7.1.2 Laser Doppler vibrometer

Besides the accelerometer fitted on the hydrofoil support, the vortex-induced vibrations is monitored with a laser Doppler vibrometer, *Polytec PDV100*. The measurement principle of this non-intrusive device is based on the detection of the frequency shift of the reflected laser beam, which is directly related to the displacement velocity of the surface,

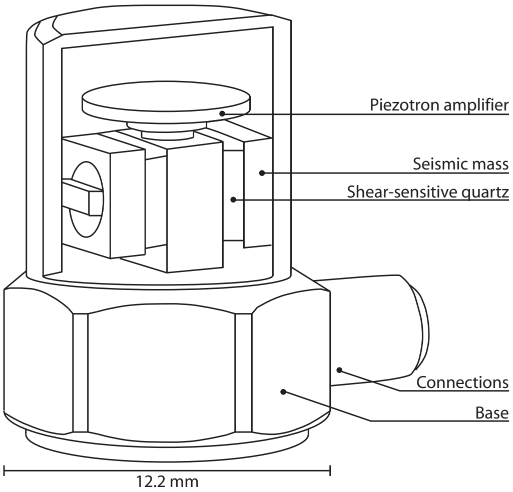

Figure 7.1: *Kistler K-shear 8702B25* accelerometer

consistent with the Doppler effect. The perceived wavelength λ_p and frequency f_p of a moving receiver with a relative velocity v_p with respect to the stationary transmitter (λ, f) is given by, [4]

$$\lambda_p = \frac{\lambda}{1-\frac{v_p}{c}} \,, \qquad f_p = \frac{c-v_p}{\lambda} = f - \frac{v_p}{\lambda} \tag{7.1}$$

The change in frequency, *i.e.* the Doppler frequency f_D, is therefore,

$$f_D = \frac{v_p}{\lambda} \tag{7.2}$$

In comparison with the frequency of laser light, the Doppler shift is negligible and thus virtually impossible to resolve directly. An optical interferometer is therefore used to mix the scattered light with a reference beam. The beat frequency on the detector is equal to the Doppler frequency. Figure 7.2 is example of an interferometer: The laser beam is split by a beamsplitter (BS 1) into a reference beam and a measurement beam. After passing through a second beamsplitter (BS 2), the measurement beam is focused onto the probe under investigation, which reflects it. The reflected beam is then deflected downwards by BS 2 and is merged with the reference beam by the third beam splitter (BS 3) onto the photo detector. As the path length of the reference beam is constant over time $r_2 = cst$, a movement of the object under investigation $r_1(t)$ generates a dark and bright fringes typical of interferometry on the detector. One complete dark-bright cycle on the detector corresponds to an object displacement of exactly half of the wavelength of the light. Indeed, supposing that two monochromatic waves, with their respective light intensities I_1 and I_2, are superposed on the detector, the resulting intensity is not just the sum of the single intensities, but is modulated according to the formula, [25]

$$I_{tot} = I_1 + I_2 + 2\sqrt{I_1 I_2}\ \cos[2\pi(r_1 - r_2)/\lambda] \tag{7.3}$$

The last term, *i.e.* the interference term, relates to the path length difference $(r_1 - r_2)$ between both beams. If this difference is an integer multiple of the laser wavelength λ, the overall intensity is four times a single intensity, the two beams interfering constructively. Correspondingly, the overall intensity is zero if the two beams have a path length difference of half of one wavelength, the two beams interfering destructively.

Due to the sinusoidal nature of the detector signal, the direction of the vibration is ambiguous. The directional sensitivity is introduced with an optical frequency shift, 70 MHz, into one arm of the interferometer to obtain a virtually velocity offset. The frequency shift is applied with the help of a Bragg cell.

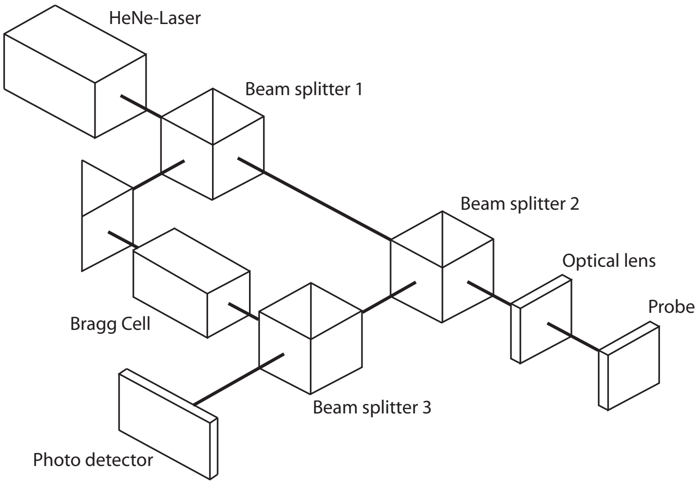

Figure 7.2: Laser interferometer

Table 7.2: Main technical data of the *Polytec PDV100* laser doppler vibrometer

Specification	
Laser type and class	$HeNe$, class II
Velocity range	$20, 100, 500$ mm/s
Frequency range	22 kHz
Low pass filter	$1, 5, 22$ kHz digital FIR type
High pass filter	100 Hz analog, 3^{rd} order Butterworth
Working distance	> 0.1 m

The settings necessary for a measurement are limited to selecting the velocity measurement range and the low and high pass filters. To optimize the signal-to-noise ratio, the smallest possible measurement range, which is not exceeded under the given measurement conditions, is used. Moreover, the laser vibrometer is calibrated in air, while hydrofoil vibration measurements are performed in water. The speed, and hence the wavelength, of light in air are larger than that in water by a factor of 1.33, the refractive index of the water. The optical path length is defined as the physical distance traveled by the light times the refractive index of the medium. Consequently, the resulting measurement have to be divided by the refractive index to obtain the physical displacement [77]. Notes that only the medium in which the object movement takes place has to be considered, as only the optical path length inside this medium changes. The refraction index of the perspex window has therefore not to be taken into account.

The optical head is mounted on a traverse system and displaced over the upper surface of the hydrofoil. Along the document, the location of the measurement point of the presented vibration signals and spectra is $(x/L,\ z/B) = (0.8,\ 0.75)$ accordingly to the system axis defined on Figures 6.4 and 7.3.

Hydrofoil eigen mode identification

As the flow velocity is changed so that the vortex shedding frequency approaches one of the natural frequency of the structure, the resonance takes place with a significant increase of the vibration amplitude. The identification of the hydrofoil eigen modes, which are involved in such hydro-elastic couplings, is performed with vibration measurements at different location on the hydrofoil upper surface. The location of the laser vibrometer measurements points is shown in Figure 7.3. Parts of the hydrofoil upper surface are not measurable due to optical access constraints. For every measurement point, the hydrofoil displacement amplitude is directly given by the laser vibrometer signal. The displacement amplitude is defined to be the displacement value at 99% of the cumulative probability density function of the signal. The displacement phase is calculated using simultaneous laser vibrometer and accelerometer measurements: The accelerometer position is fixed for all measurements and its signal is used as the reference signal. The hydrofoil displacement phase is the phase of the cross-spectrum of the laser vibrometer and accelerometer signals at the eigen frequency. The coherence function between the two signals is checked.

The cross-spectral density function is defined by, [17]

$$S_{xy}(f) = X^*(f)Y(f) \tag{7.4}$$

where $X(f)$ is the Fourier transform of $x(t)$,

$$X(f) = \int_{-\infty}^{+\infty} x(t)e^{-j2\pi ft}dt \tag{7.5}$$

with

$$\int_{-\infty}^{+\infty} x(t)dt < +\infty \tag{7.6}$$

The coherence function $\gamma_{xy}^2(f)$ of the system, with the input $x(t)$ and the output $y(t)$ is,

$$\gamma_{xy}^2(f) = \frac{\left|\overline{S_{xy}}(f)\right|^2}{\left|\overline{S_{xx}}(f)\right|\left|\overline{S_{yy}}(f)\right|} \tag{7.7}$$

where $S_{xx}(f) = X^*(f)X(f)$ and $S_{yy}(f) = Y^*(f)Y(f)$. For a linear system, the coherence function is $\gamma_{xy}^2(f) = 1$. If $x(t)$ and $y(t)$ are unrelated, the coherence function is zero. If the coherence function is between the two limits, noise is present and/or the system relating $x(t)$ and $y(t)$ is not linear. For linear systems, the coherence function is therefore interpreted as the fractional portion of the mean square value at the output $y(t)$ which is contributed by the input $x(t)$ at frequency f.

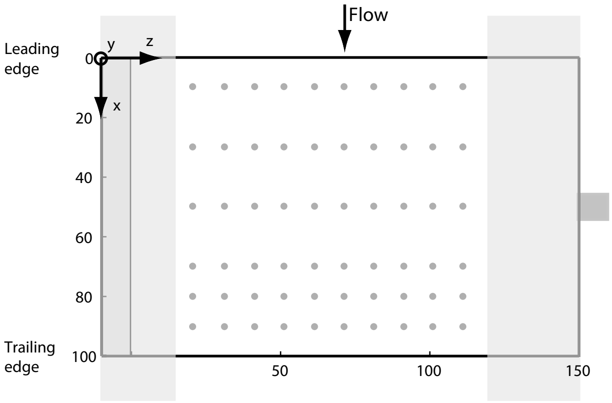

Figure 7.3: Location of the hydrofoil vibration measurement points

7.1.3 Data acquisition system

The data acquisition system, *Hewlett-Packard* based on the VXI (VMEbus Extensions for Instrumentation) standard bus technology, features a 16 bit A/D converter resolution, a memory depth of 1 MSamples per channel and a maximum sampling frequency of 51.2 kHz per channel. The typical acquisition parameters are the maximum sampling frequency and a block size of 512 KSamples. The system is equipped with appropriate pre-amplifiers and anti-aliasing filters. The data acquisition control and storage is achieved by a software system, *NI-Labview* prgramming. For spectral computation, Fast Fourier Transform is applied to 16 equal segments of the time signal and averaging is performed. With the above mentioned typical acquisition parameters, the resolution is 1.56 Hz.

7.2 Flow measurement

7.2.1 Laser Doppler velocimetry

Laser Doppler Velocimetry (LDV) is a non intrusive optical flow velocity measurement technique. An overview of laser Doppler techniques is given in [4]. The measurement principle, Figure 7.4, is based on the analysis of the light reflection of a particle crossing the measurement volume formed by the intersection of two coherent laser beams. Due to the coherence of the laser light waves, an interference fringe pattern is formed in the measurement volume. The spacing of the fringe pattern is determined by the wavelength and the beam intersection angle θ,

$$\delta_{fringe} = \frac{\lambda}{2\sin(\theta/2)} \tag{7.8}$$

Particles, which are crossing the measurement volume, create a reflection light or *Doppler burst*. Receiving optics with high sensitive photomultipliers and dedicated signal processing devices, provide the frequency of the Doppler burst $f_{Doppler}$. The velocity component C of the particle in the direction normal to the fringe is function of the

Doppler frequency and the fringe spacing δ_{fringe},

$$C = \delta_{fringe} \cdot f_{Doppler} = \frac{\lambda f_{Doppler}}{2\sin(\theta/2)} \tag{7.9}$$

The directional sensitivity is introduced by shifting the frequency of one beam with the help of a Bragg cell. Therefore, a zero-velocity particle reflects a signal at the Bragg cells frequency. This frequency, 40 MHz, is chosen large enough that the entire expected velocity range can be measured without constraint.

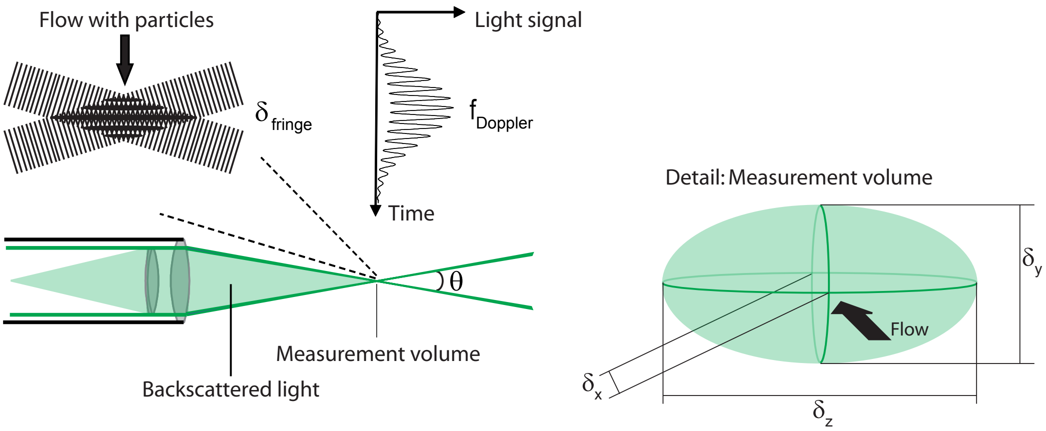

Figure 7.4: Principle measurement of Laser Doppler Velocimetry (LDV)

Single-point two-component Laser Doppler Velocimetry (LDV) is used to measure the hydrofoil boundary layer and wake flows. The seed particles are 10 μm diameter hollow glass spheres. Laser light is provided by a 10 W Argon-Ion source. The optical head has a 38.15 mm beam spacing and a 250 mm focal length (in air). The in-water control volume dimensions are 0.075 mm in diameter (x and y–*axis*) and 1.3 mm in length (z–*axis*). The head is mounted on a high-precision 3-axis traverse system and the probe is rotated on a rotation stage, *Newport*. The minimum incremental motions are 0.01 mm and 0.001°. *Dantec* software is used to validate the particle bursts and to calculate the mean flow velocities and fluctuations. During periods of higher velocity, a larger volume of fluid is swept through the measuring volume and a greater number of velocity samples are recorded. As a direct result, the statistics of the flow field evaluated using arithmetic averaging are biased in favor of the higher velocities. This velocity bias is eliminated if the particle transit time t_i is used as the weighting factor, equation (7.12), consistent with Buchhave *et al.* [28]. The mean $C_{x_{mean}}$ and fluctuating $C_{x_{stdv}}$ stream-wise velocities as well as the transit-time weighting factor η_i are defined below. The same definitions are applied for the transverse component. All data are acquired for $z/b = 0.75$.

$$C_{x_{mean}} = \sum_{i=1}^{N} \eta_{x_i} C_{x_i} \tag{7.10}$$

$$C_{x_{stdv}} = \sqrt{\sum_{i=1}^{N} \eta_{x_i} (C_{x_i} - C_{x_{mean}})^2} \tag{7.11}$$

$$\eta_{x_i} = \frac{t_{x_i}}{\sum\limits_{j=1}^{N} t_{x_j}} \tag{7.12}$$

Table 7.3: Properties of the LDV system

Specification	
Laser type/class	Ion-Argon / class IV
Laser wave length (green/blue)	488 nm / 514.5 nm
Laser power	10 W
Probe beam spacing	38.15 mm
Probe beam diameter	2.2 mm
Focal length in air	250 mm
Fringe spacing (green/blue)	3.38 μm / 3.21 μm
Control volume size in water (minor axis/major axis), green	0.075 mm / 1.30 mm
Control volume size in water (minor axis/major axis), blue	0.071 mm / 1.24 mm
Bragg cell frequency	40 MHz
Particle type	Hollow glass spheres
Particle density	1100 kg/m^3
Particle size	10 μm
Traverse resolution (linear/angular)	0.01 mm / 0.001°

7.2.2 Particle image velocimetry

The measurement principle of the Particle Image Velocimetry (PIV) is based on the analysis of two successive pictures of the flow seeded with particles and illuminated with a laser sheet. The camera pictures are divided into rectangular regions called interrogation areas. For each of these areas, the image from the first and the second pulse of the laser-sheet are correlated to produce an average particle displacement vector. The spatial cross-correlation function of the images interrogation areas I_1 and I_2 is defined by [17],

$$C_{I_1 I_2}(\xi) = \lim_{S\to\infty} \frac{1}{S} \int_S I_1(\mathbf{x}) I_2(\mathbf{x}+\xi) dS(\mathbf{x}) \tag{7.13}$$

where $dS(\mathbf{x}) = dxdy$. In the calculated cross-correlation function, the maximum correlation peak height is detected leading to the estimation of the average particle displacement. The procedure is done in every interrogation area. The time between the two successive pictures is precisely known, as it is a parameter of the PIV acquisition, so that the velocity in every interrogation area is evaluated. A velocity field is therefore available after data processing.

The span-wise organization of the vortex street is investigated with the help of PIV measurements. With the laser sheet illuminating the whole span, Figure 7.5, velocity fields are obtained in the plane of the hydrofoil. A frequency doubled Q-switched Nd:YAG laser, *Gemini Research minilaser*, with a 5 ns pulse duration is used to generate the laser sheet.

The laser wavelength is 532 nm and the peak power of a single laser is 50 mJ/pulse. The temporal range of pulse separations of a single Q-switched laser is limited, the maximum rate being 10 Hz. The time between the two successive pulses required for PIV acquisition is set typically at 5 μs but depends on the free-stream velocity and the interrogation area size. The cylindrical lens produces a 1 mm thick laser sheet. Perpendicular to this plane, a high sensitive *Dantec highsens* camera, 12 bit resolution, with a 60 mm *Nikon* lens is placed. The seeding is ensured by 10 μm diameter hollow glass spheres. The acquisitions, *Dantec* software, are double frame, single exposure. The velocity field is derived from the cross-correlation of the two consecutive frames. The interrogation area size is 32x32 pixels with an overlap of 50%. The picture size is 1280x1024 pixels. A Gaussian window function is used to reduce the cyclic noise from the correlation map. It multiplies the greyscale values with a factor between 0 and 1 depending on the position in the interrogation area. A validation of the correlation peak is done with the relative height of the highest correlation peak to that of the second highest, factor 1.2. Acquisition can be trigged via TTL 5 V signal generated on the basis of the vortex-induced vibration signal.

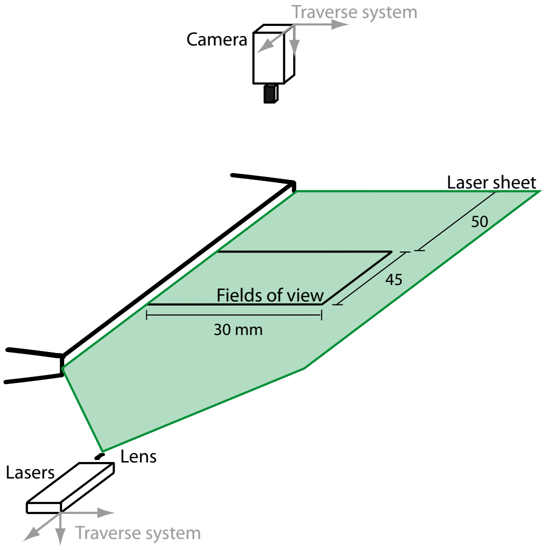

Figure 7.5: Principle measurement of Particle Image Velocimetry (PIV)

7.2.3 Double laser optical probe

A specific optical probe is developed to investigate the shedding frequency, the vortex advection velocity and the inter-vortex spacing for different wake cavitation development. As sketched in Figure 7.6, two parallel laser beams, *Spectra Physics R-33142*, 4 mm apart are set to cross the wake and thus are periodically interrupted by the cavitation vortex street. Two fast photodiodes, *Thorlabs FDS1010*, are placed to track the light beam intensities modulated by the passing cavities. The photodiodes give a periodic signal with a frequency which is twice the shedding frequency f_s. The probe is mounted on a traversing system, and measurements are performed at different locations in the wake.

The time delay $t_{correlation}$ necessary for the vortices to be advected from the position of the first laser beam to the position of the second is estimated with the help of the

Table 7.4: Properties of the PIV system

Specification	
Lasers type/class	Q-switched Nd:YAG / class IV
Lasers wave length	532 nm
Lasers pulse duration	5 ns
Lasers pulse peak power	50 mJ
High sensitive camera resolution	12 bit
Picture size	1280x1024 pixels
Particle type	Hollow glass spheres
Particle density	1100 kg/m^3
Particle size	10 μm

cross-correlation function. An estimate for the cross-correlation function of the values of $x(t)$ at time t and $y(t+\tau)$ at time $t+\tau$ is obtained by taking the product of the two values over the observation time T. The resulting product approach an exact cross-correlation function as T approaches infinity, [17]. That is,

$$C_{xy}(\tau) = \lim_{T\to\infty} \frac{1}{T} \int_0^T x(t)y(t+\tau)dt \tag{7.14}$$

The time delay $t_{correlation}$ is the specific time from the origin for which the maxima of the cross-correlation occurs. The distance separating the two laser beams d_{lasers} is known, so that the mean advection velocity of the vortices is,

$$C_{adv} = \frac{d_{lasers}}{t_{correlation}} \tag{7.15}$$

Using the measurements of the vortices advection velocity C_{adv} and their corresponding shedding frequencies f_s, the stream-wise inter-vortex spacing a_s is evaluated by

$$a_s = \frac{C_{adv}}{f_s} \tag{7.16}$$

The coherence function between the two signals is checked, equation (7.7).

Table 7.5: Properties of the double laser optical probe

Specification	
Lasers type/class	He:Ne / class III
Lasers wave length	633 nm
Lasers power	8 mW
Photodiodes rise time	45 ns
Photodiodes spectral response	$400 - 1100$ nm
Photodiodes bandwidth	8 MHz

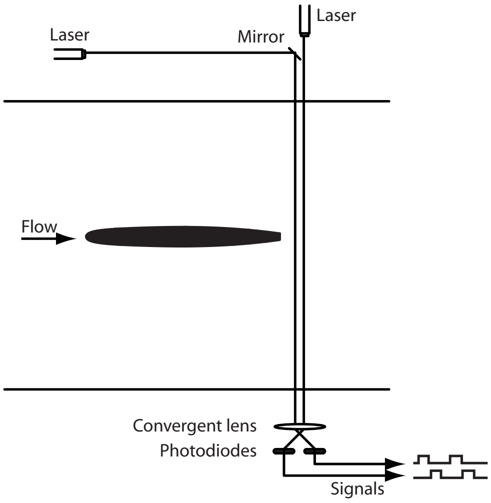

Figure 7.6: Sketch of the double laser optical probe

7.3 Flow visualization

7.3.1 Image acquisition and lighting system

The vortical cavitation structures in the hydrofoil wake are recorded using high-speed cinematography and short exposition still photographs. The video camera is a *Photron ultima APX*. The frame rate goes up to 2000 frames per second at full resolution, 1024x1024 pixels, and up to 120000 fps at reduced resolution. Typically, the CCD image resolution is 512x256 pixels at 10000 fps. The shutter speed can be set down to 4 μs. The buffer memory of the camera enables storing up to 8 GB of images. Triggering and synchronization with vibration measurements are achieved via a 5 V TTL signal. The scene is illuminated with two *Cordin* flash (model *359*) of 11 ms duration. For higher duration flow visualization, three 1000 W argon lamps are used as light sources, *Thorn lighting*. A *Nikon D100* digital camera is used for the still photographs. The flash is a *Chadwick-Helmuth Strobex* and is set to deliver a single pulse of light with a duration of 35 μs during the aperture time.

Table 7.6: Properties of high speed image acquisition and lighting systems

Specification	
High speed camera shutter speed	$4 - 1670$ μs
High speed camera frame rate	$1 - 12 \cdot 10^3$ fps
High speed camera max CCD resolution	1024x1024 pixels (up to $2 \cdot 10^3$ fps)
High speed camera buffer memory	8 GB
Flash lamps electric energy	1875 J
Flash lamps max pulse duration	11 ms
Lamps power	1000 W

Part III

Vortex cavitation

Chapter 8

Cavitation free

The results reported in this chapter and in the entire part III are related to the hydraulically smooth foil, section 6.2. Therefore, a natural turbulent boundary-layer transition can occur along the chord length. The effects of a tripped turbulent boundary layer on vortex shedding process are studied in part IV.

In cavitation free regime, the vortex-induced hydrofoil vibration is measured and analyzed for different free-stream velocities. The results are described in terms of vortex shedding frequency, normalized vortex shedding frequency and vibration amplitude. Time-frequency analysis is proposed. The hydrofoil eigen modes are identified. The vortex span-wise organization is studied with the help of PIV data. For both lock-off and lock-in conditions, traverse LDV measurements across the wake are carried out. The results are depicted in terms of time-averaged velocity profiles, velocity fluctuations and wake energies.

8.1 Vortex-induced vibration

8.1.1 Vortex shedding frequency and Strouhal number

The vortex-induced vibration are measured with the help of the laser vibrometer focused on the hydrofoil surface at $(x/L,\ z/B) = (0.8,\ 0.75)$. The waterfall spectra of the vibration signals are presented in Figure 8.1 for different free-stream velocities. Fast Fourier Transform is applied to 16 equal segments of the time signal and averaging is performed. The sampling frequency is 51.2 kHz and the block size 512 KSamples. In Figure 8.1 (a) and (b), the frequency f and the normalized frequency fh/C_{ref} are respectively displayed. Most of the spectral energy is concentrated around the vortex shedding frequency, which increases quasi-linearly with the free-stream velocity. As the vortex shedding frequency approaches one of the natural frequencies of the hydrofoil, the resonance takes place with a significant increase in vibration. A lock-in of the vortex shedding frequency onto the structural eigen frequency, $f_n = 890$ Hz, occurs and a plateau emerges, *i.e.* a constant shedding frequency for Reynolds number ranging from $Re_h = 35.4 \cdot 10^3$ to $41.9{\cdot}10^3$. For such conditions, the vibration amplitude of the hydrofoil trailing edge is large enough, so that its motion takes control of the instability mechanism that leads to vortex shedding and synchronizes the shedding frequency with the body motion frequency. Beside the lock-in, for which the hydrofoil vibration are maximized, two hydro-elastic couplings occur for Reynolds number values $Re_h = 29.0 \cdot 10^3$ and $90.2 \cdot 10^3$. Even if the resonances appear for these two flow conditions, so that the vibration levels are amplified, they are likely not high enough to force the shedding of the vortices at the eigen frequencies on a free-stream velocity range. For direct smaller or higher free-stream velocities, the hydro-elastic couplings are disabled and the vortex shedding frequency free to follow the Strouhal behavior.

The vortex shedding frequency f_s corresponding to the frequency of the dominating peak in the spectrum at the given free-stream velocity is plotted in Figure 8.2 (a) as a function of the free-stream velocity. A quasi-linear relationship between the vortex shedding frequency and the velocity is observed, provided that no hydrofoil resonance frequency is excited. The normalized shedding frequency, the Strouhal number $St_h = f_s h/C_{ref}$, is shown in Figure 8.2 (b). The Strouhal number is not constant over the entire free-stream velocity range, the trend being descending for increasing free-stream velocity. This is believed to be due to the thickening of the boundary layer at the trailing edge with increasing free-stream velocity. As turbulent boundary-layer transition occurs along the chord length, its location moves upstream towards the leading edge for increasing free-stream velocity, which leads to a thickening of the trailing-edge boundary layer. Analysis of boundary-layer flow are presented in chapter 11. Moreover, normalized vortex shedding frequency using characteristic scales of wake formation instead of body dimensions and free-stream velocity is studied in chapter 15.

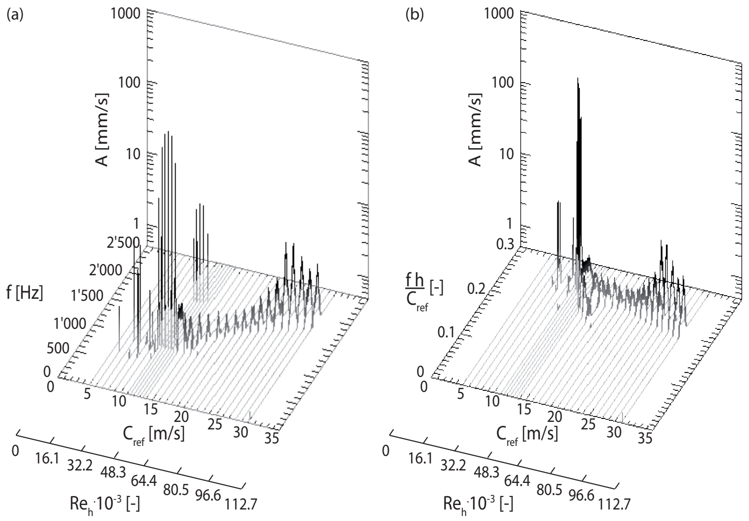

Figure 8.1: Waterfall spectra of the vortex-induced vibration signals, measured at $(x/L,\ z/B) = (0.8,\ 0.75)$, for different free-stream velocities. Cavitation free regime.

8.1.2 Vibration amplitude

The vortex-induced vibration signals for both lock-off, $Re_h = 64.4 \cdot 10^3$, and lock-in conditions, $Re_h = 38.6 \cdot 10^3$ are shown in Figure 8.3. The corresponding spectra are also presented. As the vibration signal is virtually sinusoidal for lock-in condition, the time trace for lock-off displays amplitude modulation resulting from intermittent weak shedding cycles. Three dimensional vortex shedding process and vortex dislocations

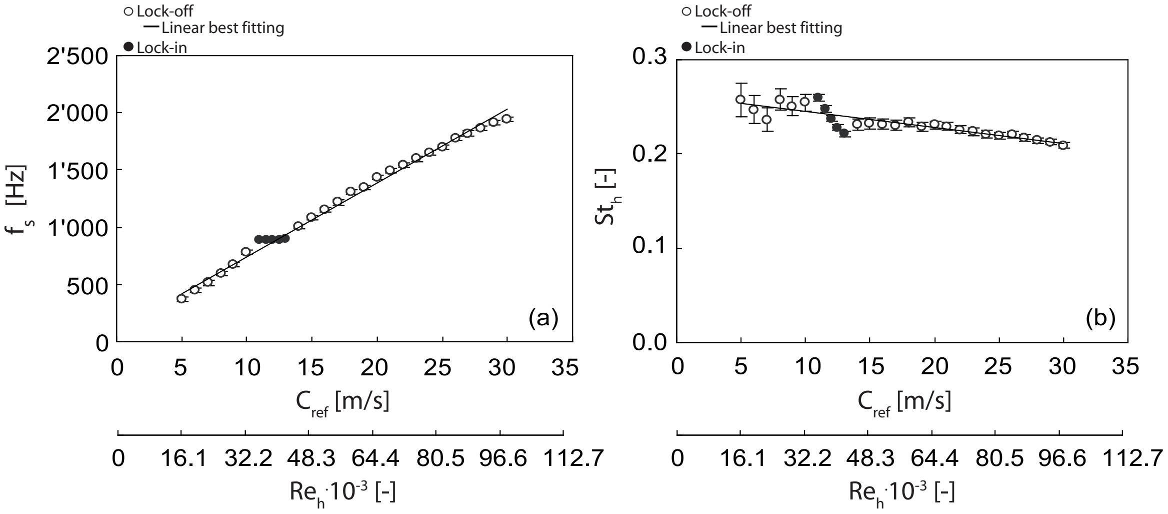

Figure 8.2: (a) Vortex shedding frequency and (b) Strouhal number for different free-stream velocities. Cavitation free regime.

obviously occur for such a condition. As a result, the vibration spectra are sharply peaked for lock-in condition and broad band for lock-off. In addition to the energy at the vortex shedding frequency, the spectra for lock-off condition shows energy at three hydrofoil eigen frequencies, the lock-in frequency being the most evidenced. As developed in appendix C for a body oscillator represented as a discrete mass, free to oscillate with one degree of freedom, linearly damped and supported by a linear spring, if the excitation spectra is broad band so that specific energies occur at the eigen frequencies of the structure, the vibration amplitudes at these frequencies will be significantly amplified because associated with peak value of the magnification factor.

Figure 8.4 presents the vibration amplitude of the hydrofoil, for different free-stream velocities. The amplitude is chosen to be the standard deviation of the displacement velocity band-pass filtered around the shedding frequency. Estimation of the standard deviation is done in the frequency domain accordingly to the Parseval theorem which denotes the energy conservation between the time and the frequency domains [17],

$$\int_{-\infty}^{+\infty} |x(t)|^2 \, dt = \frac{1}{2\pi} \int_{-\infty}^{+\infty} |X(f)|^2 \, df \tag{8.1}$$

where $X(f)$ is the Fourier transform of $x(t)$, equation (7.5). In Figure 8.4, the logarithmic scale enhances the evolution of the vibration amplitude for lock-off conditions. The vibration amplitude is maximized for lock-in, with an ascending and descending branch for increasing free-stream velocity. In comparison with lock-off conditions, the vibration levels are amplified for the two hydro-elastic couplings.

The hydrofoil vibration amplitude for lock-off condition are negligible in comparison with the hydrofoil trailing edge thickness. At the shedding frequency, the vibration is of micrometer-order amplitude. In the experimental configuration, Figure 6.4, the hydrofoil is embedded on one side while it is pivot embedded on the other side. This configuration

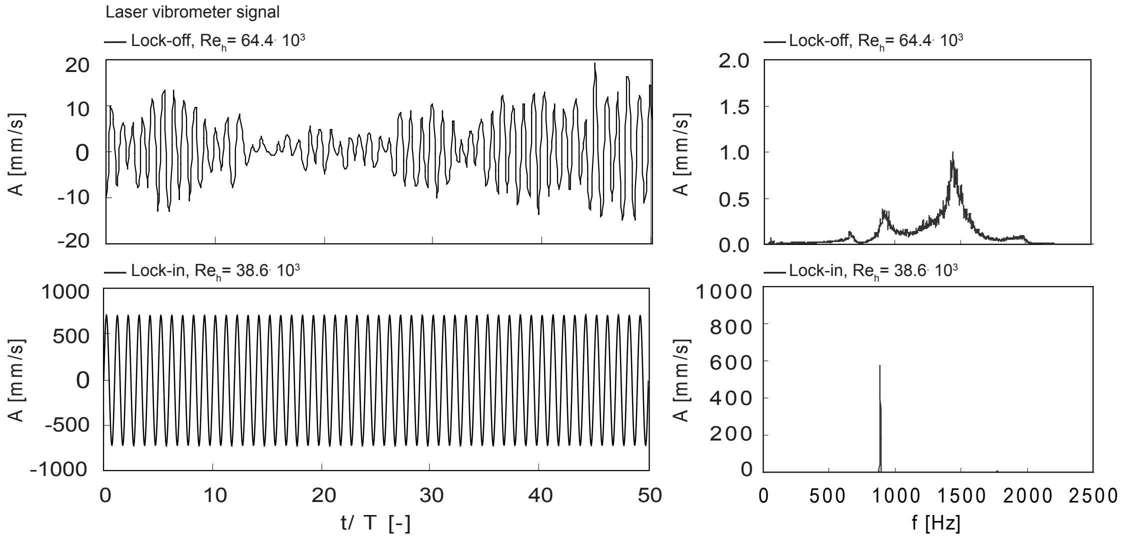

Figure 8.3: Vortex-induced vibration signals and spectra, measured at $(x/L,\ z/B) = (0.8,\ 0.75)$, for lock-off and lock-in conditions. Cavitation free regime.

leaves freedom to the hydrofoil to oscillate in torsion mode. Despite the low level of vibration outside the lock-in conditions, one may question the effect of vibration on the vortices generation mechanism. We modify the experimental case study by embedding both sides of the hydrofoil, Figure 8.5.

The vortex shedding frequencies derived from the flow-induced vibration measurements are presented in Figure 8.6 as a function of the free-stream velocity. According to the hydrofoil embedment modification, the eigen frequencies and modes are changed. The lock-in of the vortex shedding frequency in a range of upstream velocity does not occur anymore. Nevertheless and for lock-off condition, no modification of the vortex shedding frequency is observed for the two configurations. Furthermore and for the original hydrofoil setup, the normalized standard deviation of the hydrofoil displacement velocity ($A_{stdv}/C_{ref} = 0.03\%$) is found to be well below the normalized free-stream velocity fluctuation measured at the inlet of the test section ($C_{x_{stdv}}/C_{ref} = 1\%$), section 6.1. Thus, the measurements reported for lock-off condition are free of hydrofoil vibration contamination.

8.1.3 Time-frequency analysis

Amplitude modulation in the vortex-induced vibration signal and broad band spectrum typically occurs for lock-off condition, Figure 8.3. In the Fourier transform of the time signal $x(t)$,

$$X(f) = \int_{-\infty}^{+\infty} x(t) e^{-j2\pi f t} dt \tag{8.2}$$

the Fourier coefficients are computed as inner products of the signal with sinusoidal waves $e^{-j2\pi f t}$ of infinite duration. As a result, the Fourier analysis has sense if $x(t)$ is a stationary signal, that is a signal whose properties do not evolve in time. However, any

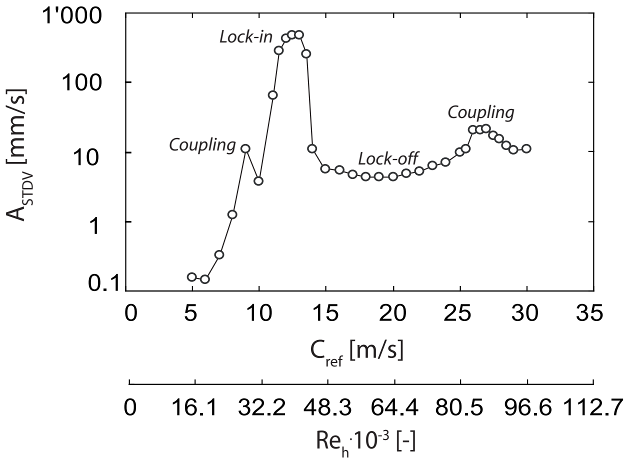

Figure 8.4: Vortex-induced vibration amplitude of the hydrofoil at location $(x/L,\ z/B) = (0.8,\ 0.75)$ for different free-stream velocities. Cavitation free regime.

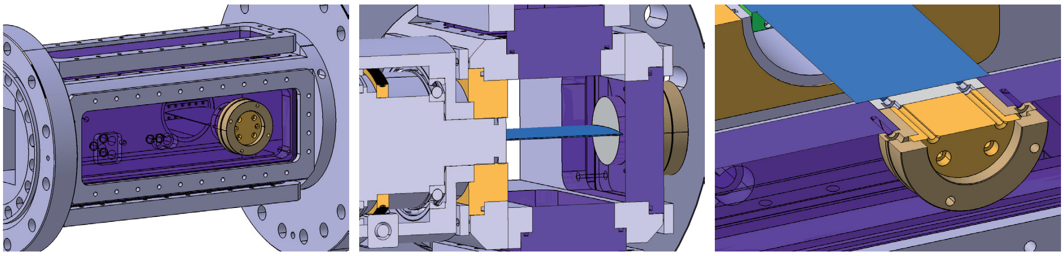

Figure 8.5: Hydrofoil setup modification: Hydrofoil embedment in the test section

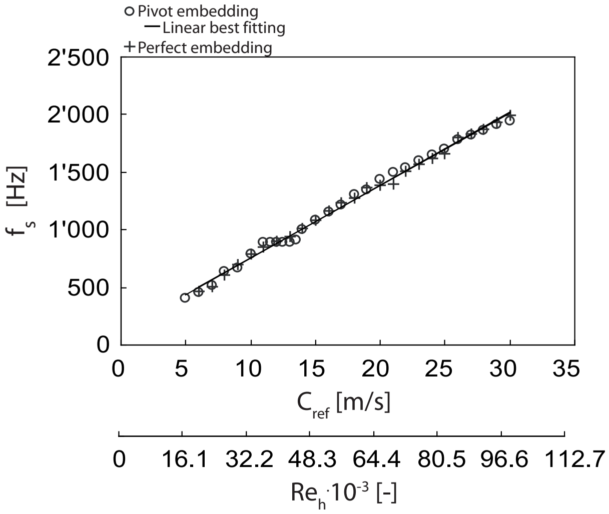

Figure 8.6: Vortex shedding frequency for different free-stream velocities and for the two hydrofoil mountings (Figures 6.4 and 8.5)

abrupt change in time in $x(t)$ is spread out over the whole frequency axis in $X(f)$. This global mix of information makes it difficult to analyze any local property of $x(t)$ from $X(f)$, [89]. For non-stationary signal, a two-dimensional time-frequency representation $S(t, f)$ is needed and composed of spectral characteristics depending on time. The Fourier transform is applied to a short time-period of the signal resulting in an estimate of the frequency content of the signal over that time-period. This estimate is assumed to represent the frequency content of the signal at the center of the window, so that by moving the window in time and repeating the process, an estimate of the time-frequency content is built up. The technique is termed short-time or windowed Fourier transform,

$$STFT\,X(f) = \int_{-\infty}^{+\infty} x(t)g(t-\tau)e^{-j2\pi ft}dt \tag{8.3}$$

where the windowed Fourier atom is constructed with a window g translated by τ and modulated by the frequency f,

$$g_{f,\tau}(t) = g(t-\tau)e^{j2\pi ft} \tag{8.4}$$

The limitation of using the short-time Fourier transform to calculate the frequency content of a signal is that it is based on the assumption that the signal is stationary in the considered window. It is therefore desirable to reduce the length of the time-period. However, reducing the window width increases the time resolution but reduces the frequency one, Heisenberg uncertainty [74]. The uncertainty is minimum when g is a Gaussian, in which case the atoms $g_{f,\tau}$ are called Gabor functions.

The short-time Fourier transform of the vortex-induced vibration signals is computed. Part of the time signal is considered, 64 Ksamples. With a window size of 4 Ksamples and an overlapping of 90% of the window width, the time and frequency resolutions are 1 Hz and 0.001 s respectively. The time-frequency representation is shown in Figure 8.7 for both lock-off and lock-in conditions. For every flow condition, the time signal and the averaged spectrum are shown besides the spectrogram. For lock-in condition, $Re_h = 38.6 \cdot 10^3$, the time signal is virtually sinusoidal and free from any amplitude modulation. As a result, the spectrogram does not reveal any change with the time. The harmonic of the eigen frequency is revealed. For lock-off conditions, severe amplitude modulation is shown. In the spectrograms, the vortex shedding frequency is progressively detached from the lock-in frequency for increasing free-stream velocity. For $Re_h = 45.1 \cdot 10^3$, the hydrofoil response frequency is broad band so that any distinction between the vortex shedding frequency and the hydrofoil eigen frequency is difficult to make. Even if the vortex shedding frequency is higher than the lock-in frequency, specific energies occur at the eigen frequencies of the structure, so that the vibration amplitudes at these frequencies are significantly amplified because associated with peak value of the magnification factor, appendix C. For $Re_h = 64.4 \cdot 10^3$, the lock-in and vortex shedding frequencies are decoupled and the intermittency of the vortex shedding process is clearly evidenced in the spectrogram. At the same frequency, cells of significant vibration amplitude are followed by ones of negligible amplitude. Moreover, cells of significant vibration amplitude coexist at the same time at different frequency around the primary vortex shedding frequency. The vortex-induced vibration integrating the pressure fluctuation along the entire span, vortex cells of different shedding frequency obviously occur along the span. As a result, the average spectrum is broad band around the primary vortex shedding frequency.

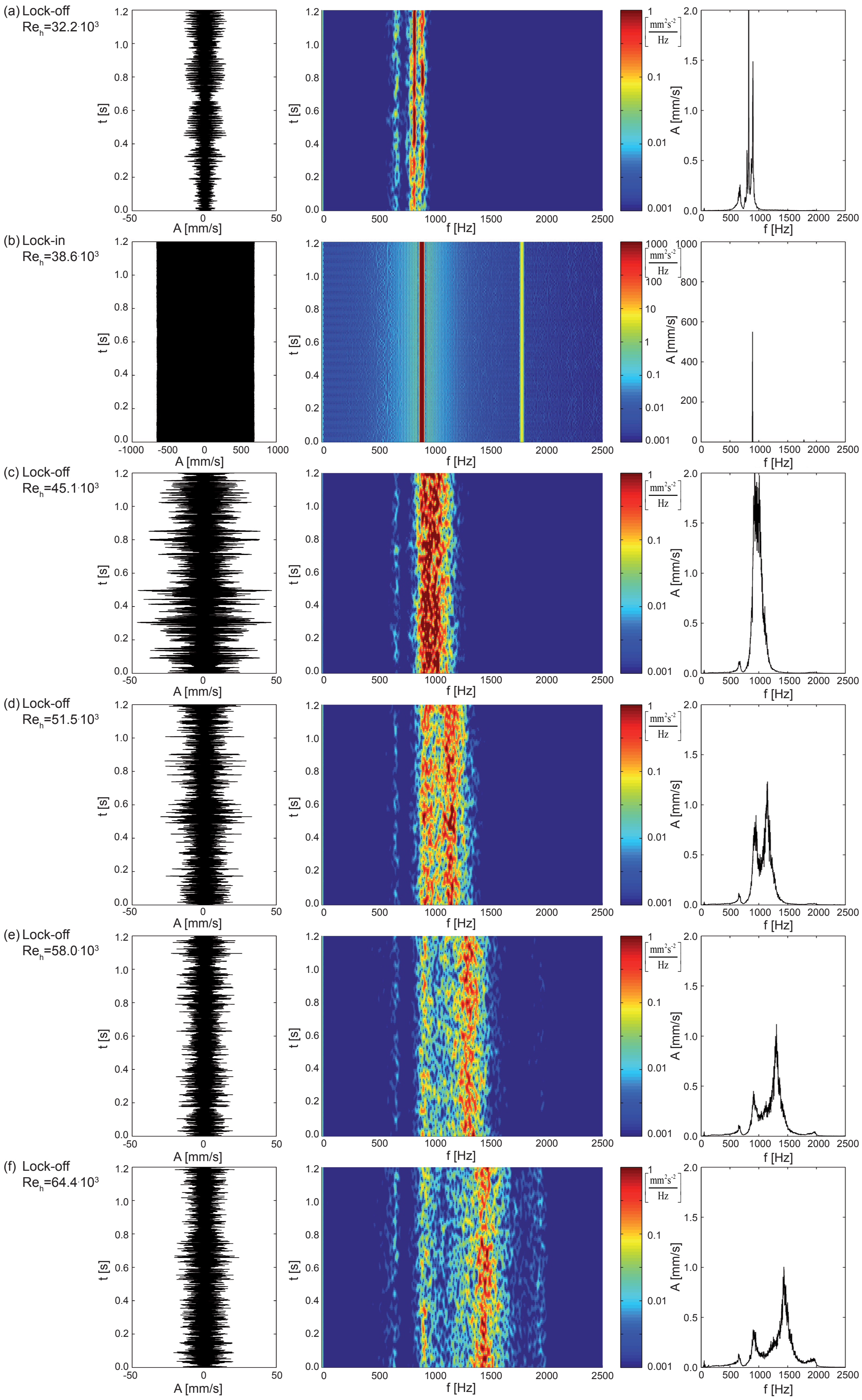

Figure 8.7: Time signal, spectrogram and averaged spectrum of the vortex-induced vibration signal, for lock-off and lock-in conditions. Cavitation free regime.

8.1.4 Hydrofoil eigen modes

For the detected lock-in and hydro-elastic coupling conditions, the hydrofoil wall vibration is surveyed by laser vibrometer measurements. The methodology is described in section 7.1. Parts of the hydrofoil upper surface are not measurable due to optical access constraints. Laser vibrometer measurements are synchronized with the accelerometer signal used as a reference for the phase. In Figure 8.8, the eigen modes are displayed through wall displacement amplitude and phase. Interpolation between the measurement points is performed. Non-significant vibration amplitude areas result from the hydrofoil perfect embedding on one side. Figure 8.8 (a) evidences the 1^{st} hydrofoil bending mode: The displacement phase is virtually constant on the measured surface and the amplitude increases for increasing distance along the span from the perfect to the pivot embedding sides. Figure 8.8 (b) displays the 1^{st} torsional mode: A neutral fiber occurs along the span at mid-chord. Maxima of the vibration amplitude occur at the leading and trailing edges and are up to 0.2 mm. The peak to peak trailing edge displacement is therefore up to 0.4 mm which is $0.12h$. The leading and trailing edges are in phase opposition; the 180° phase shift occurring along the span at mid-chord. Figure 8.8 (c) shows the 2^{nd} bending mode. The leading and trailing edges are in phase. A 180° phase shift occurs along the span at $z/B = 0.66$.

The maximal wall displacement is shown to occur for the first torsional mode. The order of magnitude is about 10 times higher for this eigen mode than for the first and the second bending modes. Figure 8.2 evidenced that a lock-in of the vortex shedding frequency in a wide range of free-stream velocity occurs only for the torsional mode. Figure 8.4 also displayed that the vibration amplitude is maximized for the lock-in condition. Therefore, one concludes to the affinity of the torsional mode with the lock-in phenomenon for two combined reasons. First and considering the boundary conditions applied to the hydrofoil, the torsional mode is the eigen mode for which the wall displacement amplitude is maximized. Moreover, the maxima displacement amplitude for the torsional mode occur at the leading and trailing edges and the trailing edge motion is in phase along the entire span. Therefore, the wall displacement interact intensively with the rolling-up of the vortices. The generation mechanism of the vortices is then influence by the transverse trailing edge motion and the lock-in emerges.

Table 8.1 summarizes the eigen modes and frequencies. The flow conditions for which resonances occur are also specified.

Table 8.1: Hydrofoil eigen modes, frequencies and flow conditions

Eigen mode	f_n [Hz]	Re_h [$-$]
First bending mode	660	$29.0 \cdot 10^3$
First torsional mode	890	$38.6 \cdot 10^3$
Second bending mode	1860	$90.2 \cdot 10^3$

In section 6.2.3, the eigen frequencies of a uniform straight bar with solid and rectangular section, are estimated. The cases of torsional and bending modes are investigated and the added mass effects are taken into account. The equations for the natural frequencies

(a) First bending mode: Re_h=29.0·10^3, f_n=660 Hz

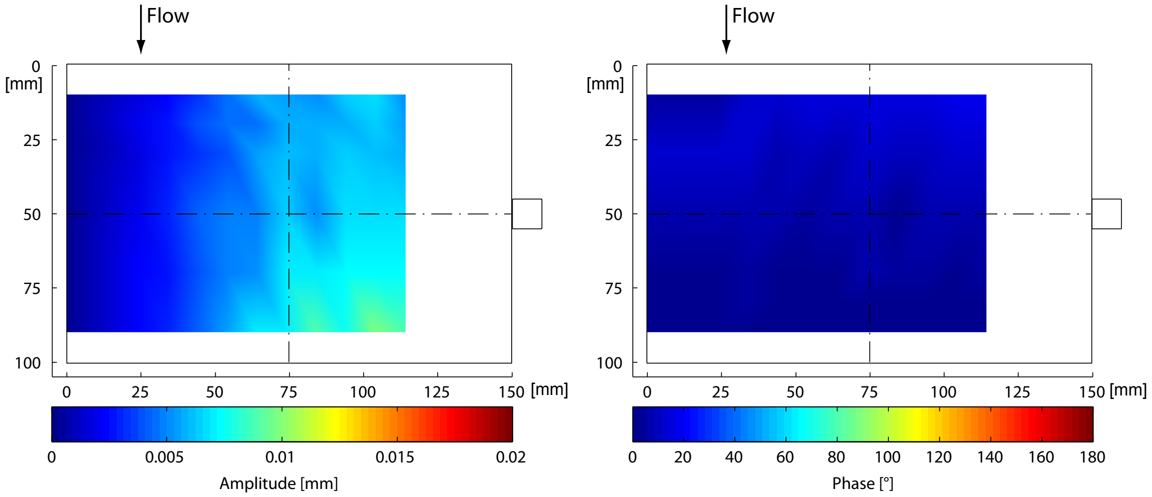

(b) First torsional mode: Re_h=38.6·10^3, f_n=890 Hz

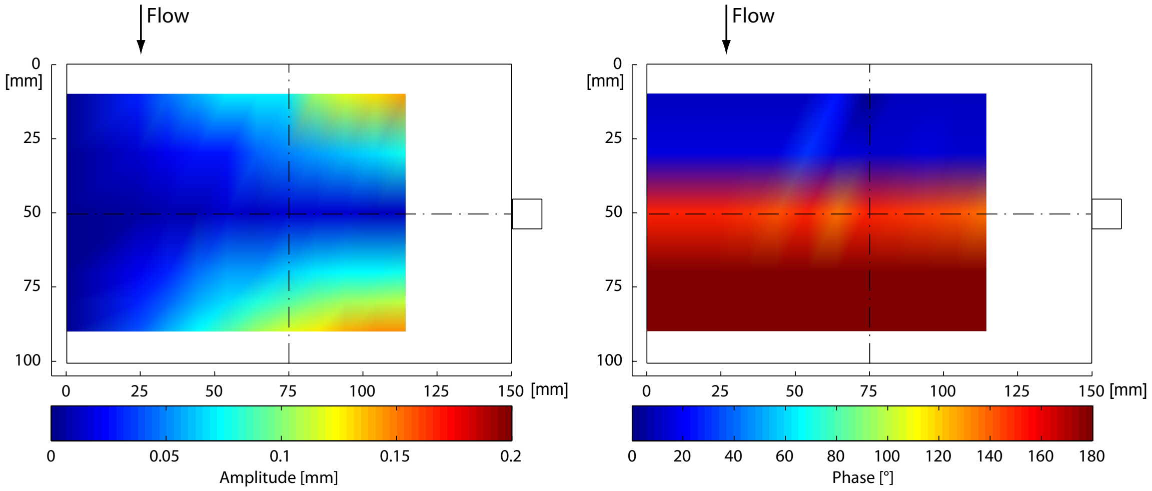

(c) Second bending mode: Re_h=90.2·10^3, f_n=1860 Hz

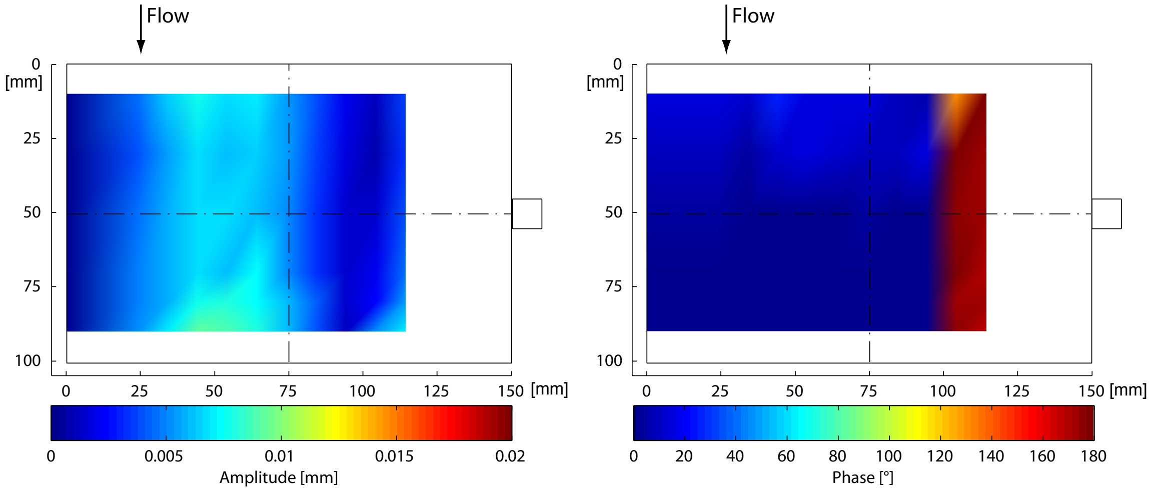

Figure 8.8: Survey of the hydrofoil wall vibration: (a) First bending mode, (b) first torsional mode and (c) second bending mode

in air are below recalled,

$$f_{torsion} = \frac{N_n}{2\pi}\sqrt{12\frac{G\beta}{\rho}\frac{h^2}{b^2(l^2+h^2)}}\,, \qquad f_{bending} = \frac{N_n}{2\pi}\frac{h}{b^2}\sqrt{\frac{E}{12\rho}} \tag{8.5}$$

where G, E, β and ρ are respectively the modulus of elasticity in shear, the Young modulus, the factor dependent on the ratio l/h and the density of the material. The length of the bar is b and the thickness and the width of its cross-section are respectively h and l. N_n is a constant referring to the mode of vibration and to the boundary conditions. Considering the added mass effects, equations (6.13) and (6.15), and applying dimensions and material properties of our case study, the analytical eigen frequencies are summarized in Table 8.2. The frequency of the first torsional mode is in accordance with the experiments. The difference is less than 5%. Besides, significant discrepancies are found for the first and second bending modes. The differences are believed to be due to the hydrofoil pivot embedding. For the analytical solution, the bar is let free on this side. When the bar is fixed on both sides, the eigen frequencies are respectively multiplied by a factor 6.36 and 2.80 due to the increases of the N_n factors, [90]. Nevertheless, no N_n factors were found in the literature for a pivot embedding of part of the bar section.

Table 8.2: Analytical uniform straight bar eigen modes and frequencies, one end fixed the other free

Eigen mode	f_n [Hz]
First bending mode	253
First torsional mode	846
Second bending mode	1581

8.2 PIV velocity fields

The span-wise organization of the vortex street is investigated with the help of PIV data in the hydrofoil wake. With the laser sheet illuminating the whole span, velocity fields are obtained in the plane of the hydrofoil. The experimental setup is described in section 7.2. Both lock-off and lock-in conditions are investigated.

8.2.1 Lock-off condition

Typical instantaneous velocity fields in the hydrofoil wake are presented in Figure 8.9 for lock-off condition, $Re_h = 64.4 \cdot 10^3$. The wake stream-wise velocity C_x is scaled by the free-stream velocity C_{ref}. It appears that the wake structures exhibits three-dimensional vortex shedding mode. The shedding process is indeed not in phase along the span. The four selected velocity fields, which are typical of the wake structure, reveal different vortex street patterns. The 3D instability does not occur at the same position along the span but is a random process. As a result, the three-dimensional vortex shedding mode is contributing strongly to a modulation of the vortex-induced vibration signal, Figure 8.3.

The relation between the vortex-induced vibration level and the vortex span-wise organization is next investigated. Figure 8.10 displays three typical instantaneous velocity fields and their corresponding vortex-induced vibration signal. The presented velocity field is the one at the origin of the time. The velocity fields reveal parallel vortex shedding, the shedding being in phase along the span. Nevertheless, some vortex breakdown appear and the coherent length is obviously shorter than the field of view. However, a direct relationship is observed between the vortices span-wise organization and the vortex-induced vibration level. For parallel-vortex shedding mode, the fluctuating force on the body is maximized and the vibration level is significantly increased. In contrast, for three-dimensional vortex shedding, the vibration level is reduced.

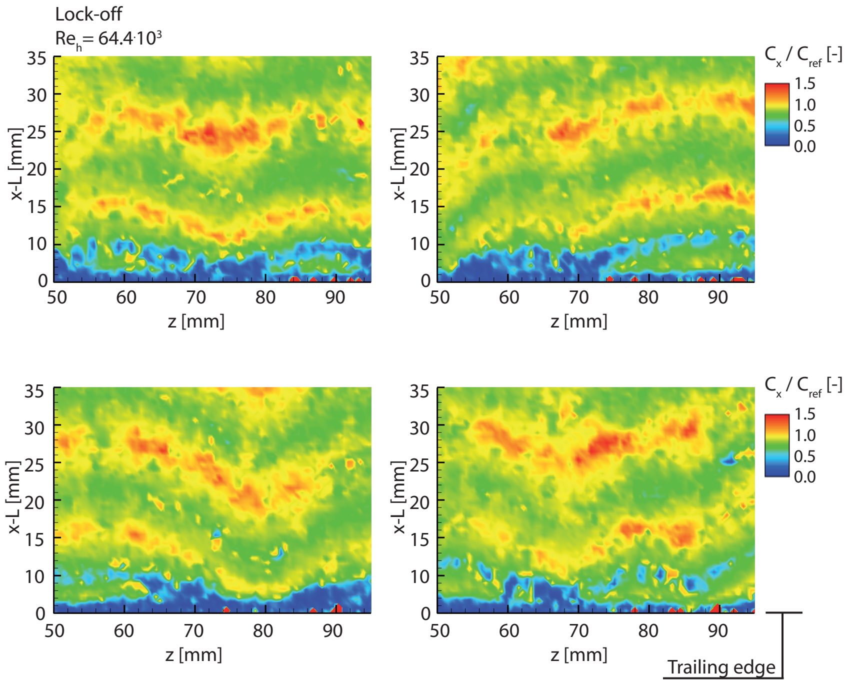

Figure 8.9: Typical instantaneous velocity fields in the hydrofoil wake for lock-off condition, $Re_h = 64.4 \cdot 10^3$ ($z = 0$ mm). Cavitation free regime.

8.2.2 Lock-in condition

For lock-in condition, $Re_h = 38.6 \cdot 10^3$, when the torsional mode is excited, Figure 8.8 (b), the transverse motion of the trailing edge significantly enhances the vortex span-wise organization. Parallel vortex shedding takes place as evidenced in Figure 8.11. In comparison with lock-off condition, the vortex structures are less diffused.

Figure 8.12 presents typical instantaneous velocity fields in the hydrofoil wake for resonance condition, first bending mode, Figure 8.8 (a). The wake structures reveal parallel vortex shedding. Nevertheless, some vortices breakdowns occur and the vortex structures are not as compact as for the torsional mode.

The instantaneous velocity fields in the hydrofoil wake for resonance condition, second bending mode, Figure 8.8 (c), reveal oblique vortex shedding process, Figure 8.13. Unlike

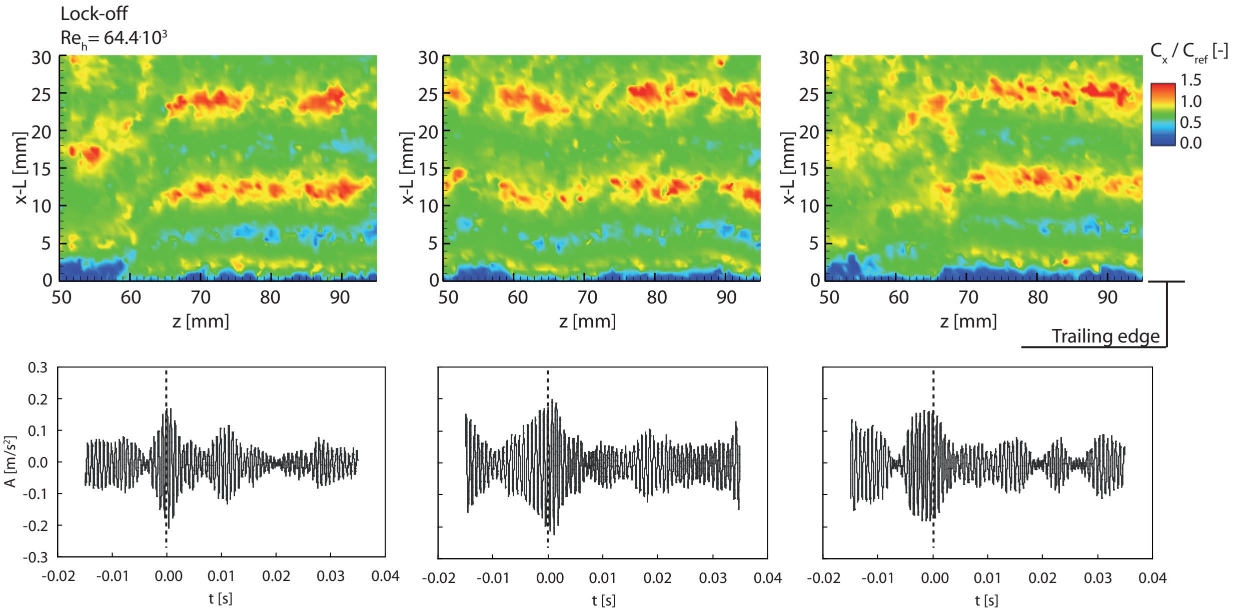

Figure 8.10: Typical instantaneous velocity fields in the hydrofoil wake for lock-off condition $Re_h = 64.4 \cdot 10^3$ ($z = 0$ mm). Acquisitions conditioned by the vortex-induced vibration level. Cavitation free regime.

the torsional or first bending modes, the trailing edge displacement along the span is not in phase and oblique vortex shedding occurs with positive or negative angle. Transition between the two angles is done by parallel vortex shedding. Description of the vortex shedding arises from experiments with a less stiff hydrofoil, appendix A.1. The vortex generation process in the case of a second bending mode is presented in Figure A.1. The vibration amplitude is macroscopic, millimeter-order amplitude. A neutral fiber is located at about $z/B = 0.66$ so that the hydrofoil wall motions apart from this line are in phase opposition. The body motion phase opposition leads to two vortex cells. The vortex shedding frequency of the two cells is identical and equal to the eigen frequency of the hydrofoil. However, their generation and advection are in phase opposition. The identical signed vorticity lines of the two vortex cells, revealed by the cavitation, are linked at the span-wise position of the neutral fiber. At this location and due to the phase opposition, oblique vortex shedding occurs. Therefore, the vorticity lines are not dislocated at the position of the neutral fiber but bent so that they remains continuous along the span. The situation is however ambiguous and oblique vortex shedding at the neutral fiber position can occur with positive or negative angle depending on the linked vorticity lines. It is believed that this phenomenon also occurs in the case of the stainless steel hydrofoil where oblique vortex shedding occurs on a large fraction of the span.

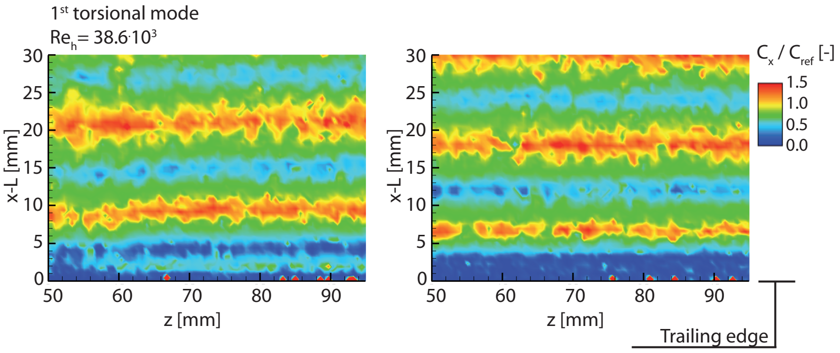

Figure 8.11: Typical instantaneous velocity fields in the hydrofoil wake for lock-in condition, first torsional mode, $Re_h = 38.6 \cdot 10^3$ ($z = 0$ mm). Cavitation free regime.

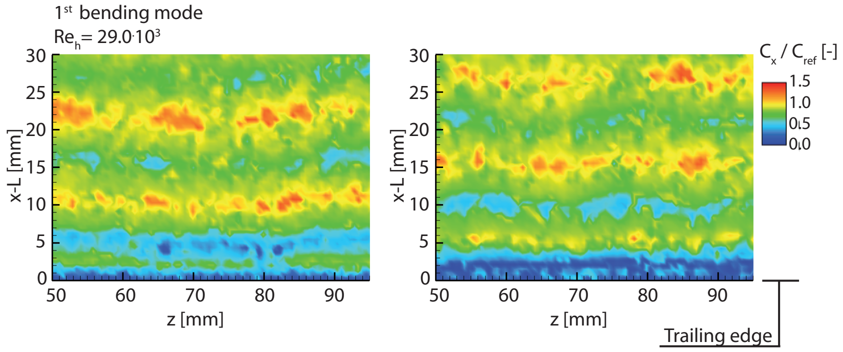

Figure 8.12: Typical instantaneous velocity fields in the hydrofoil wake for resonance condition, first bending mode, $Re_h = 29.0 \cdot 10^3$ ($z = 0$ mm). Cavitation free regime.

8.3 LDV velocity profiles

8.3.1 Time-averaged velocity profiles

Figure 8.14 illustrates, for lock-off and lock-in conditions, torsional mode, the wake flow measurements at different stations, from $x = L+h$ to $L+10h$, downstream from the trailing edge. The normalized mean (a) stream-wise and (b) transverse velocity profiles are shown as well as their fluctuations (c) and (d). For clarity, the profiles are shifted on the horizontal axis accordingly to the position from the trailing edge.

The maximum stream-wise velocity defect is higher for lock-in than for lock-off conditions, Figure 8.14 (a). This is largely due to the traverse motion of the trailing edge for lock-in which thickens the wake. Moreover, the increase of the vortex strength for lock-in condition likely increases the backflow (negative stream-wise velocity) on the wake centerline. As the flow progresses downstream, the velocity defect is reduced. The evolution of the velocity defects with downstream distance from trailing edge is presented in Figure 8.15.

The stream-wise velocity fluctuations are characterized by peaks produced by the passing of the vortices, as shown in Figure 8.14 (c). For lock-off conditions, these peaks move

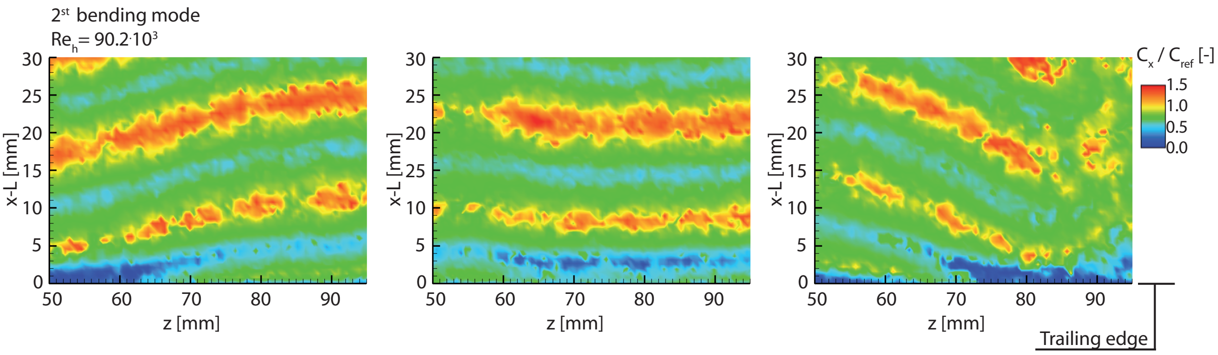

Figure 8.13: Typical instantaneous velocity fields in the hydrofoil wake for resonance condition, second bending mode, $Re_h = 90.2 \cdot 10^3$ ($z = 0$ mm). Cavitation free regime.

outward from the center line and weaken in intensity with increasing distance from the trailing edge. For lock-in, the peaks move slightly towards the center of the wake with increasing fluctuation. Afterwards, they moved outwards from the center line and weakens in intensity. The maxima of stream-wise velocity fluctuations with downstream distance from the trailing edge are shown on Figure 8.16 (a). The increases in the normalized velocity fluctuations in the context of the lock-in as compared to lock-off condition are from 10.1% for $x = L+1h$ up to 86.7% for $x = L+4h$. In addition to the increase in maximum fluctuations, the characteristic shape of the stream-wise velocity fluctuations, which defines the wake width, are held farther from the trailing edge for lock-in as compared to lock-off condition, Figure 8.14 (c). The station $x = L + 3h$ is the last position where the above-mentioned characteristic shape is recognizable for the lock-off condition, which is still the case at $x = L + 10h$ for lock-in. The increase of this distance downstream of the trailing edge indicates a reduction of the vorticity dissipation. The three-dimensional aspect of the vortex street for lock-off also plays a key role in the sense that the characteristic shape is no more recognizable for small distances from the trailing edge. As illustrated in Figures 8.9 and 8.11, it was shown that the vortex span-wise organization is significantly greater for lock-in as compared to lock-off. Moreover, beside the maximum stream-wise velocity fluctuation which occur at the immediate neighborhood of the core edges farthest from the centerline, Figure 5.1, the lock-in condition displays a second local maximum in the near wake. This position is the vertical coordinate of the vortex core edges nearest from the centerline. For increasing distance from the trailing edge, the local maxima of the upper and lower rows converge and merge on the centerline.

Figure 8.14 (b) and (d) present transverse mean velocity profiles and fluctuations. A significant increase in the transverse velocity fluctuations is observed for lock-in as compared to lock-off. The maximum fluctuation at each station is plotted on Figure 8.16 (b).

Wake energies

As defined by Roshko [92], the stream-wise and transverse energy intensities of the flow at a given point are $(C_{x_{stdv}}/C_{ref})^2$ and $(C_{y_{stdv}}/C_{ref})^2$ respectively. The integrals of the intensities over a line normal to the wake are called the wake stream-wise and transverse

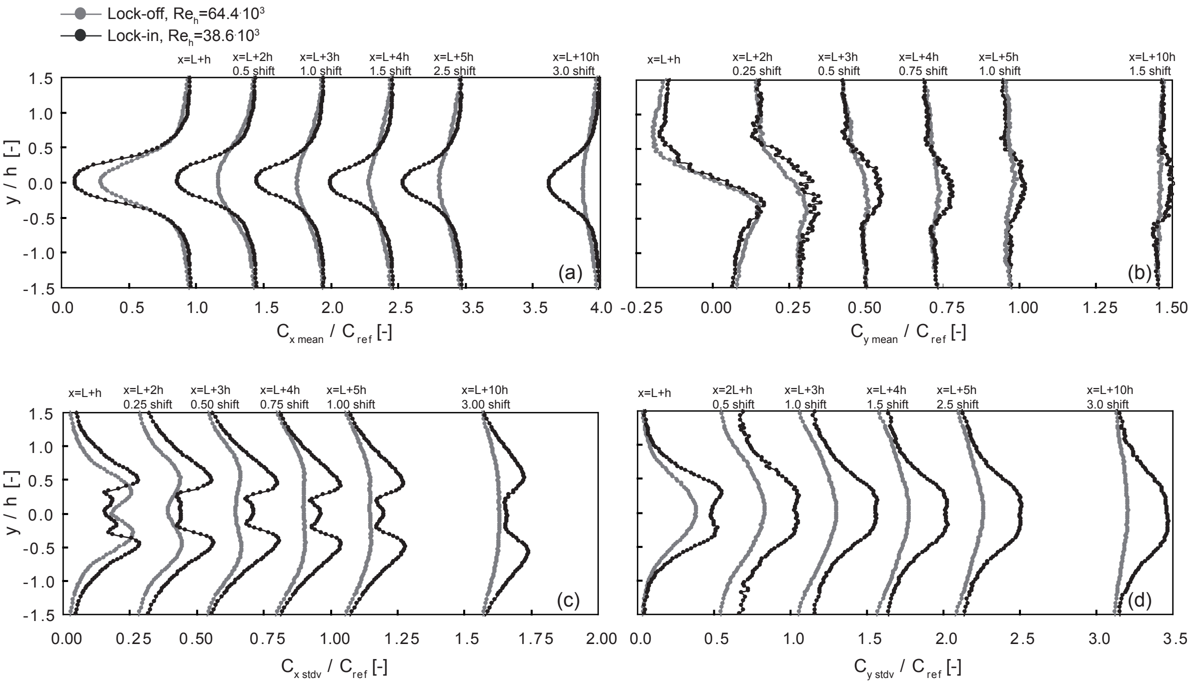

Figure 8.14: Wake flow measurements at different stations downstream from trailing edge for lock-off, $Re_h = 64.4 \cdot 10^3$, and lock-in, torsional mode $Re_h = 38.6 \cdot 10^3$, conditions: Normalized mean (a) stream-wise and (b) transverse velocity profiles and (c) stream-wise and (d) transverse velocity fluctuations

energies, their sum being the total wake energy:

$$E_x = \int_{-\infty}^{\infty} \left(\frac{C_{x_{stdv}}}{C_{ref}} \right)^2 d\left(\frac{y}{h}\right), \qquad E_y = \int_{-\infty}^{\infty} \left(\frac{C_{y_{stdv}}}{C_{ref}} \right)^2 d\left(\frac{y}{h}\right) \tag{8.6}$$

$$E = E_x + E_y \tag{8.7}$$

The wake stream-wise, transverse and total energies are presented in Figure 8.17. With increasing distance from the trailing edge, a decay in energies for lock-off condition occurs. For lock-in, the energies are maximized at $x = L + 2h$. Downstream from this position, the decay appears. In comparison with lock-off, the energies are significantly higher for lock-in condition.

For lock-in condition, phase-averaged velocity profiles are presented in appendix A.2.

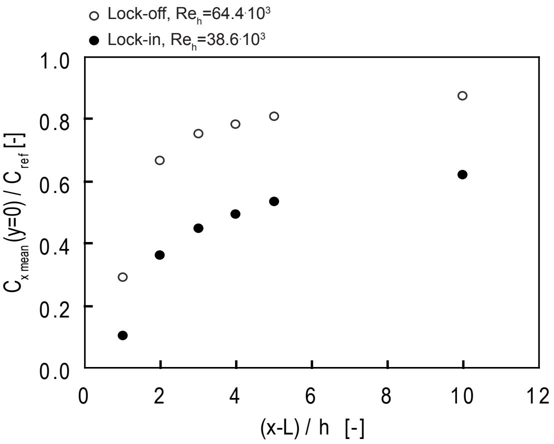

Figure 8.15: Maximum stream-wise velocity defect for measurement across the wake at different stations downstream from the trailing edge for lock-off, $Re_h = 64.4 \cdot 10^3$, and lock-in, torsional mode $Re_h = 38.6 \cdot 10^3$, conditions

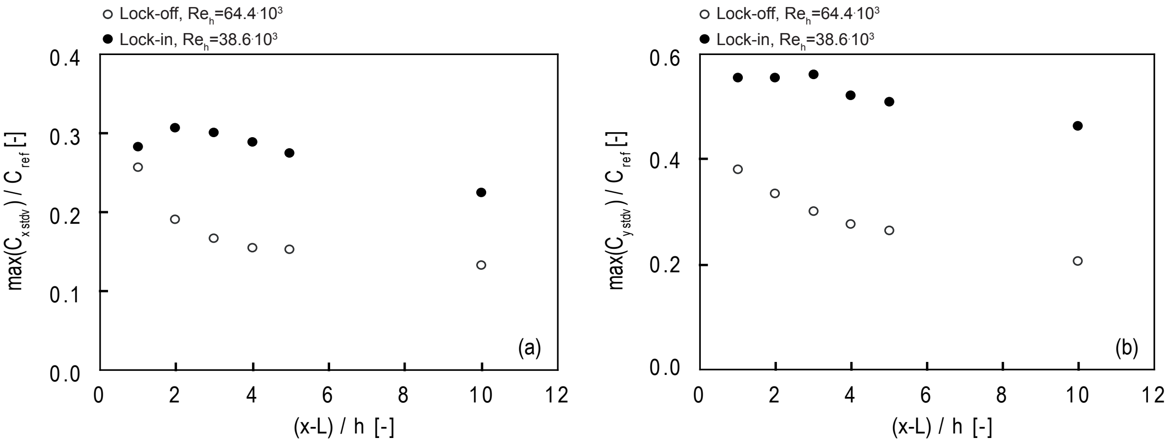

Figure 8.16: Maximum (a) stream-wise and (b) transverse velocity fluctuations for measurement across the wake at different stations downstream from trailing edge for lock-off, $Re_h = 64.4 \cdot 10^3$, and lock-in, torsional mode $Re_h = 38.6 \cdot 10^3$, conditions

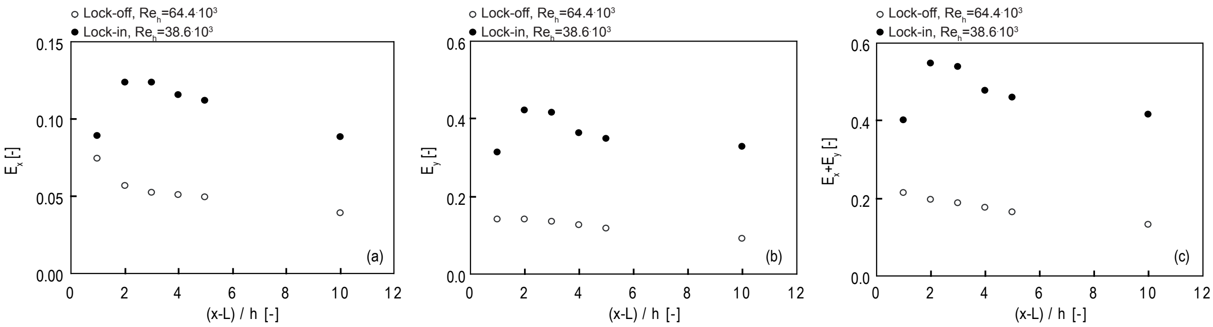

Figure 8.17: Wake (a) stream-wise (b) transverse and (c) total energies at different stations downstream from trailing edge for lock-off, $Re_h = 64.4 \cdot 10^3$, and lock-in, torsional mode $Re_h = 38.6 \cdot 10^3$, conditions

Chapter 9

Cavitation inception

Bubbles are initiated in the individual vortices centers, where the minimum pressure is reached. Models for cavitation inception in the wake of bluff bodies are found in the literature [5] and [16]. The method, based on the known pressure distribution for Rankine model, leads to a linear $\sigma_i \sim \sqrt{Re_h}$ law, which correctly predicts the correlation between the cavitation inception index and the Reynolds number for the considered range of free-stream velocities. Although successful in describing the cavitation inception for fixed bluff bodies, none of these studies provides a direct insight into the role of the trailing edge vibration on the cavitation occurrence.

9.1 Detection

In the present case study, the cavitation inception is detected visually. No significant hysteresis between cavitation incipience and desinence are observed and is due to presence of sufficient nuclei. The cavitation inception index values are presented in Figure 9.1 as a function of the square root of the Reynolds number. Distinctions are made between lock-in and lock-off conditions. For lock-off, a linear tendency between the cavitation inception index and the square root of the Reynolds number is evidenced and is in accordance with former models [5] and [16]. For lock-in conditions corresponding to the torsional mode, Figure 8.8, the cavitation inception index is significantly higher than for lock-off. Obviously, the trailing edge transverse motion influences the vortices generation process.

The increase of the cavitation inception index for lock-in condition is thereafter investigated in relation to the hydrofoil vibration level. The differences $\Delta\sigma_i$ between the cavitation inception number in lock-in conditions and the value derived from the linear regression of the cavitation inception numbers in lock-off conditions is calculated and plotted in Figure 9.2 as a function of the square of the hydrofoil trailing edge vibration velocity A scaled by the free-stream velocity C_{ref}. A linear relationship between $\Delta\sigma_i$ and A^2/C_{ref}^2 is achieved. The former models for wake cavitation inception are proposed to be extended by considering the hydrofoil trailing edge displacement velocity as [9]:

$$\sigma_i = a + b\sqrt{\mathrm{Re}} + c\frac{A^2}{C_{ref}^2} \tag{9.1}$$

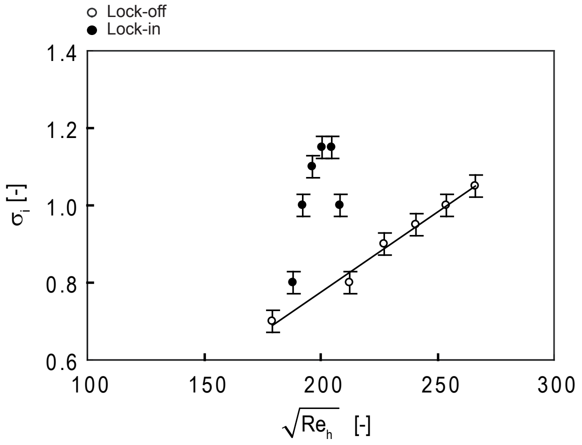

Figure 9.1: Vortices cavitation inception index versus the square root of the Reynolds number

9.2 Vortex strength

According to the detection of the cavitation inception, the vortex strength is estimated. If a cavitation free vortex is modeled as a Rankine vortex, the minimum pressure p_{min}, which is located at the vortex center, is given by

$$p_{min} = p_{ref} - \rho \left(\frac{\Gamma}{2\pi a} \right)^2 \tag{9.2}$$

where p_{ref} is the reference pressure. Cavitation occurs on the vortex axis when the minimum pressure falls below the vapor pressure p_v. According to the definition of the cavitation inception index, the above relation yields the following expression for the vortex strength Γ

$$\frac{\Gamma}{a} = \pi C_{ref} \sqrt{2\sigma_i} \tag{9.3}$$

Considering equation (9.3), the ratio Γ/a is evaluated for both lock-in and lock-off conditions. The observations of the vapor core size at cavitation inception for different upstream velocities for lock-in conditions, and therefore different vibration levels, did not show any evidence of significant size changes. It is believed that the influence of blade vibratory motion on the viscous core of the vortex is negligible and allows us to assume a constant core diameter in the lock-in free-stream velocity range. The differences $\Delta\Gamma$ between the calculated strength for lock-in conditions and the value derived from the linear regression of the strength in lock-off conditions Γ are estimated and plotted in Figure 9.3 as a function of the trailing edge vibration velocity scaled by the free-stream velocity A/C_{ref}. A linear trend for the vortex strength increase in relation to the trailing edge vibratory velocity is observed. The estimated increase in vortex strength is up to 20%. This is in formal agreement with the results obtained by Davies [33] in the wake of an oscillating cylinder. The increase in vortex strength is important in terms of fluid-structure coupling, since it implies that the hydrofoil trailing edge velocity increases the fluctuating forces on the body. This effect is additional to any increase of vortex span-wise

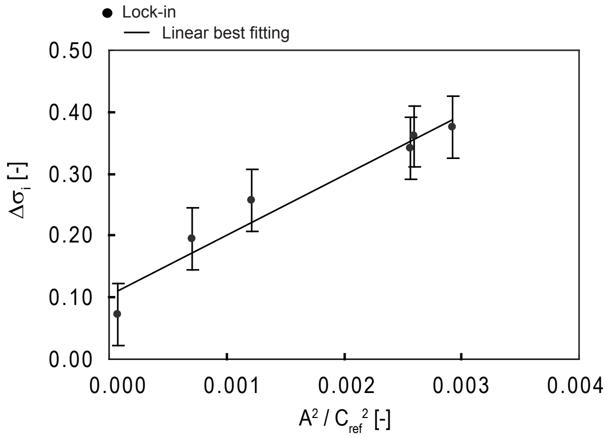

Figure 9.2: Difference between the cavitation inception number in lock-in condition and the value derived from the linear regression of the cavitation inception numbers in lock-off conditions versus the square of the hydrofoil trailing edge vibration velocity at $(x/L,\ z/B) = (0.8,\ 0.75)$ scaled by the free-stream velocity

organization, as observed for the lock-in condition, Figure 8.11. The combination of both effects obviously leads to a significant increase of the fluctuating force on the body.

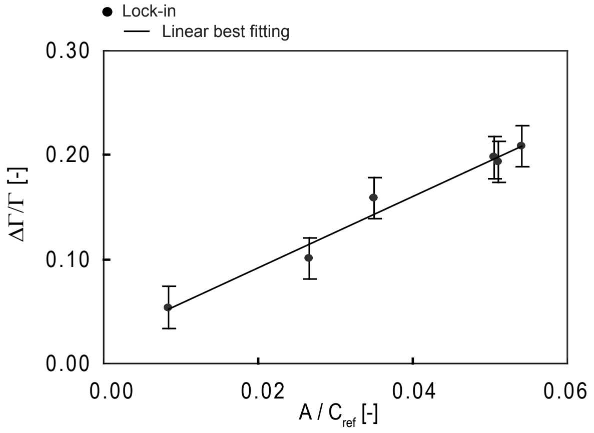

Figure 9.3: Relative vortex strength for lock-in condition versus the normalized hydrofoil vibration amplitude at $(x/L,\ z/B) = (0.8,\ 0.75)$

Chapter 10

Developed cavitation

For lock-off condition, the span-wise organization of the cavitation wake structures are compared with the one in cavitation free regime. The vortex shedding frequency, vortex-induced hydrofoil vibration, flow velocity fluctuations and inter-vortex spacings are analyzed for different values of cavitation index. For lock-in, the vortices generation mechanism is studied with the help of simultaneous wake high-speed visualization and hydrofoil vibration measurements.

10.1 Lock-off condition

10.1.1 Wake structure

Two pairs of top-view photographs of cavitation vortex street in lock-off condition for two upstream velocities, $Re_h = 51.5 \cdot 10^3$ and $64.4 \cdot 10^3$, are presented in Figure 10.1. It is observed that the wake exhibits three-dimensional vortex shedding aspect. The distortions and the spatial randomness of the vortical structures are evidenced.

Cavitation is commonly not considered to be a passive agent of visualization of the wake flow. As can be established in the following sections, it reacts on the flow as soon as it appears. At cavitation inception, it modifies likely the basic flow as vaporous cavities need a very large volume in comparison with the liquid part at their origin. When it is largely developed, it annihilates the wake structure since it replaces it by a continuous vapor cavity. Nevertheless, for the moderate development of cavitation we consider here, it is believed that the original wake morphology is kept. The comparison of the images of cavitation vortices, Figure 10.1, and the instantaneous velocity fields in cavitation free regime, Figure 8.9, does not show notable influence of the cavitation in the vortex street morphology. The 3D instability in the advection of the vortices has not its origin in the cavitation development. Moreover, cavitation does not decrease the vortex span-wise organization. For lock-off, the vortex span-wise organization is as short in cavitation free regime as for developed cavitation. Therefore, in terms of vortex span-wise organization, cavitation is considered as a passive agent of flow visualization.

Vortex dislocations are generated between span-wise cells of different frequency when the vortices in each cell move out of phase with each other. These dislocations grow rapidly in the span-wise direction into large scale structures as they travel downstream [123]. In our case study, a natural turbulent boundary-layer transition occurs along the chord length, section 6.2. It is believed that the non-uniform span-wise turbulence development in the boundary layer has a direct influence on the vortex street pattern. In chapter 13, the wake structures for the natural and the tripped turbulent transitions are compared. Significant modification of the vortex span-wise organization occurs. The intermittency and coherence of the vortex shedding process is described.

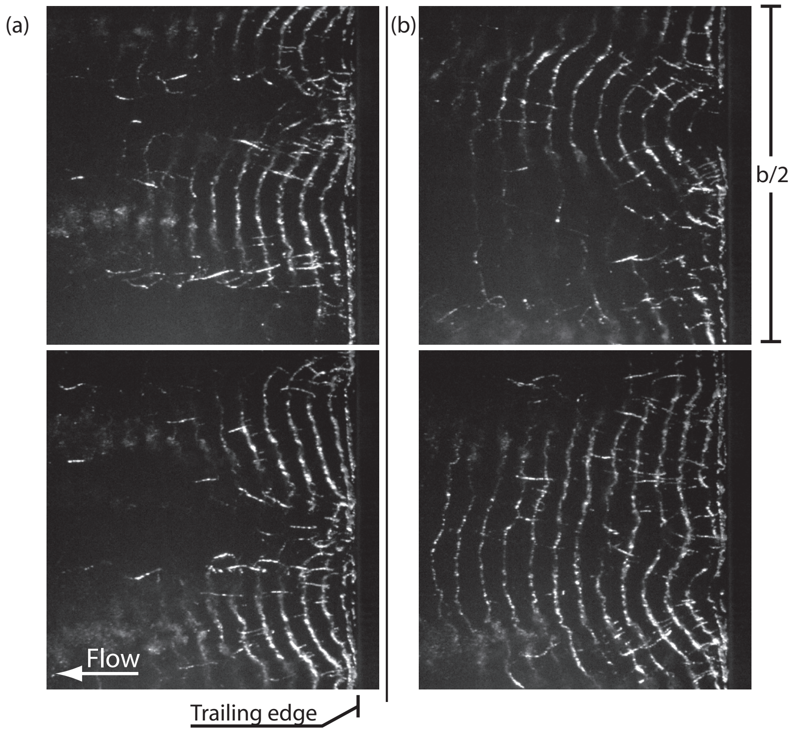

Figure 10.1: Top-view photographs of cavitation vortex street for lock-off conditions, (a) $Re_h = 51.5 \cdot 10^3$ and (b) $64.4 \cdot 10^3$

10.1.2 Vortex shedding frequency and induced vibration

For different values of cavitation index, the waterfall spectra of the laser vibrometer signals is presented in Figure 10.2, for lock-off conditions, $Re_h = 51.5 \cdot 10^3$ and $58.0 \cdot 10^3$. Notable influences of cavitation is evidenced: As soon as the cavitation appears in the core of the vortices, $\sigma/\sigma_i = 1$, an increase of the vortex shedding frequency is measured, 5%. Additionally, a significant increase of the hydrofoil vibration amplitude is observed. As the cavitation index is further reduced, the shedding frequency keeps increasing in an almost linear way and exceeds by 15% the cavitation free regime value. Although the shedding frequency increase with the development of the cavitation has already been observed in previous research for flow around wedges, [128] and [16], the above-mentioned increase of the vortex-induced vibration at early stage of cavitation has not been reported earlier. When the cavitation is fully developed $\sigma/\sigma_i < 0.6$, the vibration amplitude drops and the vortex structures merge to form a single vapor cavity at the trailing edge. Moreover, all the spectra show energy at 890 Hz corresponding to the hydrofoil torsional eigenfrequency.

The vortex shedding frequency, normalized by the lock-in frequency, is presented in Figure 10.3 for different cavitation index values and free-stream velocities, $Re_h = 51.5 \cdot 10^3$,

$58.0 \cdot 10^3$ and $64.4 \cdot 10^3$. The increase of the vortex shedding frequency at cavitation inception, $\sigma/\sigma_i = 1$, is evidenced. For developed cavitation, the vortex shedding frequency exceeds 15% the cavitation free regime value. When the cavitation index is further reduced, the vortex shedding frequency is decreased. The existence of a maximum vortex shedding frequency is reported in [128] and [16]. Nevertheless the reason of its occurrence is not clear.

Figure 10.4 presents the amplitude of the vortex-induced hydrofoil vibration for different cavitation index values and free-stream velocities. The amplitude is chosen to be the standard deviation of the hydrofoil wall displacement velocity which is band-pass filtered around the shedding frequency. The vibration amplitudes are normalized by the cavitation free regime value. It is shown that the vibration amplitude is significantly increased at cavitation inception. The increase reached respectively 50% and 35% of the cavitation free regime value for free-stream velocity of $Re_h = 51.5 \cdot 10^3$ and $58.0 \cdot 10^3$ respectively. For further cavitation index decrease, the vibration amplitude is decreasing. Nevertheless, it remains higher than the cavitation free regime for normalized cavitation index down to 0.6.

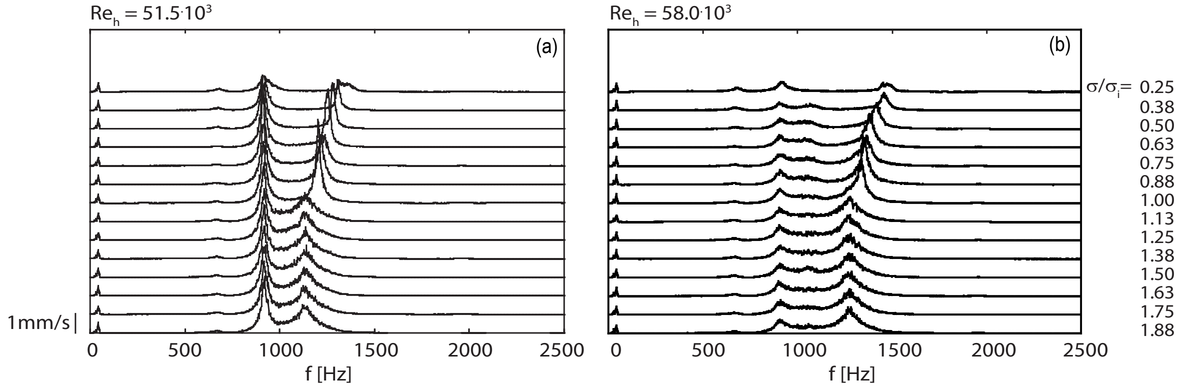

Figure 10.2: Waterfall spectra of the laser vibrometer signals, measured at $(x/L,\ z/B) = (0.8,\ 0.75)$, for different values of cavitation index and for lock-off condition, (a) $Re_h = 51.5 \cdot 10^3$ and (b) $58.0 \cdot 10^3$

The transient behavior of the vortex shedding process for different values of cavitation index, is analyzed through the computation of the short-time Fourier transform, equation (8.3), of the vortex-induced vibration signals. Part of the time signal is considered and the time-frequency representation is shown in Figure 10.5 for lock-off conditions, $Re_h = 51.5 \cdot 10^3$ and $58.0 \cdot 10^3$, for cavitation free, at inception and for fully developed cavitation. At cavitation inception, the increases of the vortex shedding frequency and vortex-induced vibration are evidenced in the spectrograms. The intermittency of the vortex shedding process is clearly evidenced. At the same frequency, cells of significant vibration amplitude are followed by ones of negligible amplitude. Nevertheless, at cavitation inception and for moderate cavitation development, the vortex shedding process appears to be less broad band, frequency speaking, than for cavitation free regime. For fully developed cavitation, the vortex shedding frequency is significantly increased and the induced vibration decreased. Apart from the vortex shedding frequency, the spectrograms reveal the eigen frequencies of the hydrofoil.

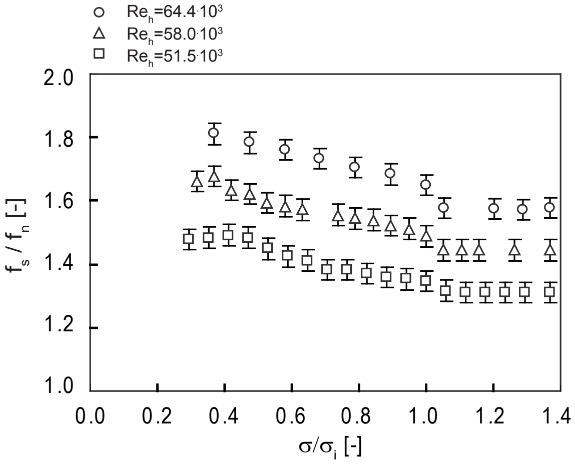

Figure 10.3: Normalized vortex shedding frequency for different values of cavitation index and free-stream velocities, $Re_h = 51.5 \cdot 10^3$, $58.0 \cdot 10^3$ and $64.4 \cdot 10^3$

10.1.3 Flow velocity fluctuations

The flow velocity fluctuations are thereafter investigated. LDV measurements are carried out for positions above the cavitation wake, $(x, y) = (L + h, h)$ and $(x, y) = (L + 2h, h)$. For different cavitation index values, stream-wise and transverse velocity fluctuations are evidenced in Figure 10.6 (a) and (b) respectively. Both stream-wise and transverse velocity fluctuations are increased for early stage of cavitation development. The maximum increases are 28% and 25% respectively. For developed cavitation and in comparisons with cavitation free regime, the velocity fluctuations are reduced. Therefore, the evolutions of the flow velocity fluctuations for different cavitation index values are in formal agreement with the one of the vortex-induced vibration, Figure 10.4.

10.1.4 Vortex advection velocity and inter-vortex spacings

For lock-off conditions, the cavitation effects on the vortex advection velocity and the inter-vortex spacings are analyzed. Data are collected with the help of the double laser optical probe: Two parallel laser beams are set to cross the wake and thus are periodically interrupted by the cavitation vortex street. Two fast photodiodes are placed to track the light beam intensities modulated by the passing cavities. The experimental setup and the data processing are described in section 7.2.

The cross-correlation signals of the two fast photodiodes signals are evidenced in Figure 10.7 for different values of cavitation index. They correspond to a lock-off condition, $Re_h = 51.5 \cdot 10^3$ and the distance from the trailing edge is $x = L + 6h$, which is sufficiently far downstream from the vortex formation region. It appears that the cross-correlation maxima occurs at specific times from the origin, $t_{correlation}$, denoting the time delay necessary for the vortices to be advected from the position of the first laser beam to the position of the second. It is shown that the above mentioned time $t_{correlation}$ is decreasing with the decrease of the cavitation index. The advection velocity of the vortices is,

$$C_{adv} = \frac{d_{lasers}}{t_{correlation}} \tag{10.1}$$

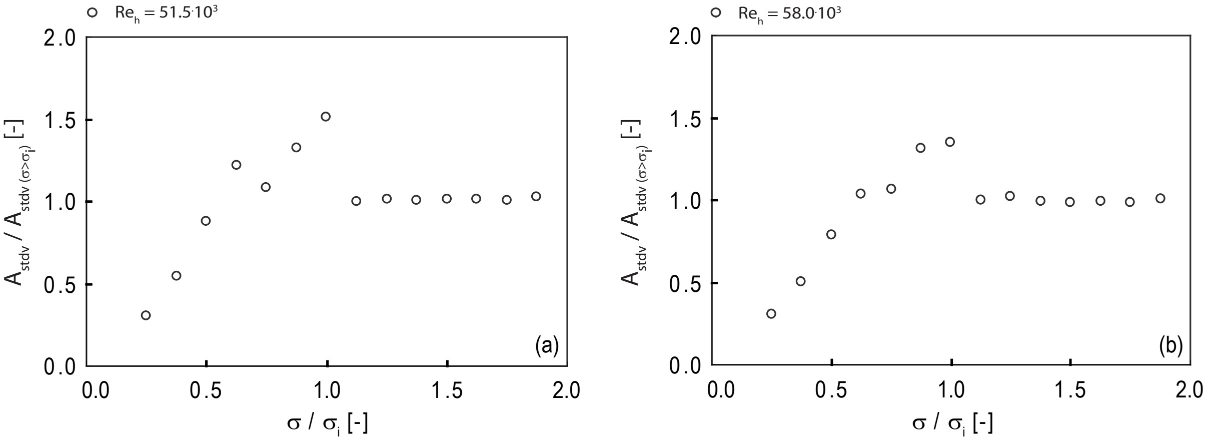

Figure 10.4: Vibration amplitude of the hydrofoil, measured at $(x/L,\ z/B) = (0.8,\ 0.75)$, for different values of cavitation index and for lock-off condition, (a) $Re_h = 51.5 \cdot 10^3$ and (b) $58.0 \cdot 10^3$

where the distance separating the two laser beams is d_{lasers}. The gap between the laser beams is maintained constant, $d_{lasers} = 4$ mm, so that a decrease of $t_{correlation}$ is directly related to an increase of the vortex advection velocity, equation (10.1). Results of the vortex advection velocity, normalized by the free-stream velocity, is presented in Figure 10.8 (a). It is observed that the advection velocity increases with the cavitation development as much as 4% for $\Delta\sigma = 0.4$. This increase is linear and occurs as soon as the cavitation appears in the wake. This effect is in formal agreement with a study on periodic wakes behind wedges [128].

Using the measurements of the vortices advection velocity C_{adv} and their corresponding shedding frequencies f_s, the stream-wise inter-vortex spacing a_s is evaluated by equation (10.2). The results for a_s are plotted in Figure 10.8 (b) for several cavitation index values. The inter-vortex spacing is found to decrease for decreasing cavitation index values.

$$a_s = \frac{C_{adv}}{f_s} \tag{10.2}$$

The cross-stream inter-vortex spacing b_s is not directly measured within this study but is estimated by two different ways. The first one consists in imposing a constant Strouhal number for the different cavitation developments. The Strouhal number is modified so that the reference length is no more the body thickness h but the cross-stream inter-vortex spacing b_s,

$$St_{b_s} = \frac{f_s b_s}{C_{ref}} \tag{10.3}$$

This normalized vortex shedding frequency is inspired by the Griffin number [59], section 5.1, for which the reference length is the wake width at the end of the vortex formation region. The Strouhal number value is chosen to be the one for cavitation free regime, $St_{b_s} = St_h = 0.23$. The second method for the estimation of the cross-stream

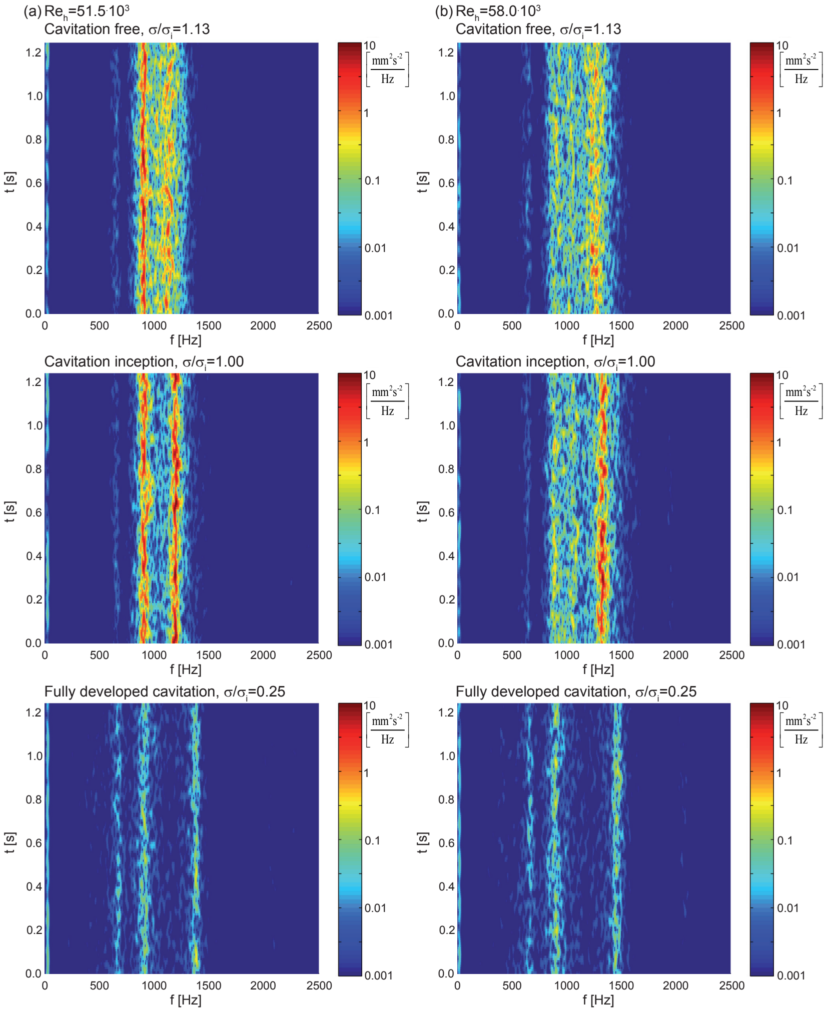

Figure 10.5: Spectrograms of the vortex-induced vibration signal for lock-off conditions for cavitation free regime, at inception and for fully developed cavitation

inter-vortex spacing consist in imposing a constant inter-vortex spacing ratio b_s/a_s. The value is chosen to be the one described by the von Kármán stability theory [116],

$$\frac{b_s}{a_s} = 0.281 \tag{10.4}$$

The results for the cross-stream inter-vortex spacing b_s for different values of the cavitation index is presented in Figure 10.9. According respectively to the ascending and descending trends of the vortex shedding frequency, Figure 10.3, and stream-wise inter-vortex spacing, Figure 10.8 (b), both methods leads to a descending trend of b_s for decreasing cavitation index values. Moreover, the gap between the two trends are not significant. Matching of the results occur for a modified Strouhal number value of 0.26 instead of 0.23 or an inter-vortex spacing ratio value of 0.25 instead of 0.281. The mechanism of narrowing of the vortex street has already been shown in [128] and [16] but is not elucidated so far. Nevertheless, the decrease of the cross-stream inter-vortex spacing is in agreement with the increase of the vortex shedding frequency with the cavitation

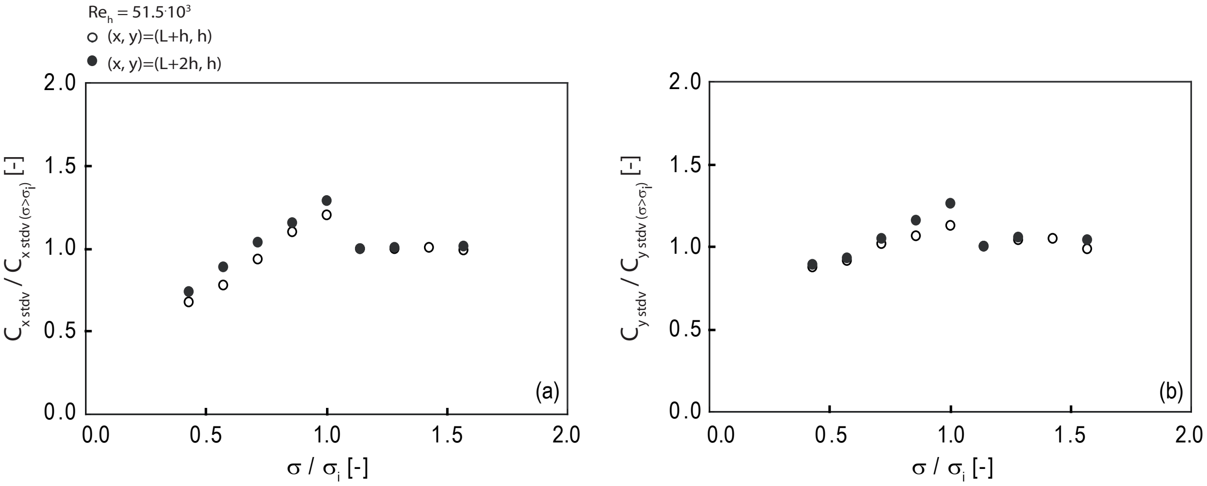

Figure 10.6: (a) Stream-wise and (b) transverse velocity fluctuations, measured at $(x, y) = (L + h, h)$ and $(x, y) = (L + 2h, h)$, for different values of cavitation index and for lock-off condition, $Re_h = 51.5 \cdot 10^3$

development since one expects that the vortex shedding frequency scales inversely with the wake width [124].

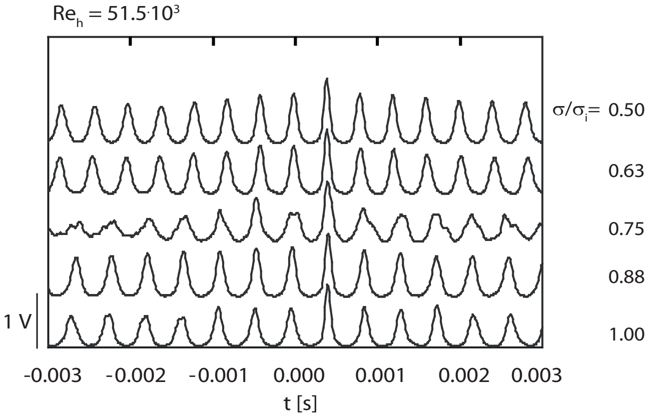

Figure 10.7: Cross-correlation signals of the two fast photodiodes signals, measured at $x/h = L + 6h$, for different values of cavitation index and for lock-off condition, $Re_h = 51.5 \cdot 10^3$

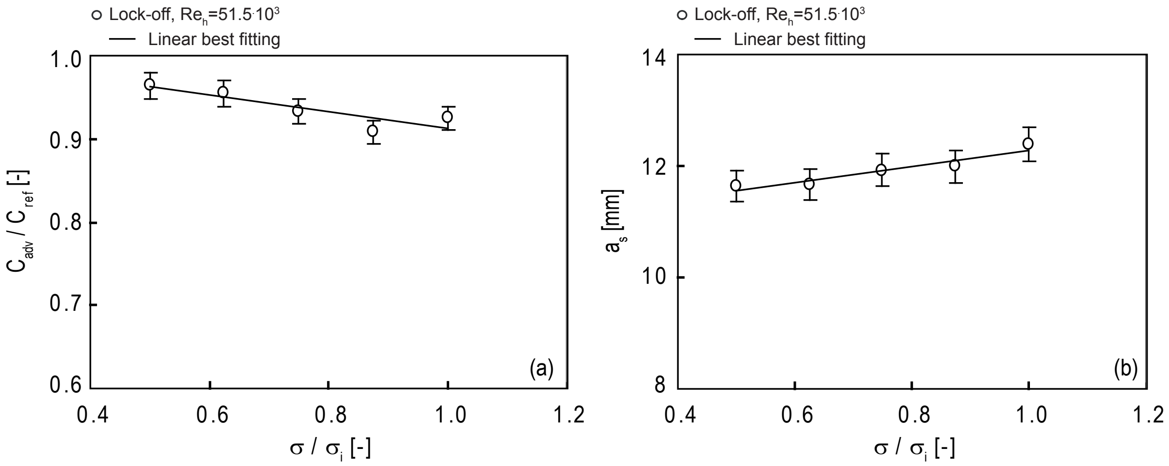

Figure 10.8: (a) Normalized vortex advection velocity and (b) stream-wise inter-vortex spacing for different values of the cavitation index and for lock-off condition, $Re_h = 51.5 \cdot 10^3$, measured at $x = L + 6h$

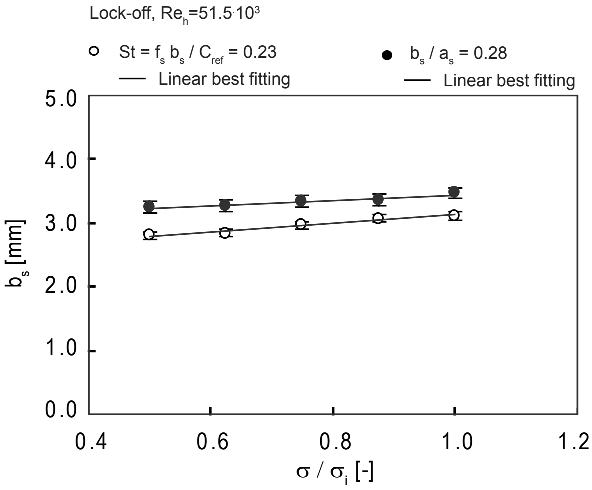

Figure 10.9: Estimation of the cross-stream inter-vortex spacing for different cavitation index values and for lock-off condition, $Re_h = 51.5 \cdot 10^3$

10.1.5 Discussion

At the present stage, it becomes obvious that cavitation cannot be considered as a passive agent for the visualization of the turbulent wake flow. Non-negligible influences of the cavitation on the vortex shedding frequency, Figure 10.3, vortex-induced vibration, Figure 10.4, flow velocity fluctuations, Figure 10.6, and vortex advection velocity and inter-vortex spacings, Figures 10.8 and 10.9, are evidenced. Nevertheless, the vortex span-wise organization is shown to be not affected by the cavitation occurrence, Figures 10.1 and 8.9.

The increase of the vortex shedding frequency with the development of the cavitation can be understood if one admits that the maximum area available for the vortex in the formation process is imposed by the geometry of the body and the free-stream velocity, [16]. When the cavitation index decreases, the cross-section area of the cavitation vortices increases and thus fill the maximum available area more quickly. The critical size of the vortex is therefore reached sooner and the shedding frequency is increased. The description of the vortex street formation made by Gerrard [51] also gives direct insight into the increase of the shedding frequency. The description postulates that a vortex continues to grow, fed by circulation from its connected shear layer, until it is strong enough to draw the opposing shear layer across the near wake. Sridhar and Katz [105] show that few microscopic bubbles fragment the core of the vortex into regions with peak vorticities that are 20% higher than the original maximum vorticity. In the cavitation growing vortex, this higher vorticity draws sooner the opposing shear layer across the wake than in the cavitation free vortex. Consequently, the approach of oppositely signed vorticity cuts off sooner the supply of circulation to the growing vortex. The vortex shedding frequency is thus increased. Furthermore, the increases of the vortex-induced vibration and flow velocity fluctuations at early stage of cavitation development is attributed to the above-mentioned vorticity increase. Considering a Rankine vortex, Arndt and Keller [8] established that the maximum velocity in the cavitation vortex is $\sqrt{2}$ higher than in the cavitation free vortex and support our claim. Accordingly to the increase of the vortex shedding frequency, the vortex advection velocity and the inter-vortex spacings are believed to be modified for stability of the vortex street.

The vortex street is known to be directly related to the state of the boundary layer along the hydrofoil. Nevertheless, boundary layer measurements does not reveal any significant changes for cavitation and cavitation free regimes. The increase of the vortex shedding frequency is therefore not due to a thinning of the boundary layer at the trailing edge. In order to take into account the boundary-layer thickness at the trailing edge, the proposed modified Strouhal number is the following,

$$St_{(h+2\delta_1)} = \frac{f_s(h+2\delta_1)}{C_{ref}} \tag{10.5}$$

where δ_1 is the boundary-layer displacement thickness. Nevertheless, for the considered free-stream velocities, the boundary layer at the trailing edge is less than 1 mm thick. In the same time, the increase of the vortex shedding frequency for decreasing cavitation index value is up to 15%. Considering equation (10.5) and imposing a constant Strouhal number, the value for cavitation free regime would lead to a negative boundary-layer displacement thickness ! Moreover, investigations does not reveals any modification of the turbulent boundary-layer transition location.

For largely developed cavitation, the vortex-induced vibration and the flow velocity fluctuations are decreased in comparison of cavitation free regime. One conceives that each vortex can enter in contact with the preceding and the following ones of the other vortex row. Exchanges of opposite circulations between both rows are possible and thus diminishes the vorticity [16]. For extremely developed cavitation, the cavitation annihilates the wake structure forming at the rear face of the body since it replaces it by a continuous vapor cavity.

10.2 Lock-in condition

10.2.1 Wake structure

For lock-in, the trailing edge vibration leads to more organized wake structures. When the torsional mode is excited, Figure 8.8, the transverse motion of the trailing edge significantly increases the vortex span-wise organization, and parallel vortex shedding takes place as evidenced in Figure 10.10. The comparison of the images of cavitation vortices, Figure 10.10, and the instantaneous velocity fields in cavitation free regime, Figure 8.11, does not show notable influence of the cavitation in the vortex span-wise organization. Parallel vortex shedding mode is kept for cavitation development. Therefore, in terms of vortex span-wise organization, cavitation can be considered as a passive agent.

For lock-in condition, torsional mode, the generation process of the vortex street is analyzed with the help of simultaneous wake high-speed visualization and vortex-induced vibration. Pictures of wake structures and the simultaneous hydrofoil vibration signals are presented in Figure 10.11. The hydrofoil velocity and displacement signals are virtually sinusoidal. The velocity is plotted in black line and the displacement in grey. The frames display one generation cycle of the vortex street. It is observed that during the motion of the trailing edge, the volume of vapor in the recirculation zone increases and starts rolling-up without being advected by the mean flow. When the hydrofoil reaches the center-line position so that displacement velocity is maximized, frames number one and between six and seven, the vortex detaches from the trailing edge and accelerates in the wake. As soon as the upper/lower vortex is detached, the lower/upper vortex is generated and cavitation appears in its center.

For several cavitation index values, frames of high speed visualizations of the vortex street for lock-in condition are presented in Figure 10.12. At cavitation inception and for moderated cavitation development, it appears that cavitation occurs in the primary vortices. As the cavitation index is decreased so that the volume of vapor is increasing, the wake exhibits secondary cavitation vortices. These stream-wise vortices link the primary vortices of opposite signed vorticity and are called shear layer vortices, Kourta *et al.* [72] among others.

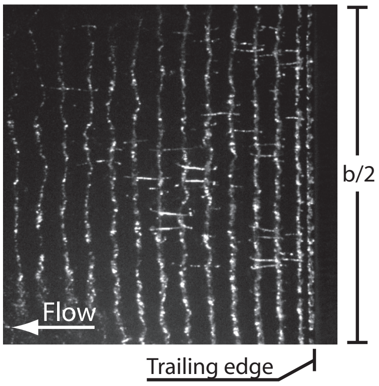

Figure 10.10: Top-view photographs of cavitation vortex street for lock-in condition, torsional mode, $Re_h = 38.6 \cdot 10^3$

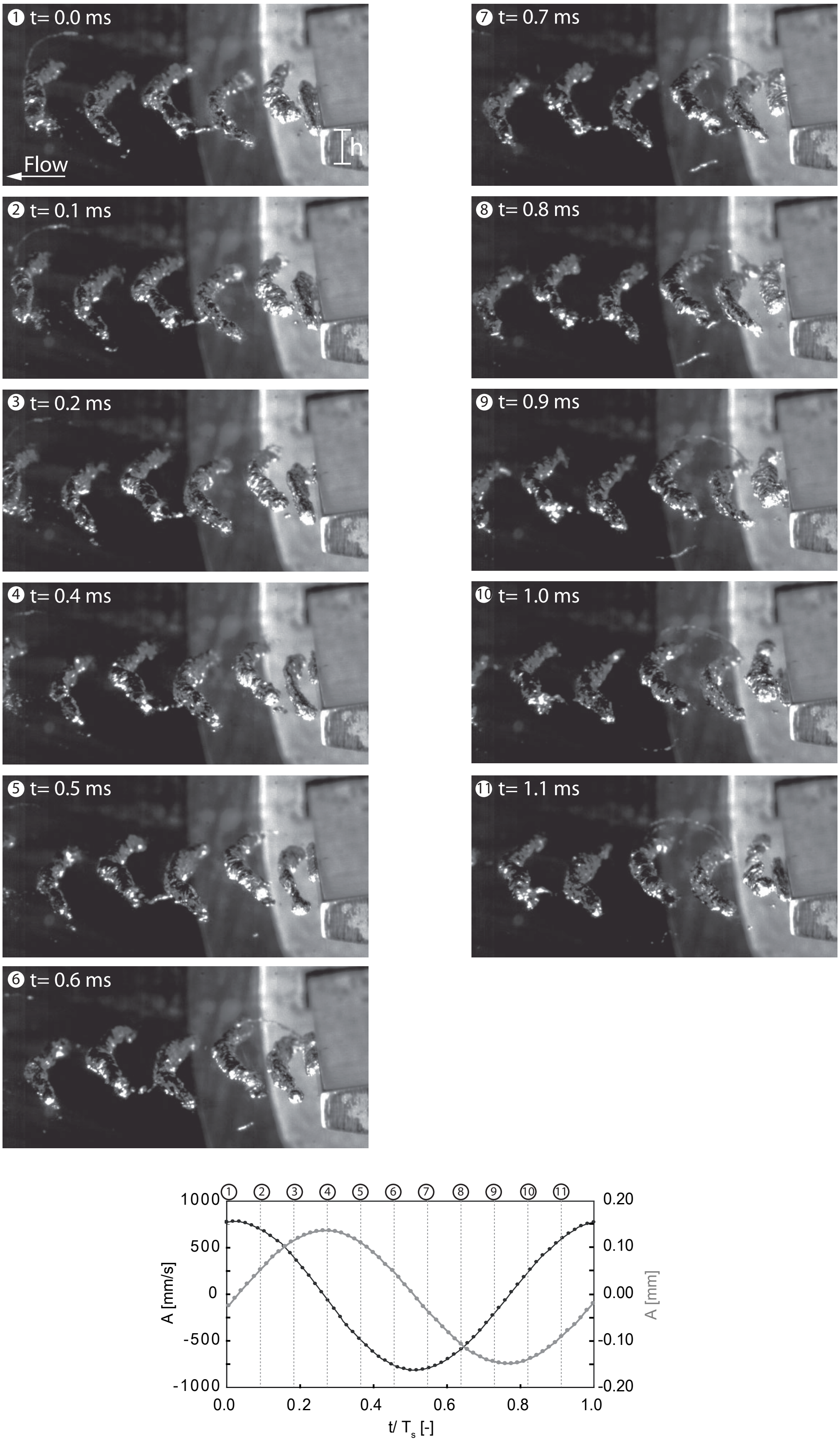

Figure 10.11: Side-view visualization of cavitation vortex street and vortex-induced vibration signal for lock-in condition, torsional mode, $Re_h = 38.6 \cdot 10^3$, $\sigma/\sigma_i = 0.85$

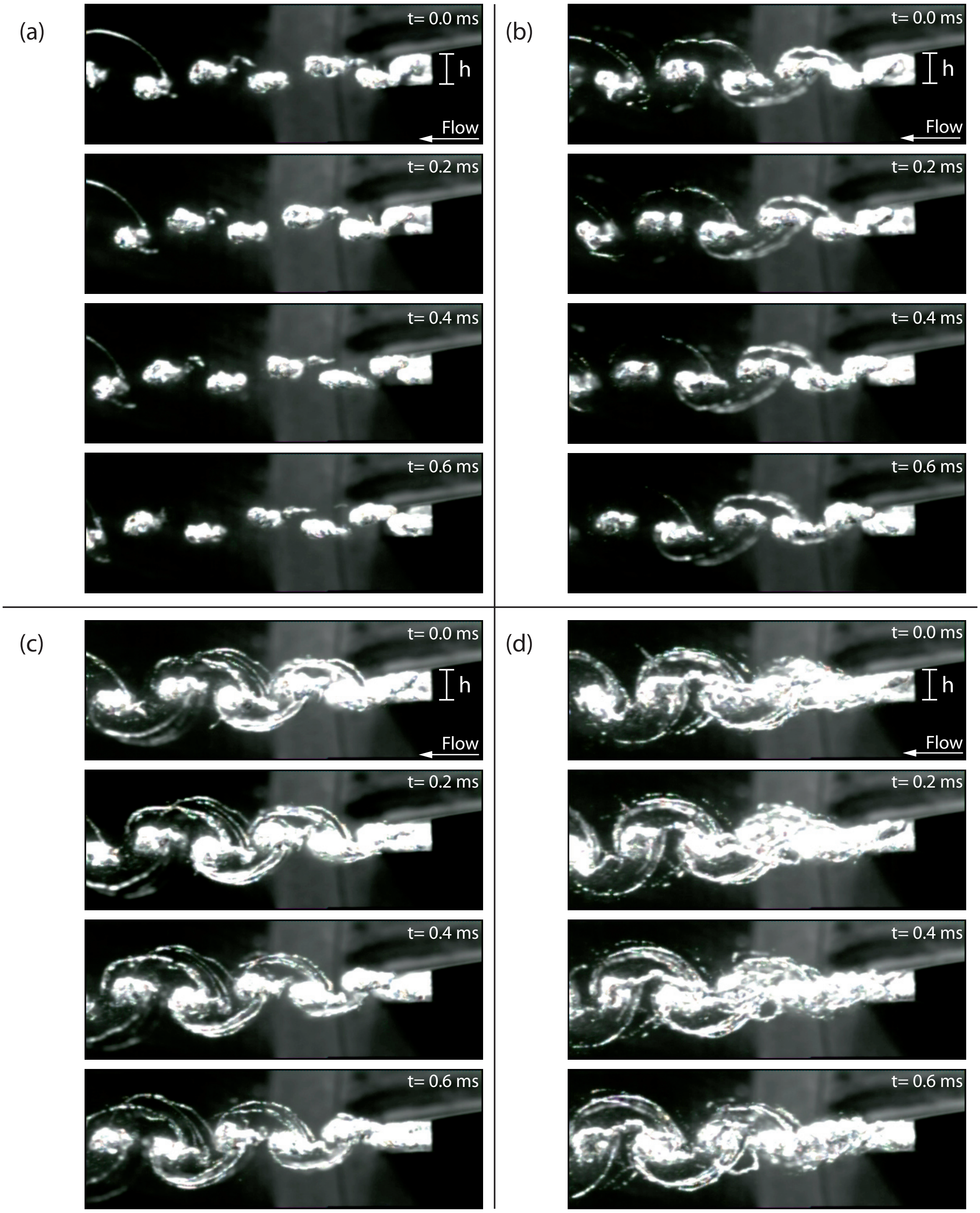
(a)
(b)
(c)
(d)
t= 0.0 ms
t= 0.2 ms
t= 0.4 ms
t= 0.6 ms
h
Flow

Figure 10.12: Frame series (half cycle) of cavitation vortex street for lock-in condition, $Re_h = 38.6 \cdot 10^3$, and for four cavitation indices, (a) $\sigma/\sigma_i = 0.85$, (b) $\sigma/\sigma_i = 0.80$, (c) $\sigma/\sigma_i = 0.70$ and (d) $\sigma/\sigma_i = 0.60$

10.2.2 Vortex shedding frequency and induced vibration

As the vortex shedding frequency increases with the cavitation development, Figures 10.2 and 10.3, it is found possible to enable or disable hydro-elastic couplings by permitting a sufficient cavitation development while keeping the free-stream velocity constant. In Figures 10.13, the hydrofoil resonance is disabled when the free-stream velocity is maintained at $Re_h = 40.3 \cdot 10^3$, for which the torsional mode is excited in the cavitation free regime. In Figure 10.13 (a), the waterfall spectra of the accelerometer signals for different values of cavitation index is presented. Figure 10.13 (b) illustrates the vortex shedding frequency f_s, normalized by its corresponding value for the cavitation free regime $f_s(\sigma > \sigma_i) = f_n$ versus the cavitation index. As the cavitation appears in the wake and develops, the vortex shedding frequency increases, but at a lower rate than in the case out of resonance, Figure 10.3. Although the amplitude of vibration decreases, the resonance is maintained since the amplitudes remain significantly higher than in the lock-off condition. The structural vibration therefore tends to control the unsteady flow field and forces the vortices to be shed near the eigenfrequency. Upon further decrease of the cavitation index, the coupling is no longer maintained, so that the vortex shedding frequency increases in a more marked way.

Therefore, and because cavitation modifies the vortex shedding frequency due to flow over a body, there is a possibility of unexpected hydro-elastic coupling if a closer match between the shedding frequency and a structural mode of vibration occurs. The manufacturers of hydraulic machinery are nowadays carrying both flow and structural analysis to identify the best design and to avoid structural resonance. Cavitation effects should also be taken into account to prevent any failures.

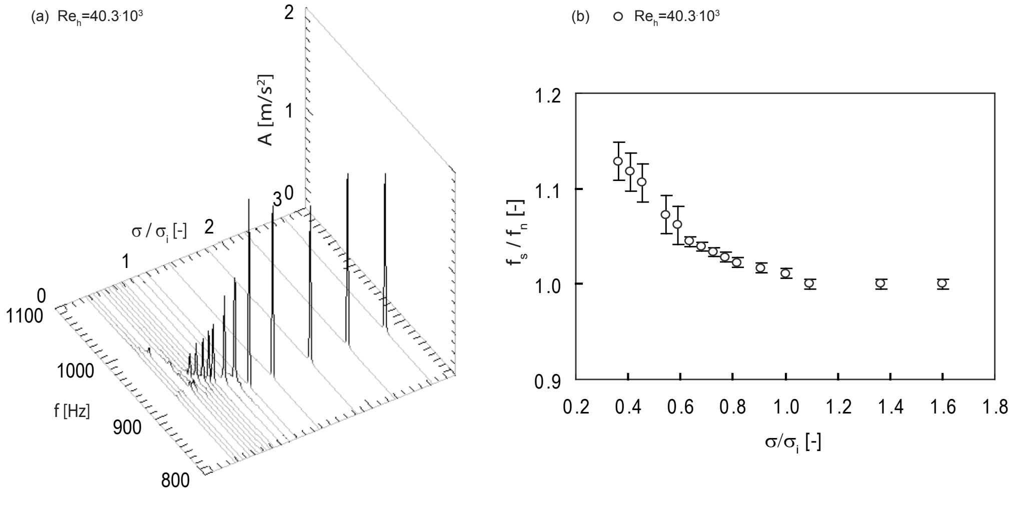

Figure 10.13: (a) Waterfall spectra of the acceleration signals and (b) normalized vortex shedding frequency for different cavitation index values and for $Re_h = 40.3 \cdot 10^3$

Part IV

Boundary layer and vortex shedding

Chapter 11

Boundary-layer flow

The effects of a tripped boundary layer on vortex shedding process are studied in this part. The results are compared with the condition of a natural boundary-layer transition. In this chapter, the boundary-layer flow is studied for the natural and the tripped laminar-turbulent transitions. The transition is tripped at the hydrofoil leading edge with the help of a distributed roughness. Boundary-layer velocity profiles are analyzed for different free-stream velocities at the trailing edge. The development of the boundary layer along the hydrofoil chord is characterized for Reynolds number $Re_h = 64.4 \cdot 10^3$, which is the benchmark condition for lock-off. The boundary-layer flow is described in terms of mean boundary-layer velocity profile, boundary-layer thickness and form factor. The boundary-layer structure is depicted with inner variables.

11.1 Reynolds effects

11.1.1 Time-averaged velocity profiles

Time-averaged boundary-layer velocity profiles at the hydrofoil trailing edge are shown in Figure 11.1 for different free-stream velocities. The surface-tangent mean velocity, $C_{x_1\,mean}$, is normalized by the external velocity, C_e, on the normal line. A zero velocity point is added to each profile at the foil surface and the velocity profiles are shifted on the horizontal axis for clarity. There is evidence of a significant increase in the boundary-layer thickness for the tripped transition. Figure 11.2 presents the boundary-layer thickness (a) and the form factor (b) of the above-mentioned velocity profiles. The boundary-layer thickness δ and the form factor H_{12} are defined in chapter 3.

11.1.2 Boundary-layer thickness and form factor

In Figure 11.2 (a), the boundary-layer thicknesses for the tripped transition and for increasing free-stream velocity show a descending trend, which is consistent with typical Reynolds effects. By contrast, the trend is ascending for the natural transition. Apparently the transition point moves upstream along the chord length with increasing free-stream velocity. The theoretical form factor value for the flat-plate laminar boundary layer is 2.6. Below 1.5, the boundary layer is considered turbulent [99]. For the natural transition and free-stream velocities up to 10 m/s, the form factor values reveals a

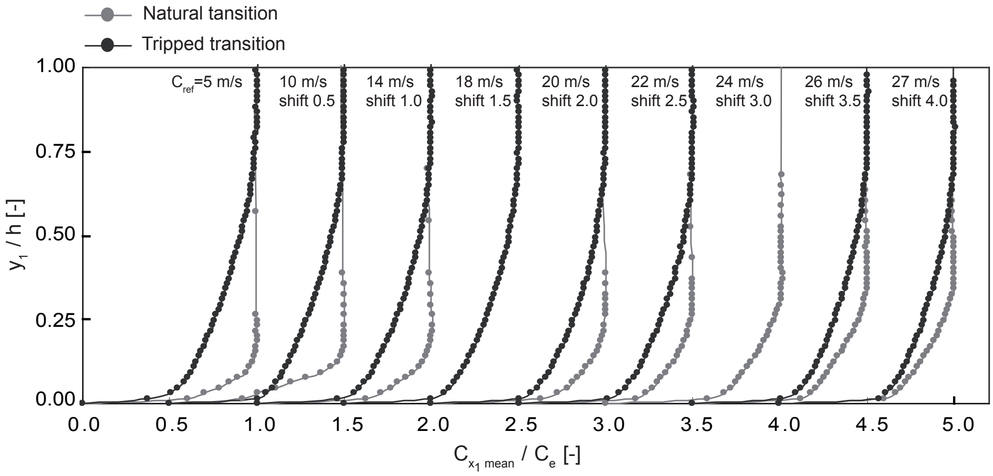

Figure 11.1: Time-averaged boundary-layer velocity profiles at the hydrofoil trailing edge for different free-stream velocities and for natural and tripped transitions

transitional boundary layer, Figure 11.2 (b). For higher free-stream velocities, the form factor decreases and one identifies turbulent boundary layers. For the tripped transition case, turbulent boundary layers are identified over the entire free-stream velocity range. Altogether, these features reveal that the distributed roughness at the leading edge acts as expected by triggering the turbulent transition. On the other hand, without any distributed roughness, a natural boundary-layer transition occurs along the chord length.

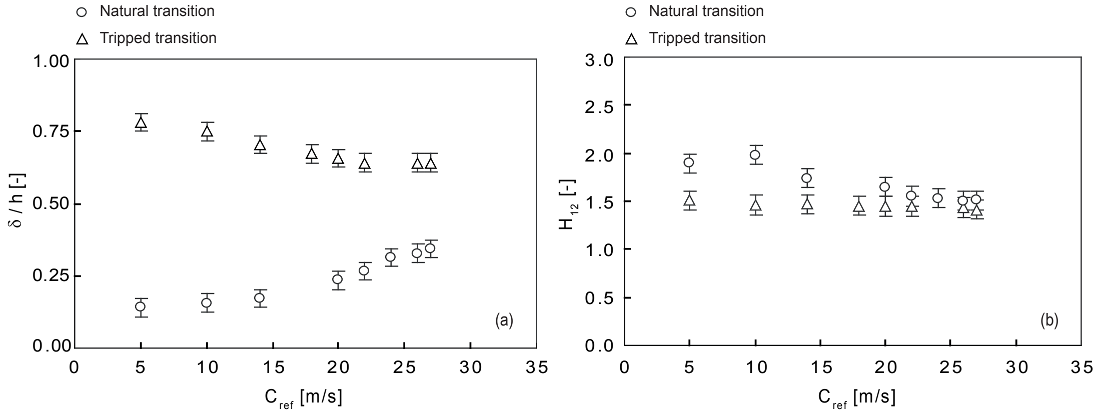

Figure 11.2: (a) Boundary-layer thickness and (b) form factor of time-averaged velocity profiles at the hydrofoil trailing edge for different free-stream velocities and for natural and tripped transitions

11.1.3 Turbulent boundary-layer transition

The location of the turbulent boundary-layer transition along the chord length is estimated with the help of the boundary-layer thickness measurement at the hydrofoil trailing edge and the theoretical flat-plate boundary layer equations. The integral parameter for laminar and turbulent flat-plate boundary layers are given in Table 3.1. The boundary-layer thickness at the trailing edge $\delta_{T.E.}$ depends on the position of the transition x_{crit} and is expressed as the sum of the laminar and turbulent boundary layers as,

$$\delta_{T.E.} = 5.0 x_{crit} Re_{x_{crit}}^{-1/2} \; + \; 0.37(L - x_{crit}) Re_{L-x_{crit}}^{-1/5} \tag{11.1}$$

where L is the hydrofoil chord length. The boundary-layer thickness at the hydrofoil trailing edge for both the natural and the tripped transitions are shown in Figure 11.2 for different free-stream velocities. According to these measurements and equation (11.1), the location of the turbulent boundary-layer transition is estimated and shown in Figure 11.3. For the natural transition case, the location of the transition moves upstream to the leading edge for increasing free-stream velocity, which is consistent with typical Reynolds effects. At 20 m/s, $Re_h = 64.4 \cdot 10^3$, free-stream velocity, the benchmark condition for natural and tripped transitions comparison, the natural transition occurs at $0.85L$. Extrapolation of the best fitting curve reveal that the transition should occur at the leading edge at about 40 m/s. Nevertheless, the boundary-layer flows are sensitive to the pressure distribution: The transition location is delayed for an accelerated flow, *i.e.* for $0 < x/L > 0.5$, whereas a pressure increase favor the transition, *i.e.* for $0.5 < x/L > 1.0$. Nevertheless, the curvature of the hydrofoil is small so that it is expected that the boundary-layer flow develops itself closely to the flat-plate boundary layer except at the direct proximity of the leading edge. For the tripped transition case, the transition location is shown to occur at the leading edge for the different tested free-stream velocities. Therefore, the distributed roughness is dimensioned so that a fully effective tripping to turbulent flow occurs.

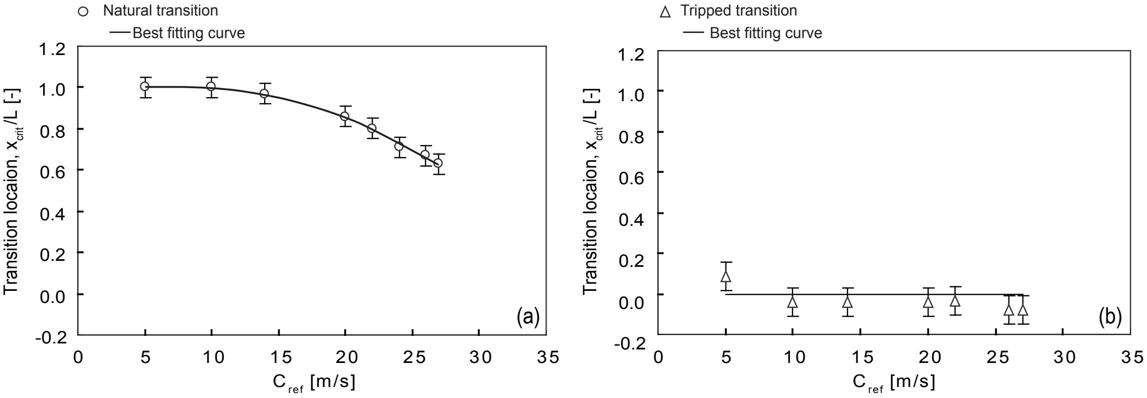

Figure 11.3: Estimation of the turbulent boundary-layer transition location for different free-stream velocities and for (a) natural and (b) tripped transitions

11.1.4 Boundary-layer structure

With inner variables (y_1^+, $C_{x1\,mean}^+$), the time-averaged boundary-layer velocity profiles, measured at the trailing edge for different free-stream velocities are shown in Figure 11.4. The inner variables are defined in section 3.1. The size of the LDV control volume with respect to the boundary-layer thickness does not permit a description of the viscous sublayer, so that the skin friction cannot be fairly estimated. The skin friction coefficient c_f of the laminar and turbulent flat-plate boundary layers is used for the estimation of the wall shear stress and the friction velocity. In Figure 11.4, the velocity profiles are shifted accordingly to the free-stream velocity on the vertical axis for clarity. The theoretical log law slope, equation (3.13), is shown for comparison. For both natural (a) and tripped transitions (b), the boundary-layer velocity profiles display the log region. Moreover, the velocity makes a noticeable departure from the log law approaching the free-stream which reveal the defect layer. These features are typical characteristic of turbulent boundary layer.

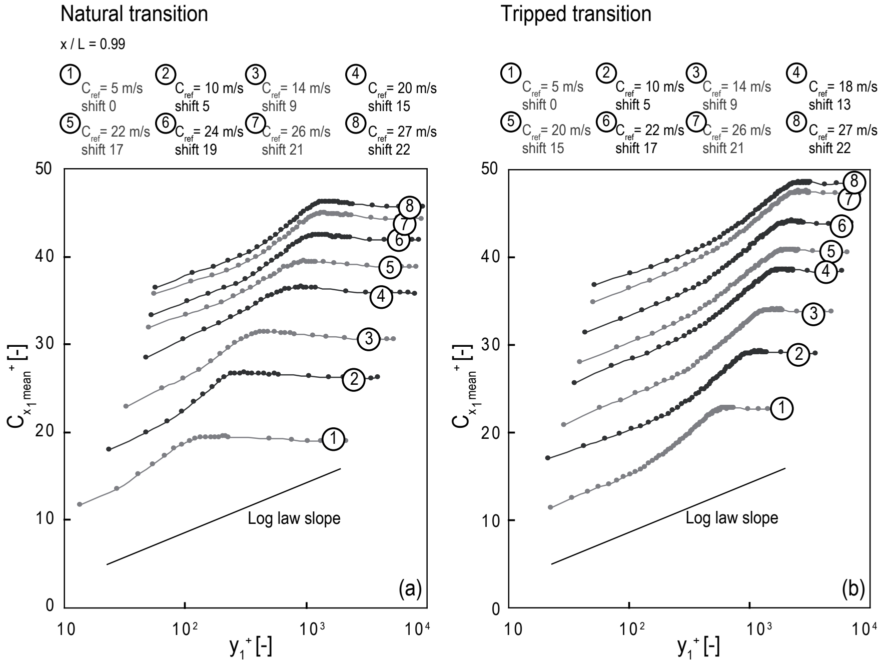

Figure 11.4: Dimensionless boundary-layer velocity profiles at the hydrofoil trailing edge for different free-stream velocities and for (a) natural and (b) tripped transitions

Comparison between the mean boundary-layer velocity profiles in inner variables for the natural and the tripped transitions is presented in Figure 11.5 for Reynolds number $Re_h = 64.4 \cdot 10^3$. It is shown that the two velocity profiles collapse particularly well onto the log law,

$$C_{x_1}^+ = \frac{1}{K} \ln\, y_1^+ + c \tag{11.2}$$

where the Kármán constant K is maintained equal to the theoretical value 0.40. The parameter c depends on the surface roughness, equation (3.14). The c value is therefore varied in order to best fit our measurements and found to be equal to 4.0. Considering equation (3.14), the non-dimensional wall roughness k_s^+ is found to be 4.95, which fulfills the criteria of hydraulically smooth surface, $k_s^+ < 5$. Besides, the measured and theoretical defect layers match particularly well. The Coles' wake strength parameter is $\Pi = 0.6$, equation (3.16),

$$C_{x_1}^+ = \frac{1}{K} \ln\, y_1^+ + c + \frac{2\Pi}{K} \sin^2\left(\frac{\pi}{2}\frac{y_1}{\delta}\right) \tag{11.3}$$

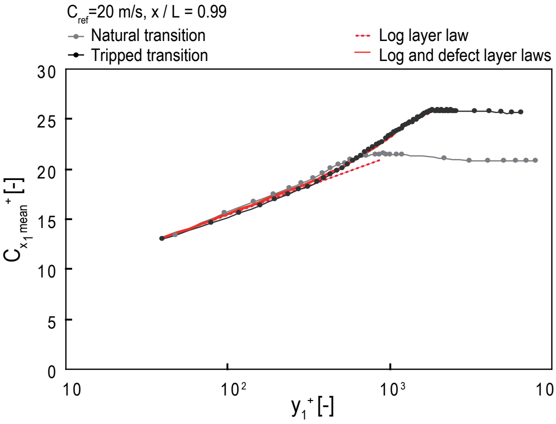

Figure 11.5: Dimensionless boundary-layer velocity profiles at the hydrofoil trailing edge for natural and tripped transitions, $Re_h = 64.4 \cdot 10^3$

11.2 Development along the hydrofoil chord

11.2.1 Time-averaged velocity profiles

Normalized time-averaged boundary layer velocities are presented in Figure 11.6 at 10, 20, 30, 40, 60, 70, 80, 90 and 99% of the chord length for $Re_h = 64.4 \cdot 10^3$ (lock-off) and for the two transition processes. Here again, a zero velocity point is added to each profile at the foil surface and the velocity profiles are shifted on the horizontal axis for clarity. Measurements at mid-chord were not recorded due to optical access constraints and additional velocity profiles at 75, 85, 95% of the chord length are presented for the natural transition.

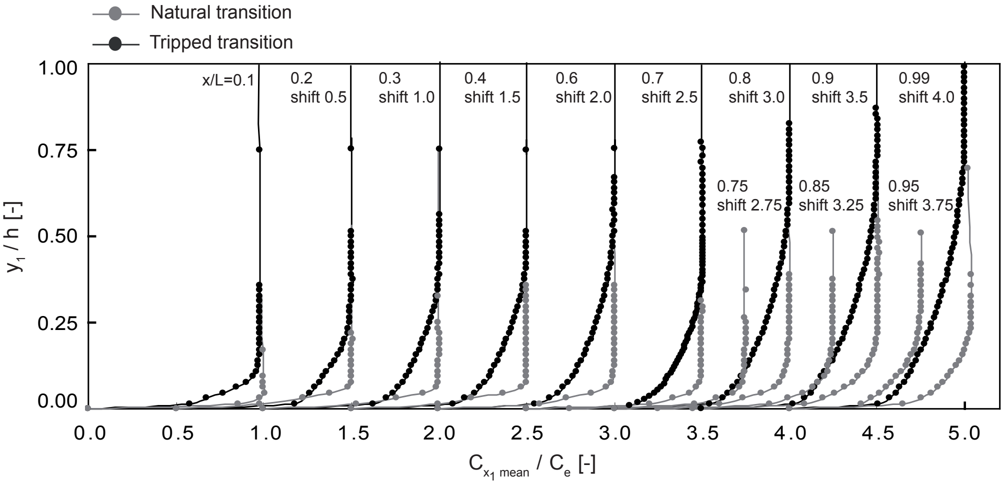

Figure 11.6: Time-averaged boundary-layer velocity profiles along the hydrofoil chord for natural and tripped transitions, $Re_h = 64.4 \cdot 10^3$

11.2.2 Boundary-layer thickness and form factor

The boundary-layer thickness and the form factor are presented in Figure 11.7 (a) and (b), respectively. For the natural transition, the boundary-layer thickness grows slightly with increasing distance from the leading edge. Downstream of 80% of the chord length, the increase is greater than upstream. Simultaneously, the form factor decreases from 2.5 to 1.6. The natural boundary-layer transition occurs at 85% of the chord length, which is in accordance with the result presented in Figure 11.3. In the case of the tripped transition, a significant increase in the growth of the boundary layer is noted, compared to the natural case. The mean form factor value is 1.46 and the turbulent boundary layer develops along the entire chord length. We observed the existence of the natural turbulent transition and confirmed the efficiency of boundary-layer tripping. Thus, the wake flow analysis for the so-called natural and tripped transitions is pertinent.

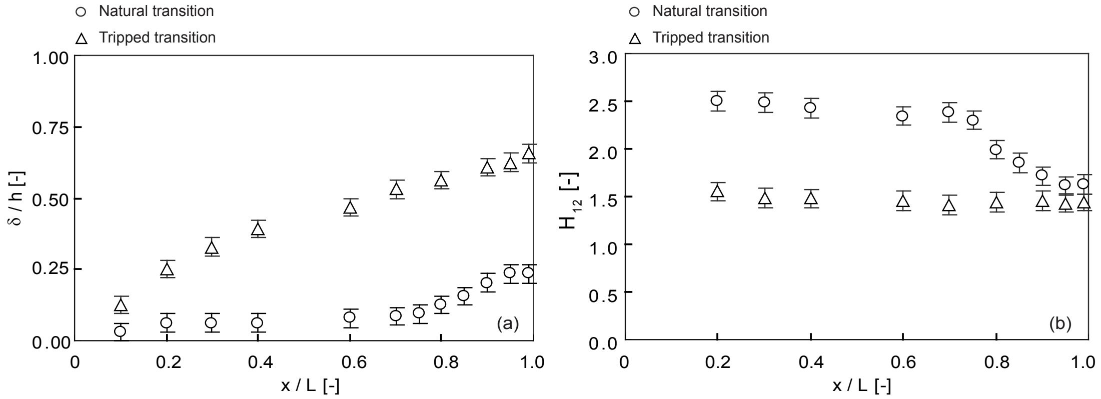

Figure 11.7: (a) Boundary-layer thickness and (b) form factor of time-averaged velocity profiles along the hydrofoil chord for natural and tripped transitions, $Re_h = 64.4 \cdot 10^3$

11.2.3 Boundary-layer structure

With inner variables (y_1^+, $C_{x_1\ mean}^+$), the time-averaged boundary-layer velocity profiles, measured at different stations along the chord length for Reynolds number $Re_h = 64.4 \cdot 10^3$ are shown in Figure 11.8. The skin friction coefficient c_f of the laminar and turbulent flat-plate boundary layers is used for the estimation of the wall shear stress and the friction velocity. The velocity profiles are shifted, accordingly to the distance from the leading edge, on the vertical axis for clarity. The theoretical log law slope is shown for comparison. For the natural transition case (a), the log region is displayed for boundary-layer velocity profiles from $x/L = 0.8$. Significant change in the velocity distribution is revealed for position upstream of 80% of the chord length. Obviously, a turbulent transition occur at this position and the velocity profiles upstream of 80% reveal a laminar boundary layer. For the tripped transition (b), the velocity profiles display the log and defect layers, which are typical characteristics of turbulent boundary layer.

Comparison between the time-averaged boundary-layer velocity profiles in inner variables for the natural and the tripped transitions at $x/L = 0.4$ is presented in Figure 11.9 for Reynolds number $Re_h = 64.4 \cdot 10^3$. It is shown that the velocity profiles collapse

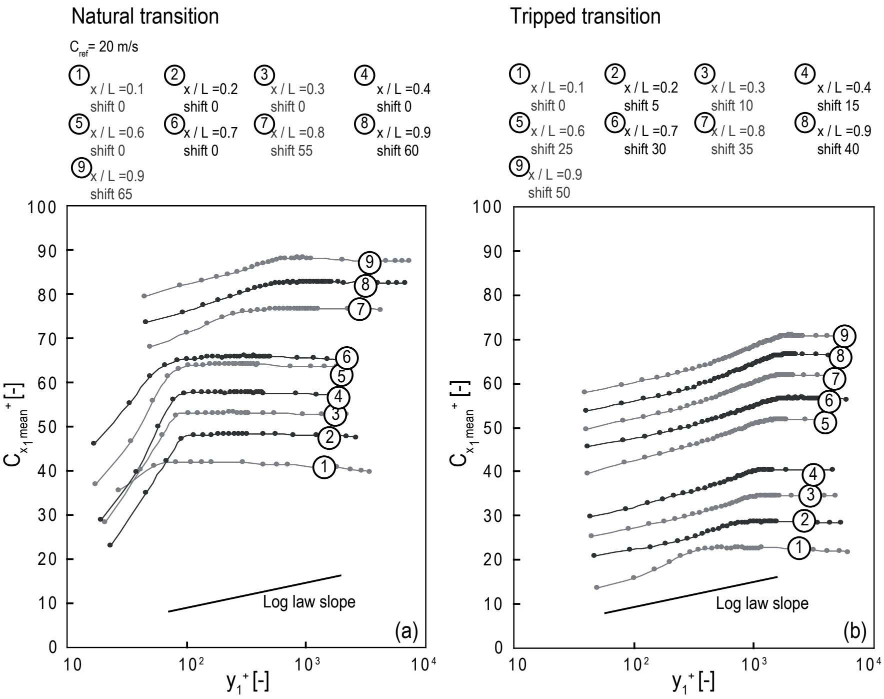

Figure 11.8: Dimensionless boundary-layer velocity profiles for different distances from leading edge and for (a) natural and (b) tripped transitions, $Re_h = 64.4 \cdot 10^3$

particularly well onto the theoretical laminar and turbulent boundary layers respectively. The displayed theoretical laminar velocity profile is the Kárman-Pohlhausen profile [95],

$$\frac{C_{x_1}}{C_e} = 2s - 2s^3 + s^4 \tag{11.4}$$

where $s = y/\delta$. The turbulent boundary-layer velocity profile is depicted by equation (11.3) where $K = 0.40$ is the Kármán constant and c found to be equal to 4.0. The Coles' wake strength is $\Pi = 0.6$.

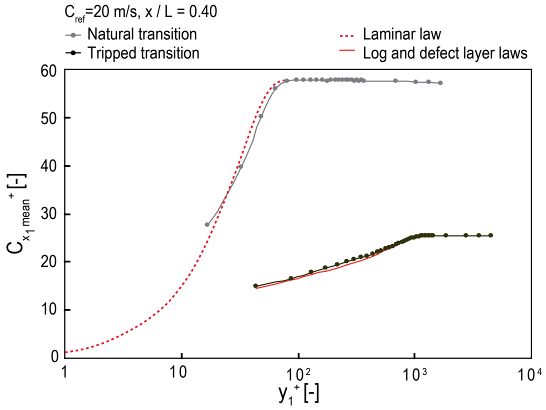

Figure 11.9: Dimensionless boundary-layer velocity profiles at $x/L = 0.4$ for natural and tripped transitions, $Re_h = 64.4 \cdot 10^3$

Chapter 12

Vortex-induced hydrofoil vibration

Vortex-induced vibration is relevant for studying the vortex shedding process since, apart from the shedding frequency, it reliably provides a convenient measure of the energy contained in the shedding mode. For the natural and the tripped transitions, the vortex-induced hydrofoil vibration is measured and analyzed for different free-stream velocities. The results are described in terms of vortex shedding frequency, normalized frequency, vortex-induced vibration amplitude and intermittency of the vortex shedding process.

12.1 Vortex shedding frequency and Strouhal number

The vortex-induced vibrations are measured with the help of the laser vibrometer focused on the hydrofoil surface at $(x/L,\ z/B) = (0.8,\ 0.75)$. For the natural (a) and the tripped (b) transitions, the waterfall spectra of the vibration signals are presented in Figure 12.1 for different free-stream velocities. The normalized frequency, fh/C_{ref}, is also shown. Most of the spectral energy is concentrated around the vortex shedding frequency, which increases quasi-linearly with the free-stream velocity. Comparison of the waterfall spectra for the two transition processes reveals that the vortex shedding frequency is lower for the tripped transition but that the spectral peak heights are increased significantly as compared to the natural transition. Besides, as the vortex shedding frequency approaches one of the natural frequencies of the hydrofoil, the resonance takes place with a significant increase in vibration. A lock-in of the vortex shedding frequency onto the structural eigenfrequency, $f_n = 890$ Hz, occurs and a plateau emerges, *i.e.* a constant shedding frequency for Reynolds number ranges from $Re_h = 35.4 \cdot 10^3$– $41.9 \cdot 10^3$ for the natural transition and from $Re_h = 48.3 \cdot 10^3$– $54.7 \cdot 10^3$ for the tripped transition.

The vortex shedding frequency, f_s, corresponding to the frequency of the dominating peak in the spectrum at the given free-stream velocity, normalized by the lock-in frequency, f_n, is plotted in Figure 12.2 (a) as a function of the reduced velocity, $C^* = C_{ref}/f_n h$, for the two transition processes. A quasi-linear relationship between the vortex shedding frequency and the velocity is observed, provided that no hydrofoil resonance frequency is excited. The vortex shedding frequency significantly decreases for the tripped transition. The Strouhal number $St_h = f_s h/C_{ref}$ is shown for the two transition cases in Figure 12.2 (b). The Strouhal number values are not constant over the entire free-stream velocity range. The trend for the natural transition is descending, while it is ascending for the

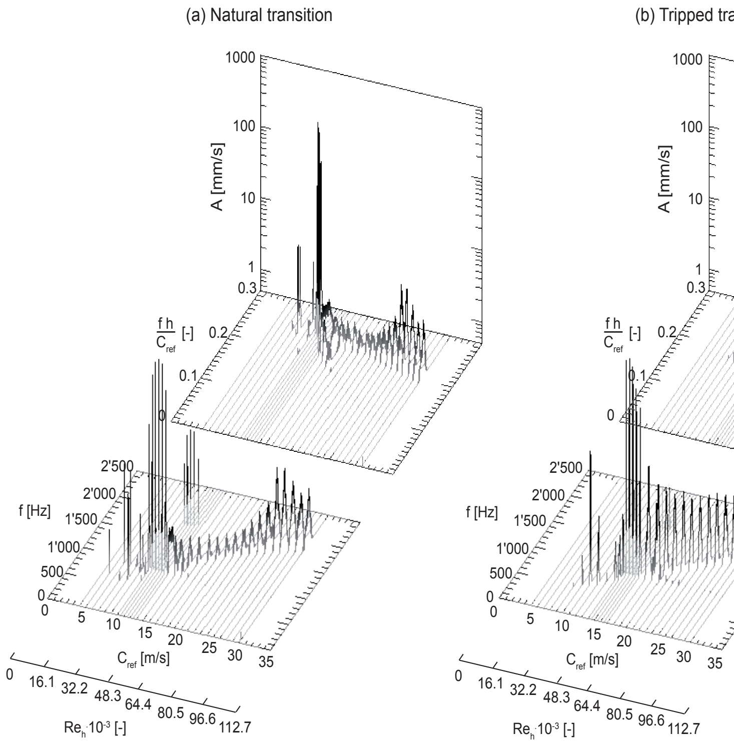

Figure 12.1: Waterfall spectra of the vortex-induced vibration signals for different free-stream velocities and for (a) natural and (b) tripped transitions, measured at $(x/L,\ z/B) = (0.8,\ 0.75)$

tripped case. This is largely due to the thickening and thinning of the boundary layer, respectively, at the trailing edge with increasing free-stream velocity. For the natural case, the boundary-layer turbulent transition moves upstream along the hydrofoil chord, which leads to a thickening of the trailing-edge boundary layer, chapter 11. For the tripped transition, a thinning of the boundary layer with increasing free-stream velocity corresponds to typical Reynolds effects. Normalized vortex shedding frequency using characteristic scales of wake formation instead of body dimensions and free-stream velocity is studied in chapter 15.

12.2 Vibration amplitude

The vibration signals for the natural and the tripped transitions for lock-off condition at $Re_h = 64.4{\cdot}10^3$ are shown in Figure 12.3. The time traces display amplitude modulation resulting from intermittent weak shedding cycles, which are typical of vortex dislocations. However, it is clearly evidenced that the vibration level is significantly increased with the tripped transition. The intermittency of the vortex shedding process appears to be reduced with the tripped transition. In Figure 12.4, the spectra of the above mentioned vibration signals are presented. The decrease of the vortex shedding frequency and the increase of the vibration level for the tripped transition are shown. Beside the vortex shedding frequency, the vibration spectra display energy in a less extent at the hydrofoil eigen frequencies. In the excitation spectra, specific energies occur at the eigen frequencies

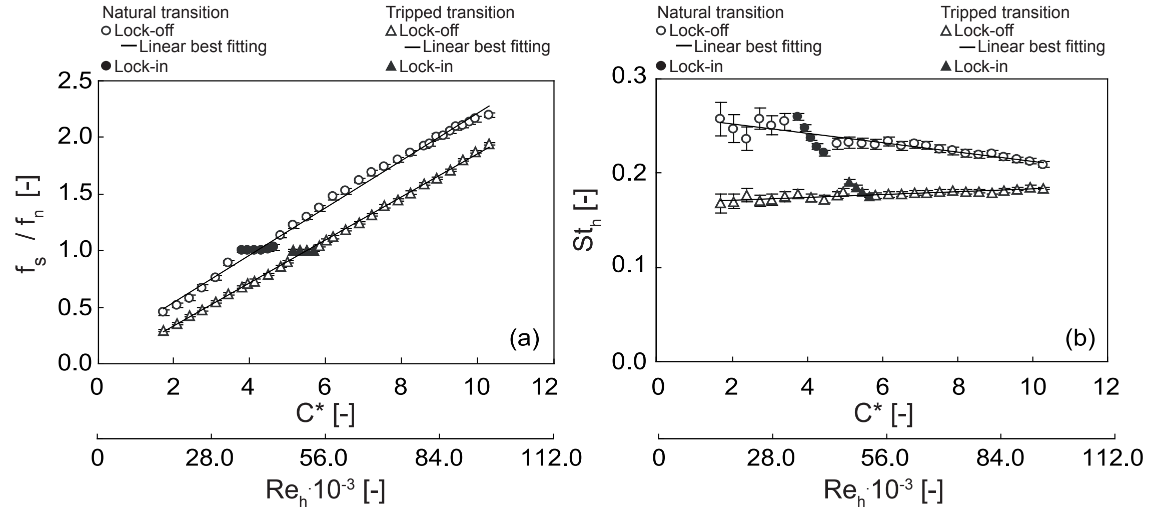

Figure 12.2: (a) Vortex shedding frequency and (b) Strouhal number for different reduced velocities and for natural and tripped transitions

of the structure and the vibration amplitudes at these frequencies are amplified because associated with peak value of the magnification factor.

The vibration amplitude of the hydrofoil, measured at $(x/L,\ z/B) = (0.8,\ 0.75)$ is presented in Figure 12.5. The amplitude is chosen to be the standard deviation of the vertical displacement velocity which is band-pass filtered around the shedding frequency. The logarithmic scale enhances the evolution for lock-off conditions and reveals a significant increase in the vibration level in the context of the tripped transition.

At this point, the increase of the vibration level with the tripped transition can arise from an increase of the vortex-span-wise organization, an increase of the vortex strength or from a combination of both. In the following chapters, this issue is investigated.

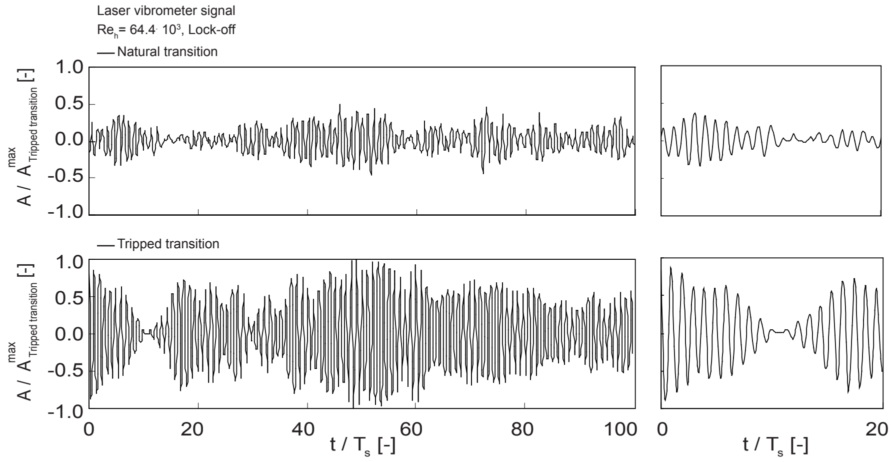

Figure 12.3: Vortex-induced vibration signal, measured at $(x/L,\ z/B) = (0.8,\ 0.75)$, for lock-off condition $Re_h = 64.4 \cdot 10^3$ and for natural and tripped transitions

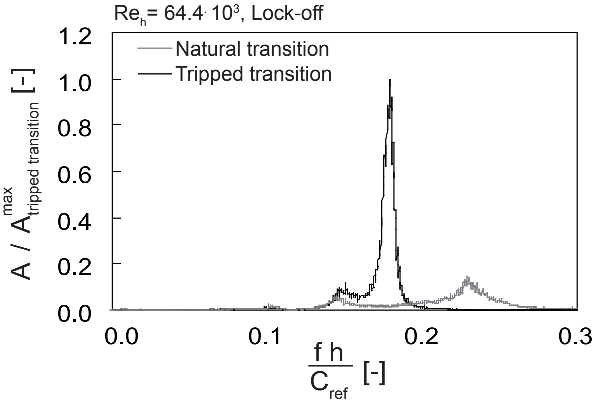

Figure 12.4: Vortex-induced vibration spectra, measured at $(x/L,\ z/B) = (0.8,\ 0.75)$, for lock-off condition $Re_h = 64.4 \cdot 10^3$ and for natural and tripped transitions

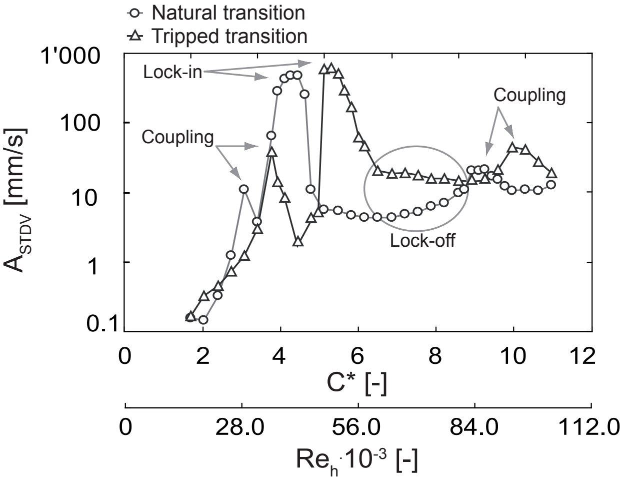

Figure 12.5: Vibration amplitude of the hydrofoil, measured at $(x/L,\ z/B) = (0.8,\ 0.75)$, for different reduced velocities and for natural and tripped transitions

Chapter 13

Wake structure

The wake structure is analyzed with the help of simultaneous wake high-speed visualization and vortex-induced vibration measurement for the two transition processes and for both lock-off and lock-in conditions. The results are described in terms of vortex span-wise organization, vortex shedding process coherence and intermittency. Time-frequency analysis of the vortex-induced vibration signals is proposed.

13.1 Simultaneous wake high-speed visualization and vortex-induced vibration

13.1.1 Lock-in condition

For the two transition processes and lock-in conditions, torsional mode, the wake structures and the related hydrofoil vibration signals are presented in Figure 13.1. Cavitation is used for the wake flow visualization. In terms of vortex span-wise organization, cavitation is a passive agent, chapters 8 and 10. The shedding process is in phase along the span and the vibrations signals virtually sinusoidal. The vortex shedding from the hydrofoil creates fluid excitation forces, which causes the structural resonance. The resultant hydrofoil eigen motion influences the flow field, giving rise to fluid-structure coupling and modifying the magnitude of the excitation forces. For the tripped transition and in comparison with the natural one, the amplitude of vibration is increased, which is mainly due to the increase of the free-stream velocity. For the tripped transition, the vortex shedding frequency being decreased, Figure 12.2, the coincidence of the shedding and resonance frequencies occurs for higher free-stream velocities.

13.1.2 Lock-off condition

For lock-off conditions, the vortex shedding is not a steady, harmonic, two-dimensional process [21]. Two-dimensional bodies in uniform flow are unlikely to shed two-dimensional vortices. Simultaneous high-speed wake visualizations and vortex-induced hydrofoil vibration measurements are presented in Figures 13.2 and 13.3 and illustrates this issue. For the natural transition, Figures 13.2 (a) and 13.3 (a), the vibration signal exhibits amplitude modulation resulting from intermittent weak shedding cycles, which are typical

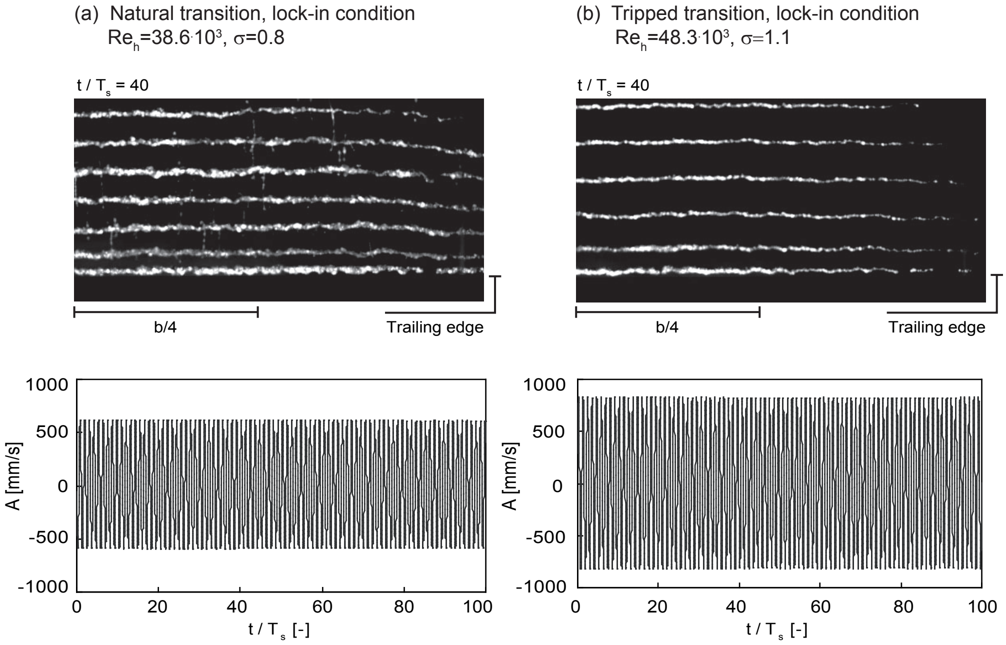

Figure 13.1: Top-view visualization of cavitation vortex street and vortex-induced vibration signal for lock-in condition, torsional mode. (a) Natural $Re_h = 38.6 \cdot 10^3$ and (b) tripped $Re_h = 48.3 \cdot 10^3$ transitions

of vortex dislocations [109]. Indeed, a direct relationship is observed between the vortices span-wise organization and the vortex-induced vibration level. For parallel-vortex shedding mode, the fluctuating force on the body is maximized and the vibration level is significantly increased. In contrast, for three-dimensional vortex shedding, the vibration level is reduced. For the tripped transition, Figures 13.2 (b) and 13.3 (b), and in comparison with the natural one shown in (a), the overall vibration level is increased, as is the vortex span-wise organization. The tripped transition promotes the re-establishment of organized vortex shedding. The cavitation vortices essentially exhibit a parallel vortex shedding mode, which is a fundamental change in the vortex generation process.

13.2 Vortex shedding process coherence

The lack of two dimensionality of the vortex shedding process is assessed by investigating the span-wise variation of some unsteady quantity related to vortex shedding, such as fluctuating surface pressure, sectional lift force or a fluctuating velocity in the wake. The coherence between two points a distance z apart is given by

$$\gamma_{xy}^2(f) = \frac{\left|\overline{S_{xy}}(f)\right|^2}{\left|\overline{S_{xx}}(f)\right| \left|\overline{S_{yy}}(f)\right|} \tag{13.1}$$

where $S_{xx}(f) = X^*(f)X(f)$ and $S_{yy}(f) = Y^*(f)Y(f)$. $X(f)$ is the Fourier transform of $x(t)$. The coherence length is defined by the integral, [15]

$$L_{coher} = \int_0^\infty \gamma_{xy}^2(f_s)dz \tag{13.2}$$

The pictures of the high speed visualizations of cavitation vortices for natural and tripped transitions for both lock-in and lock-off conditions, typical samples in Figures 13.1 to 13.3, are processed in order to investigate the span-wise variation of the unsteady pixel light. The reference point is chosen to be at the half height of the presented pictures and at about one third of the picture width from the left side. At this point the z coordinate is set to zero. The coherence of the light intensity with the reference one is calculated for every pixel in the span-wise direction. The averaging is performed on 16 equal segments of the time signal. The value of interest is the coherence at the vortex shedding frequency $\gamma_{xy}^2(f_s)$. The coherence of the wake structures is plotted in Figure 13.4 for natural and tripped transitions. For lock-off condition, Figure 13.4 (a) (b) (c) (d), the coherence value is obviously maximal in the direct proximity of the reference point, $z = 0$. For increasing span-wise distance, the decay of the coherence value is revealed. Nevertheless, the decay is clearly less pronounced for the tripped transition, (b) and (d), than for the natural one, (a) and (c). This reveals a more organized wake structure in the context of a tripped transition. For the natural transition, the coherence length, equation (13.2), is $L_{coher} = 4.0h$ and $3.7h$ for $Re_h = 64.4 \cdot 10^3$ and $70.8 \cdot 10^3$ respectively. For the tripped transition, the coherence length is respectively increased to $L_{coher} = 8.9h$ and $7.4h$. For lock-in condition, Figure 13.4 (e) (f), the coherence is maximized in the quasi-entire field of view which revealed parallel vortex shedding process. The coherence length is up to $L_{coher} = 22h$.

13.3 Vortex shedding process intermittency

The three-dimensional feature of vortex shedding process for natural and tripped boundary-layer transitions is presented in Figures 13.2 and 13.3. The vortex span-wise organization is significantly enhanced with the tripped transition. Hereafter, the intermittency of the vortex shedding process is considered with the help of the vortex-induced vibration signal. The intermittency is defined as the standard deviation of the vibration signal normalized by the maximum vibration amplitude and multiplied by a constant for comparison with the sine function, equation (13.3). The maximum vibration amplitude is defined as the vibration value at 99% of the cumulative probability density function of the vibration signal. The resulting intermittency factor is 0 for a sine function and it can increase up to 1, consistent with the intermittency level.

$$\lambda = 1 - \sqrt{2}\frac{A_{stdv}}{A_{\max}} \tag{13.3}$$

The intermittency factor is calculated for the two transition processes and for different free-stream velocities. The intermittency factor tends toward 0 for both transition processes for lock-in conditions, Figure 13.5 (a). For lock-off, Figure 13.5 (b), the intermittence values for the tripped transition are 15% below those for the natural transition. Since the vortex-induced vibration and span-wise organization are directly related, the occurrence of vortex dislocations is less frequent for the tripped transition, which is in accordance with the presented high speed visualization, Figures 13.2 and 13.3.

13.4 Time-frequency analysis

The transient behavior of the vortex shedding process for natural and tripped transitions, is analyzed through the computation of the short-time Fourier transform, equation (8.3), of the vortex-induced vibration signals. Part of the time signal is considered and the time-frequency representation is shown in Figure 13.6. For lock-in conditions, $Re_h = 38.6 \cdot 10^3$ and $48.3 \cdot 10^3$ for natural and tripped transitions respectively, the time signals are virtually sinusoidal and free from any amplitude modulation. As a result, the spectrograms do not reveal any change with the time. For lock-off conditions and natural transition, the intermittency of the vortex shedding process is clearly evidenced. Cells of significant vibration amplitude are followed by ones of negligible amplitude. For the tripped transitions, the vortex-induced vibration is significantly increased and the vortex shedding process appears to be less intermittent. In terms of frequency, the process is revealed to be broad band for the natural transition and narrow band for the tripped one. The vortex-induced vibration integrating the pressure fluctuation along the entire span, vortex cells of different shedding frequency obviously occur along the span for the natural transition. The shedding frequency difference is believed to be large enough to cause vortex dislocations, as seen in Figures 13.2 and 13.3.

13.5 Discussion

Vortex dislocations are generated between span-wise cells of different frequency when the vortices in each cell move out of phase with each other. These dislocations grow rapidly in the span-wise direction into large scale structures as they travel downstream, [123]. In the case of the natural laminar-turbulent transition, the non-uniform span-wise turbulence development in the boundary layer has a direct influence on the vortex street pattern. The transition to turbulent flow is initiated via a subsequent onset of three-dimensional perturbations, Figure 3.2. The span-wise non-uniformities in the boundary-layer flow lead to slight instantaneous variations in vortex shedding frequencies along the span, which are sufficient to trigger vortex dislocations. On the other hand, the tripped transition reduces the span-wise non-uniformities in the boundary-layer transition process. Thus, the span-wise organization of the vortices is enhanced overall. The vortices are shed in phase along the span, which leads higher amplitude and less intermittent induced vibration signals. The residual three-dimensional feature of vortex shedding is believed to arise from the turbulence of the shear layers and the wake. The intrinsically developed turbulence and secondary vortical structures of the shear layers interact in a complex manner with the stability of the vortex street, [108].

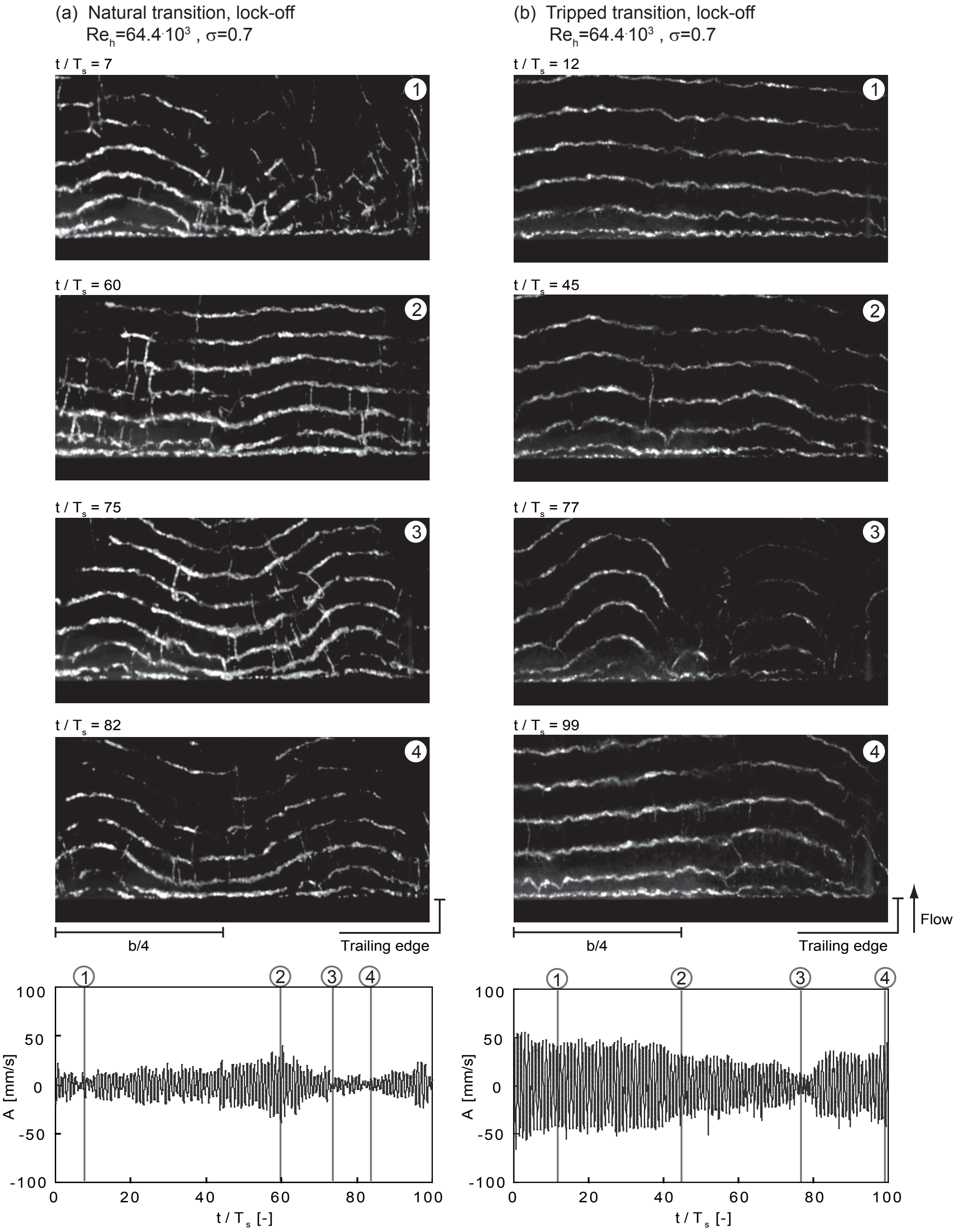

Figure 13.2: Top-view visualization of cavitation vortex street and vortex-induced vibration signal for lock-off condition, $Re_h = 64.4 \cdot 10^3$. (a) Natural and (b) tripped transitions

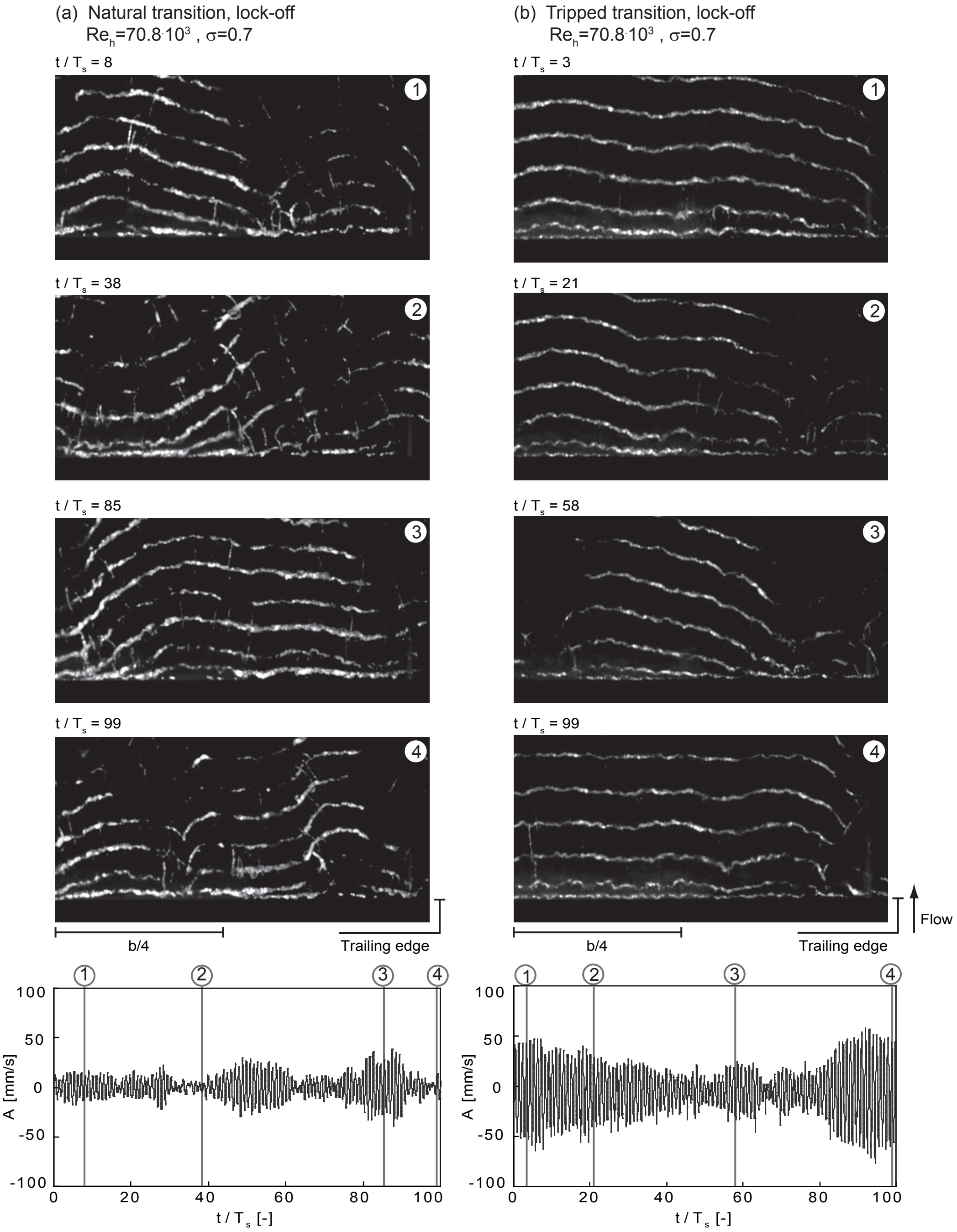

Figure 13.3: Top-view visualization of cavitation vortex street and vortex-induced vibration signal for lock-off condition, $Re_h = 70.8 \cdot 10^3$. (a) Natural and (b) tripped transitions

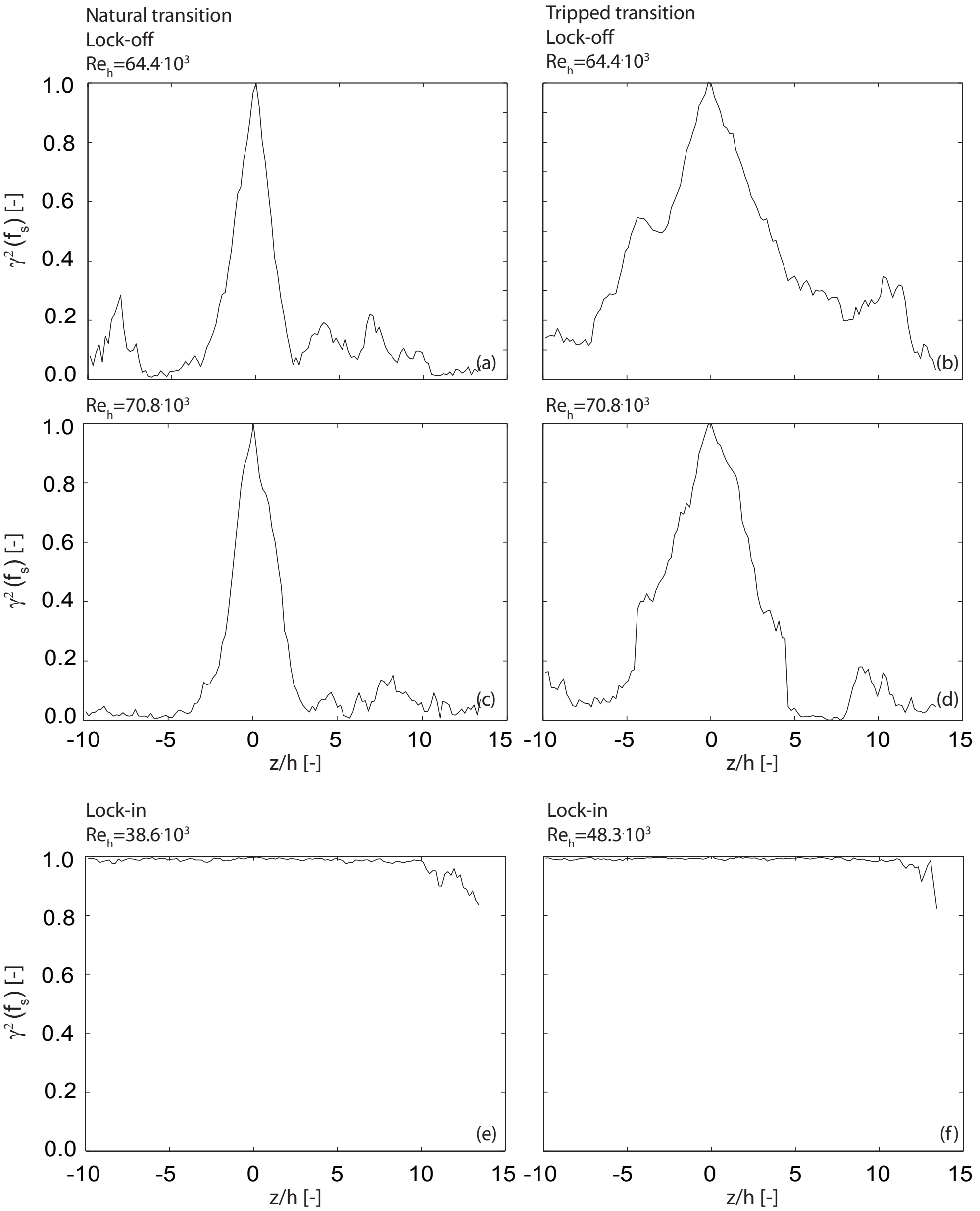

Figure 13.4: Coherence at the vortex shedding frequency of the high-speed visualization pixel light intensities, typical samples in Figures 13.1 to 13.3, for natural and tripped transitions

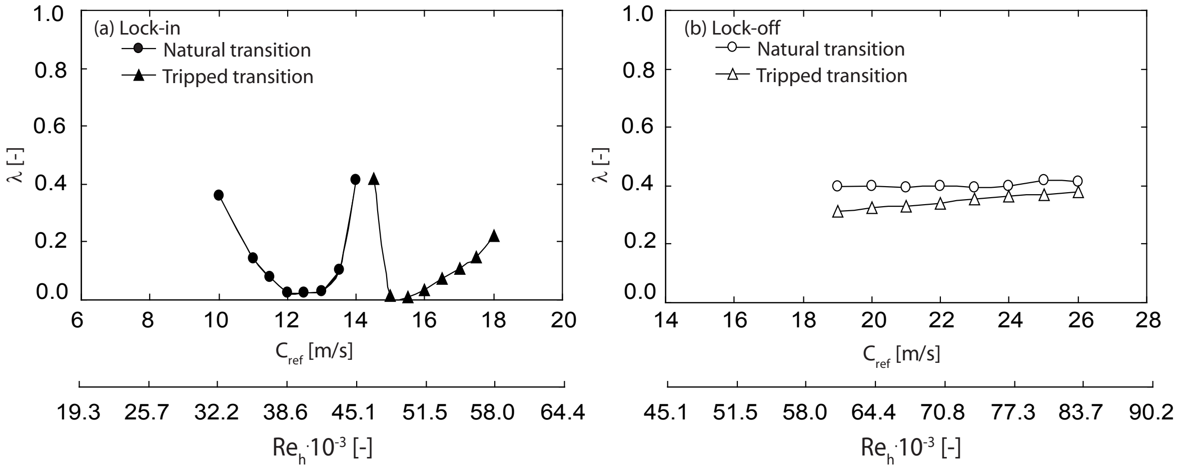

Figure 13.5: Intermittency factor of the vortex-induced vibration signal for natural and tripped transitions. (a) Lock-in, torsional mode, and (b) lock-off conditions. Cavitation free.

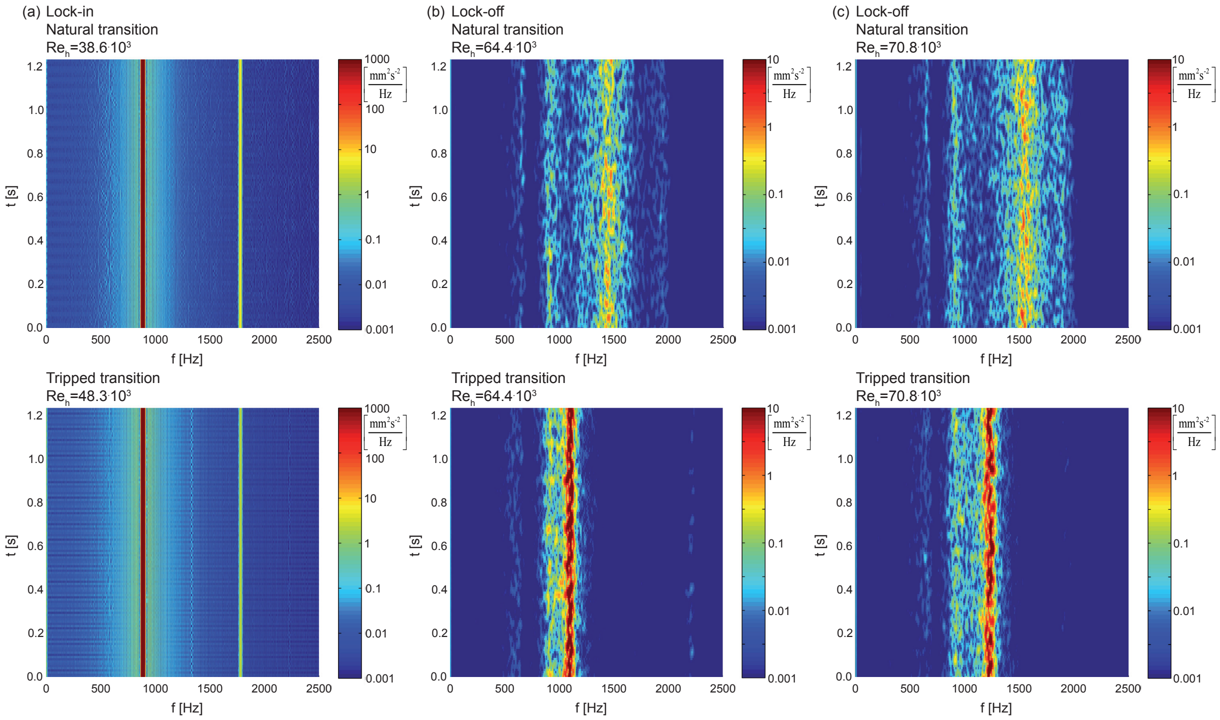

Figure 13.6: Spectrograms of the vortex-induced vibration signal for lock-in and lock-off conditions and for natural and tripped transitions. Cavitation free.

Chapter 14

Wake flow

Single-point two-component laser Doppler velocimetry is used to measure the hydrofoil wake flow for the natural and the tripped transitions. For different free-stream velocities, the vortex formation region is analyzed with traverse measurements along and across the wake. The results are described with time-averaged velocity profiles, velocity fluctuations and vortex strength. In the far field, at different distances from the trailing edge, the wake flow is analyzed in the context of traverse measurement across the wake and in terms of time-averaged velocity profiles, velocity fluctuations, wake energies and inter-vortex spacings.

14.1 LDV velocity profiles: Near field

14.1.1 Vortex formation region

The end of the vortex-formation region is determined as the position of the maximum stream-wise velocity fluctuations off the wake centerline, $y/h = 0.33$. Figure 14.1 displays these fluctuations for different free-stream velocities and for (a) natural and (b) tripped transitions. For clarity, the fluctuation velocity profiles are shifted on the vertical axis. Besides, the maximum velocity fluctuation cannot be directly compared because the traverse measurements are not made at the same position relative to the vortex center. It is shown that the vortex-formation distance decreases with increasing Reynolds number, which is in agreement with Norberg's [81] measurements in a cylinder wake. Nevertheless, this feature is more pronounced for the natural transition than for the tripped case. For free-stream velocities in the range of $Re_h = 16.1 \cdot 10^3$ to $Re_h = 87.0 \cdot 10^3$, the formation region is reduced from $(x - L)/h = 1.3$ to 0.5 and 0.9 to 0.7, respectively.

14.1.2 Time-averaged velocity profiles

Figure 14.2 presents traverse measurements across the wake at the end of the vortex formation region for natural transition and different free-stream velocities. Normalized mean (a) stream-wise and (b) transverse velocity profiles are shown with associated fluctuations, (c) and (d). For clarity, the profiles are shifted on the horizontal axis. For the tripped transition, the same wake characteristics are plotted in Figure 14.3.

For both cases and for the different free-stream velocities, the end of the vortex formation region corresponds to zero maximum stream-wise velocity defect. For shorter or

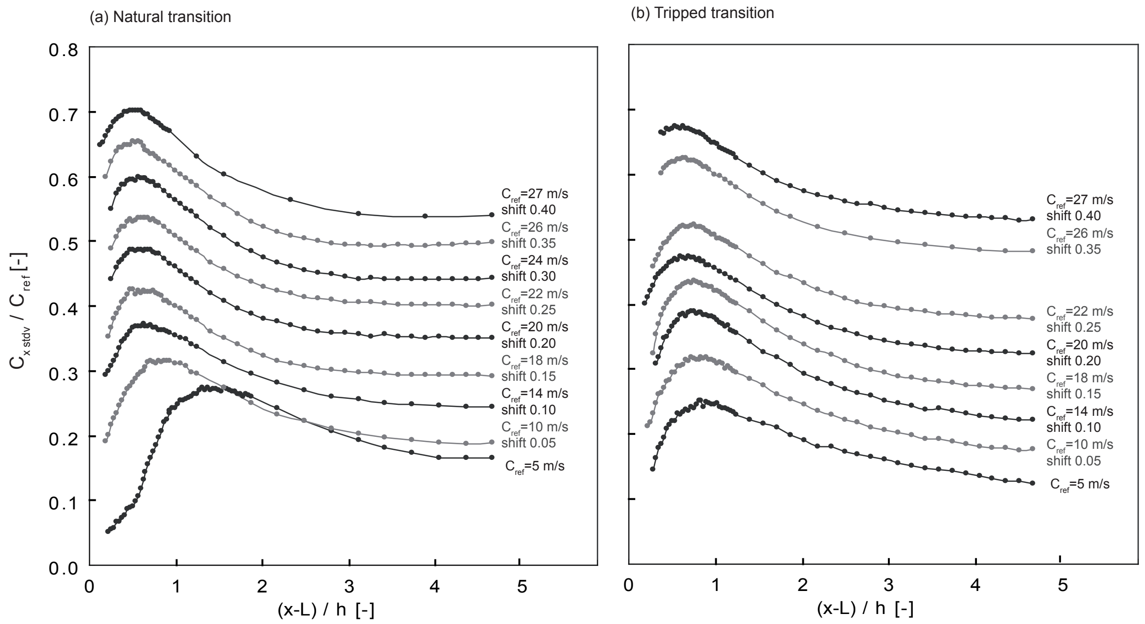

Figure 14.1: Normalized stream-wise velocity fluctuations along the wake at $y/h = 0.33$ for different free-stream velocities and for the (a) natural and (b) tripped transitions

longer distances from the trailing edge, the mean flow exhibits a backflow, negative mean velocity or coflow, positive mean velocity, respectively. Thus, the zero mean stream-wise velocity criterion can be used to define the vortex-formation region in the wake of this hydrofoil geometry. Nevertheless, the universality of this criterion has yet to be shown.

The width of the wake is defined as the cross-stream distance between the maxima of the stream-wise velocity fluctuations. For increasing free-stream velocity, the trend of the wake width for the natural transition ascends while for the tripped case it descends marginally, Figures 14.2 (c) and 14.3 (c). In chapter 15, the measurement of this characteristic wake scale permits the assessment of the normalized vortex shedding frequency proposed by Griffin [59].

Transverse mean velocity profiles, Figures 14.2 (b) and 14.3 (b), reveal positive and negative values for respectively negative and positive y-coordinates and suggest a convergence of the mean flow towards the wake centerline. The maximum transverse velocity fluctuations are shown to occur on the wake centerline, Figures 14.2 (d) and 14.3 (d).

14.1.3 Vortex strength

In chapters 12 and 13 respectively, notable influences of the tripped boundary layer on the vortex-induced vibration and vortex span-wise organization are presented. In this section, the vortex strength is estimated with the help of velocity measurements across the wake at the end of the vortex-formation region. The strength of the Rankine vortex is defined below, where a is the viscous core radius and $C_{Rankine}$ the tangential velocity at its edge,

$$\Gamma = 2\pi a C_{Rankine} \tag{14.1}$$

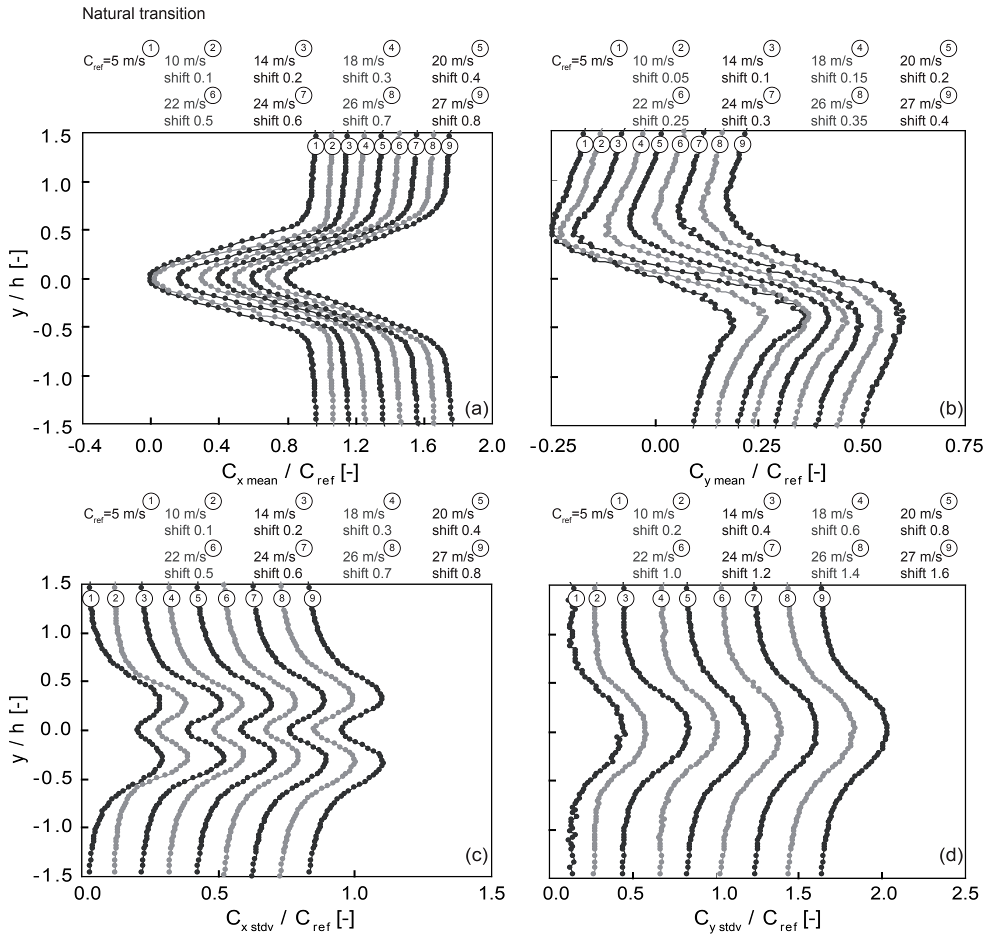

Figure 14.2: Traverse measurements across the wake at the end of the vortex-formation region, for the natural transition and different free-stream velocities: Normalized mean (a) stream-wise and (b) transverse velocity profiles and (c) stream-wise and (d) transverse velocity fluctuations

The velocity at the edge of the viscous core cannot be estimated using time-averaged velocity measurements. Instantaneous velocity must be considered in order to distinguish the velocity at the edge of the viscous core and the vortex advection velocity. Histograms of the stream-wise and transverse velocities at the end of the formation region are presented in Figure 14.4 for $Re_h = 64.4 \cdot 10^3$. For every vertical position, the number of samples per bin is scaled by the maximum number of samples. Moreover, for every vertical position, the low $C_{x_{low}}$ and high $C_{x_{high}}$ stream-wise velocities are defined as the velocities at 1% and 99% of the stream-wise velocity cumulative probability density function, respectively. These velocities profiles are plotted in Figure 14.4. The vertical coordinate of the maximum stream-wise velocity fluctuation corresponds to the farthest edge of the viscous core from the wake centerline. Similarly, the centerline vertical coordinate corresponds to the nearest edge of the viscous core from the wake centerline. Therefore, the wake width, y_f, is four times the core radius, a, which is consistent with Blake [20].

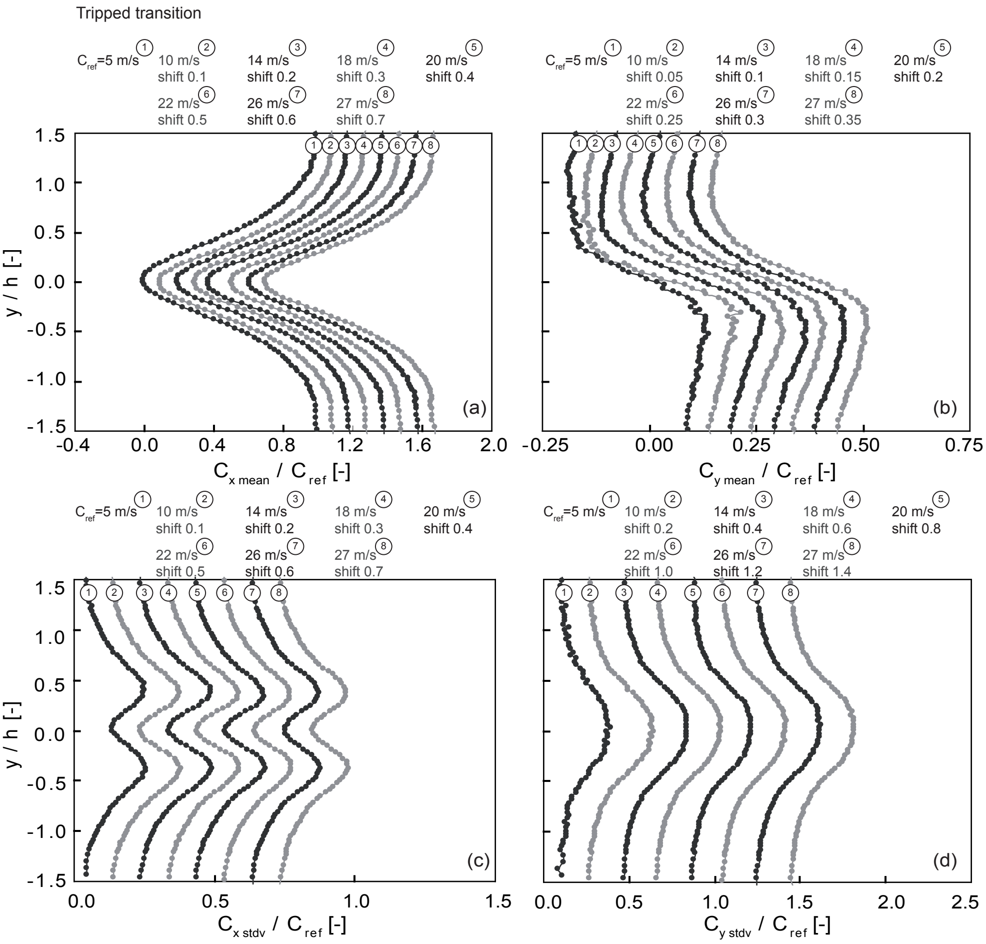

Figure 14.3: Traverse measurements across the wake at the end of the vortex-formation region, for the tripped transition and different free-stream velocities: Normalized mean (a) stream-wise and (b) transverse velocity profiles and (c) stream-wise and (d) transverse velocity fluctuations

According to these statements, the following relationships are written,

$$\begin{aligned} &C_{x_{high}}(y = \max(C_{x_{stdv}})) = C_{Rankine} + C_{adv} \\ &C_{x_{low}}(y = 0) = -C_{Rankine} + C_{adv} \end{aligned} \tag{14.2}$$

where C_{adv} is the advection velocity of the vortices, which is assumed to be constant on the vortex core diameter. The velocity at the edge of the viscous core, $C_{Rankine}$, is obtained by summing the above relations. This velocity can also be obtained with the low $C_{y_{low}}$ and high $C_{y_{high}}$ transverse velocities, which are defined as the transverse velocities at 1% and 99% of the transverse velocity cumulative probability density function, respectively. Thus, the following expression is written,

$$\max(C_{y_{high}}) = -\min(C_{y_{low}}) = C_{Rankine} \tag{14.3}$$

The differences of the vortex maximal tangential velocity obtained either with the stream-wise or transverse velocity are not significant and are subsumed by the error bar of the evaluated vortex strength. In Figure 14.5, the estimated vortex strength is presented for different free-stream velocities and for the natural and the tripped transitions. A significant increase in the vortex strength is observed with the tripped transition, from 26% at $Re_h = 16.1 \cdot 10^3$ to 12% at $Re_h = 87.0 \cdot 10^3$. Consequently, the increase of the vortex-induced vibration with the tripped transition, Figure 12.5, results from an increase in the vortex span-wise organization, shown in Figures 13.2 and 13.3, and an increase in the vortex strength, Figure 14.5.

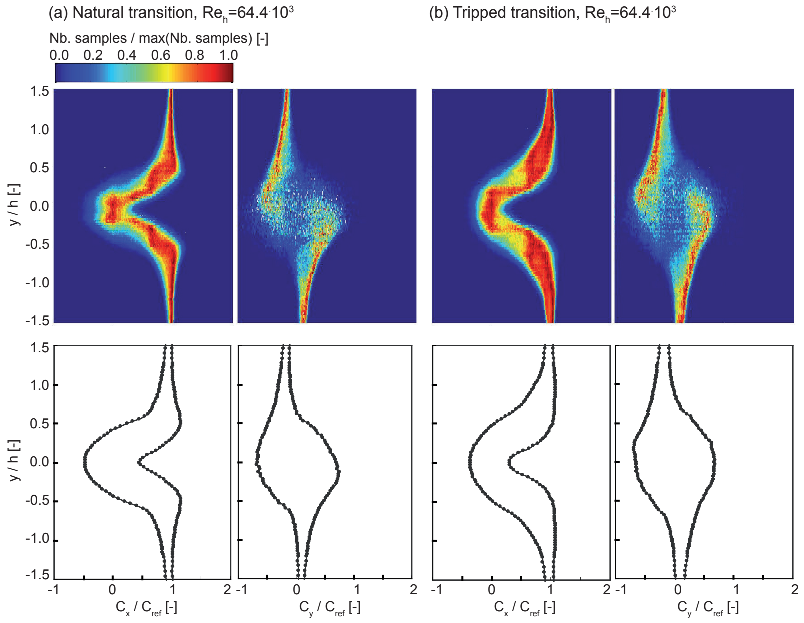

Figure 14.4: Histograms of stream-wise and transverses velocities at the end of the vortex formation region and for the (a) natural and (b) tripped transitions

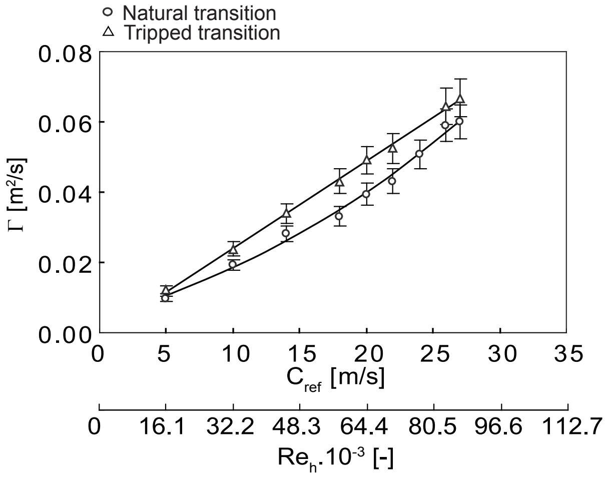

Figure 14.5: Vortex strength at the end of the formation region for different free-stream velocities and for the natural and tripped transitions

14.2 LDV velocity profiles: Far field

14.2.1 Time-averaged velocity profiles

Figure 14.6 illustrates, for the natural and tripped transitions at $Re_h = 64.4 \cdot 10^3$, the wake flow measurements at different stations, namely $x = L + h$, $L + 2h$, $L + 3h$, $L + 4h$ and $L + 5h$, downstream from the trailing edge. The normalized mean (a) stream-wise and (b) transverse velocity profiles are shown as well as their fluctuations (c) and (d). For clarity, the profiles are shifted on the horizontal axis.

The tripped transition produces a higher maximum stream-wise velocity defect compared to the natural transition. This is largely due to the thickening of the boundary layer at the trailing edge, Figure 11.1, and thus of the wake, with the tripped transition. As the flow progresses downstream, the maximum velocity defect is reduced. The evolution of the velocity defects with downstream distance from the trailing edge is presented in the Figure 14.7.

At the station $x = L + h$, the stream-wise velocity fluctuations are characterized by peaks produced by the passing of the vortices, Figure 14.6 (c). For the tripped and the natural transitions, these peaks move outward from the center line and weaken in intensity with increasing distance from the trailing edge. The maxima of stream-wise velocity fluctuations with downstream distance from the trailing edge are shown on Figure 14.8 (a). The increases in the fluctuations in the context of the tripped transition as compared to the natural transition are 4.5, 9.9, 8.2 and 6.0% for $x = L + 1h$, $L + 2h$, $L + 3h$, $L + 4h$, respectively. The increase of velocity fluctuation with the tripped transition is in accordance with the increase of the vortex strength, Figure 14.5. In addition to the increase in maximum fluctuations, the characteristic shape of the stream-wise velocity fluctuations, which define the wake width, are held farther from the trailing edge for the tripped transition as compared to the natural transition, Figure 14.6 (c). The station $x = L + 3h$ is the last position where the above-mentioned characteristic shape is recognizable for the natural transition, which is still the case at $x = L + 5h$ for the tripped transition. The increase of this distance downstream of the trailing edge indicates a reduction of the vorticity dissipation. The three-dimensional aspect of the vortex street for the natural transition also plays a key role in the sense that the characteristic shape is no more recognizable for small distances from the trailing edge. Previously, as illustrated in Figures 13.2 and 13.3, it was shown that the vortex span-wise organization is significantly greater for the tripped transition as compared to the natural transition.

Figure 14.6 (b) and (d) present transverse mean velocity profiles and fluctuations. A significant increase in the transverse velocity fluctuations is observed for the tripped transition as compared to the natural transition. Again, the increase of velocity fluctuation with the tripped transition is in accordance with the increase of the vortex strength, Figure 14.5. The maximum fluctuation at each station is plotted on Figure 14.8 (b).

14.2.2 Wake energies and velocity fluctuations

Defined by Roshko [92] and introduced in section 8.3, the stream-wise and transverse energy intensities of the flow at a given point are $(C_{x_{stdv}}/C_{ref})^2$ and $(C_{y_{stdv}}/C_{ref})^2$ respectively. The integrals of the intensities over a line normal to the wake are called the wake stream-wise and transverse energies. Their sum is the total wake energy, equations

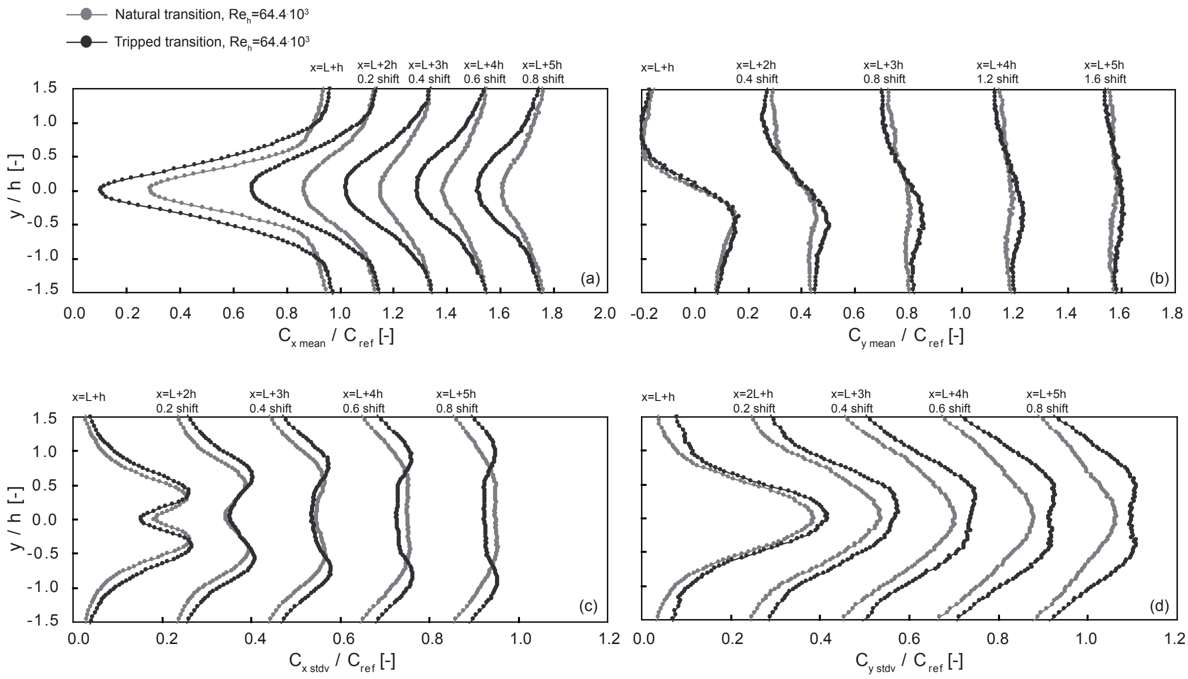

Figure 14.6: Traverse measurements across the wake at different stations downstream from trailing edge for the natural and tripped transitions: Normalized mean (a) stream-wise and (b) transverse velocity profiles and (c) stream-wise and (d) transverse velocity fluctuations

(8.6) and (8.7). The wake stream-wise, transverse and total energies are presented in Figure 14.9. With increasing distance from the trailing edge, a decay in the total energies occurs. In comparison with the natural transition, the energies are significantly increased for the tripped transition. The increase of wake energies with the tripped transition are in accordance with the increase of the vortex strength, Figure 14.5.

For different free-stream velocities and for natural and tripped transitions, the stream-wise and transverse velocity fluctuations at the position $(x, y) = (L + h, h)$ are presented in Figure 14.10. For both components, the velocity fluctuations are increased in the context of the tripped transition. As the free-stream velocity increases, the difference of velocity fluctuation between the two cases decreases: For the natural transition case, the boundary-layer transition moves upstream to the leading edge for increasing free-stream velocity so that the natural transition case tends to the tripped case. For lock-in conditions, the velocity fluctuations are maximized.

The stream-wise and transverse velocity fluctuations on the wake centerline are presented in Figure 14.11 for different reference velocities. For lock-off conditions, the velocity fluctuations increase quasi-linearly with the free-stream velocity and no particular difference are noticed between the natural and the tripped transitions. Here again, the velocity fluctuations are maximized for lock-in conditions.

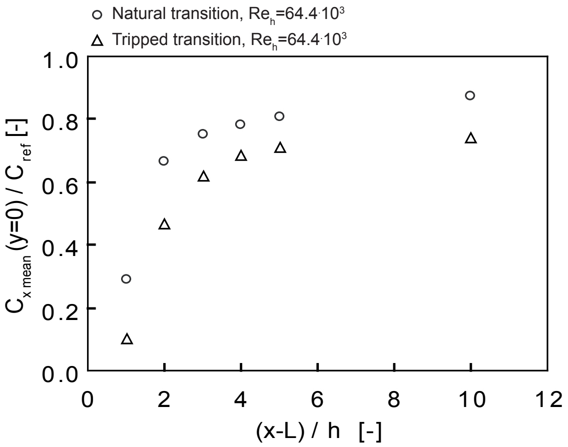

Figure 14.7: Maximum stream-wise velocity defect for traverse measurement across the wake at different stations downstream from the trailing edge

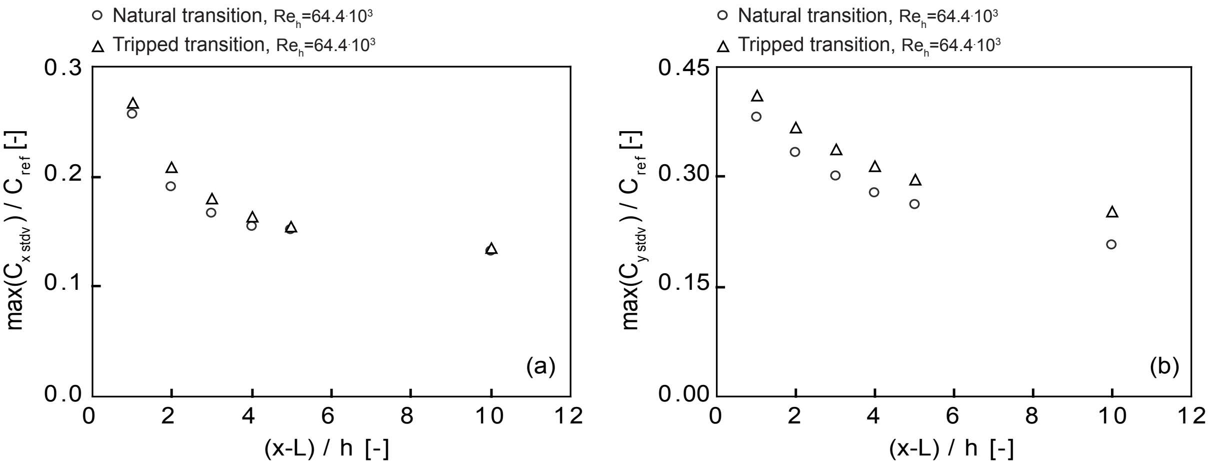

Figure 14.8: Maximum (a) stream-wise and (b) transverse velocity fluctuations for traverse measurement across the wake at different stations downstream from the trailing edge

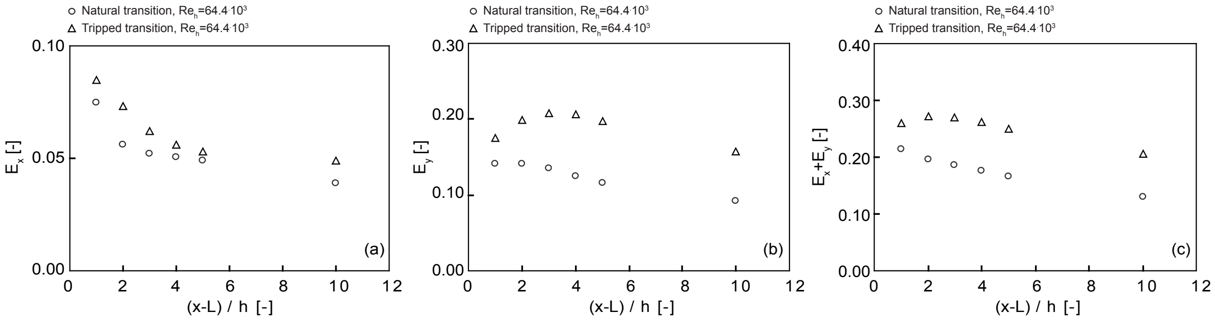

Figure 14.9: Wake (a) stream-wise (b) transverse and (c) total energies at different stations downstream from the trailing edge

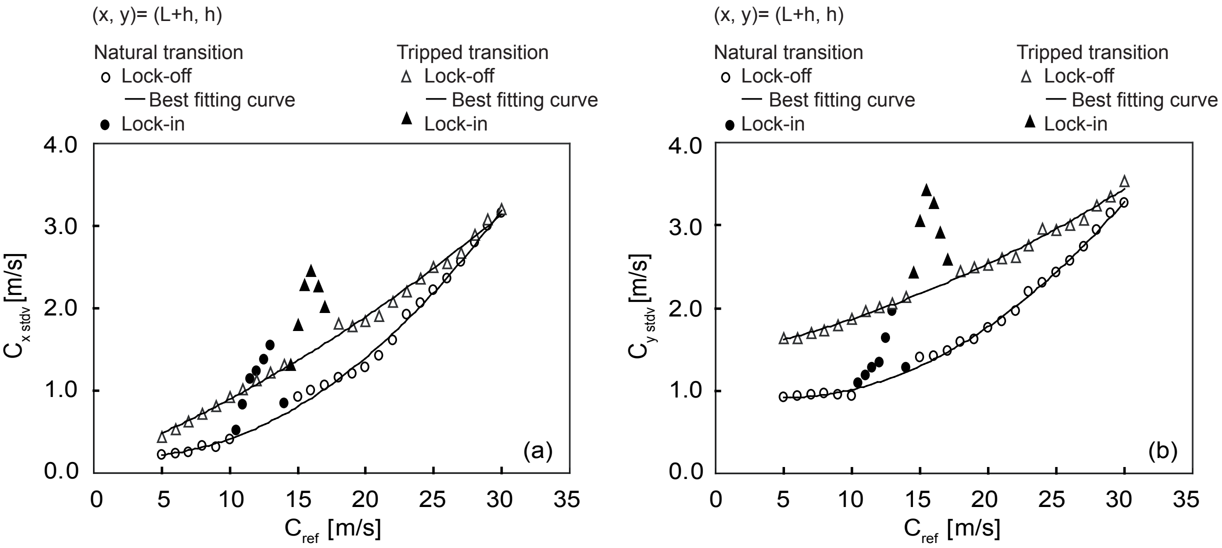

Figure 14.10: (a) Stream-wise and (b) transverse velocity fluctuations for measurement downstream from the trailing edge at $(x, y) = (L + h, h)$

14.2.3 Inter-vortex spacings

For the natural and the tripped transitions, the similarity of the wake is below investigated. The stream-wise inter-vortex spacing is noted a_s and the cross-stream inter-vortex spacing b_s. Theoretically, the stability of vortex street is obtained for specific vortex spacing ratio $b_s/a_s = 0.281$, Kárman [115] and [116]. The vortex spacings a_s and b_s are estimated with the help of the traverse velocity measurement across the wake. The stream-wise inter-vortex spacing a_s is

$$a_s = \frac{C_{adv}}{f_s} \tag{14.4}$$

where C_{adv} is the mean vortex advection velocity on the distance a_s and f_s the vortex shedding frequency. The vortex advection velocity C_{adv} is estimated with equation (14.2) described in subsection 14.1.3. Besides, the wake width y_f, which is defined as the cross-stream distance between the maxima of the stream-wise velocity fluctuations in the context of a transverse measurement across the wake, is four times the vortex core radius a, [20]. The cross-stream inter-vortex spacing is therefore,

$$b_s = \frac{y_f}{2} \tag{14.5}$$

The vortex spacing ratio b_s/a_s is estimated at different stations downstream from the trailing edge. The traverse measurements across the wake are shown in Figure 14.6. Figure 14.12 presents the evolution of the vortex spacing ratio for Reynolds number $Re_h = 64.4 \cdot 10^3$. The evolutions for the natural and tripped transitions are virtually identical. This result reveals the similarity of the wakes.

From this point, it is believed that a unique value of normalized vortex shedding frequency for the two cases study can be obtained when characteristic scales of wake

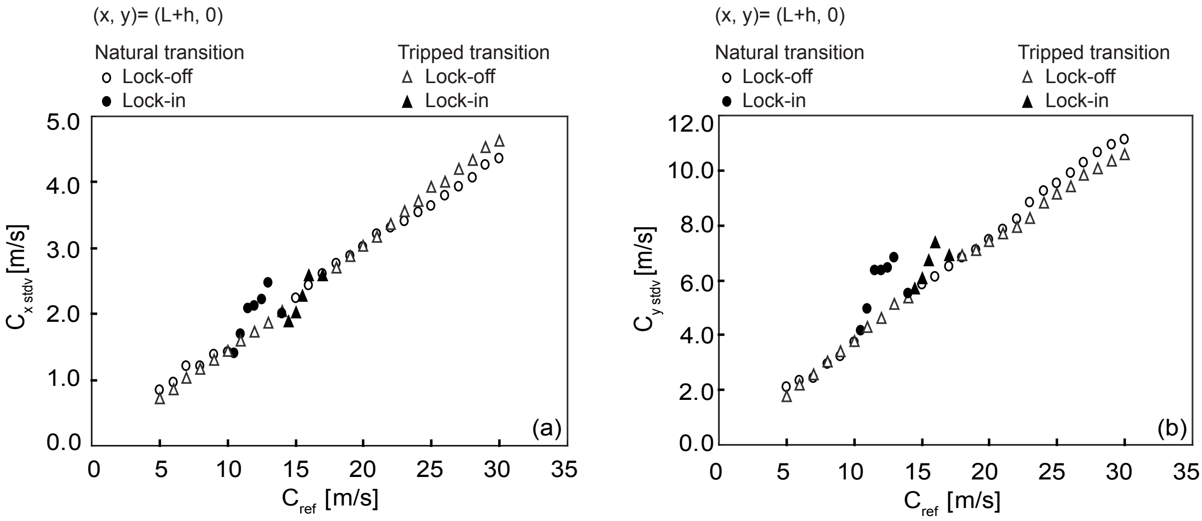

Figure 14.11: (a) Stream-wise and (b) transverse velocity fluctuations for measurement downstream from the trailing edge at $(x, y) = (L + 2h, 0)$

formation are used instead of body dimensions and free-stream velocity. Indeed, the commonly used Stouhal number $St = f_s h/C_{ref}$ plotted in Figure 12.2 is not constant on the entire free-stream velocity range and not equal for the natural and tripped transitions. Such behavior do not allow an effective prediction of the vortex shedding frequency. This issue is investigated in chapter 15.

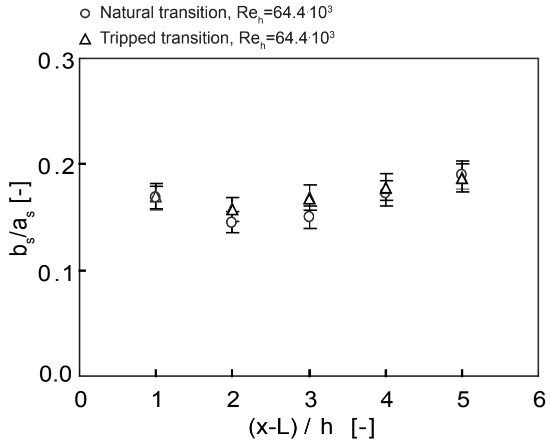

Figure 14.12: Vortex spacing ratio for natural and tripped transitions at different stations downstream from the trailing edge

Chapter 15

Normalized vortex shedding frequency

Taking advantage of boundary layer and wake flows measurements, chapters 11 and 14 respectively, normalized vortex shedding frequencies methods are assessed for the natural and the tripped turbulent transitions. Key parameters are characteristic scales of wake formation, such as boundary-layer displacement thickness at the trailing edge and wake thickness at the end of the vortex formation region, instead of body dimensions. The issue is to collapse the normalized vortex shedding frequency for the natural and the tripped transitions onto a single line, which allows an effective prediction of the vortex shedding frequency.

15.1 Modified Strouhal number

Bauer [12] normalized the vortex shedding frequency using a characteristic length scale equal to twice the boundary-layer displacement thickness plus the plate thickness, equation (15.1). The boundary-layer flow is presented in chapter 11. In particular, the boundary layer measured at the trailing edge for different free-stream velocities is shown in section 11.1. The modified Strouhal number is plotted in Figure 15.1 for different free-stream velocities and for the natural and tripped transitions.

$$St_{(h+2\delta_1)} = \frac{f_s(h+2\delta_1)}{C_{ref}} \tag{15.1}$$

For the tripped transition, a constant Strouhal number on the experimented free-stream velocity range is revealed and equal to 0.214, Figure 15.1. Consequently, the ascending trend of the Strouhal number $St_h = f_s h / C_{ref}$ with the trailing edge thickness used as the reference length, Figure 12.2, is corrected by taking into account the boundary-layer displacement thickness.

Nevertheless, a constant Strouhal number for the natural transition is not achieved, Figure 15.1. One notes a *step* in the Strouhal behavior between the two smallest experimented free-stream velocities and the others. The different states of the boundary layer between theses velocities are believed to originate the discrepancies. The form factor of the boundary-layer velocity profiles at the trailing edge for different free-stream velocities is shown in Figure 11.2 (b). The form factor values for free-stream velocities up to 10 m/s correspond to transitional boundary layer as the values for higher velocities tend to turbulent one. For free-stream velocities higher than 10 m/s, the modified Strouhal number is constant and equal to 0.235. In the same way as the tripped case, the descending feature of the Strouhal number based on the trailing edge thickness, Figure 12.2, is corrected by considering the boundary-layer displacement thickness. However, the modified Strouhal number values for the natural and the turbulent transitions are not equal. Tripping the boundary layer reduces the Strouhal number of 9%. This gap is in formal agreement with Sieverding and Heinemann [102]. Eisenlohr and Eckelmann [41] also show some dispersion of the normalized frequency data.

Therefore, it seems that the Strouhal number in which the characteristic length scale equals twice the boundary-layer displacement thickness plus the trailing edge thickness is appropriate for the normalization of the shedding frequency when the state of the boundary layer does not change with the Reynolds number. Non negligible differences in the modified Strouhal number value occur when the boundary layer is turning from laminar to turbulent state [102], and in a less extent from transitional to turbulent, this study.

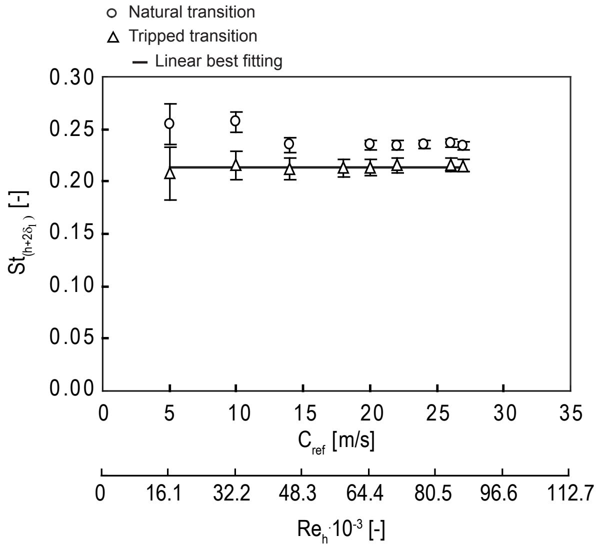

Figure 15.1: Modified Strouhal number $St_{(h+2\delta_1)} = \frac{f_s(h+2\delta_1)}{C_{ref}}$ for different free-stream velocities and for natural and tripped transitions

15.2 Roshko number

Instead of the Strouhal number, where the shedding frequency is multiplied by the inertial time scale, h/C_{ref}, Roshko [92] expressed the non-dimensional form with the help of the viscous diffusion time, h^2/ν, where ν is the kinematic viscosity. Extension of this definition to take into account the state of the boundary layer at the detachment point leads to the following relationships,

$$F_h = \frac{f_s h^2}{\nu}, \qquad F_{(h+2\delta_1)} = \frac{f_s(h+2\delta_1)^2}{\nu} \tag{15.2}$$

where δ_1 is the boundary-layer displacement thickness at the hydrofoil trailing edge. The boundary-layer velocity profiles are measured at the trailing edge for different free-stream velocities and for the natural and tripped transitions, as shown in Figure 11.1. The Roshko numbers F_h and $F_{(h+2\delta_1)}$ are plotted in Figure 15.2 with respect to the free-stream velocity. The F_h number basically displays the trend of the vortex shedding frequency versus the free-stream velocity as the reference length h and the viscosity ν are constant. Nevertheless, considering the boundary-layer displacement thickness, the $F_{(h+2\delta_1)}$ number results in a single straight line for both boundary-layer transition processes, Figure 15.2 (b). Generated using the method of least squares, the equation describing the line and its correlation coefficient are given below. Taking into account the characteristic scale of the boundary layer at the separation point leads to an effective estimation of the vortex shedding frequency.

$$
\begin{aligned}
&F_{(h+2\delta_1)} = 0.26\mathrm{Re}_h + 263.73 \\
&R^2 = 0.998
\end{aligned}
\tag{15.3}
$$

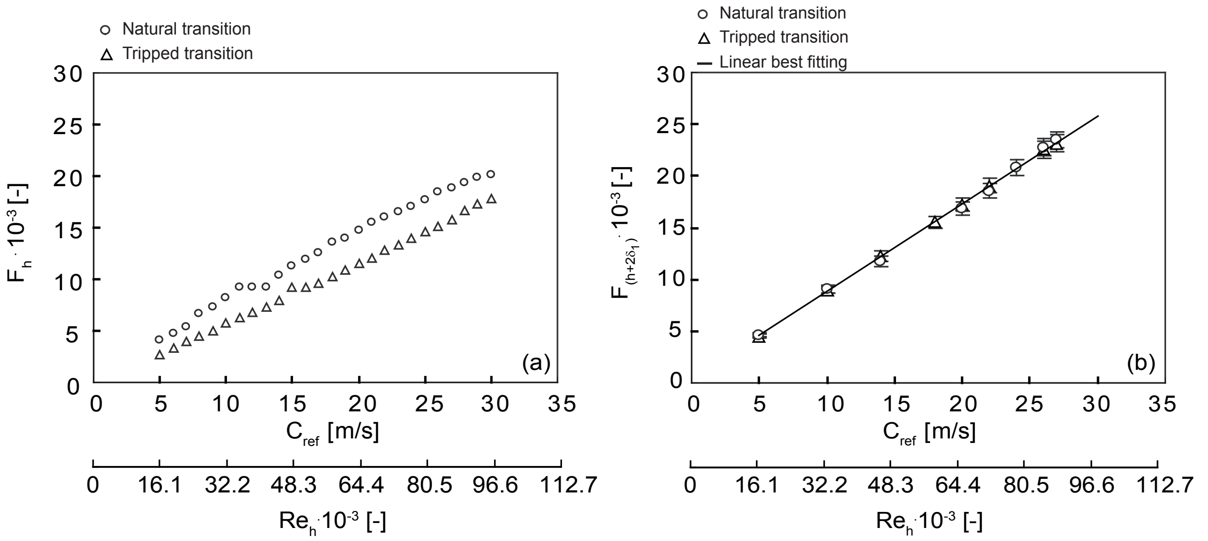

Figure 15.2: Roshko numbers (a) $F_h = \frac{f_s h^2}{\nu}$ and (b) $F_{(h+2\delta_1)} = \frac{f_s (h+2\delta_1)^2}{\nu}$ for different free-stream velocities and for natural and tripped transitions

15.3 Griffin number

For bluff body wakes, Griffin [59] introduced a normalized vortex shedding frequency, which is based on the shedding frequency, the wake width at the end of the vortex formation region and the mean velocity at the edge of the separated boundary layer on the body. This parameter was shown to collapse these characteristic scales onto a single curve for a large range of wake Reynolds numbers. The normalization is assessed here for the wake of a streamlined body and for different boundary-layer development states. The end of the vortex formation region occurs at the position downstream of the trailing edge of the maximum stream-wise velocity fluctuation, as shown in Figure 14.1. The wake width is defined as the cross-stream distance between the maxima of the stream-wise velocity fluctuation for traverse measurements across the wake at the end of the formation region, illustrated in Figures 14.2 and 14.3. The Griffin number is plotted in Figure 15.3 for different free-stream velocities and for the natural and tripped transitions. A constant normalized vortex shedding frequency is observed for the two transition processes. The mean value is 0.129. This result reveals the similarity of the wake for the two transition processes. The inter-vortex spacing ratio analysis, Figure 14.12, supports the conclusion on wake similarity.

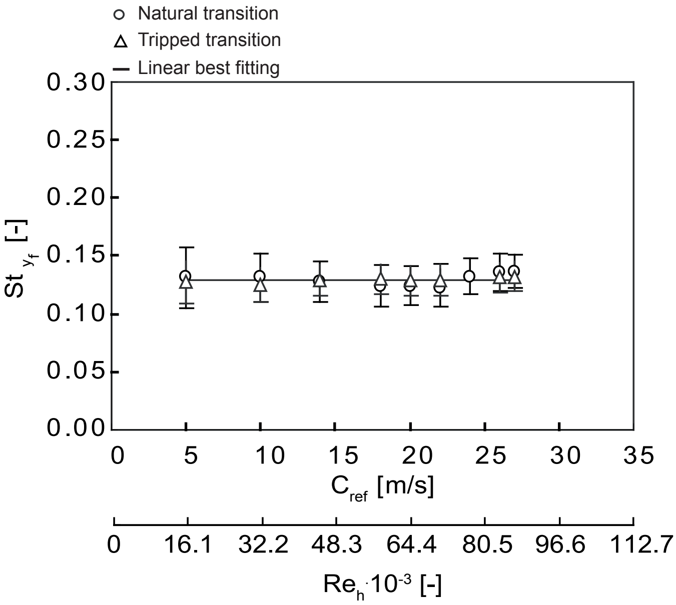

Figure 15.3: Griffin number, $St_{y_f} = \frac{f_s y_f}{C_{ref}}$, for different free-stream velocities and for natural and tripped transitions

Chapter 16

Wake flow stability property

The terms *absolute* and *convective* nature of instability describe the behavior of the impulse response of an unstable medium [79]. If an impulsively generated small amplitude transient grows exponentially in place, *i.e.* at the location of its generation, the flow is termed absolutely unstable. If, on the other hand, the transient is convected away from the source and leaves the flow ultimately undisturbed, one speaks of convective instability. Figure 16.1 summarizes the blunt-body wake situation. In the regions of absolute and convective instability, the impulse response of a one-dimensional perturbation is illustrated in the corresponding (x, t) diagrams. The range of unstable modes is limited by two rays along which the oscillation rate of the instabilities disappears. From the locally convective unstable disturbances, only downstream-traveling oscillations are propagated. In the region of absolutely unstable flow, on the other hand, the waves move upstream and downstream and therefore influence the complete area, Oertel [83]. Koch [70] suggested that the shedding frequency, occur at the location where the transition from absolute to convective instability takes place. Therefore, the existence of absolutely unstable region offers the possibility of effective wake control, the most efficient methods being achieved by avoiding the absolutely unstable region with the use of base blowing/suction, splitter plate or trailing edge geometrical modification.

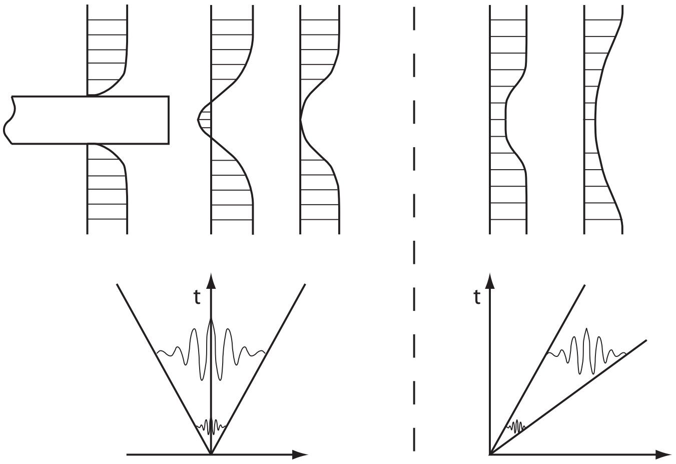

Figure 16.1: Sketch of the local wake-instability properties, Oertel [83]

16.1 Family of wake profiles and instability characteristic

A two-parameter family of symmetric wake profiles is considered [79],

$$C_x^*(y) = 1 - \Lambda + 2\Lambda F(y^*) \tag{16.1}$$

with

$$\begin{aligned} \Lambda &= (C_{x\,Cl} - C_{x\,max})/(C_{x\,Cl} + C_{x\,max}) \\ F(y^*) &= \left\{1 + \sinh^{2N}[y^* \sinh^{-1}(1)]\right\}^{-1} \end{aligned} \tag{16.2}$$

The velocities are made non-dimensional, denoted by a star superscript, with the average mean velocity $\bar{C}_x = (C_{x\,Cl} + C_{x\,max})/2$. The centerline velocity is defined by $C_{x\,Cl} = C_x(y = 0)$ and $C_{x\,max}$ is the maximum velocity which, for the family profiles considered is equal to the free-stream velocity C_{ref}. Lengths are non-dimensional with the local half-width b of the wake, which is defined by $C_x(b) = \bar{C}_x$. The two profile parameters are the velocity ratio Λ and the shape parameter N. Thereby, Λ controls the depth of the wake where $\Lambda = -1$ corresponds to a wake with zero centerline velocity. The shape parameter N controls the ratio of mixing-layer thickness to wake width. The maximum slope thickness of the mixing layer is $\delta_w = |C_{x\,max} - C_{x\,Cl}| \,/\, |dC_x/dy|_{max}$. The normalized velocity profile $F(y)$ is shown in Figure 16.2 for different N values. The boundaries for absolute and convective nature of the instability are determined as a function of the profile parameters, Λ and N^{-1}, and Reynolds number [78].

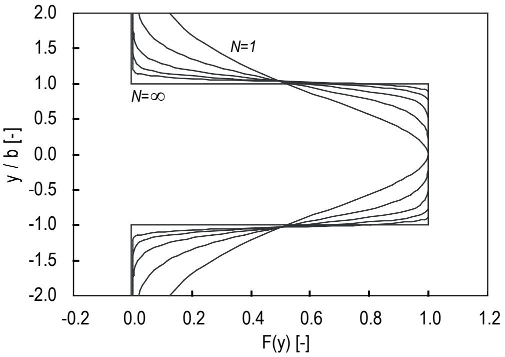

Figure 16.2: Normalized velocity profile $F(y)$, defined by equation (16.2), for $N = 1, 2, 5, 8, 16, \infty$

For our case study, the mean stream-wise velocity profiles at the end of the vortex formation region are presented in Figures 14.2 and 14.3 for the natural and tripped transitions respectively. The wake profiles, equation (16.1), are best fitted to the measured stream-wise velocity profiles with the help of Λ and N^{-1} parameters. The stability characteristics of the measured profiles are reported in Figure 16.4. The mean square error mse are shown and evidenced very good agreement between the measured and the parameter velocity profiles. Example of typical measured and parameter velocity profiles are shown in Figure 16.3 for the natural and tripped transitions, lock-off condition $Re_h = 64.4 \cdot 10^3$, and for lock-in condition $Re_h = 64.4 \cdot 10^3$.

According to the stability characteristics, Figure 16.4, and the absolute-convective instability boundaries, [78], one concludes that the instability at the end of the vortex formation region, for natural and tripped transitions, is absolutely unstable on the experimented free-stream velocity range. This result offer possibilities for wake control.

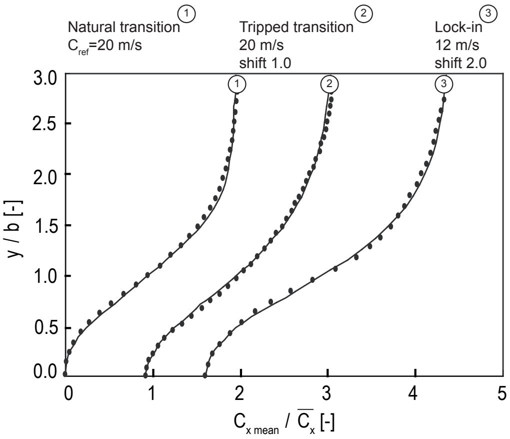

Figure 16.3: Normalized stream-wise velocity profile for natural and tripped transitions, lock-off condition $Re_h = 64.4 \cdot 10^3$, and for lock-in condition $Re_h = 64.4 \cdot 10^3$: The parameter velocity profiles, traced with a solid line, are best fitted to the measurements.

C_{ref} [m/s]	Re_h [-]	x/h [-]	$C_{x\,Cl}/C_{ref}$ [-]	$\bar{C}_x$ [m/s]	Λ [-]	b/h [-]	$\lvert dC_x/dy \rvert_{\max}$ [s^{-1}]	δ_w [mm]	N [-]	mse [-]	nature of unstability*
Lock-off: Natural transition (Tripped transition)											
5	16100	1.37 (0.90)	0.00 (-0.01)	2.43 (2.47)	-1.00 (-1.01)	0.34 (0.47)	3416 (2293)	1.36 (2.19)	1.34 (1.07)	0.07 (0.23)	Abs (Abs)
10	32200	0.71 (0.84)	-0.08 (-0.01)	4.46 (4.86)	-1.17 (-1.02)	0.31 (0.43)	8525 (4636)	1.18 (2.01)	1.40 (1.01)	0.15 (0.03)	Abs (Abs)
14	45080	0.62 (0.84)	-0.04 (-0.01)	6.47 (6.78)	-1.08 (-1.02)	0.31 (0.43)	10466 (7046)	1.29 (2.02)	1.28 (1.01)	0.10 (0.03)	Abs (Abs)
18	57960	0.71 (0.81)	0.00 (-0.01)	8.63 (8.71)	-1.01 (-1.02)	0.33 (0.42)	12500 (8969)	1.36 (2.18)	1.21 (1.00)	0.12 (0.04)	Abs (Abs)
20	64400	0.67 (0.65)	0.00 (-0.04)	9.64 (9.44)	-1.00 (-1.07)	0.33 (0.42)	12797 (10573)	1.63 (2.10)	1.18 (1.00)	0.10 (0.05)	Abs (Abs)
22	70840	0.64 (0.81)	-0.01 (0.00)	10.59 (10.76)	-1.01 (-1.00)	0.34 (0.43)	13734 (10647)	1.46 (2.03)	1.17 (1.02)	0.06 (0.07)	Abs (Abs)
26	83720	0.57 (0.78)	-0.01 (0.00)	12.40 (12.76)	-1.02 (-1.00)	0.37 (0.43)	14160 (12241)	1.63 (1.84)	1.15 (1.02)	0.10 (0.11)	Abs (Abs)
27	86940	0.53 (0.78)	0.00 (-0.01)	13.04 (13.08)	-1.00 (-1.01)	0.37 (0.42)	14310 (12851)	1.62 (2.2.11)	1.07 (1.00)	0.04 (0.04)	Abs (Abs)
lock-in: Natural transition											
12	38640	0.43	-0.16	4.87	-1.38	0.30	12587	1.37	1.11	0.06	Abs

Figure 16.4: Stability characteristics of the measured mean velocity profile at the end of the vortex formation region, * Abs=Absoluteyl unstable, Conv=Convectively unstable

The nature of the instability at different stations downstream from the trailing edge is thereafter investigated. The mean stream-wise velocity profiles are presented in Figure 14.6. Figure 16.5 presents, for natural and tripped transitions, (a) the wake centerline velocity and (b) the maximal velocity gradient at different stations from the trailing edge. The lock-in condition produces the maximum velocity defect. The maximal velocity gradient is higher for the tripped transition in comparison with the natural case but is maximized for lock-in condition, Figure 16.5 (b). Again, the wake profiles, equation (16.1), are best fitted to the measured stream-wise velocity profiles with the help of Λ and N^{-1} parameters. The stability characteristics are reported in Figure 16.6. According to the stability characteristics and the absolute-convective instability boundaries [78], one concludes that the instability downstream of the vortex formation region, for natural and tripped transitions, is convectively unstable.

Finally, the end of the vortex formation region is the farthest position from the trailing edge where the instability is absolutely unstable. This result reveal that deep wakes, including wakes with back flow, are more likely than shallow wakes to support growing disturbances that travel upstream. For farther distance, transition occurs and the instability is convectively unstable.

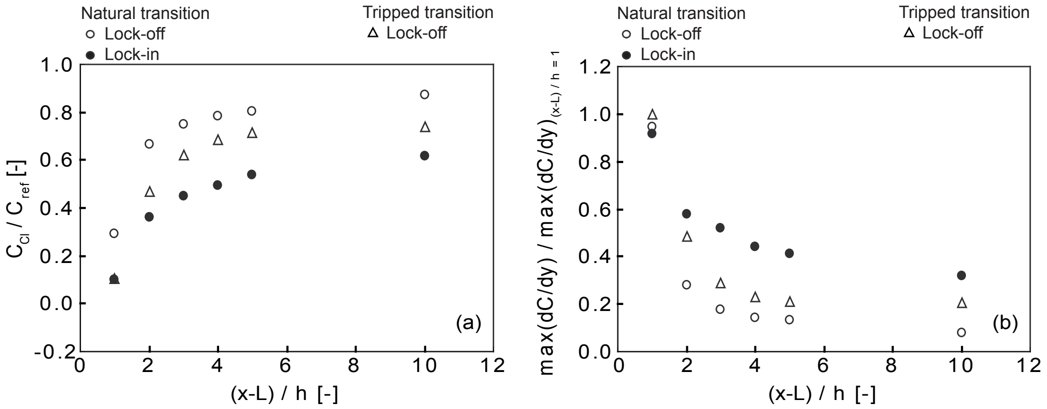

Figure 16.5: (a) Wake centerline velocity and (b) maximal velocity gradient at different stations downstream from the trailing edge and for the natural and tripped transitions

C_{ref} [m/s]	Re_h [-]	x/h [-]	$C_{x\,Cl}/C_{ref}$ [-]	$\bar{C}_x$ [m/s]	Λ [-]	b/h [-]	$\lvert dC_x/dy\rvert_{\max}$ [s^{-1}]	δ_w [mm]	N [-]	mse [-]	nature of unstability*
Lock-off: Natural transition (Tripped transition											
20	64400	1.00	0.29 (0.10)	12.37 (10.75)	-0.55 (-0.81)	0.17 (0.25)	7510 (7965)	1.89 (2.26)	1.06 (1.01)	0.04 (0.03)	Conv (Conv)
		2.00	0.66 (0.47)	15.96 (14.17)	-0.20 (-0.36)	0.06 (0.11)	2213 (3875)	3.04 (2.74)	1.24 (1.10)	0.01 (0.01)	Conv (Conv)
		3.00	0.75 (0.62)	16.93 (15.66)	-0.14 (-0.23)	0.04 (0.07)	1388 (2290)	3.59 (3.31)	1.14 (1.17)	0.00 (0.00)	Conv (Conv)
		4.00	0.78 (0.69)	17.33 (16.34)	-0.12 (-0.19)	0.04 (0.06)	1120 (1840)	3.91 (3.41)	1.00 (1.13)	0.00 (0.00)	Conv (Conv)
		5.00	0.81 (0.71)	17.66 (16.64)	-0.11 (-0.17)	0.03 (0.05)	1069 (1691)	3.64 (3.40)	1.00 (1.15)	0.00 (0.00)	Conv (Conv)
		10.00	0.87 (0.74)	18.48 (17.21)	-0.07 (-0.15)	0.02 (0.05)	626 (1641)	4.09 (3.18)	1.16 (1.16)	0.00 (0.00)	Conv (Conv)
Lock-in: Natural transition											
12	38640	1.00	0.10	6.37	-0.82	0.25	7296	1.48	1.23	0.04	Conv
		2.00	0.36	7.84	-0.47	0.15	4608	1.67	1.00	0.01	Conv
		3.00	0.45	8.39	-0.38	0.12	4143	1.60	1.00	0.02	Conv
		4.00	0.49	8.74	-0.34	0.11	3496	1.74	1.00	0.01	Conv
		5.00	0.54	9.04	-0.30	0.09	3256	1.71	1.00	0.01	Conv
		10.00	0.62	9.65	-0.24	0.07	2547	1.80	1.00	0.00	Conv

Figure 16.6: Stability characteristics of measured mean velocity profile at different stations downstream from trailing edge, * Abs=Absoluteyl unstable, Conv=Convectively unstable

Part V

Conclusions and Perspectives

Chapter 17

Conclusions

Experiments on vortex shedding from a blunt trailing edge symmetric hydrofoil operating at zero angle of attack in a uniform high speed flow, $Re_h = 16.1 \cdot 10^3 - 96.6 \cdot 10^3$ where the reference length h is the trailing edge thickness, are reported. The effects of cavitation on the generation mechanism of the vortex street are investigated. Furthermore, the effects of a tripped turbulent boundary layer on the wake characteristics are analyzed and compared with the condition of a natural turbulent transition.

For lock-off condition, the shed vortices exhibit strong span-wise instabilities and dislocations. A direct relation between vortex span-wise organization and vortex-induced vibration amplitude is found. In the case of resonance, the vortex shedding process coherence is significantly enhanced. The eigen modes are identified so that the lock-in of the vortex shedding frequency on a free-stream velocity range occurs for the torsional mode.

The vortex cavitation inception index is linearly dependent on the square root of the Reynolds number for lock-off condition. For lock-in, it is significantly increased and makes clear that the vortex roll-up is amplified by the phase locked vibrations of the trailing edge. For the cavitation inception index and considering the trailing edge displacement velocity, a new correlation relationship that encompasses the lock-off and the lock-in conditions is proposed and validated. In addition, it is found that the transverse velocity of the trailing edge increases the vortex strength linearly.

Cavitation developing in the vortex street cannot be considered as a passive agent for the visualization of the turbulent wake flow. The cavitation reacts on the wake as soon as it appears. At early stage of cavitation development, the vortex-induced vibration and flow velocity fluctuations are significantly increased. For fully developed cavitation, the vortex shedding frequency increases up to 15%, which is accompanied by the increase of the vortex advection velocity and reduction of the stream-wise and cross-stream inter-vortex spacings. These effects are addressed and thought to be a result of the increase of the vorticity by cavitation. Besides, it is shown that the cavitation does not obviously modify the vortex span-wise organization. Moreover, hydro-elastic couplings are found to be enabled/disabled by permitting a sufficient vortex cavitation development.

The effects on the wake characteristics of a tripped turbulent boundary layer, as opposed to the natural turbulent transition, are investigated. The foil surface is hydraulically smooth and a fully effective boundary-layer tripping at the leading edge is achieved with the help of a distributed roughness.

The vortex shedding process is found to be strongly influenced by the boundary-layer development. The tripped turbulent transition promotes the re-establishment of organized vortex shedding. In the context of the tripped transition and in comparison with the natural one, significant increases in the vortex span-wise organization, the induced hydrofoil vibration, the wake velocity fluctuations, the wake energies and the vortex strength are revealed. The vortex shedding process intermittency is decreased and the coherence is increased. Although the vortex shedding frequency is decreased, a modified Strouhal number based on the wake width at the end of the vortex formation region is constant and evidences the similarity of the wakes. This result leads to an effective estimation of the vortex shedding frequency.

Chapter 18

Perspectives

The complexity inherent to the wake flow calls for further experimental investigations. Moreover, the experimental results form an extensive database potentially useful for the development and the validation of computational tools.

Vortex cavitation

Cavitation in vortical structures is a common but complex problem in engineering applications. Most research has focused in the inception process and only limited results concerns developed cavitation. Even in simple case studies, both the bubble dynamics and the detailed viscous flow structure in the minimum pressure region are not clearly understood, so that studying cavitation in the vortex street is a challenging task. Tip vortex cavitation captures the essential physics associated with vortex cavitation. Its quasi-steady position is an non-negligible advantage. Analyzing the velocity field outside of the vapor phase and comparing with the one for cavitation free can give useful information in the comprehension process of vortex cavitation.

Wake flow control

Because vortex-induced vibration can cause tremendous damage to all kind of engineering structures, attempting to control the wake flow with the practical goal of reducing its fluctuations without drag penalty is an important issue. For scientific point of view, any methods can be employed for reaching the above mentioned goal. Care should be given to the fact that the method should act in the absolutely unstable region, namely the vortex formation region. Nevertheless, for industrial applications, both trailing edge geometry optimization and active control of flow blowing and/or suction through slots on the rear part of the structure seem realistic.

Fluid-structure coupling

The hydrofoil experiences an instability-induced excitation, which is the alternate vortex shedding. The control of the instability is fluid-elastic, because dependent of the flow conditions and the resonating body. The lock-in of the vortex shedding frequency on a range of free-stream velocity evidences the fluid-structure coupling phenomenon. For industrial applications, avoiding the coupling is a paramount issue. Nevertheless, modification in that sense often means the changing of the hydrodynamic shape. Advanced composites having orthotropic properties, *i.e.* different materials properties in different orthogonal directions, offer advantages in the design process: The behavior to desired targets can be tailored without necessarily changing the hydrodynamic shape. Consequently, for industrial applications, the fluid-structure coupling can be reduced/avoided by acting on the structural eigen modes and frequencies. Contrarily, for scientific point of view, the vibration amplitude can be amplified in order to strengthen the fluid-structure coupling. For such cases, interesting fields are the lock-in dynamic including free-stream velocity range, hysteresis effects and fluid damping.

CFD validation

The computations reproduce the sensitivity of the vortex shedding frequency to cavitation and boundary layer developments, Ait Bouziad [3] and Vu *et al.* [118] respectively. Despite the mentioned experimental and numerical accordances, which confirms the correct formulation of the models in reproducing this type of unsteady flow, the computations have still to be validated for specific wake characteristics such as mean and fluctuating wake velocities, vortex formation region length, wake width and vortex strength. The vortex shedding process being directly related to the development stage of the boundary layer along the hydrofoil, the computations of the boundary-layer flow has to be carefully validated. Finally, reproducing the vortex span-wise organization and the dislocations is an important issue for the prediction of the unsteady lift force.

In a second step, the response of the structure due to alternate vortex shedding can be carried out. Amplification of the vibration amplitude due to resonance condition and its influence on the wake flow can be reproduced by coupled fluid-structure simulations.

Recommendations for hydrofoil design and model testing

The effects of cavitation and boundary layer developments on the vortex street dynamic lead to recommendations for hydrofoil design. Because they modify the vortex shedding frequency due to flow over a body, there is a possibility of unexpected hydroelastic coupling if a closer match between the shedding frequency and a structural mode of vibration occurs. The manufacturers of hydraulic machinery are nowadays carrying both flow and structural analysis to identify the best design and to avoid structural resonance. However, cavitation and boundary layer effects should be carefully taken into account to prevent any failures.

Moreover, non negligible discrepancies in unsteady phenomena can occur between the model and prototype testings if boundary layer development along their vanes and blades are not similar. The IEC (International Electrotechnical Commission) norm 60193 [67] specifies the methods for model acceptance tests and states that the model surface roughness has to be hydraulically smooth. However, a laminar-turbulent boundary-layer transition can occur along model components even though the flow is turbulent in the prototype. During model testing, it is therefore recommended to tripped the turbulent transition on significant model components to avoid discrepancies.

Appendix

Appendix A

Other results of interest

A.1 Polyoxymethylene hydrofoil

The hydrofoil test model used in the entire study is made of stainless steel. The geometry, the boundary conditions and surface roughness are described in section 6.2. The vortex shedding in the wake of a less stiff hydrofoil leads to an amplification of the vibration amplitude. A hydrofoil made of polyoxymethylene (POM) featuring the same geometry is tested for free-stream velocity ranging $Re_h = 16.1 \cdot 10^3 - 64.4 \cdot 10^3$. The elasticity modulus in flexion of the POM is 3.2 GPa and is therefore reduced in comparison with the stainless steel, 200 GPa. In comparison with the stainless steal hydrofoil, the eigen frequencies are obviously changed so that the hydroelastic couplings occur for different free-stream velocities.

For resonance condition, the body deformation is macroscopic, millimeter-order amplitude, leading to significant fluid-structure interaction. The second-bending mode reveals an interesting wake feature. A neutral fiber is located at about $z/B = 0.66$ so that the hydrofoil wall motions apart from this line are in phase opposition. The body motion phase opposition leads to two vortex cells. The vortex shedding frequency of the two cells is identical and equal to the eigen frequency of the hydrofoil. However, their generation and advection are in phase opposition. Cavitation is used for the wake flow visualization and (a) top-view and (b) side-view photographs of the vortex street in shown in Figure A.1. The identical signed vorticity lines of the two vortex cells, revealed by the cavitation, are interestingly linked at the span-wise position of the neutral fiber. At this location, oblique vortex shedding occurs. Therefore, the vorticity lines are not dislocated at the position of the neutral fiber but bent so that they remains continuous along the span. The situation is however ambiguous and oblique vortex shedding at the neutral fiber position can occur with positive or negative angle depending on the linked vorticity lines.

A.2 LDV phase-averaged velocity profiles

Time-averaged velocity profiles of the wake flow are presented in chapters 8 and 14. For lock-in condition, torsional mode $Re_h = 38.6 \cdot 10^3$, the Figures A.2 and A.3 display phase-averaged stream-wise and transverse velocity profiles for different distances from the trailing edge, namely $x = L + 1h$, $x = L + 3h$ and $x = L + 5h$. Figure A.2 presents the velocity profiles for time $t/T_s = 0.00 - 0.25$ and $t/T_s = 0.25 - 0.50$ and Figure A.3

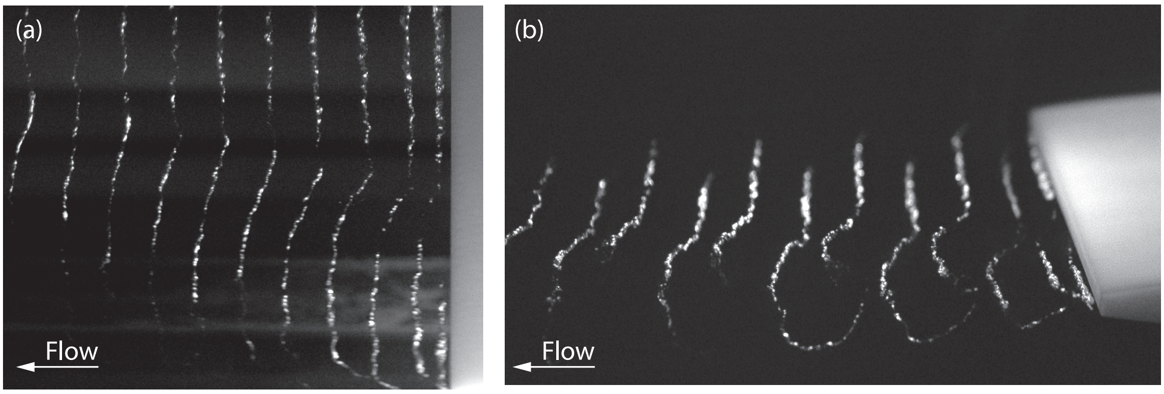

Figure A.1: (a) Top-view and (b) side-view photographs of cavitation vortex street for lock-in condition, second bending mode $Re_h = 48.3 \cdot 10^3$, $f_s = f_n = 1050$ Hz. POM hydrofoil.

presents the ones for $t/T_s = 0.5 - 0.75$ and $t/T_s = 0.75 - 1.00$. The phase averaging is perform with the help of the vortex-induced vibration signal used as the reference signal. It is connected to the LDV processor synchronization input. For lock-in condition, the vibration signal is virtually sinusoidal, Figure 8.3. As a precaution, the vibration is low pass filtered. It is amplified in order to reach the nominal high-level of the synchronization input, 2 V. The phase averaging procedure is applied directly by sorting the velocity burst signals into the corresponding phase slot based on the arrival time. 64 slots of equally time duration discretize the cycle. The vibration signal passing high-level of the synchronization input for every cycle, the time is reset for every vortex shedding cycle. The arrival rate of the synchronization pulses, *i.e.* the vortex shedding frequency, is checked during measurements. For the measurement stop criteria, according to data rate, tests have revealed that 1 min measurement duration for every vertical position is enough to have sufficient number of samples per slot. No variation of the mean value was shown for longer measurement duration. The vertical traverse measurement is depicted by 91 measurements points. For the three stations, $x = L + 1h$, $x = L + 3h$ and $x = L + 5h$, the phase reference signal remains identical, so that velocity phase shift occur for the different stations.

In Figure A.2, the origin of the time matches with the passing of the vortices center of the lower row at $x = L + 3h$. At this time and this position downstream from the trailing edge, the maximum stream-wise velocity is recorded at the vortex core edge farthest from the street centerline. The recorded velocity is the sum of the vortex advection velocity and the maximum tangential velocity. Accordingly, the minimum stream-wise velocity is recorded at the vortex core edge nearest from the street centerline. The velocity is the vortex advection velocity minus the vortex maximum tangential velocity. After a certain time, the minimum transverse velocity is recorded which is the maximal vortex tangential velocity. Symmetrically and for the vortex of the upper row, the maximum stream-wise velocity is recorded at the vortex core edge farthest from the street centerline at $t/T_s = 0.5$. After a certain time, the minimum transverse velocity is recorded. The flow is then described similarly for $t/T_s = 0.5 - 0.75$ and $t/T_s = 0.75 - 1.00$, Figure A.3. Conditioned by the symmetry of the hydrofoil and by the zero angle of attack, the maximum/minimum stream-wise velocity for the upper and lower vortex rows are virtually identical as well as the maximum/minimum transverse velocity. The phase signal remaining the same for the three stations, a velocity phase shift is evidenced for the different positions downstream from the trailing edge.

With the help of selected phase-averaged stream-wise velocity profiles, the vortex advection velocity, the vortex maximum tangential velocity, the vortex core radius and the vortex center position are estimated for the upper and lower vortex rows, Figure A.4. In Figure A.4 (a), the increase of the vortex advection velocity for increasing distance from the trailing edge is evidenced, the velocity tending to the reference velocity. Due to vorticity dissipation, the maximum vortex tangential velocity is decreased for increasing distance from the trailing edge, Figure A.4 (b). Besides, the vortex core radius is increasing in size, Figure A.4 (c). Finally, the trajectory of the vortices is depicted in Figure A.4 (d). For small distances from the trailing edge, the vertical position of the upper/lower row vortex center moves in towards the center of the wake. Downstream of $x = L + 3h$, the position moves outwards from the center line. This trajectory, which is not straight, is believed to be due to the vertical displacement of the hydrofoil trailing edge.

A.3 Computational fluid dynamics validation

The hydraulic turbines containing a casing with stay vanes face the potential dynamic problem of stay vane vortex shedding. For hydraulic efficiency purposes the stay vanes tend to be relatively slender in the direction normal to the flow thus being flexible in this direction. As a result structural vibrations may be excited by the vortex shedding at the trailing edge of the vanes. When the excitation frequency coincides with one of the natural frequencies of the stay vane, resonance occurs, which potentially initiates premature cracks.

The traditional method of determining the vortex shedding frequency is by using the empirical Strouhal number with the given blade thickness and free-stream velocity at the vane trailing edge. But this approach is not valid for geometries that are different from standard ones and the dependency of the Strouhal number on the flow Reynolds number prevent from obtaining a good empirical correlation with experimental data. A CFD methodology for the prediction of the vortex shedding frequency using unsteady flow computation is an important issue for manufacturers. An accurate prediction of excitation frequency and exciting forces is paramount in order to prevent damage. Therefore an experimental and numerical investigation of the vortex shedding phenomenon has been initiated in the context of the EPFL-Hydrodyna project. The reliable experimental measurements help to benchmark and to fine tune the CFD tools such as the choice of mesh size, computational time step, type of turbulence model or wall function. Complete description of the computational approach and flow analysis are given by Ait Bouziad [3] and Vu *et al.* [118]. The focus is thereafter put on the issue of boundary layer modeling on vortex shedding frequency estimation.

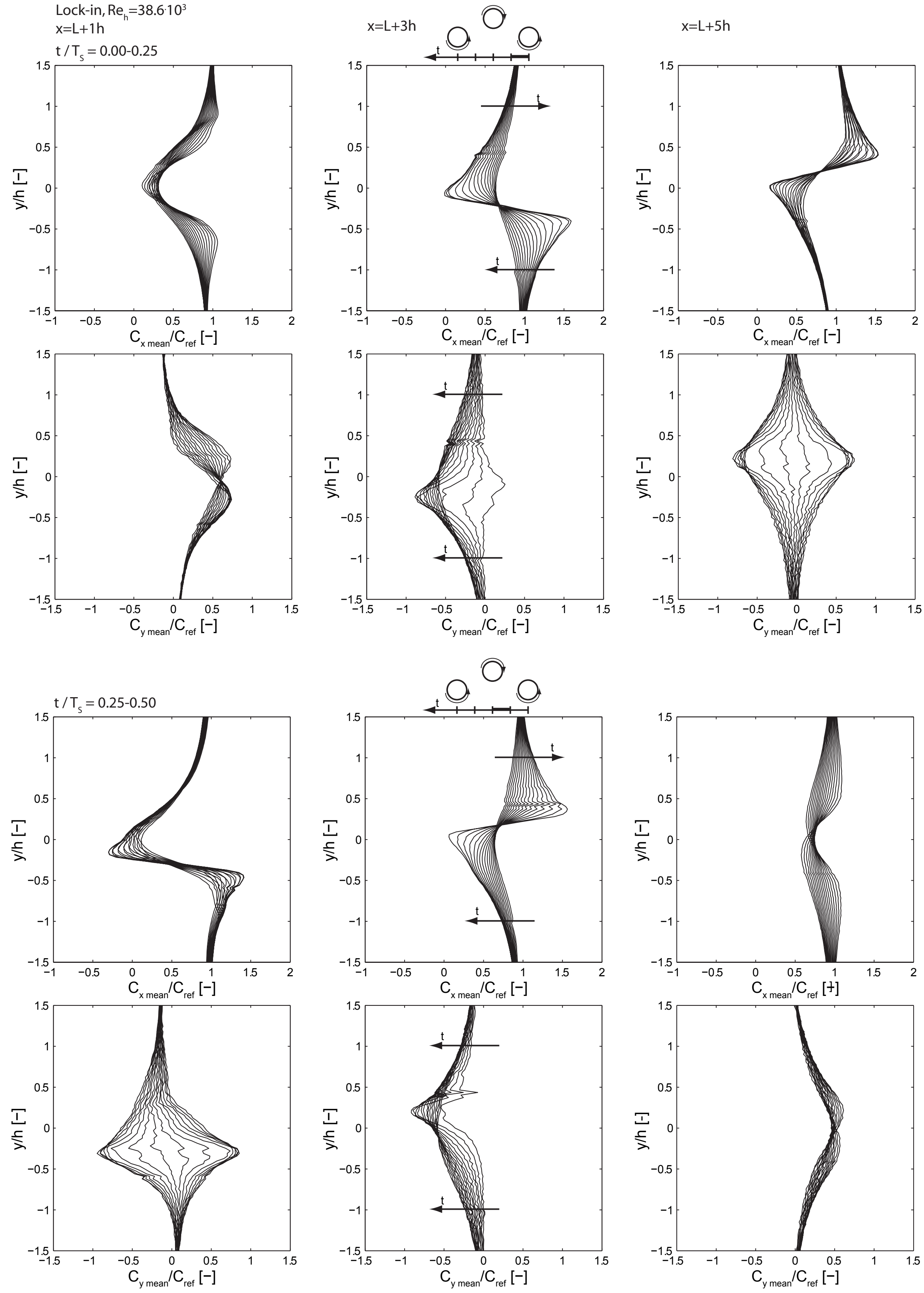

Figure A.2: Phase-averaged stream-wise and transverse velocity profiles for different distances from the trailing edge, $x = L + 1h$, $x = L + 3h$, $x = L + 5h$, for lock-in condition, torsional mode $Re_h = 38.6 \cdot 10^3$. $t/T_s = 0.00 - 0.25$ and $t/T_s = 0.25 - 0.50$

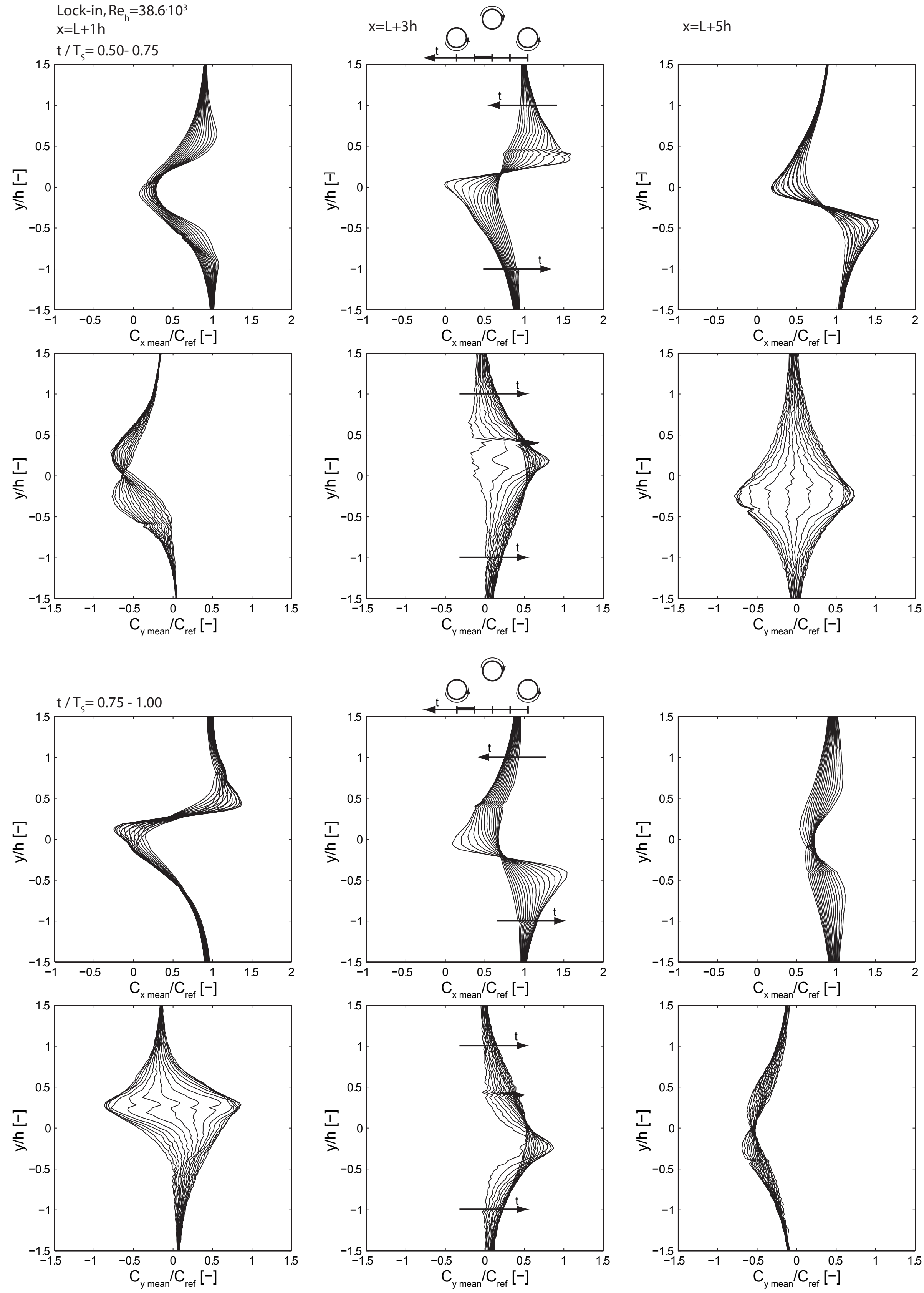

Figure A.3: Phase-averaged stream-wise and transverse velocity profiles for different distances from the trailing edge, $x = L + 1h$, $x = L + 3h$, $x = L + 5h$, for lock-in condition, torsional mode $Re_h = 38.6 \cdot 10^3$. $t/T_s = 0.5 - 0.75$ and $t/T_s = 0.75 - 1.00$

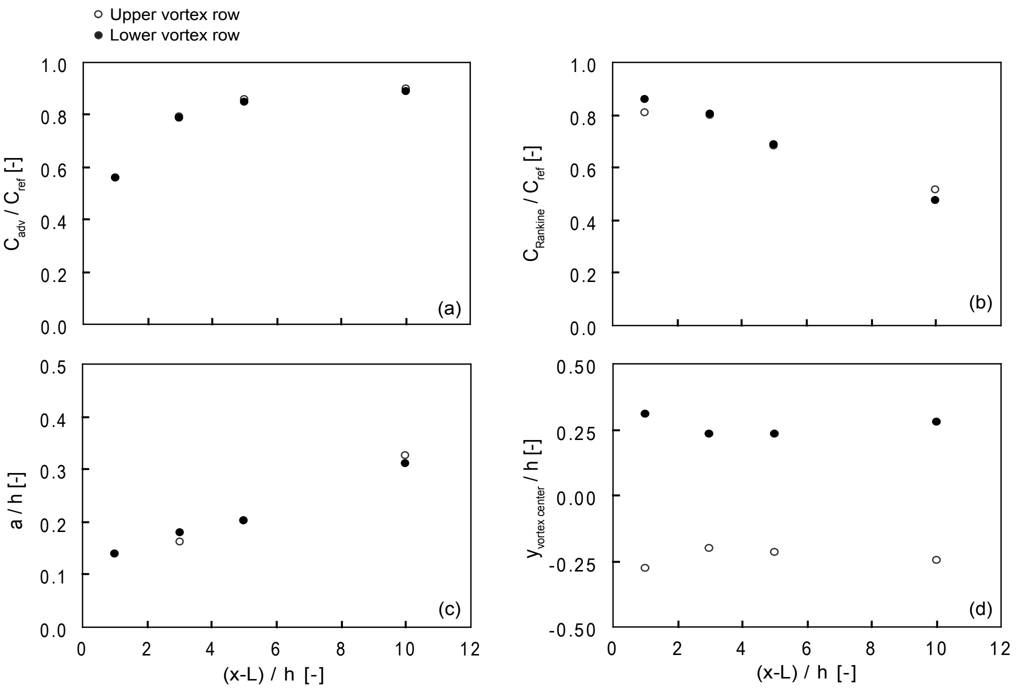

Figure A.4: Normalized (a) vortex advection velocity, (b) vortex maximum tangential velocity, (c) vortex core radius and (d) vortex center position for different distances from the trailing edge, $x = L + 1h$, $x = L + 3h$, $x = L + 5h$, $x = L + 10h$, for lock-in condition, torsional mode $Re_h = 38.6 \cdot 10^3$

Computational approach

The vortex shedding phenomenon is significantly influenced by the boundary layer development along the hydrofoil chord, part IV. Therefore it is important to obtain a good boundary layer resolution for an accurate prediction. The computational domain is the equivalent $2D$ test section of the hydrodynamic tunnel. The number of mesh nodes is 150000 and the values of the first grid points off the wall remain about $y^+ = 1$. The whole mesh generation process is carried out with the help of the *ICEMCFD* software and the simulation code is *ANSYS-CFX*. Available turbulence models for this task are standard k–ω, SST (shear stress transport) and Reynolds–Stress–ω. The difference in the vortex shedding frequency estimation among the three turbulence models is less than 1% and therefore negligible for practical purposes. In conjunction with the SST turbulence model, *ANSYS-CFX* provides a model for the laminar-turbulent boundary-layer transition.

Vortex shedding frequency

The Figure A.5 presents the experimental results of the vortex shedding frequency for different free-stream velocities and for natural and tripped turbulent transitions, chapter 12. A quasi-linear relationship between the vortex shedding frequency and the velocity is observed, provided that no hydrofoil resonance frequency is excited. The vortex shedding frequency is significantly decreased in the context of the tripped transition.

Concerning the prediction of the vortex shedding frequency, the exact configuration of the test setup has to be considered in order to specify the boundary conditions and to select appropriate turbulence model for the computation. In practical CFD calculations, the flow is considered fully turbulent which is generally valid for prototype test situations. However, the tested hydrofoil is hydraulically smooth so that the boundary-layer flow along the chord starts out as laminar and exhibits a laminar-turbulent transition, chapter 11. Therefore, using fully turbulent boundary layer model, initial attempts to validate calculations with the measurements failed. In Figure A.5 however, the computational results with the SST turbulence model match accurately enough with the experimental vortex shedding frequencies for the tripped transition case, $\Delta f_s = 7\%$. For the natural transition, the computational result with the SST-transition turbulence model is in very good agreement with experiments. One concludes that the boundary layer modeling is the main issue for an accurate vortex shedding frequency estimation.

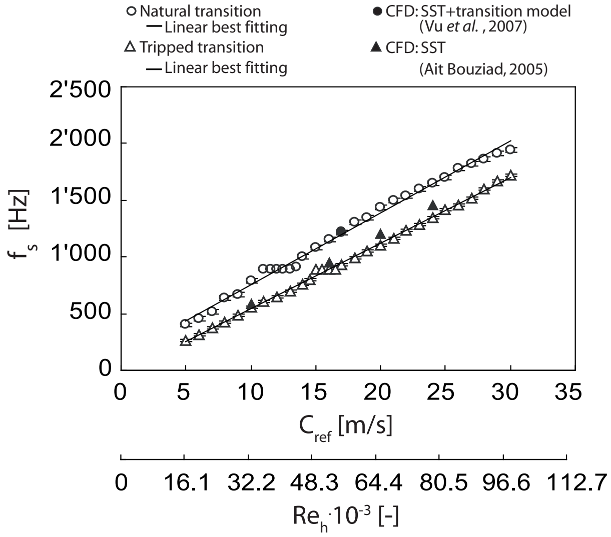

Figure A.5: Vortex shedding frequency for different reference velocities and for natural and tripped transitions: CFD validation

Appendix B

Hydro-elastic coupling: Similarity law

As the flow velocity is changed so that the vortex shedding frequency approaches one of the natural frequency of the foil, the resonance takes place with a significant increase of the vibration amplitude. The question arises as to how the free-stream velocity implying hydro-elastic coupling during model testing is modified for the prototype assuming geometrical similarity. The torsion and bending of a uniform straight bar with rectangular cross-section are investigated.

Torsion of a straight bar

A bar of rectangular section under pure torsion with following assumptions is considered in Figure B.1: The bar is straight, of uniform rectangular solid section and of homogeneous isotropic material. It is loaded only by equal and opposite twisting torque, which are applied at its end in planes normal to its axis. Finally, the bar is not stressed beyond the elastic limit. As a result, the bar twists, each section rotating about its torsional center. In the case of a hydrofoil, the length l is the chord length, h the thickness and b the span.

The moment M_t exerted on the bar having length b is proportional to the angle of twist ϕ so that,

$$\phi = \frac{M_t b}{G I_p'} \tag{B.1}$$

where $G = E/2(1+\mu)$ is the modulus of elasticity in shear for the material, E and μ the Young modulus and the Poisson ratio respectively. I_p' is a factor dependent on the form and dimensions of the cross section, Roark [90]. For a circular section, I_p' is the polar moment of inertia I_p. For other sections, I_p' may be a very small fraction of I_p.

If J denotes the mass moment of inertia of the bar about the *x–axis*, $\ddot{\phi}$ its angular acceleration and K the torsional stiffness, the differential equation of motion is,

$$J\ddot{\phi}(t) + K\phi(t) = 0 \tag{B.2}$$

Assuming a rotational vibration so that $\phi(t) = Ae^{i\omega t}$, the above equation becomes,

$$(K - J\omega^2)Ae^{i\omega t} = 0 \tag{B.3}$$

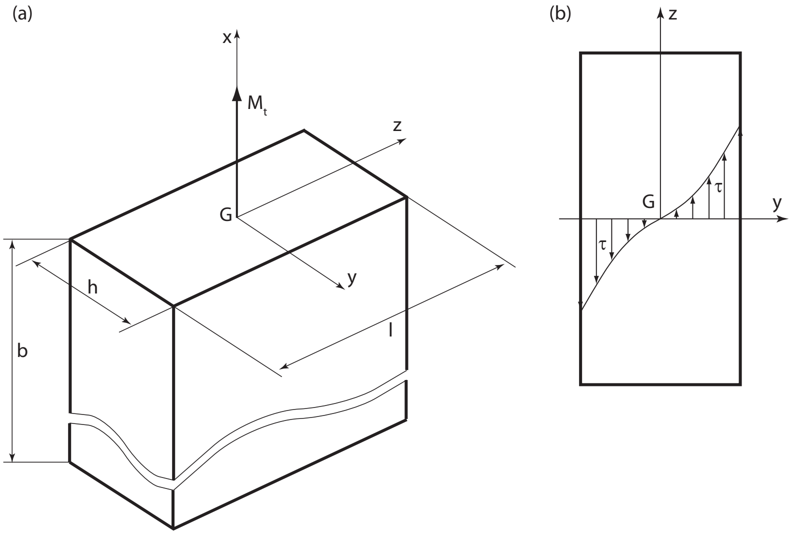

Figure B.1: Bar of rectangular section under pure torsion. (a) Geometry description and (b) shear stress distribution [34]

The equation (B.3) is satisfied if the period ω_0 and the natural frequency f_0 of the system are respectively,

$$\omega_{torsion} = \sqrt{\frac{K}{J}} \qquad f_{torsion} = \frac{\omega_{torsion}}{2\pi} = \frac{1}{2\pi}\sqrt{\frac{K}{J}} \tag{B.4}$$

For a uniform bar, which the mass is uniformly distributed along the *x–axis*, in torsional vibration with one end fixed and the other free, the factor N_n is introduced according to the mode of vibration n, Table B.1. The natural frequency (B.4) is therefore expressed by

$$f_{torsion} = \frac{N_n}{2\pi}\sqrt{\frac{K}{J}} \tag{B.5}$$

Table B.1: Constants referring to the mode of vibration for a uniform bar in torsional vibration, one end fixed the other free [90]

Eigen mode	Torsional mode: N_n value
1^{st}	1.57
2^{nd}	4.71
3^{rd}	7.85

The inertia to be taken into account in the torsional stiffness is [90]

$$I'_p = \beta l h^3 \tag{B.6}$$

where β is a factor dependent on the ratio l/h. Therefore, the torsional stiffness is,

$$K = \frac{GI'_p}{b} = G\beta\,\frac{lh^3}{b} \tag{B.7}$$

The mass moment of inertia J is

$$J = \frac{m(l^2 + h^2)}{12} = \frac{\rho bhl(l^2 + h^2)}{12} \tag{B.8}$$

Finally, the natural frequencies are

$$f_{torsion} = \frac{N_n}{2\pi}\sqrt{\frac{K}{J}} = \frac{N_n}{2\pi}\sqrt{12\frac{G\beta}{\rho}\frac{h^2}{b^2(l^2 + h^2)}} \tag{B.9}$$

Besides, the Strouhal number St_h, whose reference length is the thickness h of the bar, is

$$St_h = \frac{f_s h}{C_{ref}} \tag{B.10}$$

Matching the vortex shedding frequency and the natural frequency of the system $f_s = f_{torsion}$ means,

$$\frac{St_h C_{ref}}{h} = \frac{N_n}{2\pi}\sqrt{12\frac{G\beta}{\rho}\frac{h^2}{b^2(l^2 + h^2)}} \tag{B.11}$$

According to equation (B.11), the torsional resonance occurs for a free-stream velocity given by,

$$C_{ref} = \frac{N_n}{2\pi\, St_h}\sqrt{12\frac{G\beta}{\rho}\,\frac{h^4}{b^2(l^2 + h^2)}} \tag{B.12}$$

The geometrical similarity between the model $()_M$ and the prototype $()_P$ leads to

$$\left(\frac{h^4}{b^2(l^2 + h^2)}\right)_M = \left(\frac{h^4}{b^2(l^2 + h^2)}\right)_P \tag{B.13}$$

β is function of the ratio l/h, so that

$$(\beta)_M = (\beta)_P \tag{B.14}$$

Finally, the ratio G and ρ are properties of the material

$$\left(\frac{G}{\rho}\right)_M = \left(\frac{G}{\rho}\right)_P \tag{B.15}$$

The Strouhal number St_h being constant on specific free-stream velocity range and considering equations (B.13) to (B.15), the condition (B.12) becomes,

$$\underline{(\mathbf{C_{ref}})_{\mathbf{M}} = (\mathbf{C_{ref}})_{\mathbf{P}}} \tag{B.16}$$

Accordingly to the above development and assuming the geometrical similarity, if the torsional resonance occurs during model testing, it is expected to excite the torsional mode in the prototype at the same free-stream velocity.

Bending of a straight bar

Similarly to the torsion of a straight bar, the analysis of the bending is proposed. A bar of solid rectangular section under bending with following assumptions is considered in Figure B.2. The bar is straight and of homogeneous material that has the same modulus of elasticity in tension and compression. All loads and reactions are perpendicular to the axis of the beam and lie in the same plane, which is the longitudinal plane of symmetry. Finally, the bar is not stressed beyond the elastic limit. As a result, the beam bends: The fibers in the convex side lengthen and fibers on the concave side shorten. Plane sections remain plane and hence fiber strains and stresses are proportional to distance from the neutral surface.

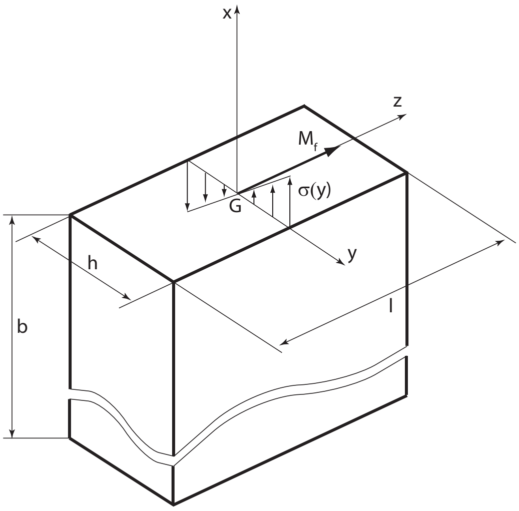

Figure B.2: Bar of rectangular section under bending [34]

At any point, there is a longitudinal fiber stress σ, which is tensile if the point lies between the neutral and convex surfaces of the bar and compressive if the point lies between the neutral and concave surfaces of the bar. Let J the moment of inertia of the section of the beam with respect to the neutral axis and E the modulus of elasticity of the material, the fiber stress σ at any point is

$$\sigma(y) = \frac{M_f y}{J} \tag{B.17}$$

where M_f is the bending moment at the section containing the considered point and y the distance from the neutral axis to the point.

Two normal sections F_1 and F_2 of the bar, which are separated by a distance dx, are considered. After deformation, the section F_2' forms an angle $d\varphi$ with the section F_1'. The neutral fiber becomes an arc, whose radius is ϱ. By definition, the neutral fiber does not lengthen nor shorten so that,

$$dx = \varrho d\theta \tag{B.18}$$

A fiber separated by a distance y from the neutral fiber is lengthened of εdx. According to the Hooke law and equation (B.17), the deformation is

$$\varepsilon dx = \frac{\sigma}{E} dx = \frac{M_f y}{EJ} dx \tag{B.19}$$

As $\varepsilon dx = y d\theta$, the above equation becomes,

$$d\theta = \frac{M_f}{EJ} dx \tag{B.20}$$

According to equation (B.18) and (B.20), the curvature is

$$\frac{1}{\varrho} = \frac{M_f}{EJ} \tag{B.21}$$

Geometrically and assuming small deformations, the curvature can be shown to be

$$\frac{1}{\varrho} = \frac{y''}{(1+y'^2)^{3/2}} \cong y'' \tag{B.22}$$

where $y' = dy/dx$ and $y'' = d^2y/dx^2$. Therefore and according to (B.21) and (B.22), the general differential equation of the elastic bar is

$$y'' = \frac{M}{EJ} \tag{B.23}$$

Solution of this equation for the vertical deflection y is effected by writing out the expression for $M(x)$, integrating twice and determining the constants of integration by the boundary conditions. The deflection is given in [34] for various load types and boundary conditions. For a uniform load p per unit length, the maximal deflection is

$$y_{max} = \frac{5}{384} \frac{pb^4}{EJ} \tag{B.24}$$

The bending stiffness is therefore,

$$K = \frac{p}{y_{max}} = \frac{384}{5} \frac{EJ}{b^4} \tag{B.25}$$

The natural frequency of the system is

$$f_{bending} = \frac{N_n'}{2\pi} \sqrt{\frac{K}{p}} = \frac{N_n}{2\pi} \sqrt{\frac{EJ}{pb^4}} \tag{B.26}$$

where N_n depends on boundary conditions and on the mode of vibrations. The values for N_n are given in Table B.2, [90]

According to the direction of M_f, Figure B.2, the moment of inertia J for the rectangular section is,

$$J = \frac{lh^3}{12} \tag{B.27}$$

Table B.2: Constants referring to the mode of vibration for a uniform bar under bending, one end fixed the other free [90]

Eigen mode	Bending mode: N_n value
1^{st}	3.5
2^{nd}	22.0
3^{rd}	61.7

The mass per unit length of the bar is

$$m = \rho h l \tag{B.28}$$

Finally, the natural frequency, equation (B.26), becomes

$$f_{bending} = \frac{N_n}{2\pi} \frac{h}{b^2} \sqrt{\frac{E}{12\rho}} \tag{B.29}$$

The Strouhal number St_h, whose reference length is the thickness h of the bar, is

$$St_h = \frac{f_s h}{C_{ref}} \tag{B.30}$$

Matching the vortex shedding frequency and the natural frequency of the system $f_s = f_{bending}$, *i.e.* lock-in, and arranging terms lead to

$$C_{ref} = \frac{N_n}{2\pi \, St_h} \left(\frac{h}{b}\right)^2 \sqrt{\frac{E}{12\rho}} \tag{B.31}$$

As observed for the straight bar under pure torsion, assuming geometrical similarity between the model and the prototype, if the bending resonance occurs during model testing, it is expected to excite the bending mode in the prototype at the same free-stream velocity,

$$\underline{(\mathbf{C_{ref}})_{\mathbf{M}} = (\mathbf{C_{ref}})_{\mathbf{P}}} \tag{B.32}$$

Appendix C

Body oscillator

Because the main goal is to identify the mechanism by which hydrofoil vibrations are induced, the structural dynamics are presented in the simplest way throughout this chapter. Therefore, the vibrating structure is represented as a discrete mass m, free to oscillate with one degree of freedom, linearly damped and supported by a linear spring.

Free vibration

An initial displacement x_0 produces free vibrations which is analyzed with the equation of motion,

$$m\ddot{x} = \sum F_x \tag{C.1}$$

where $\ddot{x} = d^2x/dt^2$. In the case of a linear spring of constant k, the restoring force is $-kx$. Including a linear damping, the equation (C.1) takes the form,

$$m\ddot{x} + c\dot{x} + kx = 0 \tag{C.2}$$

One introduce following notations

$$\omega_0 = \sqrt{\frac{k}{m}}\ , \qquad \lambda = \frac{c}{2m}\ , \qquad \eta = \frac{c}{2m\omega_0} = \frac{\lambda}{\omega_0} \tag{C.3}$$

where ω_0 is the eigen pulsation of the undamped system, λ the damping factor and η the relative damping factor. Dividing equation (C.2) by the mass and introducing above notations leads to

$$\ddot{x} + 2\lambda\dot{x} + \omega_0^2 x = 0 \tag{C.4}$$

The solution of this equation is

$$x = Ae^{r_1 t} + Be^{r_2 t} \tag{C.5}$$

with $r_1 = -\lambda + \sqrt{\lambda^2 - \omega_0^2}$ and $r_2 = -\lambda - \sqrt{\lambda^2 - \omega_0^2}$.

Forced vibration

Harmonic exciting force

If the simple oscillator is acted upon by a harmonic exciting force

$$f(t) = F \cos \omega t \tag{C.6}$$

the equation of motion takes the form

$$\ddot{x} + 2\lambda\dot{x} + \omega_0^2 x = \frac{1}{m} F \cos \omega t \tag{C.7}$$

We are looking for a steady solution of the form

$$x(t) = A \cos \omega t + B \sin \omega t \tag{C.8}$$

Introducing the displacement $x(t)$, equation (C.8), and its derivatives into (C.7), we find

$$x(t) = X \cos(\omega t - \varphi) \tag{C.9}$$

where $X = \sqrt{A^2 + B^2}$ and $\tan \varphi = B/A$ so that

$$X = \frac{F}{\sqrt{\left(k - \omega^2 m\right)^2 + \omega^2 c^2}}\ , \qquad \tan \varphi = \frac{\omega c}{k - \omega^2 m} \tag{C.10}$$

In addition to (C.3), one introduce the quantities

$$\beta = \frac{\omega}{\omega_0}\ , \qquad X_s = \frac{F}{k}\ , \qquad \mu = \frac{X}{X_s} \tag{C.11}$$

where β is the relative pulsation, X_s the static displacement due to a constant force F and μ the magnification factor. Equation (C.10) becomes

$$X = \frac{F/k}{\sqrt{\left(1 - \frac{\omega^2 m}{k}\right)^2 + \frac{\omega^2 c^2}{k^2}}} = \frac{X_s}{\sqrt{\left(1 - \left(\frac{\omega}{\omega_0}\right)^2\right)^2 + 4\eta^2 \left(\frac{\omega}{\omega_0}\right)^2}} \tag{C.12}$$

The magnification factor is given by

$$\mu = \frac{1}{\sqrt{(1 - \beta^2)^2 + 4\eta^2\beta^2}} \tag{C.13}$$

Besides and accordingly to equation (C.10), the phase angle is

$$\tan \varphi = \frac{2\eta\beta}{1 - \beta^2} \tag{C.14}$$

Independently of the relative damping factor η, the external force and the displacement are in phase $\varphi = 0$ when the pulsation tends to zero and in phase opposition $\varphi = \pi$ when the pulsation tends to infinity. The phase is $\varphi = \pi/2$ in case of resonance, $\omega = \omega_0$ ($\beta = 1$). In Figure C.1, the magnification factor is plotted versus the relative pulsation β and for different values of the relative damping factor η. The phase angle φ by which the response x lags the exciting force f is also evidenced.

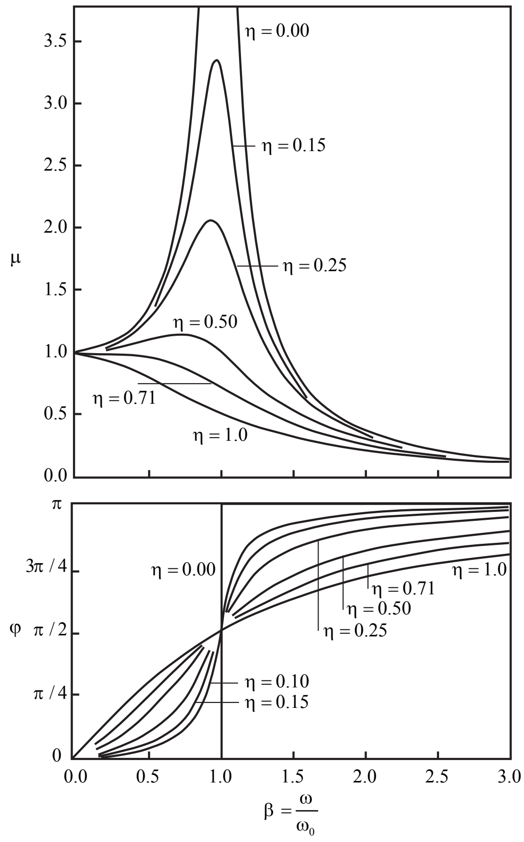

Figure C.1: Magnification factor and phase angle for forced vibration of a linear body oscillator [34]

Periodic exciting force

When the exciting force is not harmonic, it can be represented by a series of harmonic functions whose frequencies are integer multiples of a fundamental frequency ω. The external force is therefore written as

$$f(t) = \frac{1}{2}F_0 + \sum_{N=1}^{\infty} A_n \cos n\omega t + B_n \sin n\omega t \tag{C.15}$$

Grouping the sine and cosine function of identical pulsation leads to

$$f(t) = \frac{1}{2}F_0 + \sum_{N=1}^{\infty} F_n \cos(n\omega t - \psi_n) \tag{C.16}$$

where $F_n = \sqrt{A_n^2 + B_n^2}$ and $\tan\psi_n = B_n/A_n$. If the system of the body is linear, linear differential equation (equation C.7), its responses to the different harmonics can be deduced separately and then added. Accordingly to equation (C.9), we have

$$x(t) = \frac{1}{2}\frac{F_0}{k} + \sum_{N=1}^{\infty} X_n \cos(n\omega t - \psi_n - \varphi_n) \tag{C.17}$$

Clearly, the response $x(t)$ is periodic just as is $f(t)$. If the value of one of the harmonics $n\omega$ of the excitation is close to the natural frequency ω_0 of the system, this harmonic will provide a relatively larger contribution to the response because associated with peak value of the magnification factor $\mu(\omega)$.

Non periodic exciting force

Non periodic and random excitation are analyzed by means of spectrum. If one treats the body oscillator as a linear system, then the relationship between the excitation and the response spectra is given by [80]

$$S_x(f) = \left(\frac{\mu(f)}{k}\right)^2 S_F(f) \tag{C.18}$$

where S_F and S_x are the exciting force and the response power spectral densities. The equation implies that one has to multiply each amplitude of the excitation spectrum with the corresponding value of $(\mu/k)^2$ to obtain the amplitude of the response spectrum. Therefore, if the excitation spectra is broad band so that specific energies occur at the eigen frequencies of the structure, the vibration amplitudes at these frequencies will be significantly amplified because associated with peak value of the magnification factor.

References

References

[1] Achenbach, E., and Heinecke, E. On vortex shedding from smooth and rough cylinders in the range of Reynolds numbers $6 \cdot 10^3$ to $5 \cdot 10^6$. *Journal of Fluid Mechanics 109* (1981), 239–251.

[2] Ahlborn, F. Ueber den Mechanismus des Hydro-Dynamischen Widerstandes. *Abh. Geb. Naturwiss* (1902).

[3] Ait Bouziad, Y. *Physical modelling of leading edge cavitation : Computational methodologies and application to hydraulic machinery.* PhD thesis, EPFL, No 3353, 2005.

[4] Albrecht, H., Borys, M., Damaschke, N., and Tropea, C. *Laser doppler and phase doppler measurement techniques.* Springer, 2003.

[5] Arndt, R. E. A. Semi-empirical analysis of cavitation in the wake of a sharp-edged disk. *Journal of Fluids Engineering, Transactions of the ASME 98*, 3 (1976), 560–562.

[6] Arndt, R. E. A. Cavitation in fluid machinery and hydraulic structures. *Annual Review of Fluid Mechanics 13* (1981), 273–328.

[7] Arndt, R. E. A. Cavitation in vortical flows. *Annual Review of Fluid Mechanics 34* (2002), 143–175.

[8] Arndt, R. E. A., and Keller, A. P. Water quality effects on cavitation inception in a trailing vortex. *Journal of Fluids Engineering, Transactions of the ASME 114*, 3 (1992), 430–438.

[9] Ausoni, P., Farhat, M., Escaler, X., Egusquiza, E., and Avellan, F. Cavitation influence on von Kármán vortex shedding and induced hydrofoil vibrations. *Journal of Fluids Engineering, Transactions of the ASME 129*, 8 (2007), 966–973.

[10] Avellan, F., Henry, P., and Rhyming, I. A new high speed cavitation tunnel for cavitation studies in hydaulic machinery. In *American Society of Mechanical Engineers, Fluids Engineering Division FED* (1987), vol. 57, pp. 49–60.

[11] Baker, W. F., Korista, D. S., and Novak, L. C. Burj Dubai: Engineering the world's tallest building. *The Structural Design of Tall and Special Buildings 16(4)* (2007), 361–375.

[12] Bauer, A. B. Vortex shedding from thin flat plates parallel to the free stream. *Journal of the Aerospace Sciences 28*, 4 (1961), 340–341.

[13] Bearman, P. W. Investigation of flow behind a 2-dimensional model with a blunt trailing edge and fitted with splitter plates. *Journal of Fluid Mechanics 21*, Part 2 (1965), 241–255.

[14] Bearman, P. W. On vortex shedding from a circular cylinder in the critical Reynolds number regime. *Journal of Fluid Mechanics 37*, Part 4 (1969), 577–585.

[15] Bearman, P. W. Vortex shedding from oscillating bluff bodies. *Annual review of fluid mechanics 16* (1984), 195–222.

[16] Belahadji, B., Franc, J. P., and Michel, J. M. Cavitation in the rotational structures of a turbulent wake. *Journal of Fluid Mechanics 287* (1995), 383–403.

[17] Bendat, J., and Piersol, A. *Random data: Analysis and measurement procedures.* Wiley-Interscience, John Wiley, 1971.

[18] Bernitsas, M. M., Raghavan, K., Ben-Simon, Y., and Garcia, E. M. H. Vivace (vortex induced vibration aquatic clean energy): A new concept in generation of clean and renewable energy from fluid flow. *Journal of Offshore Mechanics and Arctic Engineering 130* (2008), 041101.

[19] Blackburn, H. M., and Melbourne, W. H. The effect of free-stream turbulence on sectional lift forces on a circular cylinder. *Journal of Fluid Mechanics 306* (1996), 267–292.

[20] Blake, W. K. *Mechanics of flow induced sound and vibration.* Academic Press INC, Orlando, United States of America, 1986.

[21] Blevins, R. D. The effect of sound on vortex shedding from cylinders. *Journal of Fluid Mechanics 161* (1985), 217–237.

[22] Blevins, R. D. *Flow-induced vibration.* Van Nostrand Reinhold, 1990.

[23] Bloor, M. S. The transition to turbulence in the wake of a circular cylinder. *Journal of Fluid Mechanics 19*, 2 (1964), 290–304.

[24] Bénard, H. Formation de centres de giration à l'arrière d'un obstacle en mouvement. *Comptes rendus de l'Académie des Sciences, Paris 147* (1908), 839–842.

[25] Born, M., and Wolf, E. *Principles of optics.* Pergamon press, 1980.

[26] Brennen, C. E. A review of added mass and fluid inertial forces. *Naval Civil Engineering Laboratory, Port Hueneme, California CR82.10* (1982), 1–50.

[27] Briggs, L. J. Limiting negative pressure of water. *Journal of Applied Physics 21* (1950), 721–722.

[28] Buchhave, P., George Jr., W. L., and Lumley, J. L. The measurement of turbulence with the laser-doppler anemometer. *Annual Review of Fluid Mechanics 11* (1979), 443–503.

[29] Cadot, O., and Lebey, M. Shear instability inhibition in a cylinder wake by local injection of a viscoelastic fluid. *Physics of Fluids 11(2)* (1999), 494–496.

[30] Cheung, J. C. K., and Melbourne, W. H. Turbulence effects on some aerodynamic parameters of a circular cylinder at supercritical numbers. *Journal of Wind Engineering and Industrial Aerodynamics 14*, 1-3 (1983), 399–410.

[31] Choi, J., and Ceccio, S. L. Dynamics and noise emission of vortex cavitation bubbles. *Journal of Fluid Mechanics 575* (2007), 1–26.

[32] Coles, D. The law of the wake in the turbulent boundary layer. *Journal of Fluid Mechanics 1* (1956), 191–226.

[33] Davies, M. E. Comparison of the wake structure of a stationary and oscillating bluff body, using a conditional averaging technique. *Journal of Fluid Mechanics 75*, MAY27 (1976), 209–231.

[34] Del Pedro, M., and Gmür, T. *Eléments de mécaniques des structures.* PPUR presses polytechniques, 2001.

[35] Donaldson, R. M. Hydraulic turbine runner vibration. *Journal of Engineering for Power 78* (1956), 1141–1147.

[36] Drazin, P. G., and Reid, W. H. *Hydrodynamic stability.* Cambridge university press, 2004.

[37] Drela, M., and Giles, M. B. Viscous-inviscid analysis of transonic and low Reynolds number airfoils. *AIAA Journal 25*, 10 (1987), 1347–1355.

[38] Dryden, H. L. Review of published data on the effect of roughness on transition from laminar to turbulent flow. *Journal of the Aeronautical Sciences 20*, 7 (1953), 477–482.

[39] Dupont, P. *Etude de la dynamique d'une poche de cavitation partielle en vue de la prédiction de l'érosion dans les turbomachines hydrauliques.* PhD thesis, EPFL, N0 931, 1993.

[40] Dupont, P., Avellan, F., and M., W. Wake flow analysis for a hydrofoil with and without hydroelastic lock-in. In *Proc. Int. Conf. on Flow Induced Vibrations, BHRA, Bowness-on-Windermere, England* (1987).

[41] Eisenlohr, H., and Eckelmann, H. Observations in the laminar wake of a thin plate with a blunt trailing edge. *Experimental Heat Transfer, Fluid Mechanics and Thermodynamics 1* (1988), 264–268.

[42] Eisenlohr, H., and Eckelmann, H. Vortex splitting and its consequences in the vortex street wake of cylinders at low Reynolds number. *Physics of Fluids A 1(2)* (1989), 189–192.

[43] El-Gammal, M., and Hangan, H. Three-dimensional wake dynamics of a blunt and divergent trailing edge airfoil. *Experiments in Fluids 44*, 5 (2008), 705–717.

[44] Feng, C. C. *The measurement of vortex-induced effects in flow past stationary and oscillating circular and D-section cylinders.* PhD thesis, University of British Columbia, 1968.

[45] Fisher, R. K., Seidel, U., Grosse, G., Gfeller, W., and Klinger, R. A case study in resonant hydroelastic vibration: The causes of runner cracks and the solutions implemented for the Xiaolangdi hydroelectric project. *Proceedings of the Hydraulic Machinery and Systems 21st IAHR Symposium, Lausanne* (2002), 895–906.

[46] Flachsbart, O. *Geschichte der experimentellen Hydro- und Aeromechanik, insbesondere der Widerstandsforschung.* Handbuch der Experimentalphysik, 1932.

[47] Franc, J.-P., Avellan, F., Belahadji, B., Billard, J.-Y., Briançon-marjolet, L., Fréchou, D., Fruman, D. H., Karimi, A., Kueny, J.-L., and Michel, J.-M. *La cavitation: Mécamismes physiques et aspects industriels.* Presses universitaires de Grenoble, 1995.

[48] Franc, J. P., and Michel, J. M. *Fundamentals of cavitation.* Kluwer academic publishers, 2004.

[49] Fransson, J. M. H. Flow control of boundary layers and wakes. *Technical reports from Royal Institute od Technology* (2003), 1–59.

[50] Gerich, D., and Eckelmann, H. Influence of endplates and free ends on the shedding frequency of circular cylinders. *Journal of Fluid Mechanics 122* (1982), 109–122.

[51] Gerrard, J. H. The mechanics of the formation region of vortices behind bluff bodies. *Journal of Fluid Mechanics 25*, Part 2 (1966), 401–413.

[52] Gerrard, J. H. The wakes of cylindrical bluff bodies at low Reynolds number. *Philosophical Transactions for the Royal Society of London, Mathematical and Physical Sciences 288*, 1354 (1978), 351–382.

[53] Gilbert, S., and Sigurdson, L. Hydrogen bubble flow visualization of a self-oscillating cylinder vortex street void. *Physics of Fluids 17*, 9 (2005), 091104.

[54] Glezer, A., and Amitay, M. Synthetic jets. *Annual Reviews in Fluid Mechanics 34* (2002), 503–529.

[55] Goldwag, E., and Berry, D. G. Von Kármán hydraulic vortices cause stay vane cracking on propeller turbines at Little Long generating station of Ontario Hydro. *Journal of Engineering for Power 90*, 3 (1968), 213–217.

[56] Gongwer, C. A. A study of vanes singing in water. *Journal of Applied Mechanics 19* (1952), 432–438.

[57] Greenway, M. E., and Wood, C. J. The effect of a bevelled trailing edge on vortex shedding and vibration. *Journal of Fluid Mechanics 61(2)* (1973), 323–355.

[58] Grein, H., and Staehle, M. Rupture par fatigue d'entretoises d'avant-distributeurs de grandes turbines. *Bulletin Escher Wyss 1* (1978), 33–37.

[59] Griffin, O. M. Universal similarity in the wakes of stationary and vibrating bluff structures. *Journal of Fluids Engineering, Transactions of the ASME 103*, 1 (1981), 52–58.

[60] Griffin, O. M. Flow similitude and vortex lock-on in bluff body near wakes. *Physics of Fluids A 1*, 4 (1989), 697–703.

[61] Griffin, O. M. A note on bluff body vortex formation. *Journal of Fluid Mechanics 284* (1995), 217–224.

[62] Guennoun, M. F. *Etude physique de l'apparition et du développement de la cavitation sur une aube isolée.* PhD thesis, EPFL, N0 3574, 2006.

[63] Gummer, J. H., and Hensman, P. C. A review of stayvane cracking in hydraulic turbines. *Water Power and Dam Construction 44(8)* (1992), 32–42.

[64] Gutsche, F. Das Singen von Shiffsschrauben. *Zeitschrift des vereines deutscher Ingenieure 81* (1937), 882–883.

[65] Hammache, M., and Gharib, M. Experimental study of the parallel and oblique vortex shedding from circular cylinders. *Journal of Fluid Mechanics 232* (1991), 567–590.

[66] Heskestad, F., and Olberts, D. R. Influence of trailing edge geometry on hydraulic-turbine blade vibration. *Journal of Engineering for Power 82* (1960), 103–110.

[67] International Electrotechnic Commission. Standard hydraulic turbines, storage pumps and pump-turbines - Model acceptance tests. *IEC 60193* (1999).

[68] Kim, W., Yoo, J. Y., and Sung, J. Dynamics of vortex lock-on in a perturbed cylinder wake. *Physics of Fluids 18*, 7 (2006), 074103.

[69] Knapp, R. T., Daily, J. W., and Hammitt, F. G. *Cavitation.* McGraw-Hill Inc., New York, 1970.

[70] Koch, W. Local instability characteristics and frequency determination of self-excited wake flows. *Journal of Sound and Vibration 99(1)* (1985), 53–83.

[71] Koopmann, G. H. The vortex wakes of vibrating cylinders at low Reynolds numbers. *Journal of Fluid Mechanics 28* (1976), 501–512.

[72] Kourta, A., Boisson, H. C., Chassaing, P., and Minh, H. H. Nonlinear interaction and the transition to turbulence in the wake of a circular cylinder. *Journal of Fluid Mechanics 181* (1987), 141–161.

[73] Lockey, K. J., Keller, M., Sick, M., Staehle, M. H., and Gehrer, A. Flow-induced vibrations at stay vanes: Experience on site and CFD simulations. *The International Journal on Hydropower and Dams 5* (2006), 102–106.

[74] Mallat, S. G. *A wavelet tour of signal processing.* Academic Press, 1999.

[75] Mallock, A. On the resistance of air. *Proceeding of the Royal Society of London series A, 79* (1907), 262–265.

[76] Mathelin, L., Bataille, F., and Lallemand, A. The effect of uniform blowing on the flow past a circular cylinder. *Journal of Fluids Engineering 124* (2002), 452–464.

[77] Mattsson, R. Bending and acoustic waves in a water-filled box studied by pulsed tv holography and ldv. *Optics and Lasers in Engineering 44(11)* (2006), 1146–1157.

[78] Monkewitz, P. A. The absolute and convective nature of instability in two-dimensional wakes at low Reynolds numbers. *Physics of Fluids 31*, 5 (1988), 999–1006.

[79] Monkewitz, P. A., and Nguyen, L. N. Absolute instability in the near-wake of two-dimensional bluff bodies. *Journal of Fluids and Structures 1*, 2 (1987), 165–184.

[80] Naudascher, E., and Rockwell, D. *Flow-induced vibrations: An engineering guide.* Blakema publishers, 1994.

[81] Norberg, C. Effects of Reynolds number and a low-intensity free stream turbulence on the flow around a circular cylinder. *Dept of Applied Thermodynamics and Fluid Mechanics, Chalmers University of Technology 2* (1987), 1–55.

[82] Norberg, C. An experimental investigation of the flow around a circular cylinder: Influence of aspect ratio. *Journal of Fluid Mechanics 258* (1994), 287–316.

[83] Oertel, H. Wakes behind blunt bodies. *Annual Review of Fluid Mechanics 22* (1990), 539–564.

[84] Park, D. S., Ladd, D. M., and Hendricks, E. W. Feedback control of von Kármán vortex shedding behind a circular cylinder at low Reynolds numbers. *Physics of Fluids 6* (1994), 2390.

[85] Perry, A. E., Chong, M. S., and Lim, T. T. The vortex-shedding process behind two-dimensional bluff-bodies. *Journal of Fluid Mechanics 116* (1982), 77–90.

[86] Prasad, A., and Williamson, C. H. K. The instability of the shear layer separating from a bluff body. *Journal of Fluid Mechanics 333* (1997), 375–402.

[87] Ramamurthy, A. S., and Balachandar, R. The near wake characteristics of cavitating bluff sources. *Journal of Fluids Engineering, Transactions of the ASME 112* (1990), 492–495.

[88] Rao, B. C. S., and Petrikat, K. The vortex induced vibrations of a flat plate in cavitating flow. In *Proceedings of the IAHR symposium on hydraulic machinery and systems, Colorado* (1978).

[89] Rioul, O., and Vetterli, M. Wavelets and signal processing. *IEEE Signal Processing Magazine 8(4)* (1991), 14–38.

[90] Roark, R., and Young, W. *Formulas for stress and strain.* McGraw-Hill book compagny, 1975.

[91] Rockwell, D. Vortex-body interactions. *Annual Review of Fluid Mechanics 30* (1998), 199–229.

[92] Roshko, A. On the development of the turbulent wakes from vortex streets. *National Advisory Committee for Aeronautics 1191*, 2 (1954), 1–25.

[93] Roshko, A. Experiments on the flow past a circular cylinder at very high Reynolds number. *Journal of Fluid Mechanics 10*, 2 (1961), 345–356.

[94] Roussopoulos, K. Feedback control of vortex shedding at low Reynolds numbers. *Journal of Fluid Mechanics 248* (1993), 267–296.

[95] Ryhming, I. *Dynamique des fluides.* PPUR presses polytechniques, 2004.

[96] Sarpkaya, T. Vortex-induced oscillations - A selective review. *Journal of Applied Mechanics 46* (1979), 241–258.

[97] Sarpkaya, T. A critical review of the intrinsic nature of vortex-induced vibrations. *Journal of Fluids and Structures 19(4)* (2004), 389–447.

[98] Schaeffer, J. W., and Eskinazi, S. An analysis of the vortex street generated in a viscous fluid. *Journal of Fluid Mechanics 6*, 2 (1959), 241–260.

[99] Schlichting, H., and Gersten, K. *Boundary layer theory.* McGraw-Hill Series in Mechanical Engineering, McGraw-Hill, 1979.

[100] Shi, Q. Abnormal noise and runner cracks caused by von Kármán vortex shedding: A case study in Dachaoshan hydroelectric project. In *Proceedings of the 22sd IAHR symposium on hydraulic machinery and systems, Stockholm* (2004).

[101] Shih, W. C. L., Wang, C., Coles, D., and Roshko, A. Experiments on flow past rough circular cylinders at large Reynolds numbers. *Journal of Wind Engineering and Industrial Aerodynamics 49*, 1-3 (1993), 351–368.

[102] Sieverding, C. H., and Heinemann, H. Influence of boundary layer state on vortex shedding from flat plates and turbine cascades. *Journal of Turbomachinery 112*, 2 (1990), 181–187.

[103] Singha, S., Sinhamahapatra, K. P., and Mukherjea, S. K. Control of vortex shedding from a bluff body using imposed magnetic field. *Journal of Fluids Engineering 129* (2007), 517–523.

[104] Slaouti, A., and Gerrard, J. H. An experimental investigation of the end effects on the wake of a circular cylinder towed through water at low Reynolds number. *Journal of Fluid Mechanics 112* (1981), 297–314.

[105] Sridhar, G., and Katz, J. Effect of entrained bubbles on the structure of vortex rings. *Journal of Fluid Mechanics 397* (1999), 171–202.

[106] Stäger, R., and Eckelmann, H. The effect of endplates on the shedding frequency of circular cylinders in the irregular range. *Physics of Fluids 3* (1991), 2116.

[107] Strouhal, V. Uber eine besondere Art der Tonerregung. *Ann. Phys. und Chemie 10* (1878), 216–251.

[108] Szepessy, S. On the spanwise correlation of vortex shedding from a circular cylinder at high subcritical Reynolds number. *Physics of Fluids 6*, 7 (1994), 2406–2416.

[109] Szepessy, S., and Bearman, P. W. Aspect ratio and end plate effects on vortex shedding from a circular cylinder. *Journal of Fluid Mechanics 234* (1992), 191–217.

[110] Taneda, S. Experimental investigation of the wakes behind cylinders and plates at low Reynolds numbers. *Journal of Physical Society Japan 11(3)* (1956), 302–307.

[111] Toebes, G. H. The unsteady flow and wake near an oscillating cylinder. *Journal of Basic Engineering 91* (1969), 493–502.

[112] Tokumaru, P., and Dimotakis, P. Rotary oscillation control of a cylinder wake. *Journal of Fluid Mechanics 224* (1991), 77–90.

[113] Tritton, D. J. Experiments on the flow past a circular cylinder at low Reynolds number. *Journal of Fluid Mechanics 6* (1959), 547–567.

[114] Unal, M. F., and Rockwell, D. On vortex formation from a cylinder. Part 1. The initial instability. *Journal of Fluid Mechanics 190* (1988), 491–512.

[115] von Kármán, T. Ueber den Mechanismus des Widerstandes, den ein bewegter Körper in einer Flüssigkeit erfährt. *Nachrichten von der Gesellschaft der Wissenschaften zu Göttingen Mathematisch-Physikalische Klasse* (1911), 509–517.

[116] von Kármán, T. Ueber den Mechanismus des Widerstandes, den ein bewegter Körper in einer Flüssigkeit erfährt. *Nachrichten von der Gesellschaft der Wissenschaften zu Göttingen Mathematisch-Physikalische Klasse* (1912), 547–556.

[117] von Kármán, T. *Aerodynamics : Selected topics in the light of their historical development.* Cornell University Press, 1954.

[118] Vu, T., Nennemann, B., Ausoni, P., Farhat, M., and Avellan, F. Unsteady CFD prediction of von Kármán vortex shedding in hydraulic turbine stay vanes. In *Proceeding of Hydro 2007, Granada, Spain* (2007).

[119] White, F. M. *Viscous fluid flow.* McGraw-Hill Inc., New York, 1974.

[120] Wilcox, D. C. *Basic Fluid Mechanics.* DCW Industries, 1997.

[121] Williamson, C. H. K. Defining a universal and continuous Strouhal-Reynolds number relationship for the laminar vortex shedding of a circular cylinder. *Physics of Fluids 31* (1988), 2742.

[122] Williamson, C. H. K. The existence of two stages in the transition to three-dimensionality of a cylinder wake. *Physics of Fluids 31* (1988), 3165.

[123] Williamson, C. H. K. The natural and forced formation of spot-like 'vortex dislocations' in the transition of a wake. *Journal of Fluid Mechanics 243* (1992), 393–441.

[124] Williamson, C. H. K. Vortex dynamics in the cylinder wake. *Annual Review of Fluid Mechanics 28* (1996), 477–539.

[125] Williamson, C. H. K., and Brown, G. L. A series in $1/\sqrt{Re}$ to represent the Strouhal-Reynolds number relationship of the cylinder wake. *Journal of Fluids and Structures 12* (1998), 1073–1085.

[126] Williamson, C. H. K., and Govardhan, R. Vortex-induced vibrations. *Annual Review of Fluid Mechanics 36* (2004), 413–455.

[127] Williamson, C. H. K., and Roshko, A. Vortex formation in the wake of an oscillating cylinder. *Journal of Fluids and Structures Volume 2, Issue 4* (1988), 355–381.

[128] Young, J. O., and Holl, J. W. Effects of cavitation on periodic wakes behind symmetric wedges. *Journal of Basic Engineering 88*, 1 (1966), 163–176.

[129] Zhang, Q., Lee, S. W., and Ligrani, P. M. Effects of surface roughness and freestream turbulence on the wake turbulence structure of a symmetric airfoil. *Physics of Fluids 16*, 6 (2004), 2044–2053.

[130] Zheng, Q., Durben, D. J., Wolf, G. H., and Angell, C. A. Liquids at large negative pressures: Water at the homogeneous nucleation limit. *Science 254* (1991), 829–832.

Index

Accelerometer, 41
Added mass, 39

Boundary layer, 15, 89, 119
  displacement thickness, 15, 119
  form factor, 15, 89, 94
  inner variables, 17, 91, 94
  momentum thickness, 15
  structure, 17, 91, 94
  thickness, 15, 89, 94
  transition, 16, 90
  tripping, 16, 19, 36, 89

Cavitation, 21, 53
  developed, 73
  free, 53
  inception, 21, 69
  tunnel, 33
  types, 22
Coherence, 44, 49, 102
Computational fluid dynamics, 137
Cracks, 12
Cross-correlation, 49, 76

Eigen
  frequency, 44, 60, 135
  mode, 44, 60, 135

Fast Fourier Transform, 44
  short time, 56, 75, 104
Flow
  cylinder, 6
  quality, 34
  regime, 6
  stability, 28, 123
Free-stream turbulence, 27, 34

Griffin number, 25, 121

High-speed visualization, 50, 82, 101
Hydro-elastic coupling, 11, 28, 38, 60, 97, 135, 143
Hydrofoil, 36

Laser Doppler Velocimetry, 45
  phase-averaged, 135
  time-averaged, 65, 89, 109, 114
Laser Doppler vibrometer, 41
Lock-in, 11, 28, 53, 60, 97, 135

Particle Image Velocimetry, 47, 62

Reynolds number, 6, 10
Roshko number, 26, 120

Similarity, 38, 143
Strouhal number, 8, 25, 53, 97, 119
Surface
  hydraulically smooth, 36
  roughness, 10, 27, 36

Vortex
  advection velocity, 76
  cavitation, 23, 29
  cavitation inception, 24
  formation region, 26, 109, 121
  Rankine, 23
  spacing, 76, 117
  strength, 70
Vortex shedding
  coherence, 102
  dislocation, 27, 53, 56, 62, 73, 98, 101
  frequency, 53, 74, 85, 97
  intermittency, 56, 75, 103, 104
  normalized frequency, 53, 97, 119
Vortex strength, 110
Vortex-induced vibration, 10, 28, 54, 74, 85, 97

Wake
  control, 14
  energy, 66, 114
  structure, 73, 82, 101
  width, 26, 109, 121

Curriculum Vitae

Philippe Ausoni

Rue Carlo Boller 1
1820 Montreux
Suisse

+41 79 469 66 33
philippe.ausoni@a3.epfl.ch

Suisse
Né le 19 juillet 1980

FORMATION

2005-2009 **Doctorat ès sciences techniques**
Ecole Polytechnique Fédérale de Lausanne (EPFL), Suisse

2000-2004 **Master en Génie Mécanique, EPF**
2004: Diplôme au Laboratoire de Machines Hydrauliques
2003: ETH Zürich. Orientation: Turbomachines et Mécaniques des Fluides
2002: EPF Lausanne. Orientation: Turbomachines et Conception mécanique

1997-2000 **Baccalauréat ès sciences**
Gymnase de Burier (VD)

EXPERIENCES PROFESSIONNELLES

2005-2009 **Ecole Polytechnique Fédérale de Lausanne (EPFL), Suisse**
Laboratoire de Machines Hydrauliques (LMH)

Activités de recherche:
Thèse de Doctorat: Etude expérimentale du détachement tourbillonnaire dans le sillage d'un profil hydrodynamique symétrique

- Mesures de pressions pariétales et de vibrations
- Mesures de champs de vitesses à l'aide des techniques lasers PIV et LDV
- Visualisation à haute vitesse

Rédaction de publications scientifiques et participation à divers congrès

Activités d'enseignement:

- Participation au cours Cavitation et phénomènes d'interfaces
- Encadrement de travaux pratiques de Masters
- Préparation de séances d'exercices et d'examens

2003 **VA Tech Hydro AG, Zürich, Suisse**
Etude numérique et analytique du moment hydraulique s'exerçant sur les aubes directrices de turbines Francis et Kaplan

2001 **Bobst Group, Prilly, Suisse**
Stage d'usinage: Réalisation d'un moteur pneumatique
Collaboration dans divers secteurs de l'entreprise

dès 1998 **La Griffe Ausoni Montreux SA, Suisse**
Administrateur de l'entreprise familiale

COMPETENCES INFORMATIQUES

Systèmes	Windows, Mac OS
Programmation	Labview, Matlab, Visual Basic, C
CAO	Ideas
Bureautique	MS-Office, Latex
Multimédia	MS-Office, Suite Adobe

LANGUES

Français	Langue maternelle
Anglais	Avancé
Allemand	Avancé

List of Publications

Journal papers

1. Ausoni, P., Farhat, M., and Avellan, F., The effects of a tripped turbulent boundary layer on vortex shedding from a blunt trailing edge hydrofoil, *Physics of Fluids, Submitted for publication*

2. Münch, C., Ausoni, P., Braun, O., Farhat, M., and Avellan, F., Fluid-structure coupling for oscillating hydrofoil, *Journal of Fluids and Structures, Submitted for publication*

3. Ausoni, P., Farhat, M., Escaler, X., Egusquiza, E., and Avellan, F., Cavitation influence on von Kármán vortex shedding and induced hydrofoil vibrations, *Journal of Fluids Engineering, Transactions of the ASME, 129, 8(2007), 966-973*

Conference papers

1. Münch, C., Ausoni, P., Braun, O., Farhat, M., and Avellan, F., Hydro-elastic behavior of vibrating blades, *Proceeding of the IAHR 24th Symposium on Hydraulic Machinery and System, Foz Do Iguassu, Bresil, October 2008*

2. Ausoni, P., Farhat, M., and Avellan, F., Hydrofoil roughness effects on von Kármán vortex shedding, *Proceeding of the IAHR Int. Meeting of the Workgroup on Cavitation and Dynamic Problems in Hydraulic Machinery and Systems, Timisoara, Romania, October 2007*

3. Münch, C., Ausoni, P., Farhat, M., and Avellan, F., 2D oscillating hydrofoil, *Proceeding of the IAHR Int. Meeting of the Workgroup on Cavitation and Dynamic Problems in Hydraulic Machinery and Systems, Timisoara, Romania, October 2007*

4. Vu, T., Nennemann, B., Ausoni, P., Farhat, M., and Avellan, F., Unsteady CFD prediction of von Kármán vortex shedding in hydraulic turbine stay vanes, *Proceeding of Hydro 2007, Granada, Spain, October 2007*

5. Ausoni, P., Farhat, M., and Avellan, F., Cavitation in Kármán vortex shedding from 2D hydrofoil: Wall roughness effects, *Proceeding of the ASME JSME FEDSM2007, San Diego, USA, July 2007*

6. Ausoni, P., Farhat, M., Escaler, X., and Avellan, F., Cavitation in Kármán vortices and flow induced vibrations, *Proceeding of the Int. Symposium on Cavitation CAV2006, Wageningen, The Netherlands, September 2006*

7. Escaler, X., Ausoni, P., Farhat, M., Egusquiza, E., and Avellan, F., Cavitation monitoring of hydroturbines: Tests in a Francis turbine model, *Proceeding of the Int. Symposium on Cavitation CAV2006, Wageningen, The Netherlands, September 2006*

8. Ausoni, P., Farhat, M., Ait Bouziad, Y., Kueny, J.L., and Avellan, F., Kármán vortex shedding in the wake of a 2D hydrofoil: Measurement and numerical simulation, *Proceeding of the IAHR Int. Meeting of the Workgroup on Cavitation and Dynamic Problems in Hydraulic Machinery and Systems, Barcelona, Spain, June 2006*

9. Ausoni, P., Farhat, M., Escaler, X., Egusquiza, E., and Avellan, F., Cavitation effects on fluid-structure interaction in the case of a 2D hydrofoil, *Proceeding of the ASME FEDSM2005, Houston, USA, June 2005*